Nonlinear Dynamics of Three Dimensional Fluid Flow Separation

by

Amit Surana

B.Tech., Mechanical Engineering
Indian Institute of Technology Bombay, 2000
M.S., Mechanical Engineering
Pennsylvania State University, 2002
M.A., Mathematics
Pennsylvania State University, 2003

Submitted to the Department of Mechanical Engineering
in partial fulfillment of the requirements for the degree of

Doctor of Philosophy in Mechanical Engineering

at the

MASSACHUSETTS INSTITUTE OF TECHNOLOGY

September 2007

Author ....
Department of Mechanical Engineering
July 30, 2007

Certified by ....
George Haller
Professor of Mechanical Engineering
Thesis Supervisor

Accepted by ....
Lalit Anand
Chairman, Department Committee on Graduate Students

Nonlinear Dynamics of Three Dimensional Fluid Flow Separation

by

Amit Surana

Submitted to the Department of Mechanical Engineering
on July 30, 2007, in partial fulfillment of the
requirements for the degree of
Doctor of Philosophy in Mechanical Engineering

Abstract

Flow separation (the detachment of fluid from a no-slip boundary) is a major cause of performance loss in engineering devices, including diffusers, airfoils and jet engines. The systematic study of flow separation dates back to the seminal work of Prandtl in 1904. He showed that a two-dimensional steady flow separates from a no-slip boundary at points where the wall shear vanishes and admits a negative gradient. Three-dimensional flows, however, tend to separate along lines, as opposed to isolated wall-shear zeros. Despite widespread effort, no generally applicable extension of Prandtl's result has emerged for even three-dimensional steady flows.

In this thesis we develop a nonlinear theory for separation and attachment of steady and unsteady three-dimensional fluid flows on no-slip curved moving boundaries. The theory provides analytic criteria for locating the separation line and approximating the shape of separation surface. Based on nonlinear dynamical systems techniques, the criteria identify separation line and separation surface by locating nonhyperbolic unstable manifolds that collect and eject fluid particles from the boundary.

We verify our theory on analytic flow models, in numerical simulations of important benchmark problems and in experiments. Our theory provides a systematic tool for diagnostics, configuration design and active flow control of separation and attachment in complex three dimensional fluid flows.

Thesis Supervisor: George Haller
Title: Professor of Mechanical Engineering

Acknowledgments

I express my sincerest gratitude to Prof. George Haller for his invaluable guidance, support and encouragement. He is an outstanding advisor and excellent professor. I admire his rigorous and novel approach to problem solving. Working with him has not only strengthened my technical know how but also have greatly enhanced my writing, communication and presentation skills. It has been a great privilege for me to have got the opportunity to work with him.

I thank my committee members Prof. Thomas Peacock and Prof. Gareth McKinley for their helpful suggestions and guidance. I thank Prof. Peacock for taking a lot of interest in my work and for the experimental support. A special thanks to Mr. Andrew Gallant who provided prompt and timely support in building the experimental apparatus. I am grateful to Prof. Guus Jacobs for providing numerical data from his simulations; without which this work could not have been completed.

The past few years in the lab has been a great experience. I would like to thank my lab mates: Olivier Grunberg, Mohammed Reza Alam, Mustafa Sabri Kilic, Yildiray Yildiz, Manikandan Mathur, and Wenbo Tang for the enlightening discussions and memorable time I spent with them. I would like to thank my friends Ajay Desphande, Amit Deshpande, Binayak Roy, Kripa Varanasi, Pavithra Harsha, Sreekar Bhaviripudi and Vijay Shilpiekandula. I will forever cherish the quality time I have spent with them at MIT.

Most of all, I thank my parents, grandparents, brother, bhabhi and Anuja for their constant love, care and support. Their affection, instruction and inspiration has always provided me with the means to excel and find the right direction in life. Finally I thank Sonal for her love and affection and the joy she has brought into my life.

Contents

List of Figures

List of Tables

Chapter 1

Introduction

Fluid flow separation can be loosely defined as breaking of fluid particles from a boundary. It is an ubiquitous phenomena arising in many engineering, physical and biological systems. It occurs at many scales, ranging from insect flight to motion of clouds around terrain (see Fig. 1-1).

The accurate identification of separation patterns in three-dimensional fluid flows is important for a number of applications. For instance, separation and attachment has a major impact on mixing in combustors, and on the aerodynamic forces acting on an aircraft, a submarine, or a passenger car. In several instances, the separation location itself is crucially important to detect. Drag reduction by wall-based flow control, for example, is known to be most effective when the actuators are placed close to separation surfaces.

1.1 Prior work on three-dimensional steady separation

Prandtl [74] showed that a two-dimensional steady flow separates from a no-slip boundary at isolated points where the wall shear (skin friction) vanishes and admits a negative gradient. The extension of these criteria to unsteady 2D flows have appeared only recently [39],[52]. By contrast, numerical simulations and experiments show three-dimensional flows to separate along lines (see figure 1-2), not isolated wall-shear zeros (for e.g. see Tobak & Peake [94], Chapman [11], Simpson [84] and Délery [20] for reviews).

The most prominent on-wall signature of three-dimensional separation is the wall-shear distribution it generates. Legendre [57] proposed to analyze such distributions using the geometric theory of two-dimensional smooth vector fields. In such an analysis, one first locates zeros (critical points) of the wall-shear field, identifies their stability type, then constructs the phase portrait of wall-shear trajectories. This critical-point based local approach to three-dimensional separation was adopted and refined by several authors (e.g., Perry & Fairlie [73], Hunt et al. [45], Dallmann [16] and Yates & Chapman [11]; see Délery [20] for further references).

Taking a more global view, Lighthill [60] proposed that convergence of wall-shear

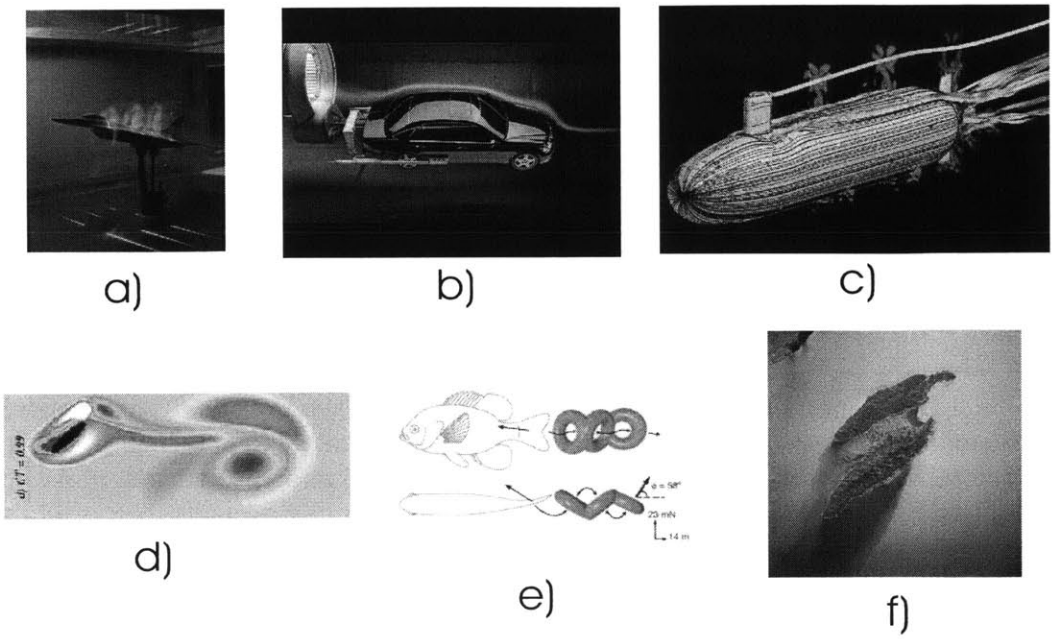

Figure 1-1: Fluid flow separation at different scales (a)Airplane (b)Car (c)Submarine (d)Insect flight (e)Fish Locomotion (f) Clouds over terrain

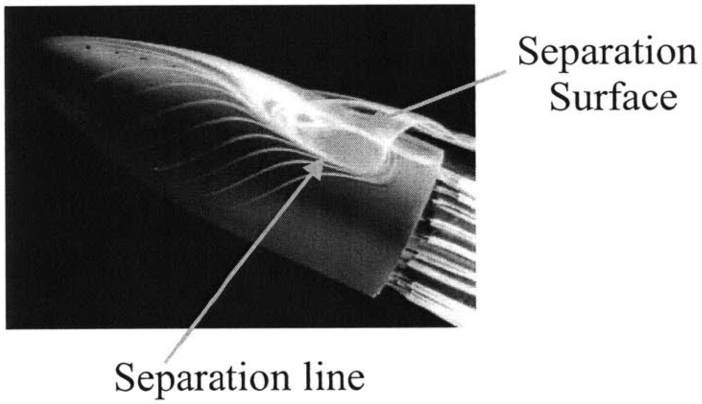

Figure 1-2: Typically 3D separation occurs along a separation surface with a associated separation line: experimental flow visualization of flow past a bullet [20].

lines is a necessary criterion for separation. He went on to deduce that separation lines always start from saddle-type wall-shear zeros and terminate at stable spirals or nodes. Ever since, this heuristic separation criterion has been helpful in interpreting a number of separated flow phenomena (see Délery [20] for a comprehensive list).

Subsequently, topology and dynamical systems theory were applied in several studies to analyze wall-shear patterns. Notably, Hunt et al. [45] obtained topological constraints on the number and type of singular points on three-dimensional bodies. Peake & Tobak [70] invoked structural stability and bifurcations to describe changes in wall-shear patterns under varying flow conditions.

Meanwhile, Wang [98, 99] challenged Lighthill's separation criterion with examples where none of the converging wall-shear lines originate from saddles. Wang termed the resulting separation open (the separation line starts or ends away from skin-friction zeros), as opposed to Lighthill's closed separation paradigm (the separation line connects skin-friction zeros). Initially contentious, open separation has gradually gained further numerical and experimental confirmation (Tobak & Peake [94]; Yates & Chapman [109])

As a new development, Wu, Gu & Wu [106] moved beyond wall-shear patterns and viewed separation as distinguished three-dimensional particle motion near the boundary. They defined the separation surface as a two-dimensional set of fluid trajectories backward-asymptotic to a saddle-type wall-shear zero. This appears to be the first suggestion that separation surfaces are unstable manifolds in the sense of nonlinear dynamics (see, e.g., Guckenheimer & Holmes [34]).

1.2 Prior work on three-dimensional unsteady separation

For unsteady velocity fields, the Lagrangian and Eulerian descriptions of separation differ. The wall-shear distribution, a prominent on-wall signature of separation, becomes time-dependent. As a result, classical techniques, such as critical point theory for autonomous vector fields, become inapplicable to the analysis of near-wall behavior. In fact, applying such techniques to instantaneous wall-shear fields leads to incorrect results, as two-dimensional examples show (Haller [40], [38], & [39]). In general, instantaneous Eulerian descriptions fail to yield a self-consistent and rigorous approach to unsteady flow separation.

On the other hand, the Lagrangian approach has been notably successful in describing 3D unsteady separation in the boundary layer equations. Continuing the two-dimensional work of Shen [83] and Van Dommelen & Shen [24], Van Dommelen & Cowley [23] derived Lagrangian criteria for the formation of a finite-time blow-up in Prandtl's boundary layer equation. They argued that such a singularity is an indication of boundary-layer separation, i.e., breakaway of the boundary layer from the wall.

Even though the above approach has been highly influential in the boundary-layer literature, linking separation to singularities in the boundary-layer equations raises as many questions as it answers. First, rigorous mathematical examples show that even the steady boundary layer equations can display fluid breakaway without any singularity formation at the breakaway point (Liu & Wan [61]). Secondly, unsteady boundary-layer equations can develop singularities without any obvious connection with separation (E & Engquist [26]). Thirdly, while material spikes do form in physical Navier-Stokes flows, singularities are generally agreed to be absent. Fourthly, computing Lagrangian conditions at off-wall-locations, as required by Lagrangian boundary-layer-separation theory, appears unrealistic in an experimental implementation.

An alternative Lagrangian approach to unsteady separation in Navier-Stokes flows was proposed by Wu et al. [108] (see also Wu, Ma & Zhou [107]), who viewed separation as a distinguished 3D motion of particles near the boundary. Working with instantaneous particle motion, they derived conditions for the simultaneous convergence and upwelling of fluid near general boundaries. These conditions, however, are heuristic, and tend to yield inaccurate separation locations away from zero-wall-shear points even for steady flows [88].

Despite the above advances, identifying exact separation and attachment locations in *even* steady three-dimensional flows has remained a challenge. Converging or diverging wall-shear lines are indicators of separation or attachment, but tend to fill open regions of the boundary. For this reason, heuristic indicators–such as zero wall shear[105] or zero streamwise wall shear[68, 9]–are commonly used to extract a single separation line candidate. These indicators are known to be inaccurate, but are still convenient choices for benchmarking, as noted by Nie and Armaly[67].

Another challenge is the identification of the two-dimensional separation surface (often called a shear layer) that emanates from the separation line. While several studies noted different particle behaviors on different sides of inferred separation surfaces [105, 87, 104], no tools have been available to extract such surfaces from numerical or experimental data. As a result, the global geometry of separated flows has only been studied thoroughly in two-dimensional cross sections or along individual streamlines.

In this thesis, we develop a nonlinear theory for predicting unsteady 3D fluid flow separation and attachment on no-slip curved moving boundaries. The theory is applicable to an arbitrary unsteady velocity field which is mass conserving and covers both laminar and turbulent flows. We verify the theory in numerical simulations and in experiments.

1.3 Preview of Chapters

Taking a Lagrangian viewpoint developed in [39],[52], we link separation over no slip boundaries in 3D fluid flows to the existence of distinguished material lines and material surfaces attached to the boundary. Such material lines and surfaces have the property of collecting fluid particles in vicinity of boundary and ejecting them into the mainstream.

From dynamical systems perspective, such a material line (surface) is a *non hyperbolic unstable manifold* of set of boundary point (points) for the system of ODE's satisfied by the fluid particles. Within this framework we can further classify the study of flow separation into three categories: *Fixed Separation*, *Moving Separation*, and *Crossflow Separation*.

In fixed separation the separation point(line) has a fixed location on the boundary for all times and the distinguished material line (surface) emanating from it acts like a classical unstable manifold. Moving separation on the other hand, means separation of varying location and also includes disappearing and reappearing of separation points (lines). Moving separation along no-slip boundaries can be attributed to finite time unstable manifolds. Unlike classical manifolds, finite time manifolds are non unique and attract nearby fluid particles only for a finite period of time.

In most cases, while separation originates and terminates at distinguished invariant sets of wall shear field, open or crossflow separation over bodies of revolution like prolate spheroid, defies this paradigm. Crossflow separation is inherently non unique and can be linked to pseudo unstable manifold associated with the attracting wall shear zero to which the crossflow separation line converges.

With this dynamical systems approach to flow separation, all our effort goes in determining exact analytic conditions for existence of the unstable manifolds, and formulae for approximating their shape. Depending on the nature of the time-dependence of the velocity field and whether separation patterns admit a unique or non-unique description in terms of invariant manifolds, different concepts from dynamical systems theory are invoked and their appropriate extensions are developed to characterize separation and attachment.

The thesis is organized into nine chapters and five Appendices. In chapter 2 we state our main assumptions, develop a general mathematical framework to analyze separation and formalize the notion of fixed, moving and crossflow separation. This framework is developed, assuming that the no slip boundary is flat and fixed; extension to curved moving boundaries is outlined in Appendix E.

In chapter 3, we obtain criteria for separation points and separation lines on fixed no-slip boundaries in steady compressible flows. These criteria imply that there are only two types of separation points and four types of basic separation lines [88]. For all these types of separation, we give conditions under which regular (i.e., unique, bounded, smooth, and robust) separation curves and surfaces emerge from the wall. We also derive a first-order prediction for the separation curve and separation surface using wall-based quantities. We obtain these criteria by invoking invariant manifold theory and Poincaré-Bendixson theory ;details are delegated to the Appendix A. We also give extension of these criteria to account for intersecting boundaries, curved boundaries, and obtain additional simplifications for Navier Stokes flows.

We extend the steady separation criteria for unsteady flows that possess a steady mean component in chapter 4. Such flows include time-periodic, quasiperiodic, and aperiodic flows with a finite temporal component. Surprisingly in such flows, separation and attachment curves (surfaces) also turn out to originate from fixed points (lines) on the boundary, even though the curves (surfaces) themselves deform in time [90]. The exact separation geometry is not captured by instantaneous Eulerian fields associated with the velocity field, but can be determined from a weighted average of the wall-shear, wall-density and wall-pressure fields. We establish this result by applying averaging theory coupled with topological invariant manifolds construction techniques in the Appendix B.

Based on the criteria derived in chapters 3 and 4, we devise algorithms to analyze fixed separation and attachment in 3D complex geometries in chapter 5. We illustrate this algorithm on analytical flow models and in numerical simulations [91]. The flow models are obtained from local expansions of the Navier-Stokes equations (derivation of these models is given in section A.5). For numerical simulations we consider three benchmark flow problems: backward facing step, lid-driven cavity , and flow past a rotating sphere. In each case, we verify our basic assumptions, predict separation points and separation lines, then obtain first order approximations of separation curves and separation surfaces. We conclude by verifying these approximate separation curves and surfaces by advecting particles close to the boundary and observing their breakaway geometry.

In chapter 6 we describe experimental results on fixed separation over a rotating sphere confined to a cylindrical container filled with a viscous fluid. Using this setup we report first experimental evidence of a limit cycle separation. This study is mainly qualitative and restricted to low Reynolds number regime.

Having studied fixed separation analytically, numerically and experimentally we proceed to the analysis of moving separation in the chapter 7. We first revisit moving separation in 2D turbulent fluid flows which possess a slowly time evolving mean. For such flows we introduce a notion of *ghost manifolds* as a means to locate the finite time unstable manifolds [89]. Using dynamic averaging, topological invariant manifold techniques and scaling analysis we obtain conditions to locate ghost manifolds in the Appendix C. These conditions translate to a criterion for moving separation when applied to flow around aerodynamic bodies. We show the use of this criterion in analytical and numerical examples of 2D flow separation. We then give a three dimensional extension of this approach and illustrate it with several analytical examples.

In chapter 8, we locate crossflow separation line as a maximizing ridge of a scalar field which best approximates the location where the bulk of fluid particles break away from the wall (associated proofs can be found in Appendix D). We compare this criterion with the existing ones in steady and unsteady flow models, and in flow past a prolate spheroid at an angle of attack.

Finally, in chapter 9 we conclude with a summary of the main contributions of our work. We also point out several possible applications and extensions of the results we have obtained.

Chapter 2

Dynamical systems approach to separation

2.1 Set-up and assumptions

Consider a *continuously differentiable* three-dimensional unsteady velocity field $\mathbf{v}(\mathbf{r}, t)$ representing a fluid flow past a boundary $\mathcal{B}(t)$, where

$$\mathbf{r} = x\mathbf{i} + y\mathbf{j} + z\mathbf{k}, \tag{2.1}$$

is the position vector in an inertial reference frame $\mathcal{R}$ and $\mathbf{i}, \mathbf{j}, \mathbf{k}$ are the unit Cartesian vectors.

The boundary $\mathcal{B}(t)$ can undergo arbitrary motion; the only requirement is that it always remains embedded in $\mathbf{R}^3$ and diffeomorphic to a sphere as it moves and deforms. Most bodies of interest like ordinary airfoils, the fuselage of common air vehicles and prolate spheroids undergoing rigid body motion admit such boundaries. Allowing for deformation of the boundary $\mathcal{B}(t)$, the theory we develop will also be applicable to bodies like fishes.

For ease of presentation, howver, we would develop the separation theory assuming that the boundary $\mathcal{B}(t)$ is flat, represented by $z = 0$ in Cartesian coordinates and is fixed in an inertial frame of reference. The theory extends in a straightforward manner to curved moving boundaries, by introducing an appropriate *curvilinear coordinate system* (x^1, x^2, x^3) in such a manner that one coordinate, say $x^3 =$ constant defines the surface while the remaining two are the coordinates within the surface. The details are outlined in the Appendix E.

On the $z = 0$ boundary, the velocity field satisfies the no-slip boundary condition

$$u(x, y, 0, t) = v(x, y, 0, t) = w(x, y, 0, t) = 0. \tag{2.2}$$

To distinguish the velocity components parallel to the boundary, we let $\mathbf{x} = (x, y)$, so that

$$\mathbf{u}(\mathbf{x}, z, t) = (u(x, y, z, t), v(x, y, z, t)), \qquad w(\mathbf{x}, z, t) = w(x, y, z, t).$$

We shall denote the wall-tangential spatial gradient by $\nabla_{\mathbf{x}} = \mathbf{e}_x\partial_x + \mathbf{e}_y\partial_y$, where $\mathbf{e}_x$ and $\mathbf{e}_y$ are unit vectors along the x and y axes.

If the velocity field is mass-conserving and admits no sinks or sources on the boundary, then the fluid density ρ satisfies the continuity equation

$$\partial_t\rho + \nabla\cdot(\rho\mathbf{v}) = 0. \tag{2.3}$$

On the $z = 0$ boundary, the no-slip boundary conditions simplify (2.3) to the linear differential equation

$$\partial_t\rho(\mathbf{x},0,t) + \rho(\mathbf{x},0,t)\partial_z w(\mathbf{x},0,t) = 0,$$

for $\rho(\mathbf{x},0,t)$; the solution to this equation is

$$\rho(\mathbf{x},0,t) = \rho(\mathbf{x},0,t_0)e^{-\int_{t_0}^{t}\partial_z w(\mathbf{x},0,s)\,ds}. \tag{2.4}$$

Taking the gradient of (2.4) gives the wall-tangential density-gradient evolution

$$\begin{aligned}\nabla_{\mathbf{x}}\rho(\mathbf{x},0,t) &= \nabla_{\mathbf{x}}\rho(\mathbf{x},0,t_0)e^{-\int_{t_0}^{t}\partial_z w(\mathbf{x},0,s)\,ds} \\ &\quad -\rho(\mathbf{x},0,t_0)e^{-\int_{t_0}^{t}\partial_z w(\mathbf{x},0,s)\,ds}\int_{t_0}^{t}\nabla_{\mathbf{x}}\partial_z w(\mathbf{x},0,s)\,ds.\end{aligned} \tag{2.5}$$

Assuming that the density and density gradient of the fluid remain bounded from below and from above for all times, we obtain from the equations (2.4)-(2.5) the estimates

$$\left|\int_{t_0}^{t}\partial_z w(\mathbf{x},0,s)ds\right| < K, \qquad \left|\int_{t_0}^{t}\nabla_{\mathbf{x}}\partial_z w(\mathbf{x},0,s)\,ds\right| < K, \tag{2.6}$$

for all t and for some constant $K > 0$. Note that for incompressible flows, we have

$$\partial_z w(\mathbf{x},0,t) \equiv 0, \tag{2.7}$$

along the wall, thus (2.6) is always satisfied.

2.2 Lagrangian framework to study separation

Flow separation is a *transport* phenomena [103], which can be studied in terms of particle behavior. Recall that fluid particles satisfy three-dimensional Lagrangian equations of motion

$$\dot{x} = u(x,y,z,t), \qquad \dot{y} = v(x,y,z,t), \qquad \dot{z} = w(x,y,z,t), \tag{2.8}$$

or, briefly,

$$\dot{\mathbf{x}} = \mathbf{u}(\mathbf{x},z,t), \qquad \dot{z} = w(\mathbf{x},z,t).$$

Following the Lagrangian viewpoint developed in ([39],[52]), we link separation in 3D fluid flows to the existence of distinguished material lines and surfaces attached to

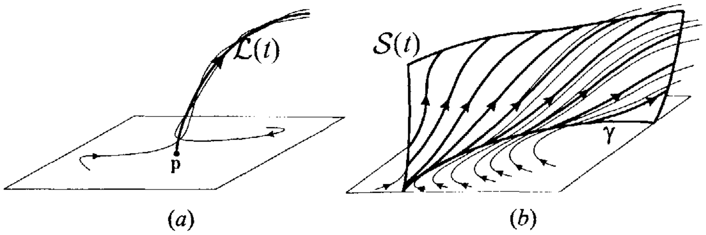

Figure 2-1: (a) Separation curve $\mathcal{L}(t)$ emanating from a separation point $\mathbf{p}$. (b) Separation surface $\mathcal{S}(t)$ emanating from a separation line γ.

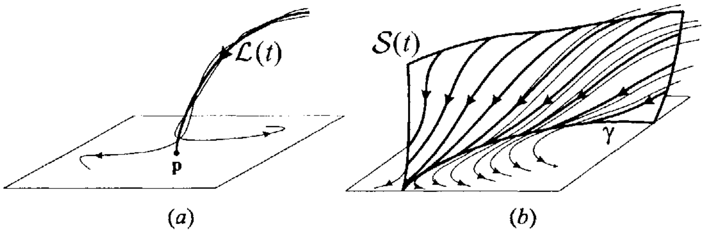

Figure 2-2: (a) Attachment curve $\mathcal{L}(t)$ emanating from a attachment point $\mathbf{p}$. (b) Attachment surface $\mathcal{S}(t)$ enacting from a attachment line γ.

the boundary. From dynamical systems perspective, such a material line (surface) is an *unstable manifold* of set of boundary point(s) for the system (2.8). The unstable manifold has the property of attracting fluid particles from the vicinity of the boundary and ejecting them into the mainstream flow. The unstable manifold is *invariant:* particles starting on it remain on it for all times. Due to noslip condition such manifolds are non-hyperbolic, which means that they cannot be located by linearization, one of the standard dynamical system techniques (see [34]).

Depending on the nature of the time-dependence of the velocity field and whether separation patterns admits a unique or non-unique description in terms of the manifolds, the study of flow separation can be broadly divided into: *Fixed Separation*, *Moving Separation* and *Crossflow Separation*, which are described next.

2.2.1 Fixed separation

We say that *fixed unsteady separation* takes place along the boundary $z = 0$ if fluid particles near the boundary converge to a time-dependent material line $\mathcal{L}(t)$ or a time dependent material surface $\mathcal{S}(t)$, along which they are ejected from the boundary. In the language of dynamical systems, $\mathcal{L}(t)$ is a one-dimensional unstable manifold (*separation curve*) of a boundary point (*separation point*); $\mathcal{S}(t)$ is a two-dimensional unstable manifold (*separation surface*) of a curve of boundary points (*separation line*), a shown in figure 2-1.

Note that while $\mathcal{L}(t)$ and $\mathcal{S}(t)$ will generally deform in time, their intersections with the boundary ($\mathbf{p}$ and γ) remain fixed because of the no-slip boundary conditions (hence the term *fixed* unsteady separation). To exclude unphysical cases, we shall only consider separation curves and surfaces that are:

(i) *Unique:* no other separation curve or surface emerges from the same set of boundary points. Also, nearby boundary points admit no separation curves or surfaces.

(ii) *Bounded:* they intersect the boundary in a bounded set.

(iii) *Smooth:* they are continuously differentiable.

(iv) *Robust:* they smoothly deform but survive under small perturbations to $\mathbf{v}$.

Properties (i)-(iii) express plausible physical features of separation; property (iv) excludes degenerate separation patterns that are not reproducible experimentally or numerically. Such patterns, as it turns out, include separation curves and surfaces tangent to the boundary.

We define attachment as separation exhibited by the flow in backward time. A *attachment point* is, therefore, a boundary point with a one-dimensional stable manifold (*attachment curve*), and a *attachment line* is a boundary curve with a two-dimensional stable manifold (*attachment surface*), as shown in figure (2-2). Again, we require properties (i)-(iv) for attachment curves and surfaces. Just as unstable manifolds, stable manifolds are also invariant material surfaces.

It turns out that fixed separation and attachment not only occurs in steady flows but is also typical in unsteady flows that have a finite asymptotic mean. In chapter 3, we first obtain a complete classification of all physically observable (i.e. satisfying assumptions (i)-(iv) above) separation patterns in steady flows by using invariant manifold techniques and Poincaré-Bendixson theory. We also derive wall based criteria to locate such patterns. By combining averaging and topological invariant manifold technique, we extend these criteria to unsteady flows with a finite asymptotic mean, in chapter 4. Such flows include time periodic, quasiperiodic and even turbulent flows which possess a finite temporal component.

In turbulent flows which have a evolving mean component, however, fluid particles would typically be ejected at time varying location from the boundary leading to moving separation.

2.2.2 Moving separation

Moving separation means separation of varying location and also includes disappearing and reappearing of separation points and lines. Moving separation along no-slip boundaries cannot be described by classical unstable manifolds, like one used in the description of fixed separation (see the previous section, 2.2.1). The reason is that an unstable manifold, as any material line or surface, is advected by the flow, and hence its end-location remains fixed on the no-slip boundary.

A solution to this problem is to view moving separation as a material ejection due to *finite-time unstable manifolds*, see Haller [39]. A finite-time unstable manifold

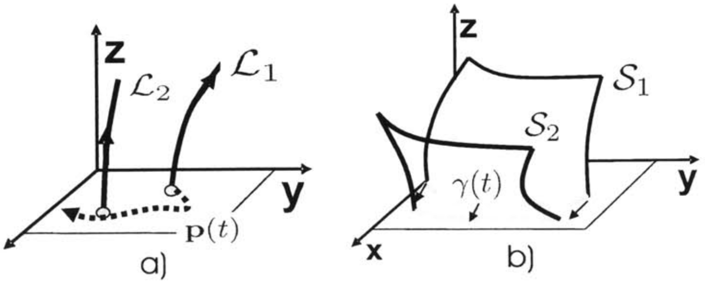

Figure 2-3: (a) Finite time one dimensional unstable curve $\mathcal{L}_1$ and $\mathcal{L}_2$, associated with moving separation point $p(t)$. (b) Finite time two dimensional unstable surface $\mathcal{S}_1$ and $\mathcal{S}_2$, associated with moving separation line $\gamma(t)$.

is a material line (surface) that acts as an unstable manifold for a fixed point (line) only over a finite time interval. In physical terms, a finite-time unstable manifold is a material line that attracts all nearby fluid particles over that finite interval of time.

When a finite-time unstable manifold ceases to attract, another nearby material line (surface) may become attracting. Then the second material line will act as a separation curve or separation surface for a while, attracting all nearby material lines(surfaces), including the one that used to be the separation curve (surface). Later, the second material line may also loose its attracting property, and give its place to a nearby third material line (surface) that has just become attracting. If the above process repeats itself, we observe a sliding separation point (line) created by attachment points of different material lines, each of which acts as a finite-time separation curve (surface). Similarly, moving attachment can be thought of as the sliding of finite-time attracting material lines (surfaces) along a no-slip wall.

As opposed to classical manifolds, finite-time manifolds are never unique: they are always surrounded by a streak of other finite-time manifolds [40],[38]. Therefore, relaxing assumption (i) of the section 2.2.1, we look for finite-time manifolds which are bounded, smooth and robust.

In chapter 7 we revisit moving separation in 2D turbulent fluid flows which possess a slowly time evolving mean. For such flows, we introduce notion of *ghost manifold* as a means to locate the finite time unstable manifolds. The ghost manifold lies off the no slip boundary and yet influences the boundary layer dynamics. Nevertheless, the ghost manifolds turn out to have a virtual footprint on the boundary; this footprint can be detected and hence the moving spike formation can be predicted.

We summarize these findings in a numerically assisted analytic criterion for moving separation that we derive using a combination of rescaling, dynamic averaging, topological invariant techniques and wavelet analysis. Our moving spike criterion translates to a criterion for moving separation when applied to flow around aerodynamic bodies. We then give a three dimensional extension of this approach.

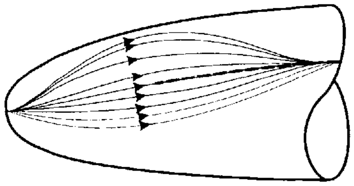

Figure 2-4: Sketch of wall shear lines on a round-nosed body of revolution at higher angles of attack.

2.2.3 Open or Crossflow separation

In most cases, separation line originates and terminates at distinguished invariant sets (e.g. equilibrium points and limit cycles) of wall shear field. However, there can be instances where this condition is violated: a classic example arises in separated flows over round nosed bodies of revolution like prolate spheroid (see introduction and chapter 8 for a literature review). Recall that this type of separation is commonly know as *open* separation [98, 99, 15] or *crossflow* separation [101] and features separation without wall-shear zeros at, atleast one end of the separation line.

We sketch the wall-shear pattern on a section of prolate spheroid in the figure 2-4. In an incompressible flow, converging wall-shear trajectories, such as those figure 2-4, indeed lead to the ejection of particles from the vicinity of the boundary.

Based on the wall-shear topology shown in the figure 2-4, one is tempted to designate the attracting portion of a wall-shear line, such as the dashed segment, as a line of separation. Note, however, that the above designation is arbitrary: the dashed line segment is no more distinguished than any other nearby segment: all such segments attract wall-shear lines, connect the same wall-shear zeros, and repel off-wall fluid trajectories. Even if one heuristically designates a segment γ of a wall-shear line as a separation line, there is no unique separation surface emanating from γ.

As a well-defined separation structure in such problems, one may instead choose the one-dimensional separation curve emanating from the attracting wall shear zero. A more global description can however be obtained by linking this form of separation to *pseudo manifold* associated with the wall shear zero. Such manifolds are inherently non unique and we locate the most influential one as a ridge of a scalar field in chapter 8. The scalar field measures cumulative upwelling along uniformly hyperbolic wall shear trajectories and therefore its maximizing ridge locates region where the bulk of fluid particles break away. We justify dynamical this approach using differential invariant manifold techniques in Appendix D.

2.3 Separation Geometry

In addition to obtaining the criteria to locate the separation point and separation line, we also determine the separation geometry. While characterizing the global geometry is beyond the reach of our approach, we seek local approximations to the separation

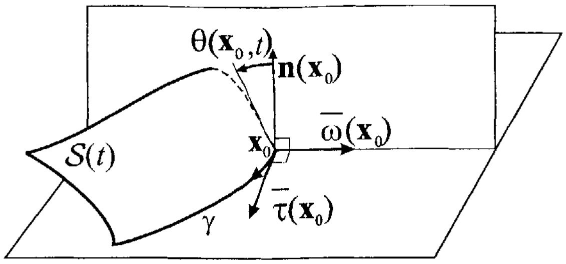

Figure 2-5: Definition of the separation angle.

curve and the separation surface.

Recall that a separation curve $\mathcal{L}(t)$ is a time-dependent material line emanating from the separation point $\mathbf{p}$. Being transverse to the boundary, it can locally be represented as

$$\mathbf{x} = \mathbf{p} + z\mathbf{g}_0(t) + \mathcal{O}(z^2), \tag{2.9}$$

where $\mathbf{g}_0(t)$ denotes the time-dependent slope of $\mathcal{L}(t)$.

For a separation surface $\mathcal{S}(t)$ emanating from the separation line γ, we define the separation angle $\theta(\mathbf{x}_0, t)$ at a point $\mathbf{x}_0$ of γ as follows: $\theta(\mathbf{x}_0, t)$ is the angle between the wall normal and the tangent of $\mathcal{S}(t)$ in the normal section at $\mathbf{x}_0$ (see figure 2-5).

2.4 Remarks

Before proceeding further, we stress two points related to our description of separation:

1 First, our approach does not distinguish between small scale recirculation and large scale boundary–layer separation: both involve material ejection from the boundary, but take place on different scales.

2 Second, the thin smoke and dye spikes commonly observed in flow visualization confirm that separation indeed takes place along unstable manifolds as we assume here. The question, however, remains: do these observed spikes (manifolds) emanate directly from the wall or from nearby off-wall locations.

Based on available flow visualization results, we argue that the spikes typically form along wall-based unstable manifolds. Such wall-based manifolds have footprints in the wall-shear field that are commonly observed in numerical and laboratory experiments on boundary-layer separation (Peake & Tobak [70], Délery [20], and Simpson [84]). In steady flow over an infinite moving boundary (Sears & Tellionis [79]) or around a rotating cylinder (Elliott, Smith & Cowley [28]), however, Lagrangian separation appears to originate off the boundary. Such off-boundary separation, if indeed exists in physical flows, is not amenable to the boundary-based invariant manifold approach taken here.

With these assumptions and description of separation, all our effort in quantifying separation goes in determining exact analytic conditions for existence of the unstable manifolds and formulae for approximating their shape. Mathematically this is a challenging problem as

1 the manifolds are *non-hyperbolic* due to no-slip boundary condition,

2 we allow for general time dependence of the velocity field,

3 the manifolds can be *non-unique* (see section 2.2.2,2.2.3).

2.5 Normal form for Particle Dynamics

For application of dynamical system techniques, it is convenient to work with a normal form of particle equations of motion. Using the no-slip boundary conditions (2.2), equation (2.8) can be rewritten as

$$\dot{\mathbf{x}} = z\mathbf{A}(\mathbf{x}, z, t), \qquad \dot{z} = zB(\mathbf{x}, z, t), \tag{2.10}$$

where

$$\mathbf{A}(\mathbf{x}, z, t) = \int_0^1 \partial_z \mathbf{u}(\mathbf{x}, s\,z, t)\,ds, \qquad B(\mathbf{x}, z, t) = \int_0^1 \partial_z w(\mathbf{x}, s\,z, t)\,ds. \tag{2.11}$$

Equation (2.10) is a preliminary normal form for the flow; we shall further refine this normal form below.

Note that for incompressible flows, we have

$$\nabla_{\mathbf{x}} \cdot \mathbf{u} + \partial_z w = 0, \tag{2.12}$$

which implies $B(\mathbf{x}, 0, t) \equiv 0$ in (2.10) by the boundary conditions (2.2). Thus, in the incompressible case, (2.10) becomes

$$\dot{\mathbf{x}} = z\mathbf{A}(\mathbf{x}, z, t), \qquad \dot{z} = z^2 C(\mathbf{x}, z, t), \tag{2.13}$$

with

$$C(\mathbf{x}, z, t) = \int_0^1 \int_0^1 \partial_z^2 w(\mathbf{x}, spz, t)p\ dp\,ds. \tag{2.14}$$

2.5.1 Locally incompressible normal form

It turns out that compressible particle motion can also be transformed to the form (2.13) by letting

$$z = \tilde{z} e^{\int_{t_0}^{t} \partial_z w(\mathbf{x},0,\tau)d\tau}. \tag{2.15}$$

Indeed, under this transformation, the equations of motion become

$$\dot{\mathbf{x}} = \tilde{z}\mathbf{A}_1(\mathbf{x}, \tilde{z}, t), \qquad \dot{\tilde{z}} = \tilde{z}^2 C_1(\mathbf{x}, \tilde{z}, t), \tag{2.16}$$

where

$$\begin{aligned}
\mathbf{A}_1(\mathbf{x}, \tilde{z}, t) &= e^{\int_{t_0}^{t} \partial_z w(\mathbf{x},0,\tau)d\tau} \mathbf{A}(\mathbf{x}, \tilde{z} e^{\int_{t_0}^{t} \partial_z w(\mathbf{x},0,\tau)d\tau}, t), \\
C_1(\mathbf{x}, \tilde{z}, t) &= e^{\int_{t_0}^{t} B(\mathbf{x},0,\tau)d\tau} \partial_z B(\mathbf{x}, 0, t) + O(\tilde{z}) \\
&= \frac{1}{2} e^{\int_{t_0}^{t} \partial_z w(\mathbf{x},0,\tau)d\tau} \partial_z^2 w(\mathbf{x}, 0, t) + O(\tilde{z}).
\end{aligned}$$

For curved moving boundaries also, there exists a change of coordinates in which particle equation of motion can be transformed into the canonical form (2.16) (see Appendix E for details).

Chapter 3

Steady Separation

In steady flows material lines and material surfaces are streamlines and streamsurfaces, respectively. It can be easily shown that one-dimensional unstable manifolds (separation curves) emanate from zeros of the wall-shear field; such manifolds can be found and approximated by classic results in nonlinear dynamics.

By contrast, two-dimensional unstable manifolds (separation surfaces) emanate from distinguished wall-shear lines, the separation lines. Wall shear line is a finite union of wall-shear trajectories. We argue that the distinguishing feature of separation lines is their strong saddle-type instability relative to an appropriately rescaled local flow near the boundary. We identify such instabilities by solving the time-dependent equation of variations along scaled wall-shear lines.

As a result, we obtain asymptotic conditions for separation lines and explicit formulae for separation angles. Invoking the Poincaré-Bendixson theory of planar vector fields and using invariant manifold theory ([30]), we find that only four types of locally unique separation lines are possible in physical fluid flows: (S1) saddle-spiral connections; (S2) saddle-node connections; (S3) saddle-limit cycle connections and (S4) limit cycles.

(S1) and (S2) separation have been known as closed separation; (S3) and (S4) separation have been undocumented until recently (see chapter 5 and chapter 6), even though (S3)-type wall-shear patterns have been observed in at least one instance (Hsieh and Wang [44]). Based on common terminology, the latter two separation types should be characterized as open. They differ from common examples of open separation in that they admit unique separation lines and surfaces (cf. chapter 8).

For all four types of separation, we give conditions under which regular (i.e., unique, bounded, smooth, and robust) separation surfaces emerge from the wall. We also obtain first-order approximations for these surfaces from our separation angle formula. For incompressible Navier-Stokes flows, the separation slope can also be computed from wall pressure and wall-shear measurements (cf. section 3.7). An extension of above results to account for separation near corners formed by transverse no-slip boundaries is given in section 3.6.

3.1 Rescaled Particle Dynamics

The steady continuity equation

$$\nabla \cdot (\rho \mathbf{v}) = 0. \tag{3.1}$$

and the no slip condition (2.2) implies that the flow is incompressible along the boundary:

$$\nabla \cdot \mathbf{v}(\mathbf{x}, 0) = 0. \tag{3.2}$$

Hence, we can always rewrite the steady velocity field as

$$\mathbf{u}(\mathbf{x}, z) = z\mathbf{A}(\mathbf{x}, z), \qquad w(\mathbf{x}, z) = z^2 C(\mathbf{x}, z), \tag{3.3}$$

where

$$\mathbf{A}(\mathbf{x}, z) = \int_0^1 \partial_z \mathbf{u}(\mathbf{x}, qz)\, dq, \qquad C(\mathbf{x}, z) = \int_0^1 \int_0^1 \partial_z^2 w(\mathbf{x}, qrz) r\, dr\, dq. \tag{3.4}$$

With this notation, (3.1) becomes

$$\nabla \rho \cdot \left(z\mathbf{A}, z^2 C\right) + \rho z \left[\nabla_{\mathbf{x}} \cdot \mathbf{A} + 2C + z\partial_z C\right] = 0. \tag{3.5}$$

The above must hold for all z, therefore, we must have

$$\nabla \rho \cdot (\mathbf{A}, zC) + \rho \left[\nabla_{\mathbf{x}} \cdot \mathbf{A} + 2C + z\partial_z C\right] = 0. \tag{3.6}$$

Using Eq. (2.2) in the continuity equation (Eq.3.1), we can express $\partial_z^2 w(\mathbf{x}, 0)$ from wall-based quantities as

$$\partial_z^2 w\left(\mathbf{x}, 0\right) = -\nabla_{\mathbf{x}} \cdot \tau\left(\mathbf{x}\right) - \frac{1}{\rho(\mathbf{x}, 0)} \nabla_{\mathbf{x}} \rho\left(\mathbf{x}, 0\right) \cdot \tau\left(\mathbf{x}\right). \tag{3.7}$$

By (3.3), fluid particle motions satisfy the differential equations

$$\dot{\mathbf{x}} = z\mathbf{A}(\mathbf{x}, z), \qquad \dot{z} = z^2 C(\mathbf{x}, z), \tag{3.8}$$

for which the $z = 0$ plane is a set of fixed points, a highly degenerate object. We remove this degeneracy by introducing the rescaled time

$$s = \int_{t_0}^{t} z(r)\, dr \tag{3.9}$$

along each trajectory $(\mathbf{x}(t), z(t))$ of (3.8) (see, e.g., Wu et al. [106]). The scaling (3.9) turns (3.8) into

$$\mathbf{x}' = \mathbf{A}(\mathbf{x}, z), \qquad z' = zC(\mathbf{x}, z), \tag{3.10}$$

with the prime referring to differentiation with respect to s. As (3.6) shows, the rescaled flow (3.10) is compressible at the wall except at points where $C(\mathbf{x}, 0) =$

0. Note that s is a well-defined time-like variable for (3.10) even on the boundary, although the transformation (3.9) between (3.8) and (3.10) breaks down at $z = 0$.

The trajectories of the scaled flow (3.10) are identical to those of (3.8) away from the boundary. On the boundary, however, (3.10) generates fictitious trajectories tangent to the *wall shear* field

$$\tau(\mathbf{x}) = \mathbf{A}(\mathbf{x}, 0) = \partial_z \mathbf{u}(\mathbf{x}, 0). \tag{3.11}$$

Another quantity of interest will be the *wall-vorticity* field

$$\omega(\mathbf{x}) = \mathbf{A}^{\perp}(\mathbf{x}, 0) = \partial_z \mathbf{u}^{\perp}(\mathbf{x}, 0), \tag{3.12}$$

where we used the notation $(a, b)^{\perp} = (-b, a)$.

3.2 Separation points and curves

3.2.1 Separation points

A separation curve $\mathcal{L}$ for the fluid flow (3.8) is also an invariant curve for the scaled flow (3.10), because the trajectories of (3.8) and (3.10) coincide away from the boundary. As a result, the intersection point $\mathbf{p}$ of $\mathcal{L}$ with the invariant plane $\{z = 0\}$ must be invariant under the scaled flow. The point $\mathbf{p}$ is, therefore, a fixed point of (3.10), i.e., a zero of the wall shear field (3.11):

$$\mathbf{A}(\mathbf{p}, 0) = \partial_z \mathbf{u}(\mathbf{p}, 0) = \mathbf{0}. \tag{3.13}$$

The fixed point $\mathbf{p}$ admits an unstable manifold satisfying the properties (a)-(e) if and only if the linearized scaled flow,

$$\begin{pmatrix} \xi' \\ \eta' \end{pmatrix} = \begin{pmatrix} \nabla_{\mathbf{x}} \mathbf{A}(\mathbf{p}, 0) & \partial_z \mathbf{A}(\mathbf{p}, 0) \\ \mathbf{0} & C(\mathbf{p}, 0) \end{pmatrix} \begin{pmatrix} \xi \\ \eta \end{pmatrix}, \tag{3.14}$$

has a single positive eigenvalue with the corresponding eigenvector transverse to the $z = 0$ plane. This follows from the stable manifold theorem for fixed points of vector fields (see Guckenheimer & Holmes [34]).

The eigenvalues λ_i of the linear system (3.14) satisfy

$$\lambda_1 + \lambda_2 = \nabla_{\mathbf{x}} \cdot \mathbf{A}(\mathbf{p}, 0), \qquad \lambda_3 = C(\mathbf{p}, 0). \tag{3.15}$$

Because the eigenvector corresponding to λ_3 is the only one off the boundary, and λ_3 is the only one that is positive, we must have

$$\det \nabla_{\mathbf{x}} \mathbf{A}(\mathbf{p}, 0) > 0, \qquad \nabla_{\mathbf{x}} \cdot \mathbf{A}(\mathbf{p}, 0) < 0, \tag{3.16}$$

at the separation point.

In conclusion, (3.11), (3.13) and (3.16) give the following sufficient and necessary

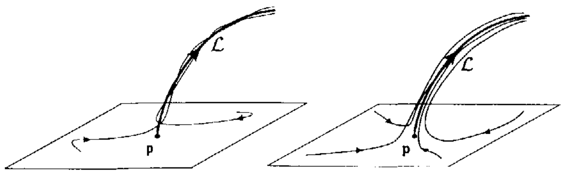

(a) (b)

Figure 3-1: Two types of robust separation points a) Stable node and b) Stable foci.

conditions for a separation point $\mathbf{p}$ to exist on the boundary:

$$\tau(\mathbf{p}) = 0, \qquad \det \nabla_{\mathbf{x}}\tau(\mathbf{p}) > 0, \qquad \nabla_{\mathbf{x}} \cdot \tau(\mathbf{p}) < 0, \qquad \partial_z^2 w(\mathbf{p}, 0) > 0. \tag{3.17}$$

Attachment points, by contrast, satisfy

$$\tau(\mathbf{p}) = 0, \qquad \det \nabla_{\mathbf{x}}\tau(\mathbf{p}) > 0, \qquad \nabla_{\mathbf{x}} \cdot \tau(\mathbf{p}) > 0, \qquad \partial_z^2 w(\mathbf{p}, 0) < 0. \tag{3.18}$$

3.2.2 Separation curves

Recall that a separation curve $\mathcal{L}$ is the off-wall streamline emanating from a separation point $\mathbf{p}$. Let $\mathcal{L}$ be locally represented by

$$\mathbf{x} = \mathbf{p} + z\mathbf{G}(z), \tag{3.19}$$

where $\mathbf{G}$ admits the Taylor-series expansion

$$\mathbf{G}(z) = \mathbf{g}_0 + z\mathbf{g}_1 + \frac{1}{2}z^2\mathbf{g}_2 + \frac{1}{6}z^3\mathbf{g}_2 + \dots \tag{3.20}$$

with

$$\mathbf{g}_0 = \mathbf{G}(0), \qquad \mathbf{g}_1 = \partial_z\mathbf{G}(0), \qquad \mathbf{g}_2 = \partial_z^2\mathbf{G}(0), \qquad \dots, \qquad \mathbf{g}_n = \partial_z^n\mathbf{G}(0).$$

Because $\mathcal{L}$ is an invariant curve for the flow (3.8), differentiation of (3.19) in time yields

$$\dot{\mathbf{x}} = \dot{z}(\mathbf{G}(z) + z\mathbf{G}'(z)),$$

or, equivalently,

$$\mathbf{A}(\mathbf{p} + \mathbf{G}(z), z) = zC(\mathbf{p} + \mathbf{G}(z), z)\left[\mathbf{G}(z) + z\mathbf{G}'(z)\right], \tag{3.21}$$

as an implicit equation for the separation curve.

In (3.21), we substitute (3.20) for $\mathbf{G}$ and Taylor-expand at $z = 0$. Comparing the $\mathcal{O}(z)$ terms on both sides gives an expression for the slope of the separation curve,

$$\mathbf{g}_0 = -\left[2\nabla_{\mathbf{x}}\tau(\mathbf{p}) - \partial_z^2 w(\mathbf{p}, 0)\mathbf{I}\right]^{-1} \partial_z^2\mathbf{u}(\mathbf{p}, 0), \tag{3.22}$$

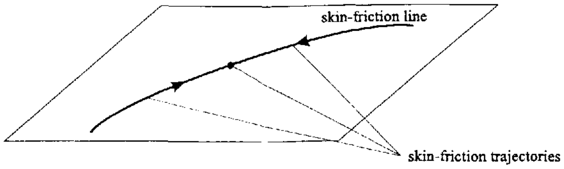

Figure 3-2: Wall shear line consisting of three distinct wall shear trajectories.

with $\mathbf{I}$ denoting the two-dimensional identity matrix.

Equating the $\mathcal{O}(z^2)$ terms in (3.21) gives an expression for the separation curvature:

$$\begin{aligned} \mathbf{g}_1 &= \frac{1}{2}[\nabla_{\mathbf{x}}\partial_z \mathbf{u}(\mathbf{p},0) - \partial_z^2 w(\mathbf{p},0)\ \mathbf{I}]^{-1} \\ &\times \left\{ -\frac{1}{3}\partial_z^3 \mathbf{u}(\mathbf{p},0) + \left[\frac{1}{3}\partial_z^3 w(\mathbf{p},0)\mathbf{I} - 3\nabla_{\mathbf{x}}\partial_z^2 \mathbf{u}(\mathbf{p},0)\right]\mathbf{g}_0 \right. \\ &\qquad \left. +2\left[-\nabla_{\mathbf{x}}^2\partial_z^2\mathbf{u}(\mathbf{p},0)\mathbf{g}_0 + \left(\nabla_{\mathbf{x}}\partial_z^2 w(\mathbf{p},0)\mathbf{g}_0\right)\mathbf{I}\right]\mathbf{g}_0 \right\}. \end{aligned} \tag{3.23}$$

The above slope and curvature formulae are equally valid for attachment curves. Higher-order approximations for separation and attachment curves can be obtained by comparing the higher-order terms in (3.21).

3.3 Separation lines

3.3.1 Wall shear lines

A separation surface $\mathcal{S}$ for the fluid flow (3.8) is an invariant surface for the scaled flow (3.10). As a result, a separation line γ, the intersection of $\mathcal{S}$ with the invariant plane $\{z = 0\}$, must be an invariant curve for (3.10). By (3.11), such an invariant curve is a *wall shear line*, i.e., a smooth curve tangent to the wall shear field $\tau(\mathbf{x})$.

A wall shear line, however, is typically *not* a single trajectory of (3.10); rather, it is a connected union of such trajectories, with each trajectory $\mathbf{x}(s;\mathbf{x}_0)$ satisfying

$$\mathbf{x}'(s;\mathbf{x}_0) = \mathbf{A}\left(\mathbf{x}\left(s;\mathbf{x}_0\right),0\right), \qquad \mathbf{x}(0;\mathbf{x}_0) = \mathbf{x}_0, \tag{3.24}$$

as shown in figure 3-2.

The fundamental question of three-dimensional separation is the following: What distinguishes separation lines from other wall-shear lines? As we argue below, their distinguishing feature is *strong hyperbolicity.*

3.3.2 Strong hyperbolicity

A wall shear line γ is *strongly hyperbolic* with respect to the scaled flow (3.10) if: (1) some infinitesimally close trajectories of (3.10) are attracted to γ in forward time and

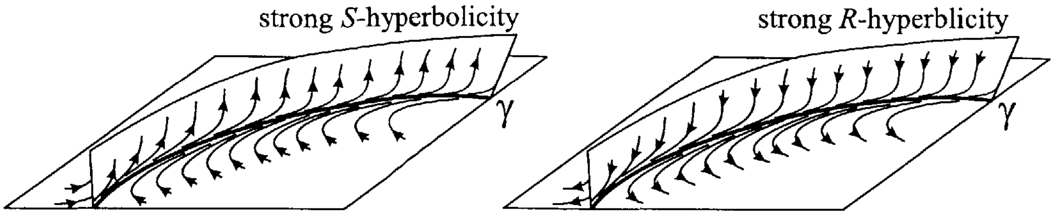

Figure 3-3: S-type and R-type strong hyperbolicity of a wall shear line with respect to the scaled flow (3.10).

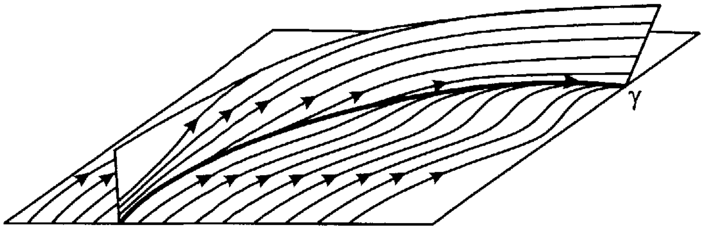

Figure 3-4: Hyperbolic but not strongly hyperbolic wall shear line in the scaled flow (3.10).

repelled by γ in backward time; (2) other infinitesimally close trajectories of (3.10) are attracted to γ in backward time and repelled by γ in forward time; (3) all these attraction and repulsion rates are nondegenerate, i.e., exponential in the rescaled time s.

If the forward-time attracted trajectories lie in the $z = 0$ plane and the backward-time attracted ones lie off the $z = 0$ plane, we call γ *strongly S-hyperbolic* with respect to (3.10), with "S" referring to separation. If the forward-time attracted trajectories lie off the $z = 0$ plane and the backward-time attracted ones lie in the $z = 0$ plane, we call γ is *strongly R-hyperbolic* with respect to (3.10), with "R" referring to attachment (see figure 3-3).

The qualifier *strong* in the above definitions signals a difference from the classical definition of hyperbolicity in dynamical systems (see, e.g., Fenichel [30]). Specifically, classical definitions only require some trajectories to be exponentially attracted to γ in forward time (but not necessarily repelled by γ in backward time), and other trajectories to be exponentially attracted to γ in backward time (but not necessarily repelled by γ in forward time).

As a result, classical hyperbolicity does not necessarily describe experimentally or numerically observable separation along γ: it only requires γ to collect tracers near the wall for large s values. Tracers, therefore, may only accumulate near a part of γ, as shown in Figure 3-4. The same figure also highlights another shortcoming of hyperbolicity in describing observable separation: tracers may not be ejected everywhere along γ.

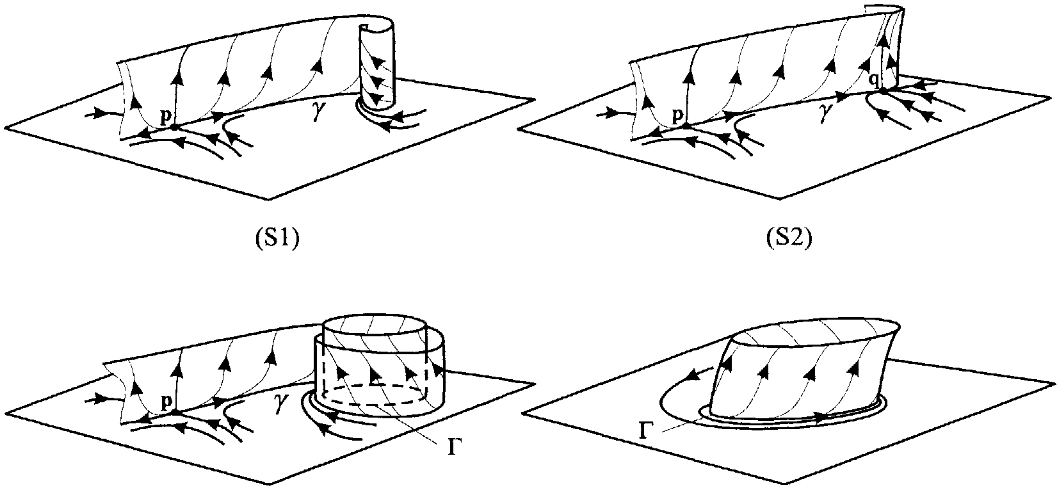

(S1) (S2) (S3) (S4)

Figure 3-5: The four basic separation patterns satisfying properties (i)-(v) of section 2.2.1. For an open-closed classification of these patterns, see section 3.9.

3.4 Criteria for separation and attachment lines

Any bounded wall shear line γ with strong S-hyperbolicity is a separation-line candidate: tracers along the wall converge towards γ then leave the vicinity of the wall due to the instability of γ. To find actual separation lines, we have to find computable conditions under which: (a) a wall shear line γ is strongly S-hyperbolic; (b) a separation surface $\mathcal{S}$ satisfying properties (i)-(iv) of section 2.2.1 emerges from the wall along γ.

As we show in Appendix A.1, a bounded wall shear line γ is a *separation line* if and only if one of the following holds (see figure (3-5)):

(S1) γ originates from a saddle $\mathbf{p}$ with $\partial_z^2 w\,(\mathbf{p},0) > 0$, and ends at a stable spiral $\mathbf{q}$ with $\partial_z^2 w\,(\mathbf{q},0) > 0$.

(S2) γ originates from a saddle $\mathbf{p}$ with $\partial_z^2 w\,(\mathbf{p},0) > 0$, and ends at a stable node $\mathbf{q}$ with $\partial_z^2 w\,(\mathbf{q},0) > 0$. Also, γ is tangent to the direction of weaker attraction at $\mathbf{q}$.

(S3) γ originates from a saddle $\mathbf{p}$ with $\partial_z^2 w\,(\mathbf{p},0) > 0$, and spirals onto a stable limit cycle Γ with $\int_\Gamma \partial_z^2 w\,(\mathbf{x}\,(s;\mathbf{x}_0)\,,0)\;ds > 0$.

(S4) γ is a stable limit cycle with $\int_\gamma \partial_z^2 w\,(\mathbf{x}\,(s;\mathbf{x}_0)\,,0)\;ds > 0$.

Since the unstable manifold of saddle-type wall shear zero always has two components, a combination of the (S1) and (S2) separation may also arise, as shown in

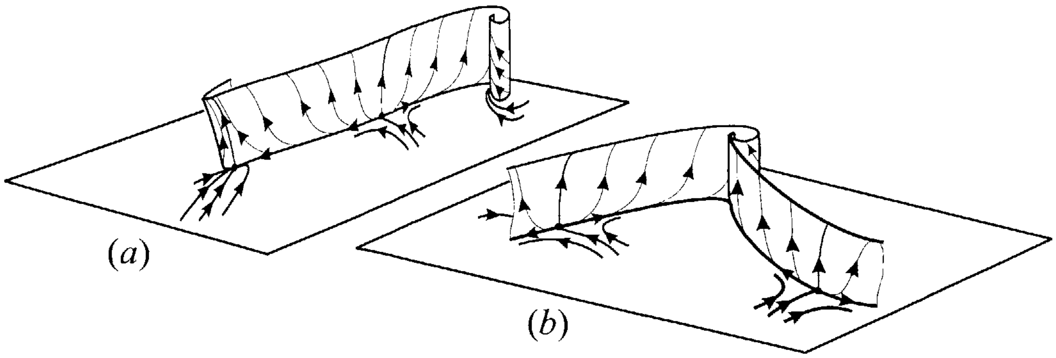

Figure 3-6: (a) (S1) and (S2) separation lines emanating from the same saddle-type wall shear zero. (b) Two (S2) separation lines terminating at the same spiral-type wall shear zero.).

figure 3-6(a). Two identical separation types may also coexist and terminate at the same wall shear zero or limit cycle, as shown in figure 3-6(b).

Similar results apply to attachment lines after a reversal of time: a bounded wall shear line γ on the $z = 0$ boundary is a *attachment line* if and only if one of the following holds:

(R1) γ originates from an unstable spiral $\mathbf{p}$ where $\partial_z^2 w(\mathbf{p}, 0) < 0$, and ends at a saddle $\mathbf{q}$ where $\partial_z^2 w(\mathbf{q}, 0) < 0$.

(R2) γ originates from an unstable node $\mathbf{p}$ with $\partial_z^2 w(\mathbf{p}, 0) < 0$, and ends at a saddle $\mathbf{q}$ with $\partial_z^2 w(\mathbf{q}, 0) < 0$. Also, γ is tangent to the direction of weaker repulsion at $\mathbf{p}$.

(R3) γ spirals off from an unstable limit cycle Γ with $\int_\Gamma \partial_z^2 w(\mathbf{x}(s; \mathbf{x}_0), 0)\ ds < 0$, and ends at a saddle $\mathbf{q}$ with $\partial_z^2 w(\mathbf{q}, 0) < 0$.

(R4) γ is an unstable limit cycle with $\int_\gamma \partial_z^2 w(\mathbf{x}(s; \mathbf{x}_0), 0)\ ds < 0$.

All wall shear zeros and limit cycles featured above (i.e. in (S1)-(S4) and (R1)-(R4)) must be nondegenerate, i.e., must attract or repel nearby wall shear trajectories exponentially in the rescaled time s. We compute all the nondegeneracy conditions in Appendix A.2, which are summarized below. Specifically, a nondegenerate node $\mathbf{p}$ satisfies

$$[\nabla_{\mathbf{x}} \cdot \tau(\mathbf{p})]^2 > 4 \det \nabla_{\mathbf{x}} \tau(\mathbf{p}) > 0; \tag{3.25}$$

a nondegenerate saddle $\mathbf{p}$ satisfies

$$\det \nabla_{\mathbf{x}} \tau(\mathbf{p}) < 0; \tag{3.26}$$

a nondegenerate spiral $\mathbf{p}$ satisfies

$$0 < [\nabla_{\mathbf{x}} \cdot \tau(\mathbf{p})]^2 < 4 \det \nabla_{\mathbf{x}} \tau(\mathbf{p});$$

and a nondegenerate limit cycle Γ satisfies

$$\int_\Gamma \left.\frac{\omega \cdot (\nabla_{\mathbf{x}} \tau\ \omega)}{|\omega|^2}\right|_{\mathbf{x}=\mathbf{x}(s,\mathbf{x}_0)} ds \neq 0. \tag{3.27}$$

The above conditions will generically be true away from corners formed by the $z = 0$ plane and another no-slip wall. Separation near corners is discussed in section 3.6.

The above separation and attachment criterion extends to curved boundaries and spheroid surfaces, as discussed in section 3.8. For incompressible Navier-Stokes flows, the criterion can be reformulated using wall pressure and wall shear only (see section 3.7). We discuss the practical implementation of the criterion as an algorithm in chapter 5.

3.5 Slope of separation and attachment surfaces

Recall that the separation angle $\theta(\mathbf{x}_0)$ at a point $\mathbf{x}_0$ of a separation line γ is the angle between the wall normal and the tangent of the curve that lies in the intersection of $\mathcal{S}$ with a plane normal to γ (see figure 2-5).

As shown in Appendix A.1, the separation slope satisfies

$$\tan\theta(\mathbf{x}_0) = \int_{-\infty}^{0} e^{\int_0^s [C(\mathbf{x}(r;\mathbf{x}_0),0) - S_\perp(r)]\ dr} \left.\frac{\partial_z^2 \mathbf{u} \cdot \omega}{2|\omega|}\right|_{\mathbf{x}=\mathbf{x}(s,\mathbf{x}_0),\ z=0} ds, \tag{3.28}$$

where

$$S_\perp(s) = \left.\frac{\omega \cdot (\nabla_{\mathbf{x}} \tau \omega)}{|\omega|^2}\right|_{\mathbf{x}=\mathbf{x}(s,\mathbf{x}_0)} \tag{3.29}$$

measures the wall shear stretching rate normal to the wall shear trajectory $\mathbf{x}(s, \mathbf{x}_0)$ starting from $\mathbf{x}_0$ at time $s = 0$.

Attachment slopes obey a similar formula with the limit taken in forward time

$$\tan\theta(\mathbf{x}_0) = -\int_{0}^{+\infty} e^{\int_0^s [C(\mathbf{x}(r;\mathbf{x}_0),0) - S_\perp(r)]\ dr} \left.\frac{\partial_z^2 \mathbf{u} \cdot \omega}{2|\omega|}\right|_{\mathbf{x}=\mathbf{x}(s,\mathbf{x}_0),\ z=0} ds. \tag{3.30}$$

In case γ is a limit cycle with period T, the improper integral in (3.28) can be reduced to an integral over the period (see Appendix A.4 for details) leading to

$$\tan\theta(\mathbf{x}_0) = \frac{\int_0^T e^{\int_0^s [C(\mathbf{x}(r;\mathbf{x}_0)) - S_\perp(r)] dr} \frac{\partial_z^2 \mathbf{u}\cdot\omega}{2|\omega|}\big|_{\mathbf{x}=\mathbf{x}(s,\mathbf{x}_0),\ z=0}}{e^{\int_0^T [C(\mathbf{x}(r;\mathbf{x}_0)) - S_\perp(r)]\ dr} - 1}. \tag{3.31}$$

3.6 Separation and attachment at corners

The conditions in Eqns. (3.25-3.27) will hold for general flows as long as $\mathbf{p}$ and γ are bounded away from corners. Flows that separate or attach at corners, however, will violate Eqns.(3.25 or Eq. 3.26); examples include the backward facing step flow and the lid-driven cavity flow analyzed in chapter 5.

To see this, consider the case of a vertical wall satisfying $x = 0$ in Fig. 3-7. Due to the no-slip condition on the $z = 0$ and $x = 0$ planes, the velocity field can be written as

$$\mathbf{v}(\mathbf{x}, z) = (x^2 zA, xzB, xz^2 C), \tag{3.32}$$

where

$$\begin{aligned} A(\mathbf{x}, z) &= \int_0^1 \int_0^1 \int_0^1 \partial^3_{xxz} u(rqx, y, sz) q \; dqdrds, \\ B(\mathbf{x}, z) &= \int_0^1 \int_0^1 \partial^2_{xz} v(rx, y, sz) \; dsdr, \\ C(\mathbf{x}, z) &= \int_0^1 \int_0^1 \int_0^1 \partial^3_{xzz} w(sx, y, rqz) q \; dqdrds. \end{aligned} \tag{3.33}$$

Consequently, the wall shear field on the $z = 0$ boundary, its divergence, and the determinant of its gradient vanish identically at the corner formed by the intersection of $x = 0$ and $z = 0$. We now discuss higher-order analogs of the nondegeneracy conditions in Eqns. (3.25) and (3.26) under which (S1)-(S4) and (R1)-(R4) remain applicable at corners. As we show in the Appendix A.3, a point $\mathbf{p}$ lies in the intersection of a wall-shear line and the $x = z = 0$ corner if

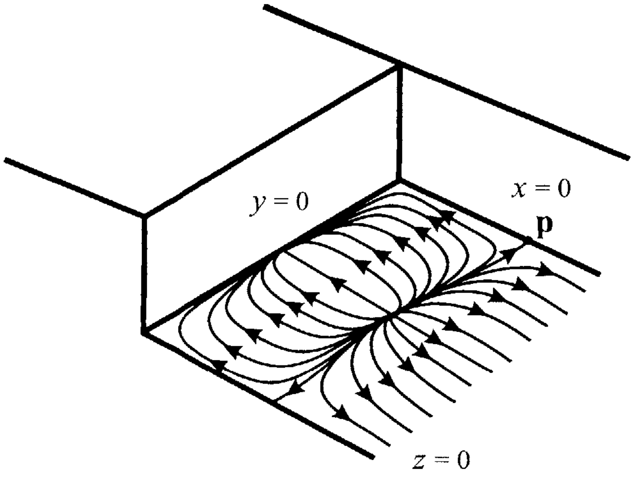

Figure 3-7: Separation at corners.

$$\partial^2_{xz} v(\mathbf{p}, 0) = 0.$$

We further show that the leading-order stretching rate off the $z = 0$ plane at the point $\mathbf{p}$ is now given by

$$\partial^3_{xzz} w(\mathbf{p},0) = -\nabla_{\mathbf{x}} \cdot \partial_x \tau\,(\mathbf{p})\,. \tag{3.34}$$

A comparison of Eqns. (3.7) and (3.34) reveals that τ must be replaced by $\partial_x\tau$ in all conditions on nodes and saddles in (S1)–(S3) and (R1)–(R3). In addition, Eqns. (3.25) and (3.26) are replaced by the following two conditions: $\mathbf{p}$ is a nondegenerate node if

$$[\nabla_{\mathbf{x}} \cdot \partial_x \tau\,(\mathbf{p})]^2 > 4 \det \nabla_{\mathbf{x}} \partial_x \tau\,(\mathbf{p}) > 0, \tag{3.35}$$

whereas, $\mathbf{p}$ is a nondegenerate saddle if

$$\det \nabla_{\mathbf{x}} \partial_x \tau\,(\mathbf{p}) < 0. \tag{3.36}$$

3.7 Separation in Navier-Stokes flows

In flows governed by the Navier-Stokes equations, the separation slope and angle formulae can be simplified to depend on on-wall quantities only. To illustrate this, we consider the general compressible Navier-Stokes momentum equations

$$\frac{\partial\,(\rho\mathbf{v})}{\partial t} + \nabla \cdot (\rho\mathbf{v}\mathbf{v}) = -\nabla p + \nabla \cdot \sigma, \tag{3.37}$$

with ρ, and p, denoting the density and pressure, and $\mathbf{vv}$ denoting the dyadic product of $\mathbf{v}$ with itself. The stress tensor σ is given by

$$\sigma = \lambda(\nabla \cdot \mathbf{v})\mathbf{I} + 2\mu\mathbf{D},$$

where $\mathbf{I}$ is the 3×3 identity matrix, $\mathbf{D} = \frac{1}{2}[\nabla\mathbf{v} + (\nabla\mathbf{v})^T]$ is the rate-of-strain tensor, and μ and λ are the first and second coefficients of viscosity. Invoking the Stokes hypothesis $3\lambda + 2\mu = 0$, we rewrite the stress tensor in component form as

$$\sigma_{ij} = -\frac{2}{3}\mu\frac{\partial v_k}{\partial x_k}\delta_{ij} + \mu\left[\frac{\partial v_i}{\partial x_j} + \frac{\partial v_j}{\partial x_i}\right], \tag{3.38}$$

with δ_{ij} denoting the Kronecker delta, with $(x_1, x_2, x_3) \equiv (\mathbf{x}, z)$ and $\mathbf{v} = (v_1, v_2, v_3) \equiv (u, v, w)$, and with summation understood over repeated indices.

Under the assumption that the viscosity coefficients are constant and the flow is steady, Eq. 3.37 becomes

$$\frac{\partial\,(\rho v_i v_j)}{\partial x_j} = -\frac{\partial p}{\partial x_i} + \mu\frac{\partial \sigma_{ij}}{\partial x_j}. \tag{3.39}$$

Consider the x_1-component of Eq. 3.39,

$$\frac{\partial\,(\rho uu)}{\partial x} + \frac{\partial\,(\rho uv)}{\partial y} + \frac{\partial\,(\rho uw)}{\partial z} = -\frac{\partial p}{\partial x} + \mu\left[\frac{\partial \sigma_{xx}}{\partial x} + \frac{\partial \sigma_{xy}}{\partial y} + \frac{\partial \sigma_{xz}}{\partial z}\right]. \tag{3.40}$$

Note that on the boundary $x_3 \equiv z = 0$, we have

$$\frac{\partial(\rho u u)}{\partial x} + \frac{\partial(\rho u v)}{\partial y} + \frac{\partial(\rho u w)}{\partial z} = 0,$$
$$\frac{\partial \sigma_{xx}}{\partial x} = 0, \qquad \frac{\partial \sigma_{xy}}{\partial y} = 0, \qquad \frac{\partial \sigma_{xz}}{\partial z} = \frac{\partial^2 u}{\partial z^2},$$

which, coupled with Eq. 3.40, yields

$$u_{zz}(\mathbf{x},0) = \frac{1}{\mu} p_x(\mathbf{x},0).$$

A similar equation can be derived for the x_2–component. Combining the equations for the x_1–component and x_2–component leads to the relationship

$$\partial_z^2 \mathbf{u}(\mathbf{x},0) = \frac{1}{\rho\nu} \nabla_{\mathbf{x}} p(\mathbf{x},0). \tag{3.41}$$

The generalization of this relation in arbitrary curvilinear coordinate system is given in section E.1.2 in the Appendix E.

Given Eq. 3.41, the separation slope formula (Eq. 3.22) and the separation angle formula (Eq. 3.28) become

$$\mathbf{g}_0 = -\frac{1}{\rho\nu} \left[2\nabla_{\mathbf{x}} \tau(\mathbf{p}) + \nabla_{\mathbf{x}} \cdot \tau(\mathbf{p})\, \mathbf{I}\right]^{-1} \nabla_{\mathbf{x}} p(\mathbf{p},0), \tag{3.42}$$

and

$$\tan\theta(\mathbf{x}_0) = -\frac{1}{2\rho\nu} \lim_{s\to-\infty} \int_0^s e^{\int_0^r \left[\frac{1}{2}\partial_z^2 w(q) - S_\perp(q)\right] dq} \frac{(\nabla_{\mathbf{x}} p, \omega)}{|\omega|} \bigg|_{\mathbf{x}=\mathbf{x}(r,\mathbf{x}_0),\ z=0}. \tag{3.43}$$

Recall that $\partial_z^2 w(q)$ can be computed from on-wall density and wall-shear, using Eq. 3.7. Attachment slopes and angles satisfy Eqns.(3.42) and (3.43) (with $s \to +\infty$).

3.8 Separation on curved boundaries and spheroids

3.8.1 Curved boundaries

Keeping the notation $\mathbf{x} = (x, y)$, we now assume that the flow boundary satisfies $z = f(\mathbf{x})$ for some smooth function $f(\mathbf{x})$. The no-slip boundary condition for the velocity field $\mathbf{v} = (u, v, w)$ then becomes

$$u(\mathbf{x}, f(\mathbf{x})) = v(\mathbf{x}, f(\mathbf{x})) = w(\mathbf{x}, f(\mathbf{x})) = 0.$$

As earlier, we assume that the steady continuity equation (3.1) holds, which again implies local incompressibility along the boundary:

$$\nabla \cdot \mathbf{v}\left(\mathbf{x}, f(\mathbf{x})\right) = 0. \tag{3.44}$$

We flatten out the boundary by replacing z with the new coordinate

$$\tilde{z} = z - f(\mathbf{x}),$$

which transforms the particle motion equations (3.8) to the form

$$\frac{d}{dt}\mathbf{x} = \tilde{\mathbf{u}}\left(\mathbf{x}, \tilde{z}\right), \qquad \frac{d}{dt}\tilde{z} = \tilde{w}\left(\mathbf{x}, \tilde{z}\right), \tag{3.45}$$

with

$$\tilde{\mathbf{u}}\left(\mathbf{x}, \tilde{z}\right) = \mathbf{u}\left(\mathbf{x}, \tilde{z} + f(\mathbf{x})\right), \qquad \tilde{w}\left(\mathbf{x}, \tilde{z}\right) = w(\mathbf{x}, \tilde{z} + f(\mathbf{x})) - \nabla_{\mathbf{x}} f(\mathbf{x}) \cdot \mathbf{u}(\mathbf{x}, \tilde{z} + f(\mathbf{x})).$$

Because

$$\det\left[\frac{\partial\left(\mathbf{x},\tilde{z}\right)}{\partial\left(\mathbf{x}, z\right)}\right] = 1,$$

the transformation $(\mathbf{x}, z) \mapsto (\mathbf{x},\tilde{z})$ preserves volume. As a result, the flow remains locally incompressible in the $(\mathbf{x},\tilde{z})$ coordinates along the $\tilde{z} = 0$ boundary. The transformed velocity field $\tilde{\mathbf{v}} = (\tilde{\mathbf{u}}, \tilde{w})$, therefore, can again be written in the form

$$\tilde{\mathbf{u}}(\mathbf{x}, \tilde{z}) = \tilde{z}\tilde{\mathbf{A}}(\mathbf{x}, \tilde{z}), \qquad \tilde{w}(\mathbf{x}, \tilde{z}) = \tilde{z}^2\tilde{C}(\mathbf{x}, \tilde{z}), \tag{3.46}$$

with the functions

$$\tilde{\mathbf{A}}(\mathbf{x}, \tilde{z}) = \int_0^1 \partial_{\tilde{z}}\tilde{\mathbf{u}}(\mathbf{x}, s\tilde{z})\, ds, \qquad \tilde{C}(\mathbf{x}, \tilde{z}) = \int_0^1 \int_0^1 \partial_{\tilde{z}}^2\tilde{w}(\mathbf{x}, sq\tilde{z})q\, dq\, ds.$$

By analogy between (3.3) and (3.46), our previous results for separation on flat boundaries carry over to the present case. Specifically, if instead of the true wall shear and wall-vorticity fields, we use their $\mathbf{x}$-projections,

$$\begin{aligned} \tau\left(\mathbf{x}\right) &= \partial_z\mathbf{u}(\mathbf{x}, f(\mathbf{x})), \\ \omega(\mathbf{x}) &= \mathbf{A}^{\perp}\left(\mathbf{x}, f(\mathbf{x})\right), \end{aligned} \tag{3.47}$$

then the separation and attachment criteria of section 3.4 continue to hold. The separation slope and curvature formulae also remain valid in the $(\tilde{\mathbf{x}},z)$ coordinates, as long as we evaluate (3.22), (3.23) and (3.28) at $z = f\left(\mathbf{x}\right)$ instead of $z = 0$.

A procedure to derive an expression for the separation slope in the original coordinates $(\mathbf{x},z)$ can be found in Appendix E, where we also develop a more general approach to deal with arbitrary curved boundaries (i.e. boundaries which cannot be globally represented as a graph of form $z = f(\mathbf{x})$), by introducing non-orthogonal curvilinear coordinate system.

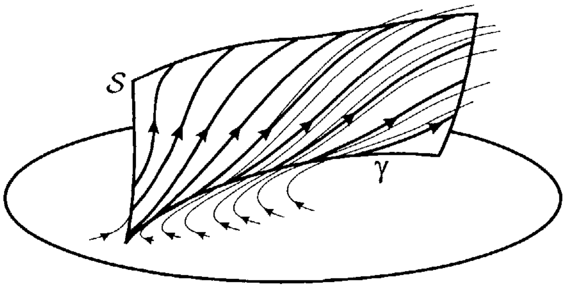

Figure 3-8: Separation on a spheroid surface.

3.8.2 Spheroids

Spheroids are surfaces obtained from smooth deformations of a two-dimensional sphere (see figure 3-8). Recall that our mathematical argument in Appendix A.1, utilizes the *global* geometry of the boundary. Specifically, a crucial ingredient, the classic Poincaré-Bendixson theory (see, e.g., Guckenheimer & Holmes [34]), applies to bounded planar wall shear fields. By this theory, all bounded wall shear lines must emanate from, and converge to, one of the following types of sets: a wall shear zero, a wall shear limit cycle, or a set of wall shear zeros connected by wall shear trajectories .

The classic Poincaré-Bendixson theory, however, extends to any surface that is diffeomorphic to a sphere , i.e., any surface that is the image of a sphere under a continuously differentiable invertible mapping with a differentiable inverse (see Hartman [43]). As a result, the separation theory developed here carries over to common aerodynamic objects, such as ordinary airfoils, fuselages, projectiles, and prolate spheroids. In specific separation and attachment on them can be studied globally using the approach outlined in Appendix E.

Boundaries that are formally not covered by our theory are two-dimensional manifolds on which the Poincaré-Bendixson theory fails: toroidal surfaces and surfaces with handles. Our results, however, do apply even to such boundaries if the separation or attachment line γ is fully contained in a boundary domain satisfying $z = f(\mathbf{x})$ (cf. 3.8.1).

3.9 Open-closed classification of separation patterns

A consequence of the previous sections is the following general result: three-dimensional steady separation or attachment is either *closed* (γ connects zeros of τ), *open* (γ is a limit cycle of τ), or *open-closed* (γ connects a saddle-type zero of τ to a limit cycle). There is no other steady separation or attachment pattern that satisfies all the basic requirements (i)-(iv) we put forward in section 2.2.1.

The (S3) open-closed separation has apparently been overlooked as a possibility in

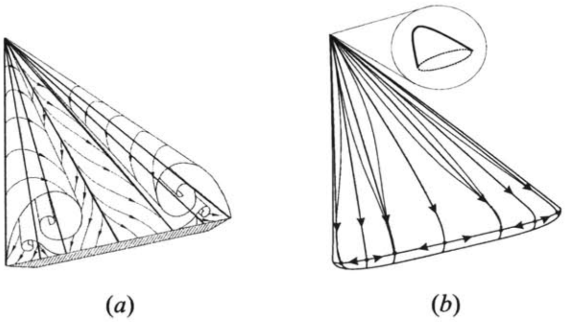

Figure 3-9: a) Common illustration of separation on a delta wing (from Délery [20]). (b) Simplest complete separation pattern on the full delta wing.

earlier studies. Hsieh and Wang [44] however, do observe connections between saddle-type zeros and limit cycles of the wall shear field on a cylinder with a hemispherical cap. On the other hand, the (S4) type open separation has never been reported in literature. We show first numerical and experimental demonstration of this separation pattern in chapters 5 and 6, respectively.

Recall that (S3) and (S4) separation patterns admit unique separation line and separation surface; and therefore differ from crossflow separation, the classic example of open separation that typically arises in flow past round nosed bodies of revolution (see section 2.2.3 and chapter 8).

Another frequently cited example of open separation is that over a delta wing, as sketched in figure 3-9(a). In this example, as often remarked, the straight wall shear lines emanating from the tip of the wing do not terminate in wall shear zeros.

Note, however, that the wall shear pattern in figure 3-9(a) is incomplete. The full wing is a two-dimensional spheroid, thus by the Poincaré-Bendixson theory, all wall shear lines must emanate from, and converge to, one of the three types of sets described in section 3.8.2: a wall shear zero, a wall shear limit cycle, or a set of wall shear zeros connected by wall shear trajectories

A full wall shear pattern consistent with the Poincaré-Bendixson theory is shown in 3-9(b). This pattern exhibits closed separation: all separation lines connect zeros of the τ-field. The wall shear lines near the tip may be intricate, but must terminate in one of the three types of sets mentioned above.

Other proposed examples of open separation involve flows defined on infinite domains (Kenwright, Henze & Levit [51]). The Poincaré-Bendixson theory is invalid on unbounded domains: an unbounded separation line may indeed not converge to zeros or limit cycles of the τ-field. However, we have excluded unbounded separation lines as unphysical (see (iii) of section 2.2.1).

In summary, the separation theory described in this chapter allows for open separation, but not of the type suggested in earlier studies. Some of those studies proposed examples with incomplete separation patterns; others proposed examples with unbounded or nonunique separation surfaces. Open separation with nonunique separation will be discussed in chapter 8.

Chapter 4

Fixed Unsteady Separation

Here we extend the results of previous chapter on steady separation to *fixed unsteady separation* in 3D flows. Recall, by fixed unsteady separation, we mean fluid departure from the boundary near time-independent points/lines on the boundary. Such fixed separation points/lines might seem counterintuitive for an unsteady flow, but turn out to be ubiquitous in flows with a temporal mean component. In such flows, oscillations of the velocity field around its mean give rise to well-defined averaged locations where particles break away from the boundary. The surfaces that these particles follow, however, have general time dependence.

To locate separation curves and surfaces in unsteady flow with a steady mean, we apply the mathematical theory of averaging (Sanders & Verhulst [76]). Averaging is applicable here because in appropriate local coordinates, the differential equation for Lagrangian particle motion becomes slowly varying near the boundary. In these coordinates, averaging theory allows us to derive mathematically exact criteria for wall-based unstable manifolds. Despite their unsteadiness, separation curves and surfaces have a steady base that remains fixed on the no-slip boundary. We predict these fixed locations by applying the steady three-dimensional separation criteria derived in the previous chapter to a weighted time average of the wall-shear field. We also obtain leading-order approximations for the time-varying separation curves and surfaces near the wall.

4.1 Weakly unsteady particle dynamics near the boundary

In this section, we show that under assumptions listed below, unsteady flow near a no slip boundary is very close to the flow generated by an appropriately scaled and averaged version of the velocity $\mathbf{v}$.

Our main assumption is that the velocity field $\mathbf{v}$ has a steady asymptotic mean component

$$\overline{\mathbf{v}}(\mathbf{x}, z) = \lim_{T\to\infty} \frac{1}{T} \int_{t_0-T}^{t_0} \mathbf{v}(\mathbf{x}, z, t)dt, \tag{4.1}$$

that is bounded on the flow domain of interest for any choice of the initial time t_0. Flows in this category include periodic and quasiperiodic flows, as well as turbulent flows with a steady mean component.

Finally, we assume that the integrated velocity fluctuation

$$\boldsymbol{\Delta}(\mathbf{x}, z, t) = \int_{t_0}^{t} [\mathbf{v}(\mathbf{x}, z, t) - \overline{\mathbf{v}}(\mathbf{x}, z)] dt, \tag{4.2}$$

and its spatial derivatives up to third order are uniformly bounded in time on the flow domain of interest.

4.1.1 First-order averaged normal form

To focus on the dynamics near the $z = 0$ boundary, we apply the rescaling $\tilde{z} = \epsilon \bar{z}$ with $0 < \epsilon \ll 1$, which transforms the particle equations of motion (2.16) further to

$$\dot{\eta} = \epsilon \mathbf{f}(\eta, t) + \epsilon^2 \mathbf{g}(\eta, t; \epsilon), \tag{4.3}$$

where $\eta = (\mathbf{x}, \bar{z})^T$, and

$$\mathbf{f} = \begin{pmatrix} \bar{z}\mathbf{A}_1(\mathbf{x}, 0, t) \\ \bar{z}^2 C_1(\mathbf{x}, 0, t) \end{pmatrix}, \qquad \mathbf{g} = \begin{pmatrix} \bar{z}^2[\partial_z \mathbf{A}_1(\mathbf{x}, 0, t) + \mathcal{O}(\bar{z}\epsilon)] \\ \bar{z}^3[\partial_z C_1(\mathbf{x}, 0, t) + \mathcal{O}(\bar{z}\epsilon)] \end{pmatrix}.$$

For small $\epsilon > 0$, (4.3) is a slowly varying system to which the principle of averaging is applicable. More specifically, as we show in Appendix B.1, there exists a change of coordinates (averaging transformation)

$$\eta = \zeta + \epsilon \mathbf{w}(\zeta, t), \quad \mathbf{w}(\zeta, t) = \int_{t_0}^{t} [\mathbf{f}(\zeta, \tau) - \overline{\mathbf{f}}(\zeta)] d\tau, \tag{4.4}$$

under which (4.3) becomes

$$\dot{\zeta} = \epsilon \overline{\mathbf{f}}(\zeta) + \epsilon^2 \mathbf{f}^1(\zeta, t) + \mathcal{O}(\epsilon^3), \tag{4.5}$$

with

$$\begin{aligned} \overline{\mathbf{f}}(\zeta) &= \lim_{T \to \infty} \frac{1}{T} \int_{t_0 - T}^{t_0} \mathbf{f}(\zeta, \tau) d\tau, \\ \mathbf{f}^1(\zeta, t) &= \nabla_\zeta \mathbf{f}(\zeta, t) \mathbf{w}(\zeta, t) + \mathbf{g}(\zeta, t; 0) - \nabla_\zeta \mathbf{w}(\zeta, t) \overline{\mathbf{f}}(\zeta). \end{aligned}$$

Note that explicit time-dependence now only appears in the $\mathcal{O}(\epsilon^2)$ terms of (4.5). Near the wall, therefore, the flow remains $\mathcal{O}(\epsilon^2)$ close to its steady mean when viewed in the ζ coordinates.

4.1.2 Second-order averaged normal form

Our final change of variables pushes the explicit time-dependence in (4.5) to even higher order. Namely, the second-order averaging transformation

$$\zeta = \xi + \epsilon^2 \mathbf{h}(\xi, t), \quad \mathbf{h}(\xi, t) = \int_{t_0}^{t} [\mathbf{f}^1(\xi, \tau) - \bar{\mathbf{f}}^1(\xi)] d\tau, \tag{4.6}$$

puts (4.5) in the form

$$\dot{\xi} = \epsilon \bar{\mathbf{f}}(\xi) + \epsilon^2 \bar{\mathbf{f}}^1(\xi) + \mathcal{O}(\epsilon^3), \tag{4.7}$$

where

$$\bar{\mathbf{f}}^1(\xi) = \lim_{T \to \infty} \frac{1}{T} \int_{t_0 - T}^{t_0} \mathbf{f}^1(\xi, \tau) d\tau, \tag{4.8}$$

and only the $\mathcal{O}(\epsilon^3)$ terms in (4.7) have explicit time dependence.

4.2 Fixed unsteady separation and attachment criteria

We shall first use the leading-order steady part of the second-order averaged normal form (4.7) to locate separation and attachment. This can be done based on the results of chapter 3 on steady three-dimensional separation. We then show that these steady separation and attachment locations persist if we take the additional $\mathcal{O}(\epsilon^3)$ unsteady terms into account in (4.7). We also obtain leading-order approximations for the time-varying off-wall part of the separation curves and surfaces. The mathematical details of our arguments are relegated to Appendices B.2; here we simply summarize the results.

4.2.1 Steady separation at leading order

The first-order-averaged normal form (4.5) shows that an unsteady compressible flow near a no-slip boundary can be viewed as a small perturbation to the steady velocity field

$$\mathbf{v}^0(\mathbf{x}, \bar{z}) = (\epsilon \bar{z} \bar{\tau}(\mathbf{x}), \epsilon \bar{z}^2 \overline{C}(\mathbf{x})), \tag{4.9}$$

where the weighted average of the wall shear,

$$\bar{\tau}(\mathbf{x}) = \lim_{T \to \infty} \frac{1}{T} \int_{t_0 - T}^{t_0} e^{\int_{t_0}^{\tau} \partial_z w(\mathbf{x}, 0, s)\, ds} \partial_z \mathbf{u}(\mathbf{x}, 0, \tau) d\tau, \tag{4.10}$$

is obtained from the instantaneous wall shear

$$\tau(\mathbf{x}, t) = \partial_z \mathbf{u}(\mathbf{x}, 0, t). \tag{4.11}$$

Furthermore, $\overline{C}$ in (4.9) is defined as

$$\overline{C}(\mathbf{x}) = \frac{1}{2}\lim_{T\to\infty}\frac{1}{T}\int_{t_0-T}^{t_0} e^{\int_{t_0}^{\tau}\partial_z w(\mathbf{x},0,s)ds}\partial_z^2 w(\mathbf{x},0,\tau)d\tau, \tag{4.12}$$

and measures the weighted average rate of stretching normal to the boundary.

The particle equations of motion for the velocity field (4.9) are given by

$$\begin{aligned} \dot{\mathbf{x}} &= \epsilon\bar{z}\bar{\tau}(\mathbf{x}), \\ \dot{\bar{z}} &= \epsilon\bar{z}^2\overline{C}(\mathbf{x}). \end{aligned} \tag{4.13}$$

As in chapter 3, we introduce the rescaled time variable

$$s = \epsilon\int_{t_0}^{t}\bar{z}(r)\ dr, \tag{4.14}$$

so that the above equations of motion become

$$\begin{aligned} \mathbf{x}' &= \bar{\tau}(\mathbf{x}), \\ \bar{z}' &= \bar{z}\overline{C}(\mathbf{x}), \end{aligned} \tag{4.15}$$

with prime denoting differentiation with respect to the rescaled time s.

In the rescaled system (4.15), the averaged wall shear generates a fictitious flow

$$\mathbf{x}' = \bar{\tau}(\mathbf{x}), \tag{4.16}$$

on the $z = 0$ boundary. We refer to a trajectory $\mathbf{x}(s, \mathbf{x}_0)$ of (4.16) starting from $\mathbf{x}_0$ at $s = 0$ as an *averaged wall-shear trajectory*. A connected union of wall-shear trajectories will be called an *averaged wall-shear line*, denoted by γ.

As shown in chapter 3, steady separation locations crucially depend on the rate at which wall-shear trajectories converge to, or diverge from, each other. In the context of the rescaled averaged flow (4.16), these rates are measured by the averaged normal strain rate field

$$\overline{S}_{\perp}(\mathbf{x}) = \frac{\bar{\omega}\cdot([\nabla_{\mathbf{x}}\bar{\tau}]\bar{\omega})}{|\bar{\omega}|^2}|_{\mathbf{x}},$$

where $\nabla_{\mathbf{x}}\bar{\tau}(\mathbf{x})$ is the wall-tangential gradient of $\bar{\tau}(\mathbf{x})$, and $\bar{\omega}$ is the averaged on-wall vorticity field

$$\bar{\omega}(\mathbf{x}) = \bar{\tau}^{\perp}(\mathbf{x}), \tag{4.17}$$

with the notation $(a, b)^{\perp} = (-b, a)$.

With the above quantities at hand, we can apply the results of chapter 3 to locate separation and attachment in the steady averaged velocity field $\mathbf{v}^0(\mathbf{x}, \bar{z})$. From chapter 3 we recall that $\mathbf{v}^0(\mathbf{x}, \bar{z})$ can admit two possible types of separation points $\mathbf{p}$ (see figure 3-1) and four basic types of separation lines γ (see figure 3-5).

As a second step, we shall use techniques from nonlinear dynamical systems theory to show that the above steady separation structures have nearby time-dependent counterparts in the original unsteady velocity field $\mathbf{v}$. We list the final results below, and relegate their detailed proof to Appendix B.2.

4.2.2 Criteria for fixed separation and attachment points in the unsteady flow

Theorem 1 Suppose that a point $\mathbf{p}$ satisfies

$$\bar{\tau}(\mathbf{p}) = 0, \qquad \nabla_{\mathbf{x}} \cdot \bar{\tau}(\mathbf{p}) < 0, \qquad \det\nabla_{\mathbf{x}}\bar{\tau}(\mathbf{p}) > 0, \qquad \overline{C}(\mathbf{p}) > 0. \tag{4.18}$$

Then $(\mathbf{x}, z) = (\mathbf{p}, 0)$ is a fixed unsteady separation point for the velocity field $\mathbf{v}$.

By reversing time in the proof of Theorem 1, we find that if

$$\bar{\tau}(\mathbf{p}) = 0, \qquad \nabla_{\mathbf{x}} \cdot \bar{\tau}(\mathbf{p}) > 0, \qquad \det\nabla_{\mathbf{x}}\bar{\tau}(\mathbf{p}) > 0, \qquad \overline{C}(\mathbf{p}) < 0, \tag{4.19}$$

are satisfied, then $\mathbf{p}$ is a fixed attachment point.

In summary, we have the following results for the original unsteady velocity field $\mathbf{v}$:

(S0) A separation point $(\mathbf{p}, 0)$ on the $z = 0$ boundary is either a stable node or a stable spiral of the time-averaged wall-shear field (4.10) with $\overline{C}(\mathbf{p}) > 0$.

(R0) A attachment point $(\mathbf{p}, 0)$ on the $z = 0$ boundary is either an unstable node or unstable spiral of the time-averaged wall-shear field (4.10) with $\overline{C}(\mathbf{p}) < 0$.

4.2.3 Criteria for fixed separation and attachment lines in the unsteady flow

Theorem 2 Let γ be a bounded wall-shear line of the time averaged wall-shear field (4.10). Assume that at each point $\mathbf{x}$ of γ, we have

$$\overline{S}_{\perp}(\mathbf{x}) - \overline{C}(\mathbf{x}) < 0, \qquad \overline{C}(\mathbf{x}) > 0. \tag{4.20}$$

Assume further that one of the following holds:

(S1) γ originates from a saddle $\mathbf{p}$ and ends at a stable spiral $\mathbf{q}$.

(S2) γ originates from a saddle $\mathbf{p}$ and ends at a stable node $\mathbf{q}$. Also, γ is tangent to the direction of weaker attraction at $\mathbf{q}$.

(S3) γ originates from a saddle $\mathbf{p}$ and spirals onto a stable limit cycle Γ.

(S4) γ is a stable limit cycle Γ

Then γ is a fixed separation line for the unsteady velocity field $\mathbf{v}$.

We prove Theorem 1 in section B.2.2 of Appendix B.2. By reversing time in the proof, we obtain a criterion for attachment lines. Specifically, let γ be a bounded wall-shear line of the time-averaged wall-shear field (4.10). Assume that at each point $\mathbf{x}$ of γ, we have

$$\overline{S}_{\perp}(\mathbf{x}) - \overline{C}(\mathbf{x}) > 0, \qquad \overline{C}(\mathbf{x}) < 0. \tag{4.21}$$

Assume further that one of the following holds:

(R1) γ originates from an unstable spiral $\mathbf{p}$ and ends at a saddle $\mathbf{q}$.

(R2) γ originates from a unstable node $\mathbf{p}$ and ends at a saddle $\mathbf{q}$. Also, γ is tangent to direction of weaker repulsion at $\mathbf{p}$.

(R3) γ spirals off an unstable limit cycle $\mathbf{\Gamma}$ and ends at a saddle $\mathbf{q}$.

(R4) γ is a unstable limit cycle $\mathbf{\Gamma}$.

Then γ is a fixed attachment line for the unsteady velocity field $\mathbf{v}$.

The time-averaged wall-shear zeros $\mathbf{p}$ and $\mathbf{q}$, as well as the limit cycle $\mathbf{\Gamma}$ featured above must be nondegenerate: they must attract or repel nearby time averaged wall-shear trajectories exponentially in the rescaled time s (3.9). For the details of these nondegeneracy conditions, we refer the reader to the section 3.4.

4.2.4 Fixed unsteady separation at corners

Analyzing separation at intersection of noslip boundaries requires additional care, as was discussed in section 3.6 in the context of steady flows. Here we extend the analysis to encompass unsteady velocity fields which satisfy the assumptions of this chapter.

For simplicity we consider the same geometry studied in the section 3.6. We show in the Appendix B.3, that the steady averaged normal form now becomes

$$\begin{aligned} \dot{\bar{x}} &= \bar{x}^2\bar{z}\overline{\tau}_1(\bar{x}, y), \\ \dot{y} &= \bar{x}\bar{z}\overline{\tau}_2(\bar{x}, y), \\ \dot{\bar{z}} &= \bar{x}\bar{z}^2\overline{\tau}_3(\bar{x}, y), \end{aligned} \tag{4.22}$$

where

$$\begin{aligned} \overline{\tau}_1(\bar{x}, y) &= \lim_{T\to\infty} \frac{1}{T}\int_{t_0-T}^{t_0} e^{\int_{t_0}^{t} \bar{x}C(\bar{x},y,0,\tau)d\tau}\partial^3_{xxz}u(0, y, 0, t)dt, \\ \overline{\tau}_2(\bar{x}, y) &= \lim_{T\to\infty} \frac{1}{T}\int_{t_0-T}^{t_0} e^{\int_{t_0}^{t} \bar{x}C(\bar{x},y,0,\tau)d\tau}\partial^2_{xz}v(0, y, 0, t)dt, \\ \overline{\tau}_3(\bar{x}, y) &= \lim_{T\to\infty} \frac{1}{T}\int_{t_0-T}^{t_0} e^{\int_{t_0}^{t} \bar{x}C(\bar{x},y,0,\tau)d\tau}\partial^3_{xzz}w(0, y, 0, t)dt. \end{aligned}$$

With this notation, the wall-shear field $\bar{\tau}$ (4.10) can be written as

$$\bar{\tau} = (\bar{x}^2\overline{\tau}_1, \bar{x}\overline{\tau}_2). \tag{4.23}$$

Let γ be an averaged wall-shear trajectory of (4.23) that terminates in a point $\mathbf{p} = (0, p)$ of the $y = 0$ corner of the $z = 0$ plane. Based on the analysis in Appendix A.3, we conclude that

(1) $\mathbf{p}$ satisfies

$$\overline{\tau}_2(\mathbf{p}) = 0,$$

and can only be either a saddle or a node of the $\overline{\tau}$ vector field.

(2) $\mathbf{p}$ is a nondegenerate node within the $z = 0$ plane if

$$[\overline{\tau}_1(\mathbf{p}) + \partial_y \overline{\tau}_2(\mathbf{p})]^2 > 4\overline{\tau}_1(\mathbf{p})\partial_y \overline{\tau}_2(\mathbf{p}) > 0, \tag{4.24}$$

whereas $\mathbf{p}$ is a nondegenerate saddle within the $z = 0$ plane if

$$\overline{\tau}_1(\mathbf{p})\partial_y \overline{\tau}_2(\mathbf{p}) < 0. \tag{4.25}$$

(3) For separation to take place along γ, the leading-order stretching rate off the $z = 0$ plane at the point $\mathbf{p}$ must satisfy

$$\overline{\tau}_3(\mathbf{p}) > 0,$$

and we must also have

$$\overline{S}_\perp(\mathbf{x}) - \overline{C}(\mathbf{x}) < 0, \qquad \overline{C}(\mathbf{x}) > 0, \tag{4.26}$$

for all points $\mathbf{x} \neq \mathbf{p}$ of γ.

4.2.5 Separation- and attachment-slope formulae

If we use the first-order averaged normal form (4.5) to compute $\mathbf{g}_0(t)$ or $\theta(\mathbf{x}_0, t)$, we always obtain zero values for both. We can, however, use the second-order averaged normal form (4.7) to obtain a more refined approximation for the separation slope. Specifically, as we show in Appendix B.4, we obtain that at time t_0, the slope of a separation curve emanating from $\mathbf{p}$ is given by

$$\mathbf{g}_0(t_0) = -\left[\lim_{T\to\infty} \frac{1}{T}\int_{t_0-T}^{t_0} \mathbf{P}(\mathbf{p}, \tau, t_0)d\tau\right]^{-1} \times \lim_{T\to\infty} \frac{1}{T}\int_{t_0-T}^{t_0} \mathbf{Q}(\mathbf{p}, \tau, t_0), \tag{4.27}$$

where

$$\begin{aligned}
\mathbf{P}(\mathbf{x}, \tau, t_0) &= e^{\int_{t_0}^{\tau} \partial_z w(\mathbf{x},0,s)ds}\left[\nabla_{\mathbf{x}}\partial_z \mathbf{u}(\mathbf{x}, 0, \tau) + \partial_z \mathbf{u}(\mathbf{x}, 0, \tau)\left(\int_{t_0}^{\tau} \nabla_{\mathbf{x}}\partial_z w(\mathbf{x}, 0, s)ds\right)^T\right] \\
&\quad -\frac{1}{2}e^{\int_{t_0}^{\tau} \partial_z w(\mathbf{x},0,s)ds}\mathbf{I}\partial_z^2 w(\mathbf{x}, 0, \tau), \\
\mathbf{Q}(\mathbf{x}, \tau, t_0) &= \frac{1}{2}e^{2\int_{t_0}^{\tau} \partial_z w(\mathbf{x},0,s)ds}\partial_z^2 \mathbf{u}(\mathbf{x}, 0, \tau) + \mathbf{P}(\mathbf{x}, \tau, t_0)\int_{t_0}^{\tau} e^{\int_{t_0}^{p} \partial_z w(\mathbf{x},0,s)\,ds}\partial_z \mathbf{u}(\mathbf{x}, 0, p)dp.
\end{aligned}$$

The above slope formula is equally valid for attachment curves by a time-reversal argument.

We also show in Appendix B.4 that at time t_0, the slope of a separation surface at a boundary point $\mathbf{x}_0$ satisfies

$$\tan(\theta(\mathbf{x}_0, t_0)) = \int_{-\infty}^{0} e^{\int_0^q [\overline{C}(\mathbf{x}(r,\mathbf{x}_0)) - \overline{S}_\perp(r)]dr} \frac{\overline{\mathbf{R}} \cdot \bar{\omega}}{|\bar{\omega}|} |_{\mathbf{x}=\mathbf{x}(q,\mathbf{x}_0)} dq, \tag{4.28}$$

where $\mathbf{x}(q, \mathbf{x}_0)$ is a trajectory on the separation line γ satisfying the differential equation (4.16). Furthermore, the function $\overline{\mathbf{R}}$ in (4.28) is defined as

$$\overline{\mathbf{R}}(\mathbf{x}, t_0) = \lim_{T \to \infty} \frac{1}{T} \int_{t_0 - T}^{t_0} \mathbf{R}(\mathbf{x}, \tau, t_0) d\tau,$$

where

$$\begin{aligned}
\mathbf{R}(\mathbf{x}, \tau, t_0) &= \frac{1}{2} e^{2\int_{t_0}^{\tau} \partial_z w(\mathbf{x},0,s)ds} \partial_z^2 \mathbf{u}(\mathbf{x}, 0, \tau) + \mathbf{P}(\mathbf{x}, \tau, t_0) \int_{t_0}^{\tau} [e^{\int_{t_0}^{p} \partial_z w(\mathbf{x},0,s)\, ds} \partial_z \mathbf{u}(\mathbf{x}, 0, p) - \bar{\tau}(\mathbf{x})] dp \\
&+ \left\{ \int_{t_0}^{\tau} \left(e^{\int_{t_0}^{p} \partial_z w(\mathbf{x},0,s)ds} \left[\nabla_{\mathbf{x}} \partial_z \mathbf{u}(\mathbf{x}, 0, p) + \partial_z \mathbf{u}(\mathbf{x}, 0, p) \left(\int_{t_0}^{p} \nabla_{\mathbf{x}} \partial_z w(\mathbf{x}, 0, s) ds \right)^T \right] \right. \right. \\
&- \left. \left. \nabla_{\mathbf{x}} \bar{\tau}(\mathbf{x}) \right) dp \right\} \bar{\tau}(\mathbf{x}).
\end{aligned}$$

Attachment slopes obey a similar formula with the limit in the improper integral taken in forward time:

$$\tan(\theta(\mathbf{x}_0, t_0)) = -\int_{0}^{+\infty} e^{\int_0^q [\overline{C}(\mathbf{x}(r,\mathbf{x}_0)) - \overline{S}_\perp(r)]dr} \frac{\overline{\mathbf{R}} \cdot \overline{\omega}}{|\overline{\omega}|} |_{\mathbf{x}=\mathbf{x}(q,\mathbf{x}_0)} dq. \tag{4.29}$$

In case the $\overline{\gamma}$ is a limit cycle with period T, the improper integral in (4.28) reduces to an integral over the period

$$\tan\theta(\mathbf{x}_0, t_0) = \frac{\int_0^T e^{\int_0^q \left[\overline{C}(\mathbf{x}(r,\mathbf{x}_0)) - \overline{S}_\perp(r)\right]dr} \frac{(\overline{\mathbf{R}}, \overline{\omega})}{|\overline{\omega}|} |_{\mathbf{x}=\mathbf{x}(q,\mathbf{x}_0)} dq}{e^{\int_0^T \left[\overline{C}(\mathbf{x}(r,\mathbf{x}_0)) - \overline{S}_\perp(r)\right]\, dr} - 1}, \tag{4.30}$$

similar to the simplification obtained in context of steady flows (see section 3.5).

For incompressible flows, we have $\partial_z w(\mathbf{x}, 0, t) \equiv 0$ and hence the above slope formulae simplify considerably. For incompressible Navier-Stokes flows, the formulae (4.27), (4.28) and (4.29) can further be expressed in terms of the wall shear, the wall pressure and their derivatives (see section 3.7 and Appendix E.1.2 for details).

Chapter 5

Numerical Verification of Fixed Separation Criteria

In this chapter we illustrate our fixed separation criteria on analytical flow models and in direct numerical simulations of important benchmark problems. Our analysis follows a well-defined wall-based algorithm, thus the present study of problems also provides a practical recipe to uncover the geometry of three-dimensional separated flows in more general context.

The analytic flow models are derived from the Taylor-expansion of the Navier-Stokes equations at a boundary point (Perry and Chong [72]). These flow models are sophisticated enough to exhibit the basic separation types, yet do not pose computational or experimental difficulties that would obstruct the accuracy of our predictions.

We first illustrate our analytic predictions on steady models and then consider their periodic, quasiperiodic, and aperiodic versions. In each case, we verify our basic assumptions, predict separation points and separation lines, then obtain first order approximations of separation curves and separation surfaces. We conclude by verifying these approximate separation curves and surfaces by advecting particles close to the boundary and observing their breakaway geometry.

We then outline an algorithm for systematically analyzing fixed separation and attachment in numerical and experimental data sets. We illustrate this algorithm in direct numerical simulation of backward-facing step and a lid-driven cavity flow. For the cavity flow we consider two cases, in which lid is driven steadily and in a time-periodic fashion. The simulations are performed using Staggered Grid Multi Domain Method [47]. In addition to local analysis, we also visualize the corresponding global separation and attachment surfaces, which reveal highly complex separated flow geometry.

All the separation patterns in these two flow geometries turn out to be of (S1) and (S2) type. We show (S4) type of separation in flow past a rotating sphere in which separation occurs along a limit cycle of the wall shear field. This is the first documented numerical example of (S4) separation pattern.

5.1 Analytical Examples

Here we analyze three-dimensional separation in analytic flow models obtained as truncated expansions of the Navier-Stokes equations near a boundary point (see Perry & Chong 1986). All our models are incompressible and dynamically consistent up to quartic order in the distance from the point of expansion. We give a brief summary of the derivation of these models in section A.5 of the Appendix A.

Varying free parameters in our models, we provide examples of the four basic separation patterns (S1)-(S4). We then generate streamlines numerically to confirm the predicted location and slope of the separation surface.

On all the steady examples below, we also evaluate the vorticity-based separation theory of Wu et al. [108], the only general criterion available for three-dimensional separation. Appendix A.6 contains a summary of this criterion and the corresponding separation-slope formula in Cartesian coordinates. As we shall see, the vorticity-based theory yields inaccurate separation surfaces that intersect–rather than attract and eject–nearby streamlines at the wall. This is because the theory postulates separation lines to be local maximizers (ridges) of the scalar field

$$\varphi(\mathbf{x}) = S_{\perp}(\mathbf{x})\left[S_{\perp}(\mathbf{x}) + S_{||}(\mathbf{x})\right] / \left|\omega(\mathbf{x})\right|^{2},$$

even though such ridges only coincide with wall shear lines if the τ-field is linear (see Appendix E). Near wall shear zeros, however, the τ-field is close to linear, and hence the vorticity-based prediction for separation lines becomes reasonably accurate. In the examples admitting separation lines, we shall plot the contours of $\varphi(\mathbf{x})$ over domains where the two additional separation conditions of Wu et al. [108], $S_{\perp} < 0$ and $S_{\perp} + S_{||} < 0$, are also satisfied. We shall then locate ridges of $\varphi(\mathbf{x})$ for comparison with the exact theory.

5.1.1 Example I: Tornado-type separation

A special case of the model velocity field (A.61) is given by

$$\begin{aligned} u &= -xz + yz + (\alpha + \delta x)z^{2}, \\ v &= -xz - yz + (\beta + \delta y)z^{2}, \\ w &= z^{2} - (2\delta/3)\, z^{3}, \end{aligned} \tag{5.1}$$

with the wall shear field:

$$\tau = \begin{pmatrix} -x + y \\ -x - y \end{pmatrix}.$$

This wall shear field is linear and hence does not admit any limit cycles. The only wall shear zero is $\mathbf{p} = (0, 0)$, for which

$$\det \nabla_{\mathbf{x}}\tau(\mathbf{p}) = 2 > 0, \qquad \nabla_{\mathbf{x}} \cdot \tau(\mathbf{p}) = -2 < 0, \qquad \partial_{z}^{2} w(\mathbf{p}, 0) = 2 > 0.$$

Thus, by (3.17), $\mathbf{p}$ is a separation point with a one-dimensional separation curve that

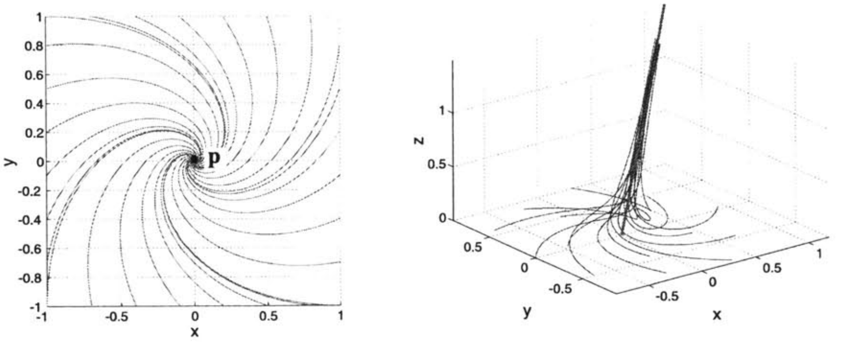

(a) *(b)*

Figure 5-1: (a) Wall shear trajectories for Example I ($\alpha = 1$, $\beta = 2$ and $\delta = 0$) (b) Predicted second-order separation curve, and nearby streamlines.

collects and ejects nearby fluid particles. A linear stability analysis reveals that $\mathbf{p}$ is an unstable spiral of the wall shear field (see figure 5-1a).

Evaluating the slope and curvature formulae (3.22) and (3.23), we find that the separation curve satisfies

$$\begin{pmatrix} x \\ y \end{pmatrix} = z \begin{pmatrix} 2/5 + z\delta/6 & 1/5 + z\delta/6 \\ -1/5 - z\delta/6 & 2/5 + z\delta/6 \end{pmatrix} \begin{pmatrix} \alpha \\ \beta \end{pmatrix} + O(z^3). \tag{5.2}$$

Figure 5-1(b) confirms that (5.2) is indeed the correct quadratic approximation for the separation curve.

5.1.2 Example II: Nonlinear saddle-type separation

In Appendix A.5, we obtain the velocity field

$$\begin{aligned} u &= axz - 3dxz^2, \\ v &= -byz + cx^2z - cz^3/3, \\ w &= (b-a)\,z^2/2 + dz^3, \end{aligned} \tag{5.3}$$

by applying the Perry-Chong procedure to the wall shear field

$$\tau = \begin{pmatrix} ax \\ -by + cx^2 \end{pmatrix}, \qquad a, b > 0.$$

Because $\det \nabla_{\mathbf{x}} \tau(\mathbf{p}) = -ab < 0$, the point $\mathbf{p} = (0, 0)$ is a nondegenerate saddle. We find the wall shear trajectories by direct integration:

$$\mathbf{x}(s; \mathbf{x}_0) = \begin{pmatrix} x_0 e^{as} \\ y_0 e^{-bs} + \frac{x_0^2}{2a+b}\left(e^{2as} - e^{-bs}\right) \end{pmatrix}.$$

Thus, the stable manifold $W^s(\mathbf{p})$ of the wall shear saddle $\mathbf{p}$ is the y-axis; the unstable manifold $W^u(\mathbf{p})$ satisfies

$$W^u(\mathbf{p}) = \{(x,y)\ :\ y = \frac{x^2}{2a+b}\},$$

as shown in Figure 5-2(a).

Because only $W^s(\mathbf{p})$ and $W^u(\mathbf{p})$ connect to a saddle point and there are no limit cycles in the τ-field, only $W^s(\mathbf{p})$ and $W^u(\mathbf{p})$ are separation and reattachment line candidates. Noting that

$$\partial_z^2 w(\mathbf{p},0) = b - a, \tag{5.4}$$

we find that for $b > a$, the unstable manifold $W^u(\mathbf{p})$ is a separation line of type (S1), (S2), (S3) or (S4) on any bounded domain. The actual type of separation depends on the forward-asymptotics of $W^u(\mathbf{p})$, a feature uncaptured by our truncated flow model.

In Figure 5-2(b), we show the difference between $\gamma = W^u(\mathbf{p})$, the separation line predicted by our theory, and the separation line obtained from the vorticity-based criterion of Wu et al. [108]. The difference is small around $\mathbf{p}$, but increases as we move away from $\mathbf{p}$.

The incompressible formula (3.28) gives the separation slope along γ:

$$\tan\theta(\mathbf{x}_0) = \frac{6x_0^2}{(2a+b)\sqrt{4x_0^2+(2a+b)^2}}, \qquad \mathbf{x}_0 = \left(x_0, \frac{x_0^2}{2a+b}\right). \tag{5.5}$$

We also compute the vorticity-based slope prediction (A.71) numerically along the dashed line of Figure 5-2(b); the results are compared in figure 5-3.

The numerically generated streamlines in Figure 5-2(c) confirm that $\gamma = W^u(\mathbf{p})$ is the correct separation line, and (5.5) is the correct separation slope. Indeed, black and green streamlines started on different sides of the predicted separation surface asymptote to the surface. By contrast, Figure 5-2(d) shows the first-order separation surface predicted by the theory of Wu et al. [108]. In this case, streamlines released on different sides of the predicted surface intersect the surface even near the wall, hence the vorticity-based prediction is inaccurate.

5.1.3 Example III: Separation-bubble flow

In Appendix A.5, we derive the separation-bubble flow

$$\begin{aligned}
u &= z\left[(x/a)^2 + (y/b)^2 - 1\right] \\
&\quad + z^2\left[\alpha + \delta x + \left(c/6 - 2/\left(3a^2\right) - 1/\left(3b^2\right)\right) z\right], \\
v &= -yz\,(cx+d) + z^2\,(\beta + \delta y), \\
w &= dz^2/2 + \left(ca^2 - 2\right) xz^2/\left(2a^2\right) - 2\delta z^3/3,
\end{aligned} \tag{5.6}$$

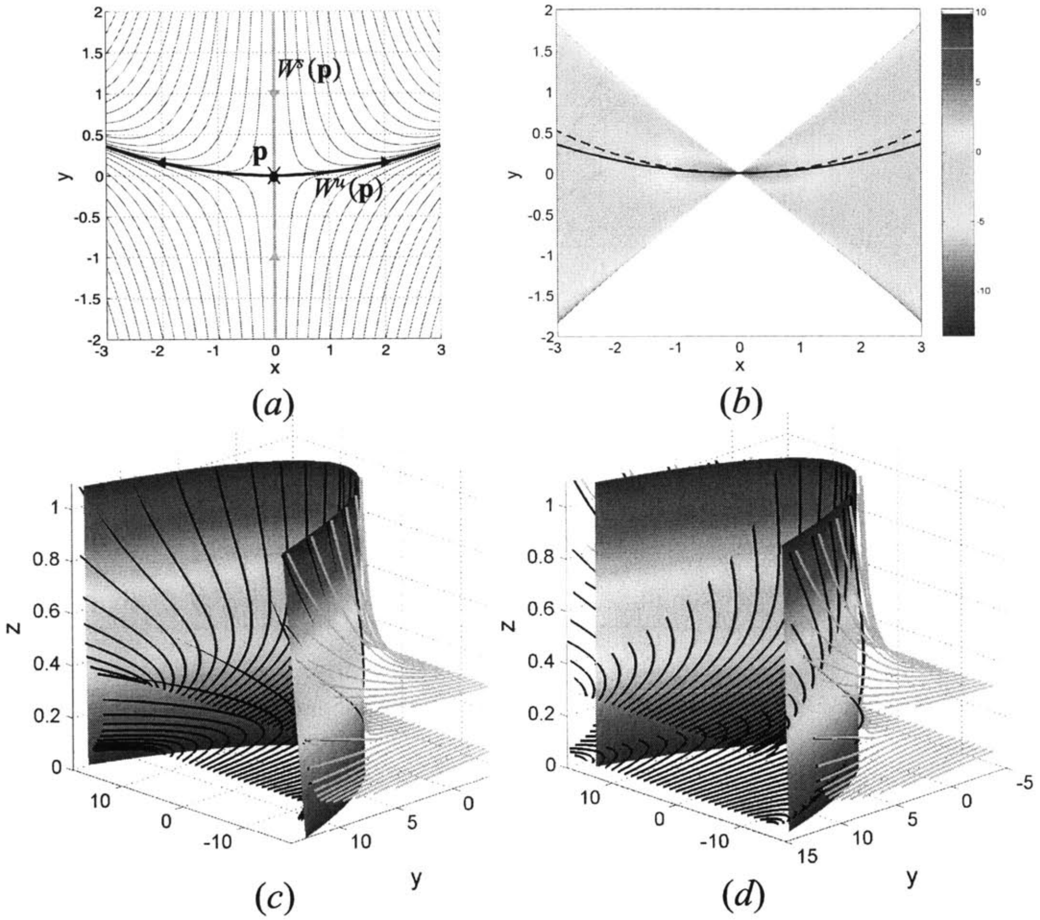

Figure 5-2: Nonlinear saddle-type separation for $a = 1$, $b = 1$, $c = 1$ and $d = 0.5$. (a) Wall shear trajectories (b) Exact separation line (solid) and its vorticity-based prediction (dashed), the ridge of the scalar field φ. The contours of φ are shown over the region where (A.68) holds. (c) Linear prediction for the separation surface by our exact theory; also shown are nearby streamlines, started in two different z-planes, in different colors on opposite sides of the surface. (d) Same for the vorticity-based separation theory.

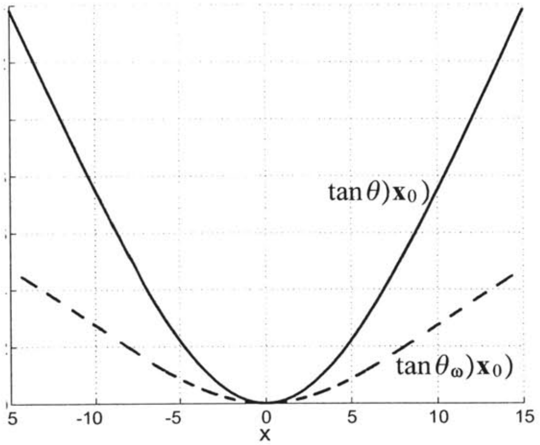

Figure 5-3: Separation slope as a function of x along the separation line in Example I: exact theory (solid line), vorticity-based theory (dashed line).

with the wall shear field

$$\tau = \begin{pmatrix} x^2/a^2 + y^2/b^2 - 1 \\ -ycx - yd \end{pmatrix},$$

with following properties:

(i) For for $d < ac$, this flow admits the four wall shear zeros

$$\begin{aligned} \mathbf{p}_1 &= \begin{pmatrix} -a \\ 0 \end{pmatrix}, \quad \mathbf{p}_2 = \begin{pmatrix} a \\ 0 \end{pmatrix}, \\ \mathbf{p}_3 &= \begin{pmatrix} -d/c \\ -b\sqrt{1 - [d/(ac)]^2} \end{pmatrix}, \quad \mathbf{p}_4 = \begin{pmatrix} -d/c \\ b\sqrt{1 - [d/(ac)]^2} \end{pmatrix}. \end{aligned}$$

(ii) Since

$$\det \nabla_{\mathbf{x}} \tau(\mathbf{p}_1) = 2a(d - ac) < 0, \quad \det \nabla_{\mathbf{x}} \tau(\mathbf{p}_2) = -2a(d + ac) < 0;$$

both $\mathbf{p}_1$ and $\mathbf{p}_2$ are, therefore, saddles and hence cannot be separation or reattachment points by (3.17)-(3.18). Because

$$\begin{aligned} \det \nabla_{\mathbf{x}} \tau(\mathbf{p}_{3,4}) &= \frac{2}{c}\left[1 - \left(\frac{d}{ac}\right)^2\right] > 0, \\ \nabla_{\mathbf{x}} \cdot \tau(\mathbf{p}_{3,4}) &= -\frac{2d}{a^2c} < 0, \quad \partial_z^2 w(\mathbf{p}_{3,4}, 0) = \frac{2d}{a^2c} > 0, \end{aligned} \tag{5.7}$$

$\mathbf{p}_3$ and $\mathbf{p}_4$ must be separation points by (3.17). A linear stability analysis reveals that $\mathbf{p}_3$ and $\mathbf{p}_4$ are stable spirals of the τ field (see figure 5-4a).

As figure 5-4(a) reveals, this flow has no nodes or limit cycles, thus it can only exhibit (S1) separation by the last inequality in (5.7); by the same inequality, no reattachment lines exist.

Separation lines in this example must therefore contain wall shear trajectories that are backward-asymptotic to $\mathbf{p}_1$ or $\mathbf{p}_2$ and forward-asymptotic to $\mathbf{p}_3$ or $\mathbf{p}_4$. The upper and lower components of the unstable manifold $W^u(\mathbf{p}_1)$ satisfy this requirement, yielding a single separation line γ connecting the upper and lower spirals through the saddle $\mathbf{p}_1$.

Figure 5-4(b) compares γ with the prediction of the vorticity-based separation theory. While the vorticity-based prediction is again correct at wall shear zeros, it suggests a separation line radically different from γ. The numerical simulations in Figure 5-4(c) confirm that γ is the correct separation line, and (3.28) is the correct separation slope, which we obtained along γ numerically.

5.1.4 Example IV: Open separation along a limit cycle

In Appendix A.5, we derive the model velocity field

$$\begin{aligned} u &= \mu xz + yz - x^3 z + 8z^3 x/3 - xy^2 z, \\ v &= -xz + \mu yz - x^2 yz - y^3 z + 8yz^3/3, \\ w &= -\mu z^2 + 2z^2 x^2 + 2z^2 y^2 - 4z^4/3, \end{aligned} \tag{5.8}$$

with the wall-shear field

$$\tau = \begin{pmatrix} \mu x + y - x^3 - xy^2 \\ -x + \mu y - yx^2 - y^3 \end{pmatrix}.$$

In this example, $\mathbf{p} = (0,0)$ is the only wall shear zero; at this point, we have

$$\det \nabla_{\mathbf{x}} \tau(\mathbf{p}) = \mu^2 + 1 > 0, \qquad \nabla_{\mathbf{x}} \cdot \tau(\mathbf{p}) = 2\mu, \quad \partial_z^2 w(\mathbf{p}, 0) = -\nabla_{\mathbf{x}} \cdot \tau(\mathbf{p}) = -2\mu,$$

thus, by (3.17)-(3.18), $\mathbf{p}$ is a separation point for $\mu < 0$ and a reattachment point for $\mu > 0$.

As μ is varied from negative to positive values, an attracting limit cycle Γ emerges at $x^2+y^2 = \mu$ (figure 5-5a). This can be verified explicitly by transforming the velocity field to polar coordinates.

The limit cycle Γ satisfies

$$\int_\Gamma \frac{\omega \cdot ([\nabla_{\mathbf{x}} \tau]\, \omega)}{|\omega|^2}\, ds = -2\mu T < 0, \qquad \int_\Gamma \partial_z^2 w \; ds = 4\mu T > 0, \tag{5.9}$$

where T is the period of Γ. By (5.9), Γ is nondegenerate (cf. Appendix A.2) and coincides with a separation line of (S3)-type. Figure 5-5(b) shows the dashed separation line predicted by the vorticity-based separation theory. In this example, the

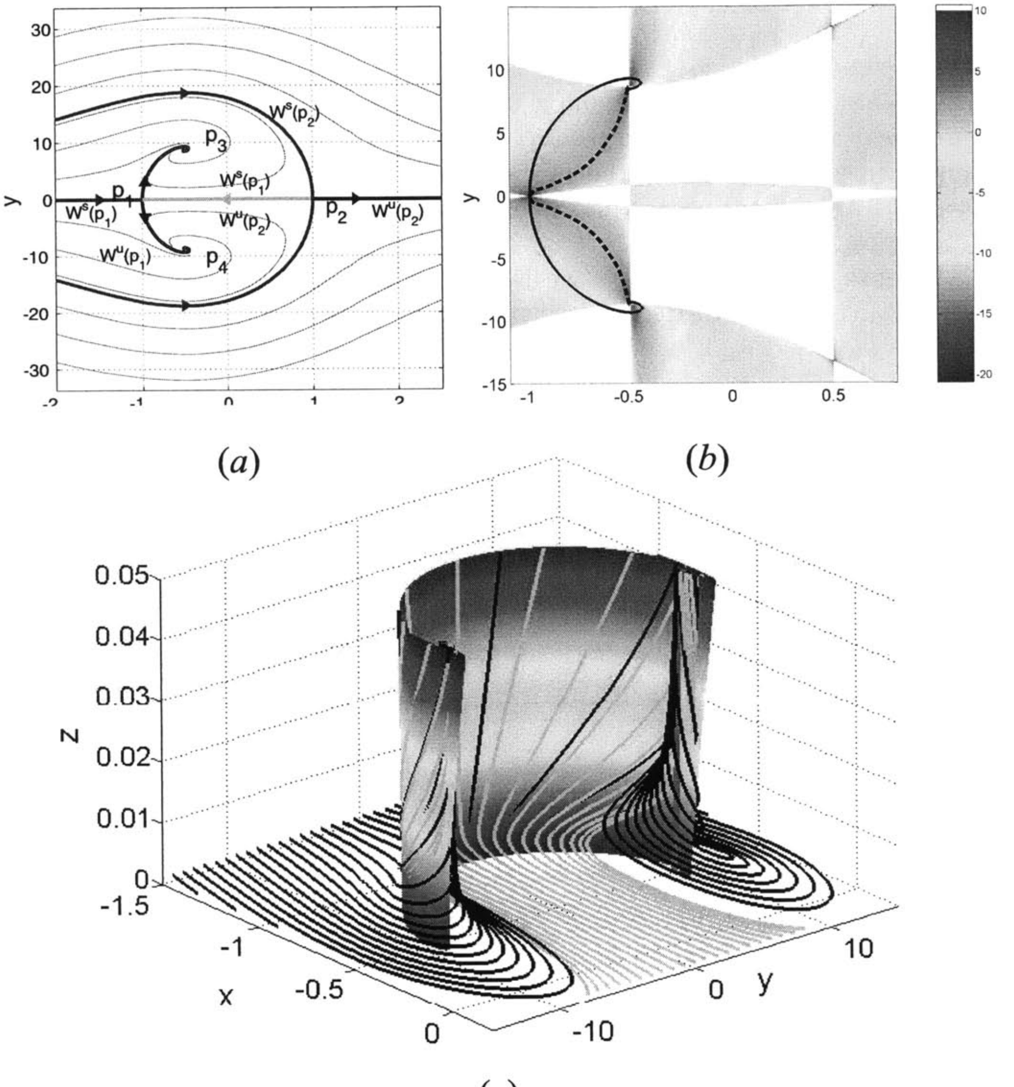

(a) *(b)*

(c)

Figure 5-4: Separation bubble model with $a = c = 1$, $b = 10$, $d = 0.5$, $\alpha = 1$, $\beta = 0$, $\delta = -1$. (a) Wall shear trajectories (b) Exact separation line (solid) and its vorticity-based prediction (dashed), the ridge of the scalar field φ. The contours of φ are shown over the region where (A.68) holds. (c) Linear prediction for the separation surface by our exact theory; also shown are nearby streamlines.

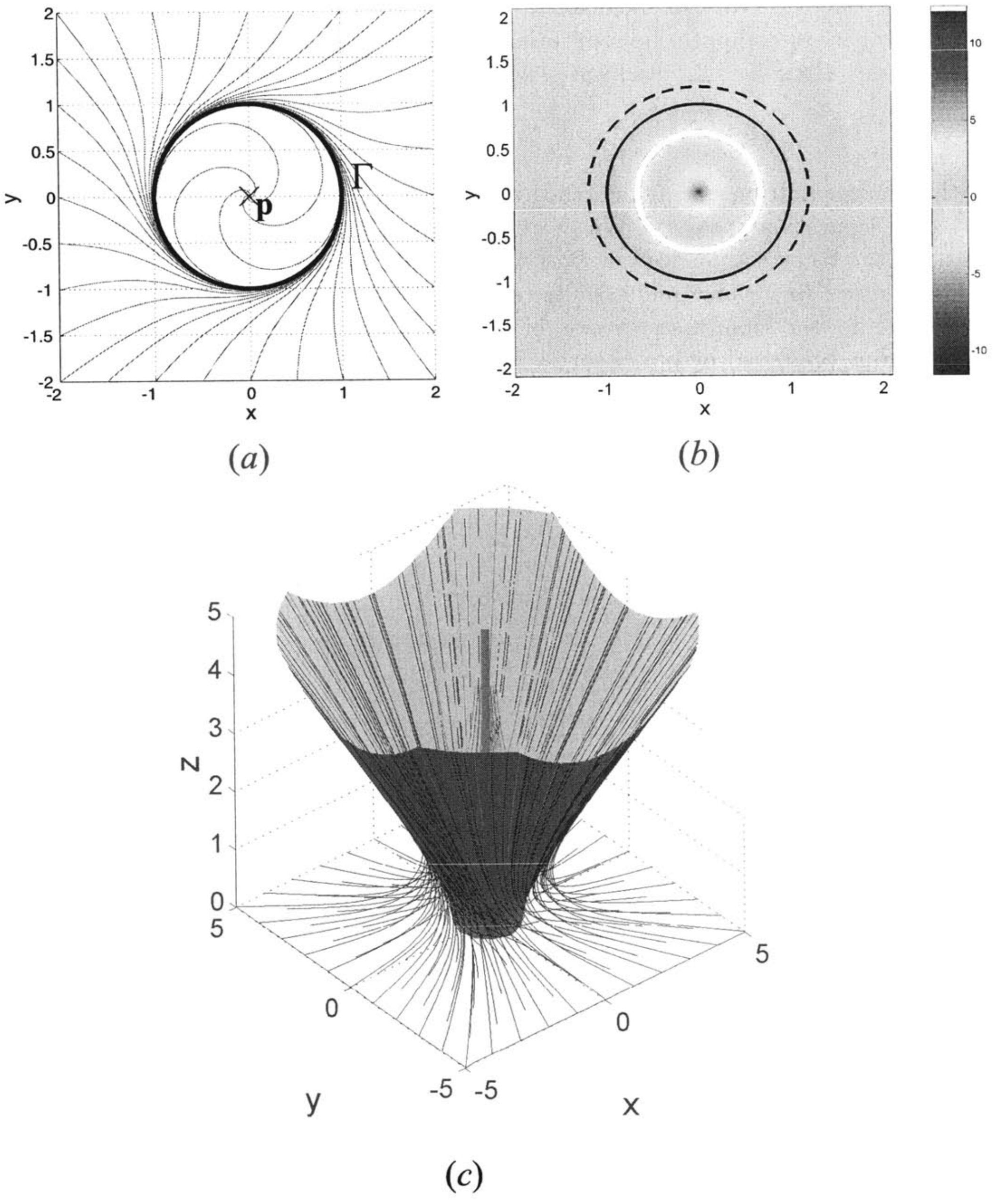

Figure 5-5: Open separation model with $\mu = 1$. (a) Wall shear trajectories (b) Exact separation line (solid) and its vorticity-based prediction (dashed), the ridge of the scalar field φ. The contours of φ are shown over the region where (A.68) holds. (c) Higher-order prediction for the separation surface by our exact theory; also shown are nearby streamlines.

dashed line is qualitatively correct, but misses the exact location of the limit cycle and is transverse to wall shear lines.

In order to compute the separation slope, we observe that $\partial_z^2 \mathbf{u} \equiv \mathbf{0}$ in the present example. Thus, by formula (3.31), we have

$$\tan\theta\,(\mathbf{x}_0) = 0,$$

thus the separation surface is orthogonal to the $z = 0$ plane. By (A.70), the vorticity-based separation theory of Wu et al. [108] also predicts orthogonal separation, but along the incorrect dashed curve of figure 5-5(b).

Figure 5-5(c) shows numerically computed streamlines and a higher-order approximation for the separation surface (cf. formula (A.64)), confirming the separation line and slope predicted by our theory.

5.1.5 Example V: Model with bifurcating separation patterns

In section A.5.6, we derive the model flow

$$\begin{aligned} u &= yz - z^3/6, \\ v &= xz + \mu yz - x^2 z + xyz + z^3/3, \\ w &= -(\mu + x)\, z^2/2, \end{aligned} \tag{5.10}$$

with the associated wall-shear field

$$\tau = \begin{pmatrix} y \\ x + \mu y - x^2 + xy \end{pmatrix}.$$

The fixed points of the τ-field are $\mathbf{p}_1 = (0,0)$ and $\mathbf{p}_2 = (1, 0\ )$. Since

$$\det \nabla_{\mathbf{x}} \tau(\mathbf{p}_1) = -1, \qquad \partial_z^2 w(\mathbf{p}_1, 0) = -\mu, \tag{5.11}$$

the point $\mathbf{p}_1$ is a saddle-type wall shear zero and hence is not a separation point. The point $\mathbf{p}_2$ satisfies

$$\det \nabla_{\mathbf{x}} \tau(\mathbf{p}_2) = 1 > 0, \qquad \nabla_{\mathbf{x}} \cdot \tau(\mathbf{p}_2) = \mu + 1, \qquad \partial_z^2 w(\mathbf{p}_2, 0) = -(\mu + 1), \tag{5.12}$$

thus, by (3.2), $\mathbf{p}_2$ is a separation point for $\mu < -1$.

A linear stability analysis shows that $\mathbf{p}_2$ is a stable spiral for $-3 < \mu < -1$, and a stable node for $\mu < -3$. We show the corresponding wall shear lines in figures 5-6(a) and 5-7(a). By (5.11) and (5.12), the bounded branch of $W^u(\mathbf{p}_1)$ satisfies the nondegeneracy conditions for (S1) and (S2) separation for $\mu < -1$. By figure 5-7(a), $W^u(\mathbf{p}_1)$ is also tangent to the direction of weaker decay at the node, as required for (S2) separation.

For $\mu > -1$, $\mathbf{p}_2$ becomes an unstable spiral encircled by a stable limit cycle Γ, which is connected to the saddle $\mathbf{p}_1$ by the bounded branch of the unstable manifold $W^u(\mathbf{p}_1)$ (see figure 5-8a). The nondegeneracy of the limit cycle can be verified numerically: for instance, for $\mu = -0.95$, we obtain

$$\int_\Gamma \frac{\omega \cdot ([\nabla_{\mathbf{x}}\tau]\,\omega)}{|\omega|^2}\, ds = -0.42 < 0, \qquad \int_\Gamma \partial_z^2 w\, ds = 0.42 > 0,$$

thus conditions (A.33) and (A.34) are satisfied.

Figures 5-6(b), 5-7(b) and 5-8(b) show the dashed separation line predicted by the vorticity-based theory of Wu et al. [108]. In the first two cases, the vorticity-based prediction remains close to the exact separation line owing to the small distance between $\mathbf{p}_1$ and $\mathbf{p}_2$. In the third case, the vorticity-based prediction fails both quantitatively and qualitatively: it still suggests a separation line between $\mathbf{p}_1$ and $\mathbf{p}_2$.

In Figure 5-7(b), the separation line predicted by our theory terminates at the wall shear node $\mathbf{p}_2$. By contrast, the vorticity-based prediction continues through the point $\mathbf{p}_2$. Beyond the fact that the latter prediction is not a wall shear line, there is no unique wall shear line that could be designated as a separation line beyond $\mathbf{p}_2$. Instead, separation beyond $\mathbf{p}_2$ is best characterized by the one-dimensional separation curve emanating from $\mathbf{p}_2$.

Figures 5-6(c), 5-7(c) and 5-8(c) show numerical confirmations of the predictions of our theory, with the separation slope calculated numerically from formula (3.28). As suggested above, Figure 5-7(c) shows all streamlines near $\mathbf{p}_2$ to converge to the one-dimensional separation curve (red curve) based at $\mathbf{p}_2$; we computed this curve up to second order from formulae (3.22) and (3.23).

5.1.6 Time-periodic stable limit-cycle flow

Consider the velocity field

$$\begin{aligned} u &= [\mu + \epsilon\cos(\omega t)]\,xz + yz - x^3 z + \left[\frac{8}{3} - \frac{\epsilon\omega}{6}\sin(\omega t)\right] xz^3 - xy^2 z, \qquad (5.13)\\ v &= -xz + [\mu + \epsilon\cos(\omega t)]\,yz - x^2 yz - y^3 z + \left[\frac{8}{3} - \frac{\epsilon\omega}{6}\sin(\omega t)\right] yz^3, \\ w &= -[\mu + \epsilon\cos(\omega t)]\,z^2 + 2z^2x^2 + 2z^2y^2 - \left[\frac{4}{3} - \frac{\epsilon\omega}{12}\sin(\omega t)\right] z^4, \end{aligned}$$

where, $\mu > 0$, ϵ and ω are parameters. The velocity has the finite asymptotic average

$$\bar{\mathbf{v}} = \begin{pmatrix} \mu xz + yz - x^3 z + \frac{8}{3} z^3 x - xy^2 z \\ -xz + \mu yz - x^2 yz - y^3 z + \frac{8}{3} yz^3 \\ -\mu z^2 + 2z^2x^2 + 2z^2y^2 - \frac{4}{3} z^4 \end{pmatrix},$$

which is bounded on bounded sets. Also, the function,

$$\boldsymbol{\Delta}(\mathbf{x}, z, t) = \frac{\epsilon}{\omega}\left[\sin(\omega t) - \sin(\omega t_0)\right] \begin{pmatrix} xz \\ yz \\ -z^2 \end{pmatrix} + \frac{\epsilon}{12}\left[\cos(\omega t) - \cos(\omega t_0)\right] \begin{pmatrix} 2xz^2 \\ 2yz^2 \\ -z^4 \end{pmatrix}$$

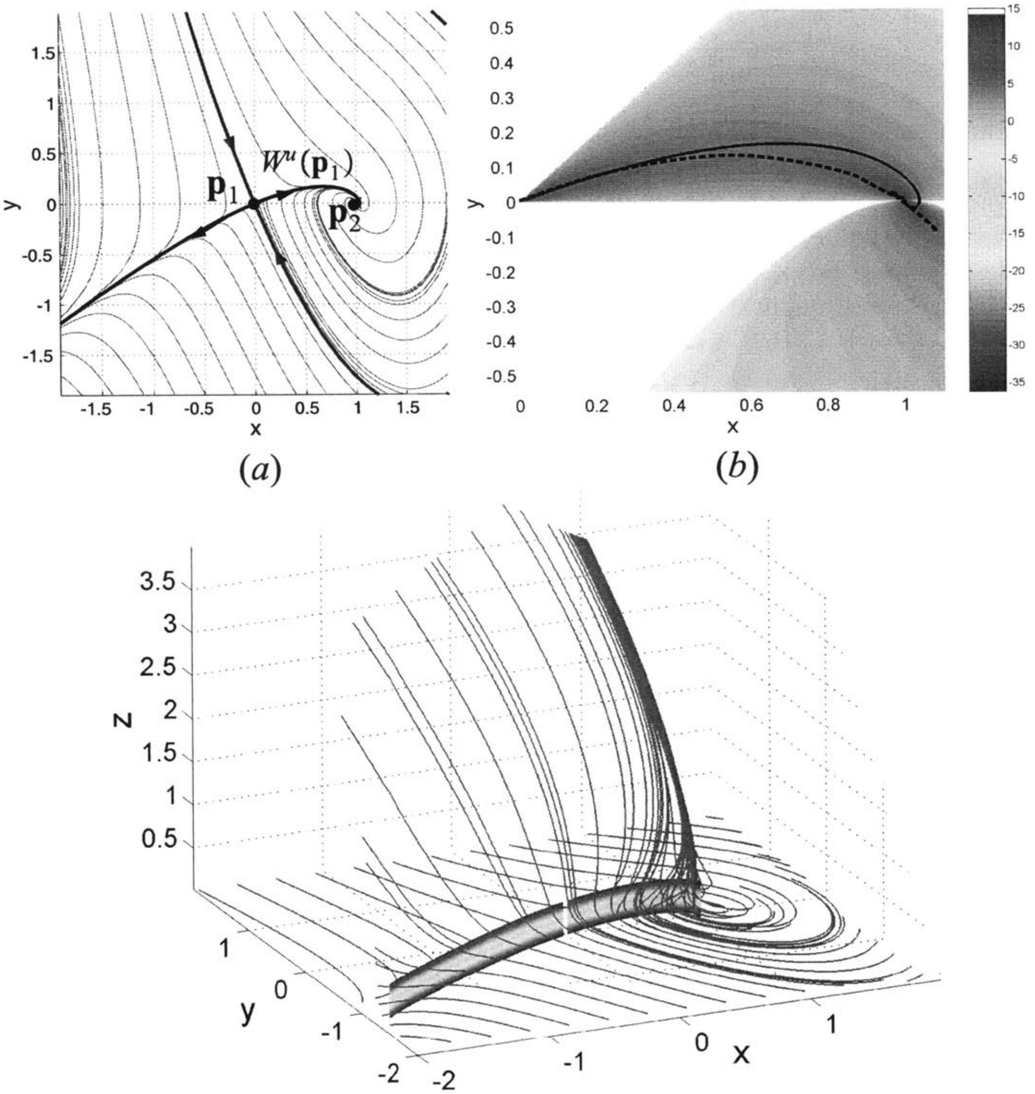

(a)

(b)

(c)

Figure 5-6: (S1) separation in the bifurcating flow model for $\mu = -2$. (a) Wall shear trajectories (b) Exact separation line (solid) and its vorticity-based prediction (dashed), the ridge of the scalar field φ. The contours of φ are shown over the region where (A.68) holds. (c) Linear prediction for the separation surface near the wall; also shown are nearby streamlines.

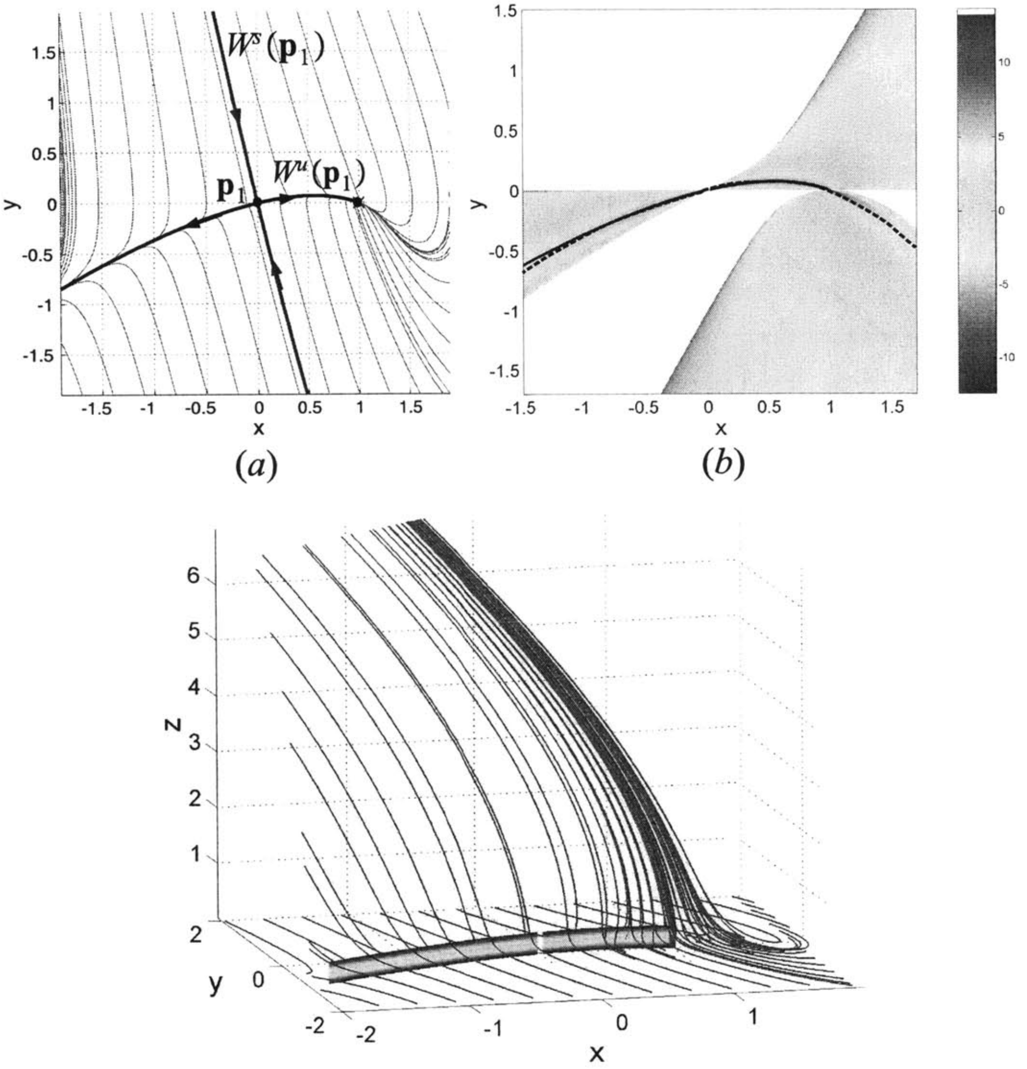

(a)

(b)

(c)

Figure 5-7: (S2) separation in the bifurcating flow model for $\mu = -4$. (a) Wall shear trajectories (b) Exact separation line (solid) and its vorticity-based prediction (dashed), the ridge of the scalar field φ. The contours of φ are shown over the region where (A.68) holds. (c) Linear prediction for the separation surface near the wall; also shown are nearby streamlines.

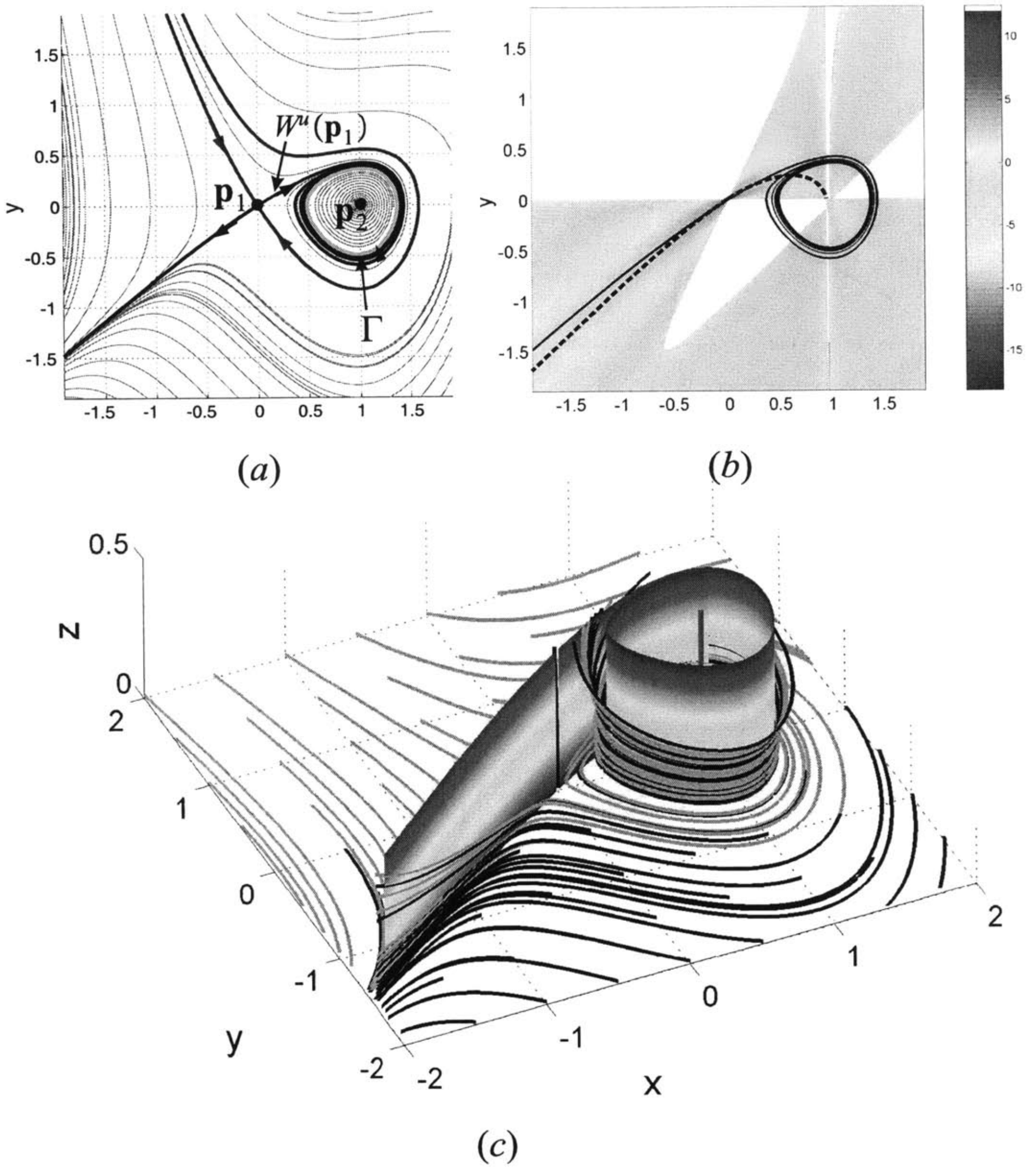

(a) *(b)*

(c)

Figure 5-8: (S3) separation in the bifurcating flow model for $\mu = -0.95$. (a) Wall shear trajectories (b) Exact separation line (solid) and its vorticity-based prediction (dashed), the ridge of the scalar field φ. The contours of φ are shown over the region where (A.68) holds. (c) Linear prediction for the separation surface by our exact theory; also shown are nearby streamlines.

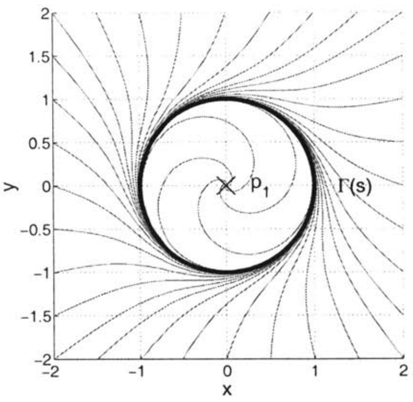

Figure 5-9: Time-averaged wall-shear field for the time-periodic limit cycle example with parameters $\mu = 1, \epsilon = 5$ and $\omega = 1$. $\Gamma(s)$, an attracting limit cycle, is the separation line, and the stable spiral p_1 is the attachment point.

and its derivatives are uniformly bounded in time on bounded sets, thus our assumptions listed in section 2.1 are satisfied.

For this velocity field, the wall-shear field $\bar{\tau}$ and the averaged normal strain rate $\bar{C}$ are of the form

$$\bar{\tau}(\mathbf{x}) = \begin{pmatrix} \mu x + y - x^3 - xy^2 \\ -x + \mu y - yx^2 - y^3 \end{pmatrix}, \qquad \overline{C}(\mathbf{x}) = 2(x^2 + y^2) - \mu.$$

The $\bar{\tau}(\mathbf{x})$ field (see figure 5-9) vanishes only at the point $\mathbf{p}_1 = (0, 0)$ where

$$\det \nabla_{\mathbf{x}} \bar{\tau}(\mathbf{p}) = \mu^2 + 1 > 0, \quad \nabla_{\mathbf{x}} \cdot \bar{\tau}(\mathbf{p}) = 2\mu, \quad \det \nabla_{\mathbf{x}} \bar{\tau}(\mathbf{p}) > [\, \nabla_{\mathbf{x}} \cdot \bar{\tau}(\mathbf{p})]^2 / 4, \quad \overline{C}(\mathbf{p}) = -\mu;$$

thus $\mathbf{p}_1$ is a spiral-type attachment point by the classification scheme given in chapter 3 for steady flows.

By (4.27), the slope of the attachment curve based at $\mathbf{p}_1$ satisfies

$$\mathbf{g}(t) = 0.$$

The $\bar{\tau}$ field also has an attracting limit cycle Γ which, in polar coordinates, is given by $r = \sqrt{\mu}$ (see figure 5-9). At any point of the limit cycle, we have

$$\overline{S}_{\perp} = -2\mu < 0, \qquad \overline{C} = \mu > 0.$$

and hence Γ is a separation line by (4.20). The slope formula (4.28) yields

$$\tan(\theta(\mathbf{x}_0, t)) = \frac{\epsilon \sin(\omega t) \sqrt{\mu}}{\omega}, \tag{5.14}$$

for every point $\mathbf{x}_0$ of Γ.

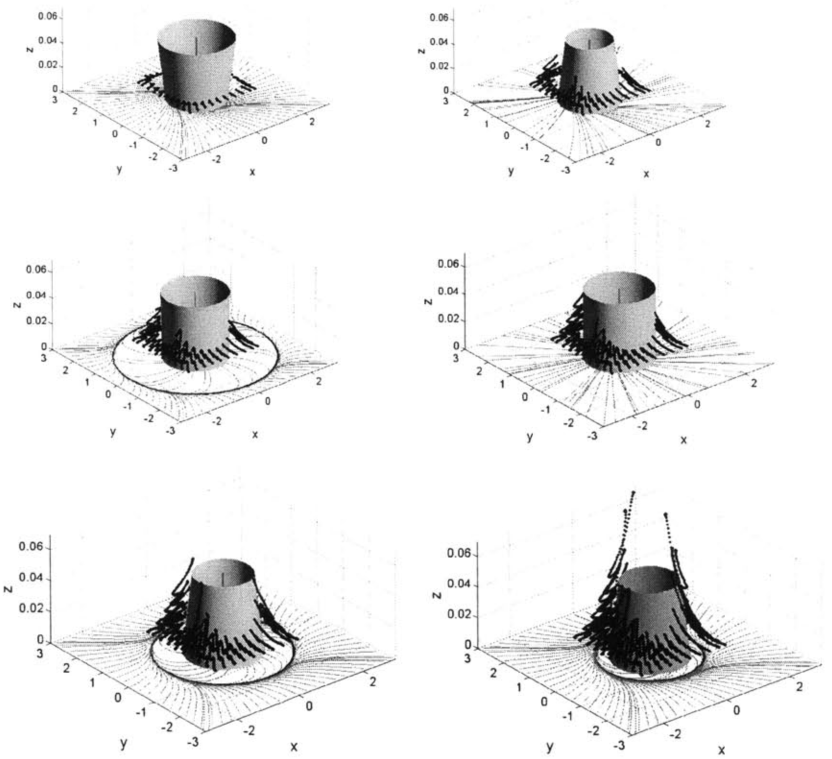

Figure 5-10: Separation in the time-periodic limit cycle example, with linear prediction of the separation surface validated by particle paths shown in black. We also plot the instantaneous wall-shear trajectories, which undergo a *Hopf* bifurcation in time. The figures correspond to t =8,17,19,22,24,30.

We show snapshots of a numerical simulation of the model (5.13) in figure 5-10. The instantaneous wall-shear field (4.11) exhibits a Hopf bifurcation in time: the limit cycle shrinks in size and disappears as the instantaneous wall shear zero at $(0,0)$ changes from an unstable spiral to a stable one. According to prior criteria based on the instantaneous topology of wall shear lines (see, e.g., Wu et al. [108]), both the location and the topology of separation should change drastically in time. By contrast, pathlines (shown in black in figure 5-10) confirm that the separation is *fixed* and occurs along the separation line Γ predicted by our theory.

5.1.7 Quasiperiodic compressible separation bubble

To illustrate our separation criteria in the compressible case, we consider a quasiperiodic compressible flow model of the form

$$\begin{aligned} u &= z\left[\left(\frac{x}{a}\right)^2+\left(\frac{y}{b}\right)^2-1\right]+z^2\left[\alpha+\delta x+\left(\frac{c}{6}-\frac{2}{3a^2}-\frac{1}{3b^2}\right)z\right], \qquad (5.15)\\ v &= -yz(cx+d+\varepsilon\sin(\omega_1 t))+z^2\left(\beta+\delta y\right),\\ w &= \frac{\sin(\omega_2 t)}{\kappa-\cos(\omega_2 t)}z+\frac{d+\varepsilon\sin(\omega_1 t)}{2}z^2+\left(\frac{c}{2}-\frac{1}{a^2}\right)xz^2-\frac{2\delta}{3}z^3, \end{aligned}$$

with parameters $a, b, c, d, \alpha, \beta, \delta, \omega_1, \omega_2, \epsilon$. We take $\kappa > 1$ and $\frac{\omega_1}{\omega_2}$ to be irrational, which leads to quasiperiodic time dependence in the model. Physically, the velocity field models the loss of stability of a steady separation bubble that develops oscillations with two dominant frequencies. For this strongly compressible flow, we have

$$e^{\int_{t_0}^{t} w_z(\mathbf{x},0,\tau)d\tau}=\frac{(\kappa-\cos\omega_2 t)^{\frac{1}{\omega_2}}}{(\kappa-\cos\omega_2 t_0)^{\frac{1}{\omega_2}}}, \qquad (5.16)$$

and thus our initial assumption on the boundedness of the density is satisfied by (2.4).

Verifying the remaining assumptions of section 4.1, we first note that (5.15), as any quasiperiodic flow, has a well-defined steady mean on bounded sets. Also, the function,

$$\mathbf{\Delta}(\mathbf{x},z,t)=\frac{\epsilon}{\omega_1}\left[\cos(\omega_1 t)-\cos(\omega_1 t_0)\right]\begin{pmatrix}0\\ yz\\ -dz^2/2\end{pmatrix}+\frac{1}{\omega_2}\ln\frac{\kappa-\cos(\omega_2 t)}{\kappa-\cos(\omega_2 t_0)}\begin{pmatrix}0\\ 0\\ z\end{pmatrix}$$

and its derivatives are uniformly bounded in time on bounded sets, thus our assumptions listed in section 4.1 are satisfied.

Choosing $\omega_2 = 1$, we obtain the averaged wall-shear and vertical strain coefficient in the form

$$\bar{\tau}(\mathbf{x})=\frac{\kappa}{\kappa-\cos(t_0)}\begin{pmatrix}\frac{x^2}{a^2}+\frac{y^2}{b^2}-1\\ -ycx-yd\end{pmatrix}, \qquad \overline{C}(\mathbf{x})=\frac{\kappa}{\kappa-\cos(t_0)}\frac{d}{2}+(\frac{c}{2}-\frac{1}{a^2})x. \qquad (5.17)$$

With these quantities at hand, we can verify the assertions (i) and (ii) of section 5.1.3 for the time averaged quantities $\bar{\tau}(\mathbf{x})$ and $\overline{C}(\mathbf{x})$ as given above. Moreover, the two conditions in (4.20) are satisfied for the separation line $W^u(\mathbf{p}_1)$, as shown in figure 5-11(b). Hence, by Theorem 2 (f.f. section 4.2.3), fixed separation occurs along $W^u(\mathbf{p}_1)$. The slopes of the separation curves at the separation points $\mathbf{p}_3$ and $\mathbf{p}_4$ are

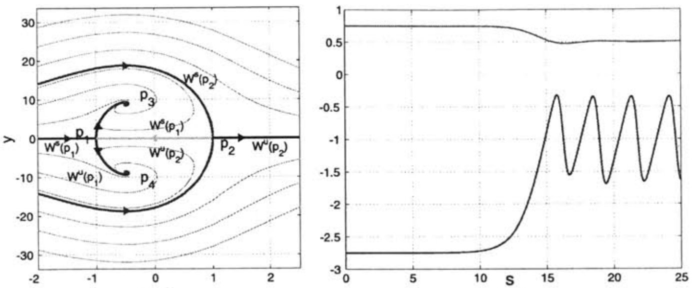

(a) *(b)*

Figure 5-11: (a) Averaged wall-shear field for time quasiperiodic bubble flow with parameters $a = 1$, $b = 1$, $c = 1$, $d = \frac{1}{20}$, $\alpha = 1$, $\beta = 2$, $\delta = 1$, $\epsilon = 1$, $\omega_1 = \sqrt{2}$, $\omega_2 = 1$ and $\kappa = 3$. (b) Blue curve represents $\overline{S}_\perp(\mathbf{x}(s)) - \overline{C}((\mathbf{x}(s)))$ and the red one is $\overline{C}((\mathbf{x}(s)))$, where $\mathbf{x}(s)$ denotes the branch of $W^u(\mathbf{p}_1)$ connecting to $\mathbf{p}_3$.

given by

$$\begin{aligned}
\mathbf{g}_0(\mathbf{p}_3, t) = -& \frac{\kappa - \cos(\omega t)}{\kappa} \begin{pmatrix} -\frac{3d}{ca^2} & -\frac{2}{b}\sqrt{1-\left(\frac{d}{ac}\right)^2} \\ cb\sqrt{1-\left(\frac{d}{ac}\right)^2} & -\frac{d}{ca^2} \end{pmatrix}^{-1} \\
& \times \left[(\kappa^2 + \frac{1}{2})\{ \begin{pmatrix} \alpha \\ \beta \end{pmatrix} + \delta \mathbf{p}_3 \} + \varepsilon \begin{pmatrix} 2\left(1-\left(\frac{d}{ac}\right)^2\right) \\ \frac{bd}{ca^2}\sqrt{1-\left(\frac{d}{ac}\right)^2} \end{pmatrix} F(t) \right], \\
\mathbf{g}_0(\mathbf{p}_4, t) = & -\frac{\kappa - \cos(\omega t)}{\kappa} \begin{pmatrix} -\frac{3d}{ca^2} & \frac{2}{b}\sqrt{1-\left(\frac{d}{ac}\right)^2} \\ -cb\sqrt{1-\left(\frac{d}{ac}\right)^2} & -\frac{d}{ca^2} \end{pmatrix}^{-1} \\
& \times \left[(\kappa^2 + \frac{1}{2})\{ \begin{pmatrix} \alpha \\ \beta \end{pmatrix} + \delta \mathbf{p}_4 \} + \varepsilon \begin{pmatrix} 2\left(1-\left(\frac{d}{ac}\right)^2\right) \\ -\frac{bd}{ca^2}\sqrt{1-\left(\frac{d}{ac}\right)^2} \end{pmatrix} F(t) \right] \quad (5.18)
\end{aligned}$$

respectively, where

$$F(t) = \frac{\kappa}{\omega_1(\omega_1^2 - 1)} \left[\omega_1^2(\cos(\omega_1 t)\cos(t) - \kappa\cos(\omega_1 t)) + \omega_1 \sin(\omega_1 t)\sin(t) + \kappa \cos(\omega_1 t) \right].$$

The separation line in this example is the union of two branches of the unstable manifold $W^u(\mathbf{p}_1)$ of $\mathbf{p}_1$. We compute the separation slope along $W^u(\mathbf{p}_1)$ numerically using formula (4.28). Shown in figure 5-12, simulations of fluid particle trajectories confirm the separation location and slopes. Note that the particles exhibit a hopping motion as they approach the separation surface, along which they are ejected into the main stream.

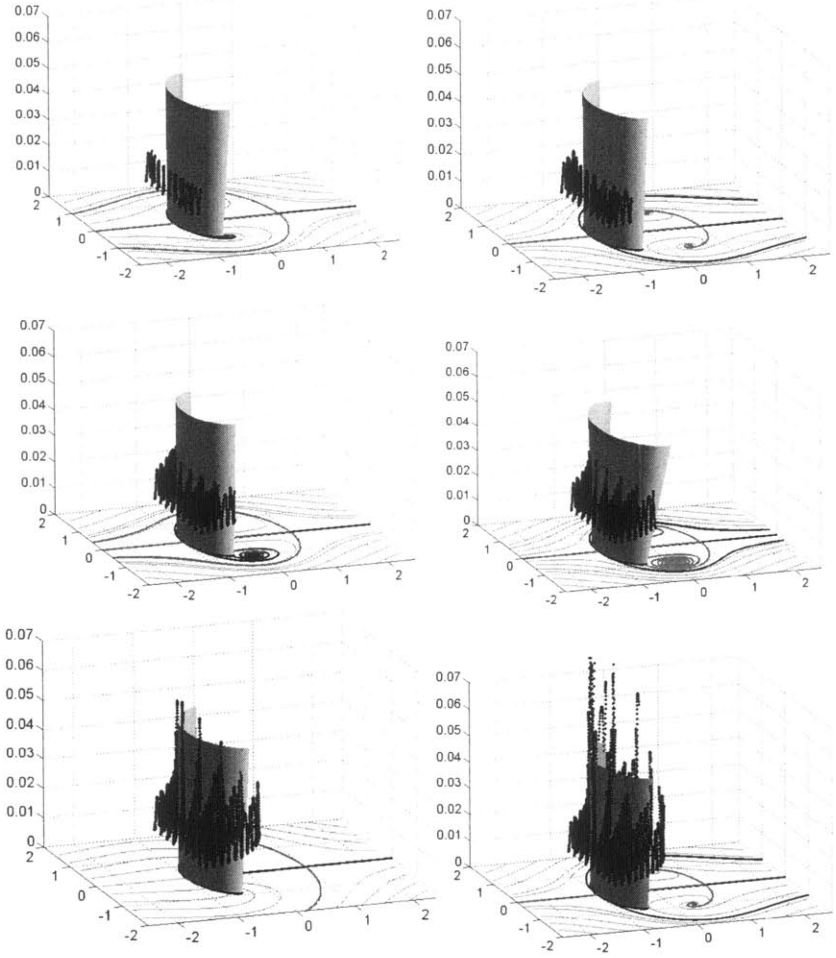

Figure 5-12: Quasiperiodic compressible separation bubble with first order prediction of time-dependent separation curve and the time-dependent separation surface. Particles marked with different colors (black and green) are released in vicinity of the wall from two sides: they are attracted by the separation surface and eventually ejected along it or swirl around the separation curve. Also shown are the instantaneous wall shear trajectories. The figures correspond to $t = 8.8, 20.8, 33.6, 44, 64, 79.2$.

5.1.8 Randomly varying separation bubble

In this section, we analyze a randomized incompressible version of the above separation bubble flow:

$$
\begin{aligned}
u &= z\left[\left(\frac{x}{a}\right)^2 + \left(\frac{y}{b}\right)^2 - 1\right] + z^2\left[\alpha + \delta x + \left(\frac{c}{6} - \frac{2}{3a^2} - \frac{1}{3b^2}\right)z\right], \\
v &= -yz\left[cx + d + \varepsilon r(t)\right] + z^2\left(\beta + \delta y\right), \qquad (5.19) \\
w &= \frac{d + \varepsilon r(t)}{2}z^2 + \left[\frac{c}{2} - \frac{1}{a^2}\right]xz^2 - \frac{2\delta}{3}z^3.
\end{aligned}
$$

Here $r(t)$ is a zero-mean random variable with normal distribution. Because, $r(t)$ has zero mean, its integral

$$F(t) = F(t_0) + \int_{t_0}^{t} r(\tau)d\tau, \qquad (5.20)$$

is bounded, leading to

$$\lim_{T\to\infty}\frac{1}{T}\int_{t_0-T}^{t_0} r(t)dt = 0. \qquad (5.21)$$

Thus, the averaged velocity field is given by the $\varepsilon = 0$ limit of (5.19), which is bounded on bounded sets. Also, the function

$$\mathbf{\Delta}(\mathbf{x}, z, t) = \epsilon F(t)\begin{pmatrix} 0 \\ -yz \\ z^2/2 \end{pmatrix},$$

and its spatial derivatives are bounded on bounded sets. All the assumptions of section 2.1 are therefore satisfied.

The assertions (i)-(ii) in section 5.1.3 can be verified to hold for the random separation bubble flow. The slopes of the separation curves at the separation points $\mathbf{p}_3$ and $\mathbf{p}_4$ are now given by

$$
\begin{aligned}
\mathbf{g}_0(\mathbf{p}_3, t) &= -\begin{pmatrix} -\frac{3d}{ca^2} & -\frac{2}{b}\sqrt{1-\left(\frac{d}{ac}\right)^2} \\ cb\sqrt{1-\left(\frac{d}{ac}\right)^2} & -\frac{d}{ca^2} \end{pmatrix}^{-1} \\
&\quad \times\left[\begin{pmatrix} \alpha \\ \beta \end{pmatrix} + \delta\mathbf{p}_3 + \varepsilon\begin{pmatrix} 2\left(1-\left(\frac{d}{ac}\right)^2\right) \\ \frac{bd}{ca^2}\sqrt{1-\left(\frac{d}{ac}\right)^2} \end{pmatrix}F(t)\right], \\
\mathbf{g}_0(\mathbf{p}_4, t) &= -\begin{pmatrix} -\frac{3d}{ca^2} & \frac{2}{b}\sqrt{1-\left(\frac{d}{ac}\right)^2} \\ -cb\sqrt{1-\left(\frac{d}{ac}\right)^2} & -\frac{d}{ca^2} \end{pmatrix}^{-1} \\
&\quad \times\left[\begin{pmatrix} \alpha \\ \beta \end{pmatrix} + \delta\mathbf{p}_4 + \varepsilon\begin{pmatrix} 2\left(1-\left(\frac{d}{ac}\right)^2\right) \\ -\frac{bd}{ca^2}\sqrt{1-\left(\frac{d}{ac}\right)^2} \end{pmatrix}F(t)\right],
\end{aligned}
$$

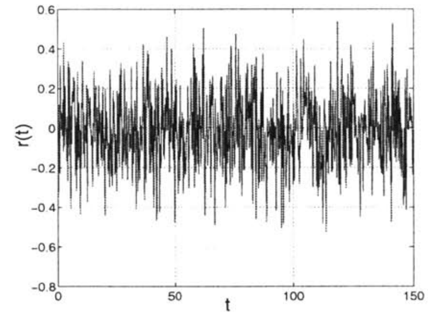

Figure 5-13: A realization of the random variable $r(t)$.

respectively. We again obtain a first-order approximation of the separation surface by evaluating (4.28) numerically.

In our numerical simulations of this model, we set the standard deviation of $r(t)$ equal to 0.2. We sampled $r(t)$ at multiples of $\Delta T = 0.2$, and used a cubic spline interpolation to obtain velocity values in (5.19) for intermediate times. For this choice, a particular realization of the random velocity coefficient $r(t)$ is shown in figure 5-13.

We show corresponding numerical simulation of fluid particle motion in figure 5-14. Despite the drastic changes in the instantaneous wall-shear topology, the separation occurs at a fixed location along the separation surface predicted by our theory.

5.2 Algorithm for locating separation and attachment

The results in chapter 3 lead to the following algorithm for locating separation and attachment in steady 3D flows:

1 For a given wall-shear field $\tau(\mathbf{x})$, find all nondegenerate zeros $\mathbf{p}_i$ and limit cycles Γ_j. Away from corners, use conditions in Eqns. (3.25-3.27); at corners, use Eqns. (3.35-3.36).

2 For the above $\mathbf{p}_i$ and Γ_j, determine the sign of $\nabla_{\mathbf{x}}\cdot\tau(\mathbf{p}_i)$ and $\int_{\Gamma_j} \nabla_{\mathbf{x}}\cdot\tau(\mathbf{x}(s;\mathbf{x}_0))\, ds$. At corners, determine the sign of $\nabla_{\mathbf{x}}\cdot\partial_x\tau(\mathbf{p}_i)$. Here, x is the coordinate introduced in section 3.6 along the corner line.

3 For each nondegenerate wall-shear saddle $\mathbf{p}_k$, find its stable and unstable manifolds in the $z = 0$ plane. The manifold $W^u(\mathbf{p}_k)$ is obtained numerically by advecting a small line segment–initially tangent to the unstable eigenvector of $\mathbf{p}_k$–using the flow of $\dot{\mathbf{x}} = \tau(\mathbf{x})$. In other words, we take an initial condition on the unstable eigenvector of $\mathbf{p}_k$ sufficiently close to $\mathbf{p}_k$, and solve the system $\dot{\mathbf{x}} = \tau(\mathbf{x})$ for that initial condition. The manifold $W^s(\mathbf{p}_k)$ is obtained by

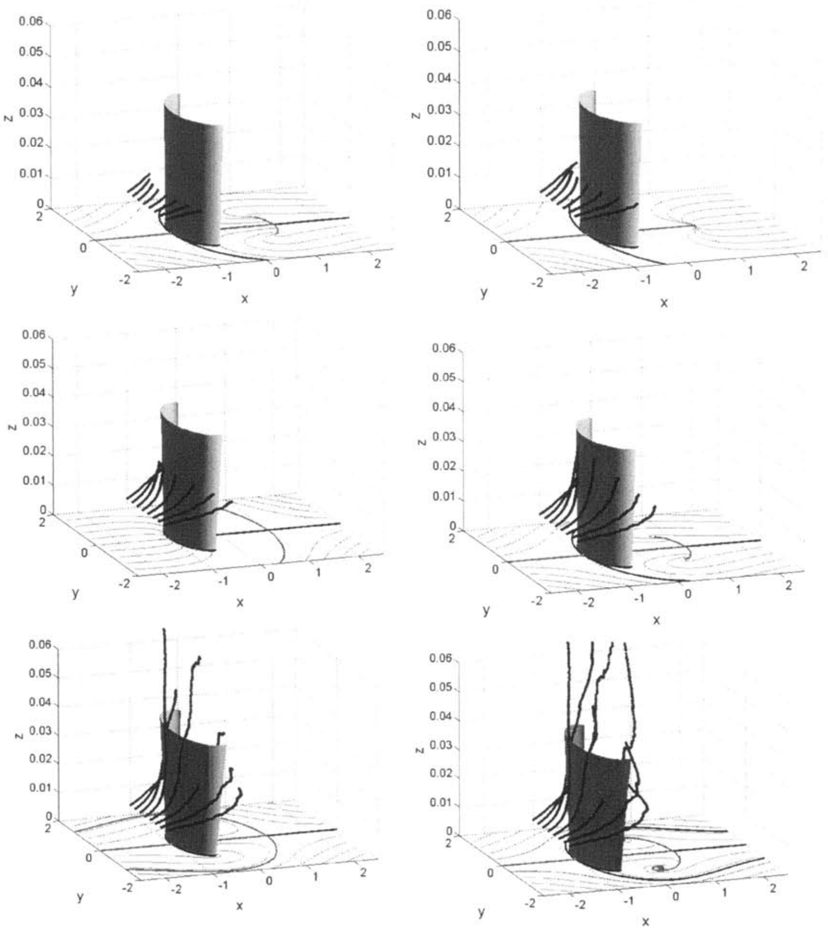

Figure 5-14: Fixed separation exhibited by fluid particles in the random separation bubble flow with parameters $a = 1$, $b = 1$, $c = 1$, $d = \frac{1}{2}$, $\alpha = 1$, $\beta = 0$, $\delta = 1$ and $\epsilon = 5$. The pictures correspond to the increasing sequence of times $t = 31.8, 49.8, 69.8, 87.8, 113.8, 143.8$.

backward-advecting a small line segment–initially tangent to the stable eigenvector of $\mathbf{p}$–using the flow of $\dot{\mathbf{x}} = \tau(\mathbf{x})$.

4 Identify separation and attachment points using the criteria (S0) and (R0).

5 Identify separation and attachment lines from the criteria (S1)-(S4) and (R1)-(R4). At corners, use $\partial_x \tau(\mathbf{p}_i)$ instead of $\tau(\mathbf{p}_i)$ in (S1)-(S3) and (R1)-(R3).

6 Compute the slope of separation and attachment curves using Eq. 3.22 or 3.42.

7 Compute first-order approximations for attachment and separation surfaces from the angle formula in Eq. 3.28 or 3.43.

8 If the velocity field off the boundary is available, compute global separation and attachment surfaces by advecting their tangent planes (obtained from the first-order approximation in 7. above) in the appropriate time direction.

Essentially the above algorithm can also be used to locate fixed separation in unsteady flows with a finite mean. The required modifications are described below:

- Replace τ in steps 1,2,3 above with the averaged wall shear field $\overline{\tau}$ (see Eq. 4.10 in chapter 4). In order to deal with corners follow the details given in section 4.2.4.
- In step 4 the separation and attachment point are identified based on (S0) and (R0) of section 4.2.2; while in step 5 separation and attachment lines are determined based on (S1)-(S4) and (R1)-(R4) of section 4.2.3, respectively.
- In steps 6 and 7 use the formulae 4.27 and (4.28) (4.29) respectively to compute the slope of time dependent separation or attachment curve and separation (attachment) surface respectively.

5.3 Numerical Examples

So far, we have only used analytical model flows to illustrate various aspects of the fixed separation theory. Now we turn to direct numerical simulations of important benchmark flow domains.

5.3.1 Numerical methodology

We consider a Newtonian fluid with zero bulk viscosity. The dynamic viscosity μ, the conductivity κ, and the specific heats at constant pressure, c_p, and at constant volume, c_v, are assumed to be independent of the temperature. Under these hypotheses, the non-dimensional governing equations expressing the conservation of mass, momentum and energy in Cartesian coordinates x_i become

$$\begin{aligned}
\frac{\partial \rho}{\partial t} + \frac{\partial (\rho v_i)}{\partial x_i} &= 0, && (5.22)\\
\frac{\partial (\rho v_i)}{\partial t} + \frac{\partial (\rho v_i v_j)}{\partial x_j} &= -\frac{\partial p}{\partial x_i} + \frac{1}{\mathrm{Re}}\frac{\partial \sigma_{ij}}{\partial x_j}, && (5.23)\\
\frac{\partial (\rho e)}{\partial t} + \frac{\partial (\rho e v_i)}{\partial x_i} &= -\frac{\partial (p v_i)}{\partial x_i} + \frac{\partial (v_j \sigma_{ij})}{\partial x_i} + \frac{1}{(\beta - 1) M_f^2 Pr}\frac{\partial^2 T}{\partial x_i^2}. && (5.24)
\end{aligned}$$

As before (c.f. 3.7), v_i denote the velocity field components; p is the mechanical pressure; T is the temperature; ρ is the density and e denotes the sum of internal and kinetic energies. The stress tensor σ_{ij} is given in Eq. (3.38). β denotes the ratio of the specific heats c_p/c_v. Eqns.(5.22-5.24) are closed with the ideal gas law

$$p = \frac{\rho T}{\beta M_f^2},$$

so that

$$e = \frac{p}{\beta - 1} + \rho \frac{u_i^2}{2}.$$

All variables are normalized by the reference length L_f, the density ρ_f, the velocity U_f, and the temperature T_f. The non-dimensional numbers in the above equation are the Reynolds number $Re = \rho_f U_f L_f / \mu$, the Prandtl number $Pr = c_p \mu / \kappa$, and the reference Mach number $M_f = U_f / C$, where $C = \sqrt{\beta R T_f}$ is the speed of sound with gas constant R.

We solve Eqns.(5.22-5.24) with a staggered-grid multi-domain spectral method. For a detailed description and validation of this method, we refer to Refs. [47] and [46].

5.3.2 Numerical models

We consider two different flow geometries: a *backward facing step* and a *lid-driven cavity*. Both are classic benchmark problems with complex separation and attachment topologies that are ideal for the validation of the separation criteria.

Backward Facing Step

We consider the two-dimensional closed backward-facing step flow studied by Gresho *et al.* [33] with a slight three-dimensional perturbation added in the periodic spanwise direction. The computational model is shown in Fig. 5-15a.

The inflow channel height and the step height are denoted by h and S, respectively; W is the spanwise width. The upstream and downstream lengths from the step are L_u and L_d. Following Ref. [33], we take $S = h = 1$, $L_u = 1$, and $L_d = 34$. We take the spanwise width to be $W = 4$.

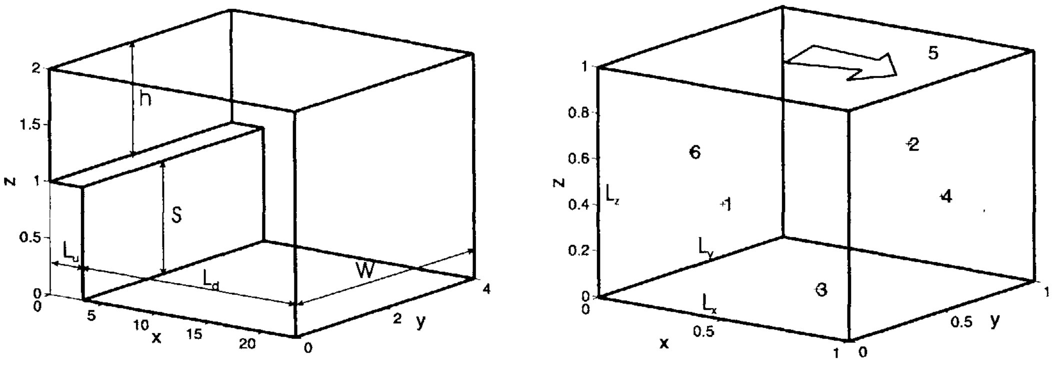

(a) (b)

Figure 5-15: Steady flow geometries studied in this paper: (a) backward facing step (b) lid-driven cavity.

At the inflow, we specify the analytical velocity and temperature curve of a flow between two infinite parallel plates:

$$
\begin{aligned}
u_0(z) &= -6\left[(z-S)^2-(z-S)\right], \\
T(z) &= T_{wall}+\left\{\frac{3(\beta-1)}{4\mathrm{Pr}}\left[1-(2(z-S)-1)^4\right]\right\}.
\end{aligned} \tag{5.25}
$$

To introduce three-dimensional features into the flow, we modify the inflow u–velocity as

$$u\left(y,z\right)=u_0\left(z\right)\left[1+0.1\cos(2\pi y/W)\right]. \tag{5.26}$$

At the outflow, we again specify velocity and temperature curves according to the analytical flow between parallel plates, so that the mass–flow rates at the inflow and outflow are equal. We compute the prescribed pressure difference between inflow and outflow from the analytical channel flow pressure gradient. The walls are no-slip and isothermal; the spanwise boundary conditions are periodic. We initialize the flow with the inflow boundary condition (Eq. 5.25).

The Reynolds number based on the bulk inflow velocity and the step height is Re = 300, ensuring laminar separation on the top wall[4]. The Mach number based on the wall temperature and the inflow bulk velocity is $Ma = 0.4$, which ensures a nearly incompressible flow without restricting the explicit time scheme step. The Prandtl number is $Pr = 0.72$.

The numerical studies of Armaly et al. [4] and Gresho et al. [33] indicate that at $Re = 300$, the backward facing step flow is two-dimensional. In order to generate three-dimensional effects, we have therefore introduced an additional spatial spanwise variation in the inlet velocity field. Since the numerical methodology we have used is similar to that described in [33], we adopt the resolution from that study. By taking the Reynolds number to be 25% less than used in Ref. [33], we reasonably expect that the same resolution still guarantees convergence despite the new three-dimensional effects.

Specifically, we take 2×1 and 4×17 domains in the $x - z$ plane upstream and downstream of the sudden expansion. In accordance with the dimensions of the elements in the $x - z$ plane, we take 6 elements in the spanwise direction. In each domain we employ a 9th-order discretization.

With this setup, the flow reaches steady state after 200 non-dimensional time units. We have reproduced the 2D steady-state solution of Gresho *et al.* [33] at $\mathrm{Re} = 400$ (not shown here). To ensure a laminar steady flow for 3D flow with the perturbed inflow boundary condition, we consider the flow at a slightly smaller Reynolds number of $\mathrm{Re} = 300$ in our 3D simulation.

In Fig. 5-16a, we show representative streamlines computed in the sudden expansion of the backward-facing step. The flow separates at the sharp edge of the expansion and reattaches further downstream at the bottom wall. The sudden expansion also creates a smaller separation bubble on the top wall behind the step. As a result of the spanwise sinusoidal inflow perturbation, the separation and attachment patterns show a spanwise three-dimensional variation, which we shall analyze below.

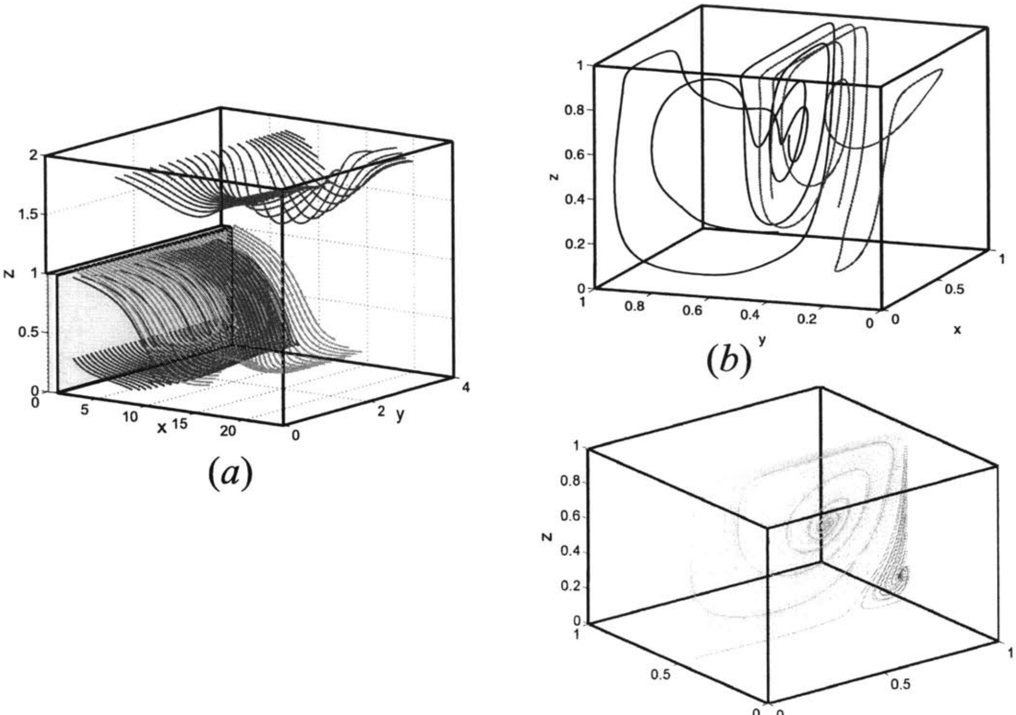

Figure 5-16: (a) Streamlines computed for the backward-facing step. (b) Streamlines computed for the lid-driven cavity. (c) Streamlines in the $y = 0.5$ symmetry plane of the lid-driven cavity.

Lid-Driven Cavity Flow

Our second study is on the lid-driven cavity. The computational model (Fig.5-15b) consists of a cube with sides L. The top wall in the z–direction is driven at a constant velocity u in the x-direction. All walls are no-slip and isothermal. The velocity distribution on the moving top wall is tapered to zero towards the sides according to a parabolic curve; this is to avoid velocity singularities at these locations.

The Reynolds number based on the top-wall velocity and the cube side is Re = 400 ensuring laminar flow[82]. The Mach number based on the wall temperature and the inflow bulk velocity is $Ma = 0.1$, rendering the flow practically incompressible; the Prandtl number is $Pr = 0.72$. Started from a quiescent state, the flow reaches steady state after 25 non-dimensional time units.

The computational grid consists of four domains with the grid refined near the walls. With each domain of seventh order, we obtain a converged solution that is in close agreement with the 2D simulations in Ref. [31]. Based on the convergence studies by Jacobs et al.[46], this resolution guarantees a well-resolved cavity flow.

For the Reynolds number Re = 400, the $y = 0.5$ midplane is invariant (i.e., composed of streamlines), as found in Ref. [82]. Fig. 5-16c shows the 2D streamline pattern in the midplane with the separation and attachment clearly visible near the x=1 wall. The streamlines in the cavity flow (Fig. 5-16b) exhibit complicated behavior[82], leading to the complex three-dimensional separation geometry we identify below.

5.4 Separation and attachment analysis

5.4.1 Backward-Facing Step

Fig. 5-17 shows the wall shear patterns on the bottom and top walls of the backward facing step. The flow is periodic in the spanwise direction, as reflected by the periodic spanwise wall-shear distribution.

We now apply steps 1–8 of the separation- and attachment detection algorithm described in section 5.2.

Steps 1-3

In Table 1, we list all zeros of τ on the top and bottom walls, along with quantities that verify the nondegeneracy of these zeros (Steps 1–2). We then determine (Step 3) the stable and unstable manifolds of all the non-degenerate wall-shear saddles S_{ij} featured in Fig. 5-17.

Steps 4 and 5

Based on Table 1, criteria (S0)-(S4) and (R0)-(R4) of chapter 3 give the following results (cf. section 5.2):

Bottom wall:

- N_{11} satisfies (R0) and hence is a *attachment point*.
- The wall-shear lines connecting N_{11} to S_{11} and S_{21} satisfy (R2), and hence form a *attachment line*.

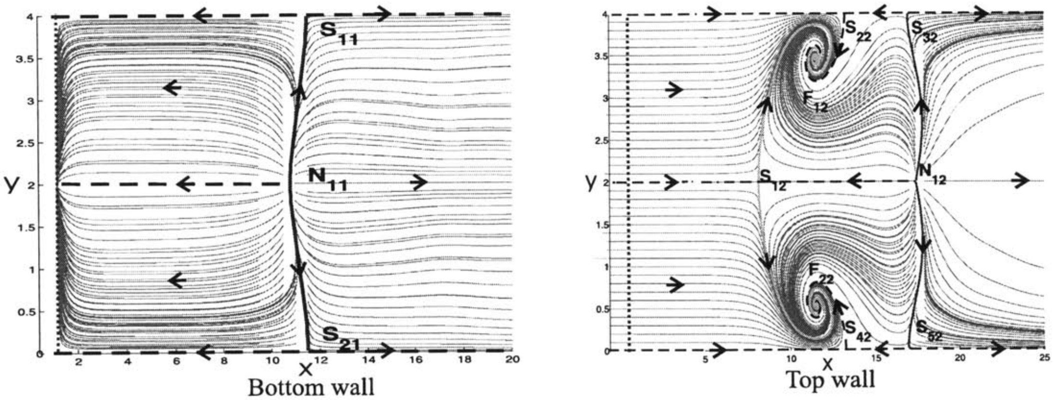

Figure 5-17: Wall-shear lines computed on the top and bottom walls behind the backward-facing step. S_{ij} refer to saddles, N_{ij} to nodes, and F_{ij} to foci (spirals). We also indicate special wall-shear lines (stable and unstable manifolds of the saddles) connecting zeros. Among these, the solid lines will turn out to be actual separation lines (green) or attachment lines (blue). The location of step at $x = 1$ is indicated by a dotted magenta line.

Top wall:

- F_{12} and F_{22} satisfy (S0) and hence are *separation points.*
- N_{12} satisfies (R0) and hence is a *attachment point.*
- The wall-shear lines connecting S_{12} to F_{12} and F_{22} satisfy (S1), and hence form a *separation line.* (Note, however, that the lines connecting S_{32} to F_{12} and F_{22} do *not* form a separation line.)
- The wall-shear lines connecting N_{12} to S_{32} and S_{52} satisfy (R2), and hence form a *attachment line.*

Steps 6 and 7

We obtain the local separation and attachment surfaces identified above by computing the angle formula (Eq. 3.43) at each point of the separation or attachment line. Figs. 5-18a and 5-19a show the resulting local analytic approximations to the separation and attachment surfaces, with nearby streamlines validating the approximations. In this example, separation and attachment curves are contained in separation and attachment surfaces, respectively, hence we do not compute them separately.

Step 8

Figs. 5-18b and 5-19b show the corresponding global separation and attachment surfaces, which we obtained by advecting trajectories starting from the local approximate surfaces.

Table 5.1: Classification of wall-shear zeros for the backward-facing step.

<table>
<tr><th colspan="4">Bottom Wall ($z = 0$)</th></tr>
<tr><th>Wall-shear zero</th><th>(x, y) coordinates</th><th>$\nabla_{\mathbf{x}} \cdot \tau$</th><th>$\det \nabla_{\mathbf{x}} \tau$</th></tr>
<tr><td>$S_{11} \equiv S_{21}$</td><td>$(11.49, 4.00)$, $(11.49, 0.00)$</td><td>1.00</td><td>−1.00</td></tr>
<tr><td>N_{11}</td><td>$(10.79, 2.00)$</td><td>2.96</td><td>1.72</td></tr>
<tr><th colspan="4">Top Wall ($z = 2$)</th></tr>
<tr><th>Wall-shear zero</th><th>(x, y) coordinates</th><th>$\nabla_{\mathbf{x}} \cdot \tau$</th><th>$\det \nabla_{\mathbf{x}} \tau$</th></tr>
<tr><td>S_{12}</td><td>$(8.15, 2.00)$</td><td>−0.54</td><td>−0.16</td></tr>
<tr><td>$S_{22} \equiv S_{42}$</td><td>$(13.25, 4.00)$, $(13.25, 0.00)$</td><td>0.05</td><td>−0.02</td></tr>
<tr><td>$S_{32} \equiv S_{52}$</td><td>$(17.09, 4.00)$, $(17.09, 0.00)$</td><td>0.12</td><td>−0.01</td></tr>
<tr><td>N_{12}</td><td>$(17.42, 2.00)$</td><td>0.68</td><td>0.11</td></tr>
<tr><td>$F_{12} \equiv F_{22}$</td><td>$(11.58, 3.46)$</td><td>−0.09</td><td>0.006</td></tr>
</table>

5.4.2 Lid-driven Cavity Flow

We study the wall-shear field on each of the walls shown in Fig. 5-20. Due to the symmetry of the flow with respect to the $y = 0.5$ plane, Walls 1 and 2 admit identical wall-shear fields. We will again go through Steps 1-8 of the algorithm presented in section 5.2.

Steps 1–3

In Table 2, we list all zeros of τ on Walls 1-4 and 6. We also list the quantities that verify the nondegeneracy of these zeros (Steps 1 and 2). In Step 3, we determine the stable and unstable manifolds of all the nondegenerate wall-shear saddles shown in Fig. 5-20. Note that Wall 5 is not fixed, and hence violates the assumption in Eq. 2.2. The corresponding wall-shear lines in Fig.5-20, however, show that there is no separation or attachment on this wall.

Steps 4 and 5

Based on Table 2, the separation and attachment criteria derived in chapter 3, give the following results (cf. section 5.2):

Walls 1 and 2:

- F_{11} satisfies (S0) and hence is a *separation point.*
- F_{21} and N_{11} satisfy (R0), and hence are *attachment points.*
- The wall-shear lines connecting S_{11} to F_{11} and N_{113} satisfy (S1) and (S2), respectively, and hence form a *separation line.*
- The wall-shear lines connecting S_{21} to F_{11} and N_{114} satisfy (S1) and (S2), respectively, and hence form a *separation line.*

Wall 3:

- N_{23} and N_{33} satisfy (S0), and hence are *separation points.*

Table 5.2: Classification of wall-shear zeros for the lid-driven cavity. The third-order derivatives were obtained by spectral differentiation of the polynomial base functions[47].

Wall 1 ($y = 0$) and Wall 2 ($y = 1$)

Wall-shear zero	(x, z)	$\nabla_{\mathrm{x}} \cdot \tau$	$\det \nabla_{\mathrm{x}} \tau$
S_{11}	$(0.33, 0.02)$	-0.36	-0.74
S_{21}	$(0.97, 0.50)$	-3.99	-17.81
F_{11}	$(0.63, 0.73)$	-15.72	103.20
F_{21}	$(0.83, 0.03)$	1.78	0.87
N_{11}	$(0.03, 0.05)$	0.82	0.17

Wall 1 ($y = 0$) corners and Wall 2 ($y = 1$) corners

Wall-shear zero	(x, z)	$\nabla_{\mathrm{x}} \cdot \partial_x \tau$	$\det \nabla_{\mathrm{x}} \partial_x \tau$
N_{114}, S_{141}	$(1.00, 0.52)$	-247.77	5076.68
S_{116}, S_{161}	$(0.00, 0.05)$	6.80	-434.07

Wall 3 ($z = 0$)

Wall-shear zero	(x, y)	$\nabla_{\mathrm{x}} \cdot \tau$	$\det \nabla_{\mathrm{x}} \tau$
S_{13}	$(0.08, 0.50)$	1.59	-5.00
N_{13}	$(0.74, 0.50)$	16.49	61.60
N_{23}	$(0.31, 0.96)$	-3.24	2.54
N_{33}	$(0.03, 0.04)$	-3.45	2.84

Wall 3 ($z = 0$) corners

Wall-shear zero	(x, y)	$\nabla_{\mathrm{x}} \cdot \partial_y \tau$	$\det \nabla_{\mathrm{x}} \partial_y \tau$
N_{113}, S_{131} or S_{132}	$(0.34, 0.00)$ or $(0.34, 1.00)$	16.63	-3256.11
S_{113}, S_{231} or S_{232}	$(0.83, 0.00)$ or $(0.83, 1.00)$	27.96	-81.12

Wall 3 at intersections with wall 4 and 6

Wall-shear zero	(x, y)	$\nabla_{\mathrm{x}} \cdot \partial_x \tau$	$\det \nabla_{\mathrm{x}} \partial_x \tau$
S_{134}, S_{143}	$(1, 0.50)$	3.30	-9219.04
N_{136}, S_{163}	$(0, 0.50)$	131.51	3180.26

Wall 4 ($x = 1$)

Wall-shear zero	(y, z)	$\nabla_{\mathrm{x}} \cdot \tau$	$\det \nabla_{\mathrm{x}} \tau$
S_{14}	$(0.50, 0.24)$	-3.89	-2.10
N_{14}	$(0.50, 0.15)$	8.03	15.90
N_{24}	$(0.08, 0.41)$	-7.24	9.09
N_{34}	$(0.92, 0.41)$	-7.15	8.36

Wall 6 ($x = 0$)

Wall-shear zero	(y, z)	$\nabla_{\mathrm{x}} \cdot \tau$	$\det \nabla_{\mathrm{x}} \tau$
N_{16}	$(0.50, 0.15)$	8.03	15.90

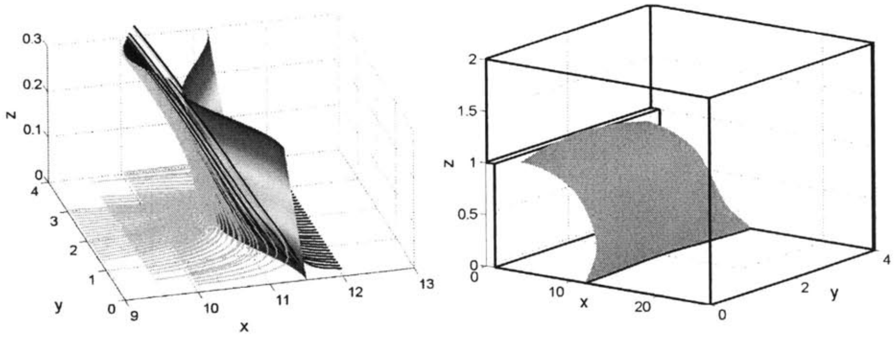

(a)

(b)

Figure 5-18: Attachment surface on the bottom wall of the backward-facing step. (a) Local analytic approximation validated by streamlines. (b) Global surface obtained from advecting the local approximation in time.

- N_{13} satisfies (R0), and hence is a *attachment point.*
- The wall-shear lines connecting N_{13} to S_{13}, S_{232}, S_{134} and S_{231} all satisfy (R2), and hence form *attachment lines.*
- The wall-shear line connecting N_{136} to S_{13} satisfies (R2), and hence is a *attachment line.*

Wall 4:

- N_{24} and N_{34} satisfy (S0), and hence are *separation points.*
- N_{14} satisfies (R0), and hence is a *attachment point.*
- The wall-shear lines connecting S_{14} to N_{24} and N_{34} satisfy (S2), and hence form a *separation line.*
- The wall-shear line connecting N_{14} to S_{143} satisfies (R2), and hence is a *attachment line.*

Wall 6:

- N_{16} satisfies (R0), and hence is a *attachment point.*
- The wall-shear line connecting N_{16} to S_{161} and S_{162} satisfies (R2), and hence is a *attachment line.*

Steps 6 and 7

Figs. 5-21a, 5-22a, and 5-23a show the local analytic approximations to separation and attachment surfaces on Walls 1, 3, and 4, respectively, along with nearby streamlines. Fig. 5-24a shows the local analytic approximation to the attachment curve of

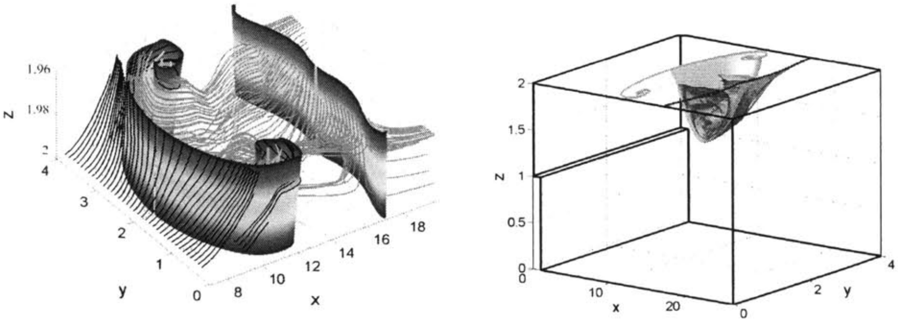

(a) (b)

Figure 5-19: Same as Fig. 5-18, but for the top wall. For better visibility, only half of the global separation surface is shown.

the point N_{16} along with nearby streamlines, obtained from Eq. 3.42. The wall-shear line connecting N_{16} to S_{161} and S_{162} represents a attachment line, but computing the first-order approximation to the corresponding separation surface would require a higher-order version of the angle formula (Eq. 3.43) due to the corner degeneracy at S_{161} and S_{162}.

Step 8

Figs. 5-21b, 5-22b, and 5-23b show the global separation and attachment surfaces obtained by advecting their local approximations in the appropriate time direction. Fig. 5-24b shows the global attachment curve of N_{16} obtained by advecting the local attachment curve in backward time.

5.4.3 Time-periodic lid-driven cavity flow

We now turn to the direct numerical simulation of a time-periodic lid-driven cavity. The nondimensionalized computational model consists of a cube with sides $L = 1$, same as in steady lid driven case considered in previous section (see figure 5-15b)). The top wall in the z–direction is now driven at a time-periodic velocity $U(t) = U_m + 0.7 \sin t$ in the x-direction, with a mean velocity $U_m = 0.3$. For details of the numerical methodology used in our simulation, we refer the reader to section 5.3.

Separation and attachment analysis

To analyze the time-averaged wall-shear field $\bar{\tau}$ on each wall shown in figure 5-25, we follow the steps described in section 5.2. Through these steps, we identify all separation and attachment points and curves, and check their nondegeneracy. For brevity, we only show the final result of this analysis in Fig. 5-25. For separation patterns involving corner points, we have used the approach sketched in section 4.2.4 in a way described in detail in section 5.2. We note that as in steady lid driven cavity flow, walls 1 and 2 admit identical wall-shear fields and corresponding separation patterns.

Note that wall 5 is not fixed and hence was analyzed in a frame co-moving with it. The moving coordinate system leaves the flow domain, but nearby particle paths reveal that there is *no* separation or attachment on the moving wall despite the presence of zeros in the corresponding wall-shear field (see figure 5-25).

Figure 5-26 shows the local analytic predictions for the time-dependent separation (green) and attachment (blue) surfaces on walls 1, 3, 4, and 6 respectively. We have used the slope formulae (4.28) and (4.29) to obtain these approximate surfaces.

In Figure 5-26, black curves represent the time-dependent wall-shear trajectories. It is evident that, despite the large variations in the topology of the time-dependent wall-shear field, the separation and attachment occurs at fixed locations. The particle paths shown in red and cyan validate this prediction.

5.4.4 Separation on a Rotating Sphere

One of the theoretically determined separation patterns in the wall shear field is a stable limit cycle ($S4$ type separation pattern). To the best of the authors knowledge no analysis of the limit cycle separation has been documented. We present the first analysis of this type of separation pattern.

We consider the low Reynolds number flow over a sphere at a Reynolds number of Re=80 based on the diameter of the sphere and the freestream velocity. In the Reynolds number range $20 < \mathrm{Re} < 130$, it is well-known that this flow features a stable, steady and closed separation behind the sphere [102]. At lower Reynolds number the flow is a Stokes flow. At higher Reynolds number the wake is unstable and unsteady. Theoretically, the wall shear field on the sphere at $\mathrm{Re} = 80$ features two nodes and a circle of degenerate fixed points. This separation pattern is not a part of the four basic separation patterns, since it is not a robust. The slightest asymmetry or nonuniformity will perturb away the closed loop of fixed points. In practice, the pattern cannot be observed for lack of perfect symmetry in any experiment.

In our attempt to obtain a limit cycle, we slightly rotate the sphere along the axis in streamwise direction. The maximum rotational velocity at the surface of the sphere is set at 5% of the free stream velocity. We compute the sphere flow using Fluents incompressible flow solver. A hexahedral block-structured grid meshes the spherical computational domain whose outer radius is fifty times the sphere diameter. This ensures a nearly unblocked spherical flow. The velocity inlet is set at the upstream hemisphere. An outflow boundary condition at the downstream hemisphere.

As the sphere is undergoing a rigid body motion, we follow the steps given in the section E.2.2 to analyze separation. Note that in this case $\mathbf{v}_{\mathcal{B}} = 0$, and we take $\mathbf{r}_{\mathbf{O}} = \mathbf{0}$. In a frame $\hat{\mathcal{R}}$ co-rotating with the sphere, we introduce orthogonal spherical polar coordinates (r, θ, ϕ), so that

$$\mathbf{r} = \Phi(\theta, \phi, t) + r\mathbf{n}, \tag{5.27}$$

where

$$\Phi(\theta,\phi,t) = R[\sin\theta\cos(\theta+\Omega t)\mathbf{i} + \cos\theta\mathbf{j} + \sin\theta\sin(\theta+\Omega t)\mathbf{k}], \tag{5.28}$$

is the parametrization of the spherical surface,

$$\mathbf{n}(\theta,\phi,t) = [\sin\theta\cos(\theta+\Omega t)\mathbf{i} + \cos\theta\mathbf{j} + \sin\theta\sin(\theta+\Omega t)\mathbf{k}], \tag{5.29}$$

is the outer unit normal, R is the radius of the sphere and Ω is the angular velocity of rotation.

With this the relevant quantities required for separation analysis can be identified as (see section E.2.2 for details)

$$\mathbf{w}(\theta,\phi,r,t) = -\Omega(R+r)\sin\theta\mathbf{e}_2, \tag{5.30}$$

$$\mathbf{v}(\theta,\phi,r,t) = \mathbf{u}(\mathbf{r},t) - \Omega(R+r)\sin\theta\mathbf{e}_2 = u_1\mathbf{e}_1 + (u_2 - \Omega(R+r)\sin\theta)\mathbf{e}_2 + u_3\mathbf{e}_3, \tag{5.31}$$

$$\mathbf{F}_c(\theta,\phi,t) = \frac{\Omega^2 R}{2}\sin 2\theta\mathbf{e}_1, \tag{5.32}$$

and

$$h_1 = r + R, \qquad h_2 = (r+R)\sin\theta, \tag{5.33}$$

with

$$\mathbf{e}_1 = [\cos\theta\cos(\theta+\Omega t)\mathbf{i} - \sin\theta\mathbf{j} + \sin\theta\sin(\theta+\Omega t)\mathbf{k}], \quad \mathbf{e}_2 = [-\sin(\theta+\Omega t)\mathbf{i} + \cos(\theta+\Omega t)\mathbf{k}]. \tag{5.34}$$

The wall shear pattern in Fig. (5-27a) & b)) shows that the flow indeed features a limit-cycle pattern. At this Reynolds number the slight rotation does not affect the stability of the separation wake. The rotation along the axis introduces a rotation of the closed wall shear trajectory. This in turn causes the wall shear lines to converge to the closed trajectory, thus leading to a limit cycle.

Along the limit cycle, numerical computation shows

$$\int_\Gamma C(\xi(s;\xi_0),0)ds = 106.66 > 0, \qquad \int_\Gamma S_\perp(s)ds = -213.29 < 0, \tag{5.35}$$

Hence, it is indeed a separation line. The predicted separation surface is shown in figures (5-27c) & d)) along with streamlines.

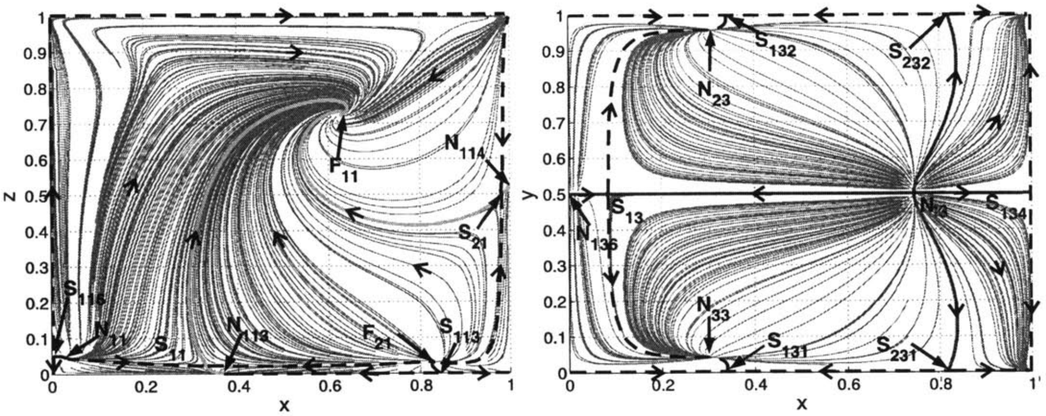

Walls 1 and 2

Wall 3

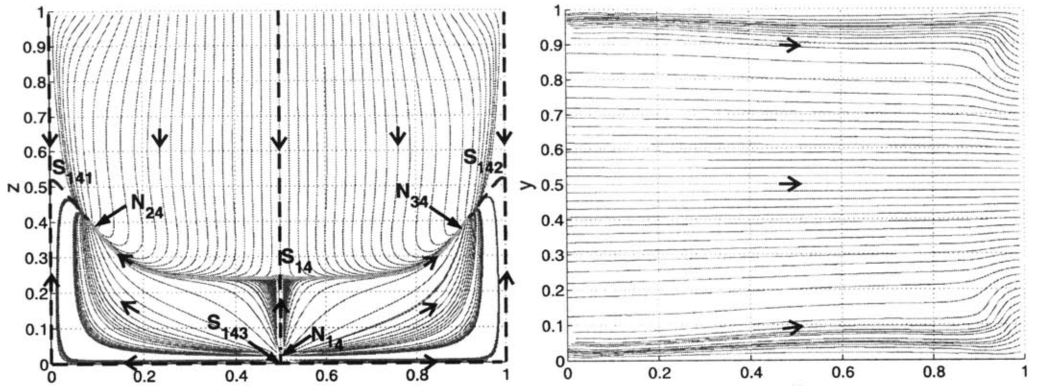

Wall 4

Wall 5

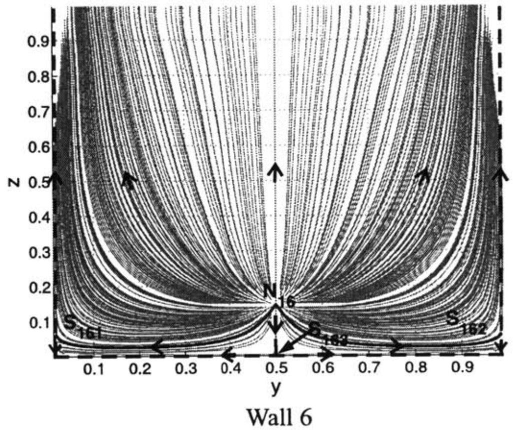

Wall 6

Figure 5-20: Wall shear fields on Walls 1, 4, 5, and 6 for the lid-driven cavity flow. We also indicate special wall shear lines (stable and unstable manifolds of the saddles) connecting wall shear zeros. Among these, the solid lines turn out to be actual separation lines (green) or attachment lines (blue) lines.

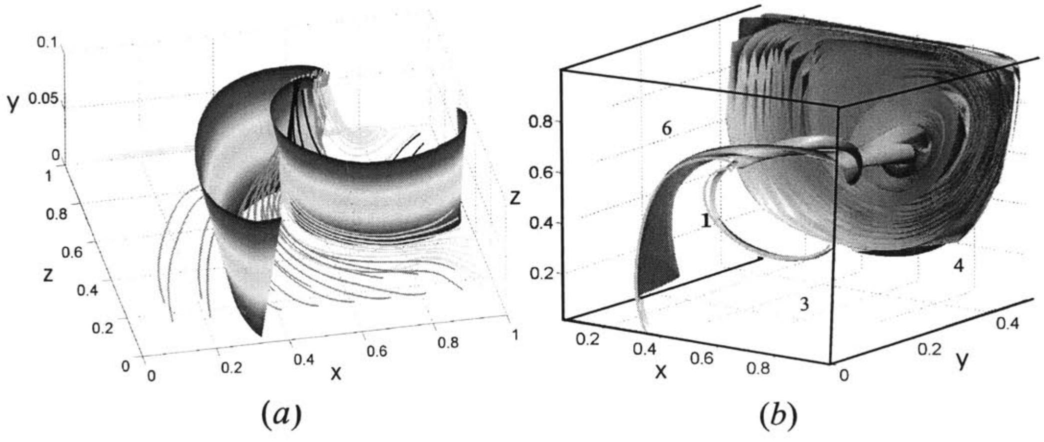

(a) (b)

Figure 5-21: (a) Local approximation to the separation surfaces for Walls 1 and 2, obtained from the slope formula in Eq. 3.43. (b) Global approximation to the separation surfaces obtained by advecting the local approximate surfaces in time.

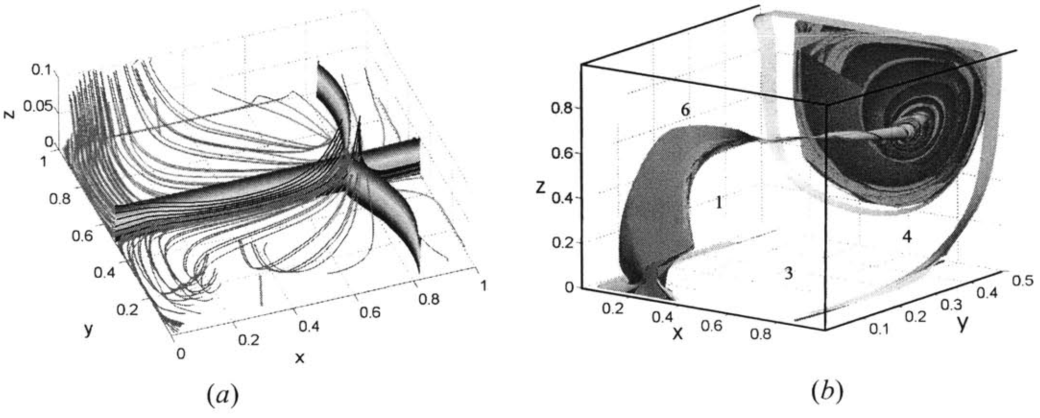

(a) (b)

Figure 5-22: Same as figure 5-21 but for Wall 3.

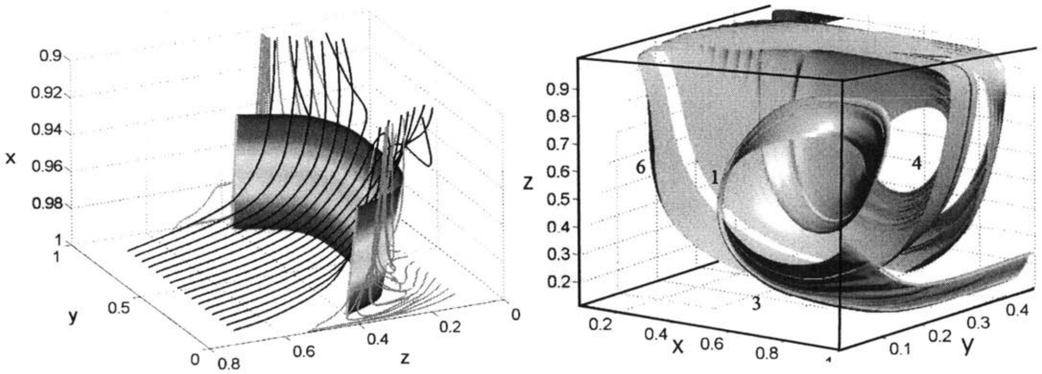

(*a*) (*b*)

Figure 5-23: Same as figure 5-21 but for Wall 4.

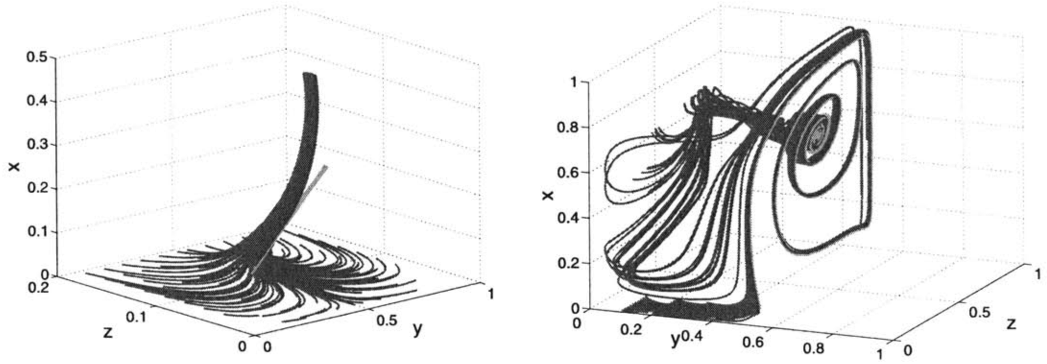

(*a*) (*b*)

Figure 5-24: (a) Local approximation to the attachment curve for Wall 6, obtained from the slope formula (3.42). (b) Global approximation to the attachment curve obtained by advecting the local approximate curve in backward time, along with the nearby streamlines.

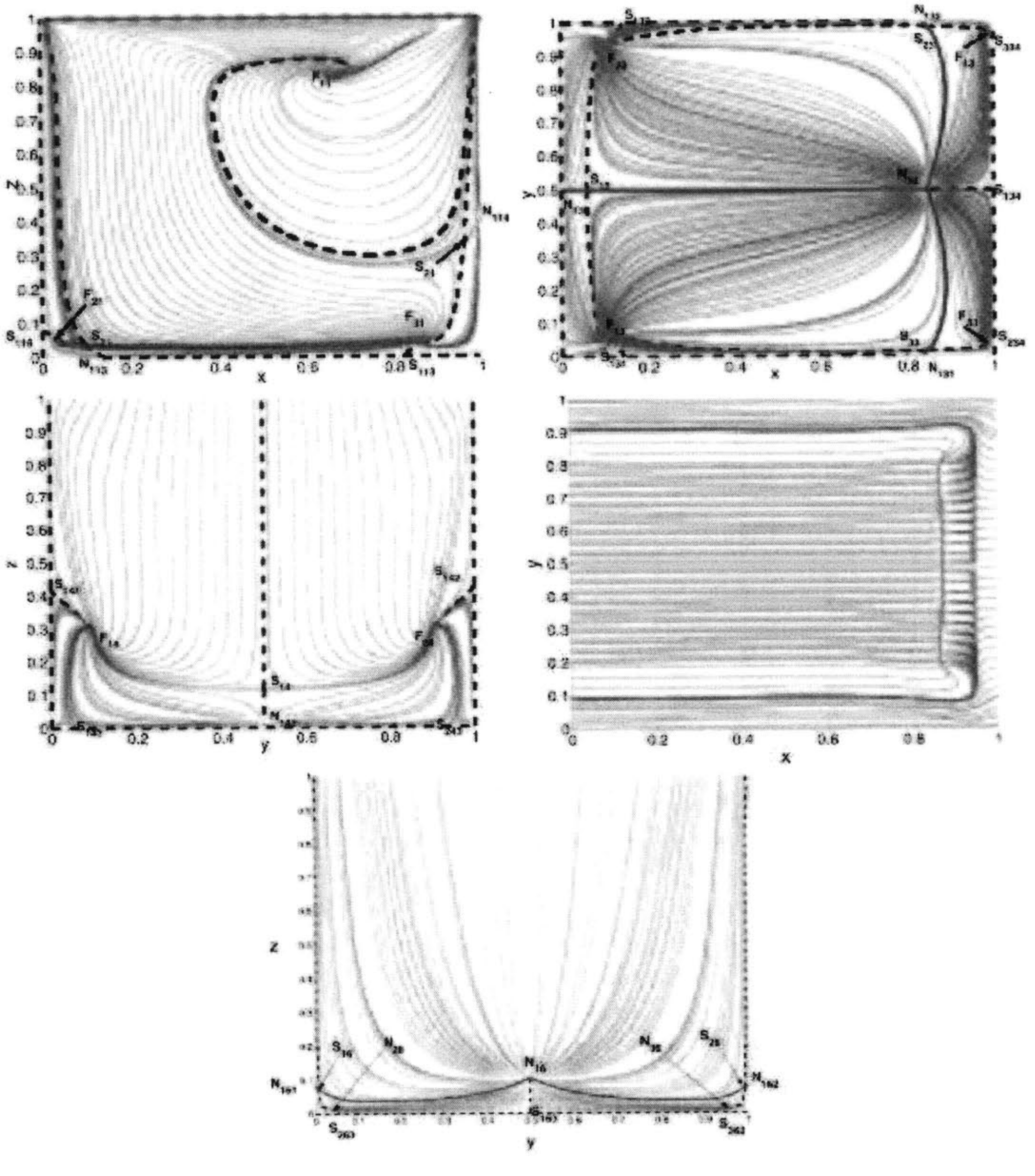

Figure 5-25: Time avearged wall-shear fields on Walls 1, 4, 5, and 6 for the time periodic lid-driven cavity flow. We also indicate special avearged wall-shear lines (stable and unstable manifolds of the saddles) connecting averaged wall-shear zeros. Among these, the solid lines turn out to be actual separation lines (green) or attachment lines (blue) lines.

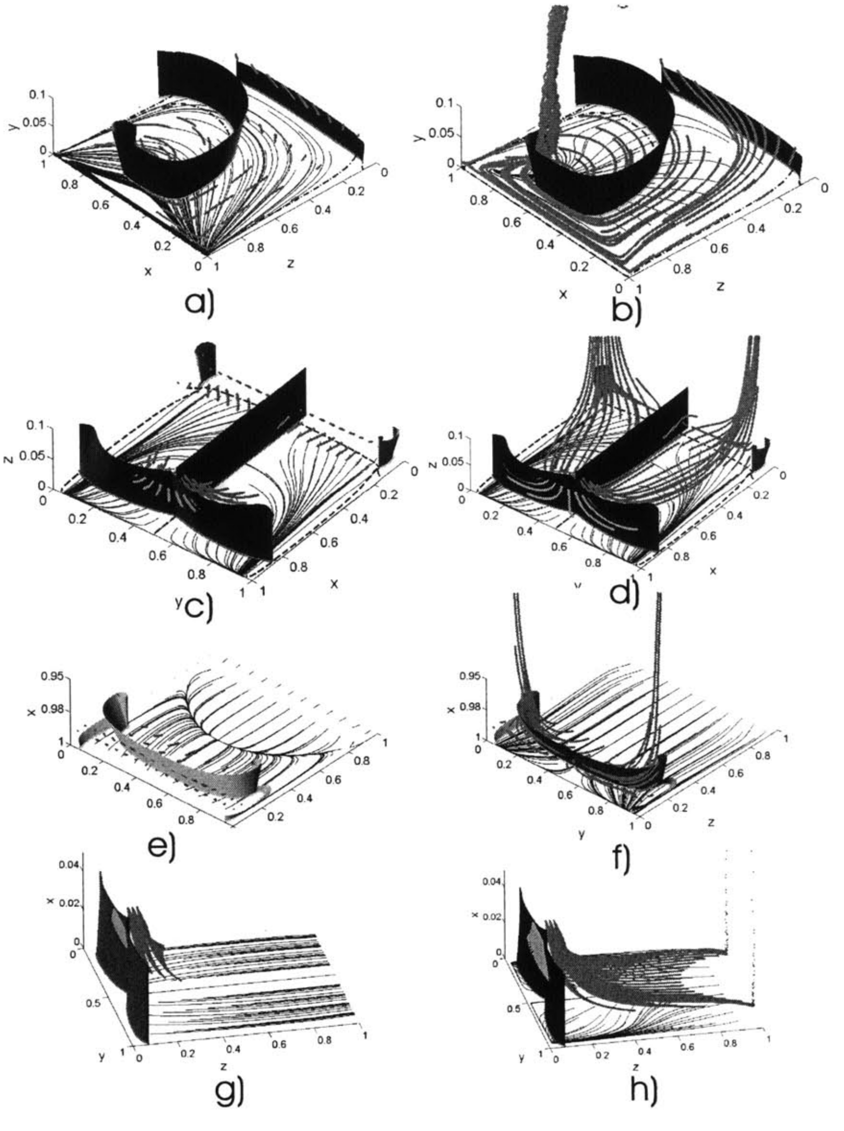

Figure 5-26: Local approximation to the time-dependent separation and attachment surfaces which appear as green and blue, respectively, for different walls of the cavity. These predictions are validated by particle paths which have been colored red and cyan. The subplots (a) and (b) show wall 1; (c) and (d) show wall 3; (e) and (f) show wall 4; (g) and (h) show wall 6.

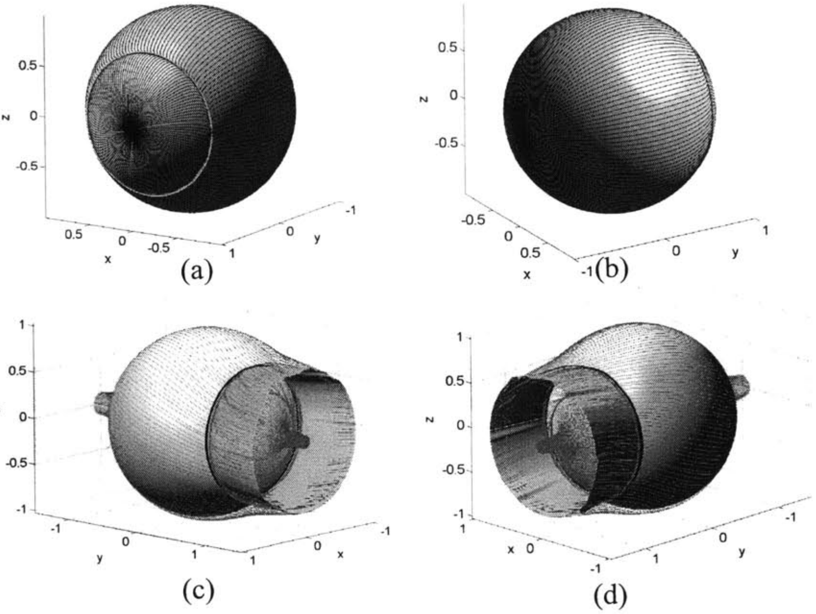

Figure 5-27: Separation over rotating sphere in a symmetrical flow. The streamlines are in the lab frame.

Chapter 6

Experimental Verification

In this chapter we present experimental work on flow separation in three-dimensional fluid flows. In specific we give first experimental demonstration of separation along a limit cycle.

In the previous chapter we showed the numerical existence of limit cycle separation in a flow past a rotating sphere, in which the axis of rotation of the sphere aligns with the far stream flow direction. Motivated by this numerical result, we could consider flow past a rotating sphere for experimental realization of a limit cycle separation. Though this arrangement presents a practical engineering application, it requires a large apparatus for implementation. Therefore, we considered an alternative setup in which the flow is generated by a sphere rotating about the longitudinal axis of a circular cylindrical vessel filled with viscous incompressible fluid. Below this fluid is placed another layer of a heavy immiscible fluid (see section for further discussion). As a result free slip boundary condition exists both at the top and bottom of the viscous liquid column.

6.1 Qualitative flow analysis

Let the sphere radius be a, R be the radius of the cylindrical vessel and H be the depth of the fluid in the vessel (see figure 6-1). We shall denote the distance of the sphere center from the interface of the viscous and the heavy fluid by h. The relevant non-dimensionalized parameter for this problem are

$$\mathrm{Re} = \frac{a^2\Omega}{\nu}, \quad \frac{h}{a}, \quad \frac{R}{a}, \tag{6.1}$$

where, Re is the Reynolds number, ν is the kinematic viscosity of the viscous fluid, and Ω is the speed of rotation of sphere. Before discussing qualitative features of this flow, we give a brief review of flow induced by rotating bodies.

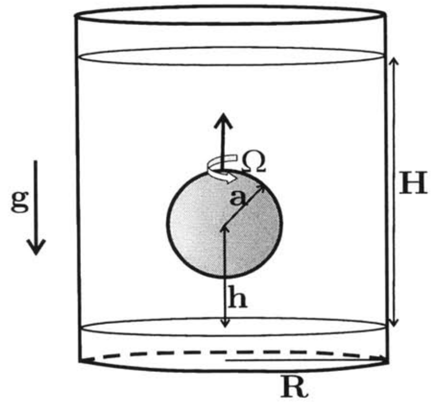

Figure 6-1: Schematic of flow geometry.

6.1.1 Flow due to rotating bodies

The flow generated by rotating bodies has long attracted interest of scientists and engineers, due to applications in fields like meteorology, astrophysics and for calibrating viscometers [49],[50],[21],[18]. We would restrict our discussion to the problem of a rotating sphere in an unbounded undisturbed (Newtonian) fluid domain. For this case, in addition to the primary rotatory flow, a secondary flow is induced by the centrifugal forces in the planes containing the axis of rotation.

In the Stokes regime i.e. for $\mathrm{Re} \ll 1$, the creeping flow induced is such that a concentric spherical shell of fluid of radius r rotates with the angular velocity $\Omega\left(\frac{a}{r}\right)^3$ [86], where (r, θ) are polar coordinates in a plane through the polar axis with the origin at the center of the sphere and $\theta = 0$ coinciding with the polar axis of rotation.

For finite but low Reynolds number, the rotating sphere essentially behaves as a centrifugal fan [56]: it causes an inflow to the sphere in the direction of the polar axis and an outflow parallel to the equatorial plane as shown in the figure 6-2. Bickley [8] calculated the first order perturbed flow in powers of Reynolds number and showed that for small values of Re the transition from inflow at the poles to outflow near equator takes place at an angle $\theta = 54.5°$. With the objective to analytically estimate the torque needed to maintain the steady rotation of sphere at low Reynolds number, further approximations to the solution in powers of Re were obtained by Collins [13], Thomas & Walters [93], and the series has been subsequently extended to eight terms by Takagi [92].

Using a series truncation method, Dennis et. al [21] obtained solutions with validity over a wider range of Reynolds number. Their results show that as the Reynolds number increases: a) the inflow region increases and the region of outflow becomes narrower, and b) the radial velocity increases at the equator, indicating the formation of a radial jet over the narrowing region of outflow. They also reported that no separation bubble appears near the equator over the Reynolds number in the range Re = 1 to Re = 100 (see figure 6-3). An extensive review of laboratory experiments on the flow induced by uniformly rotating spheres over a wide range

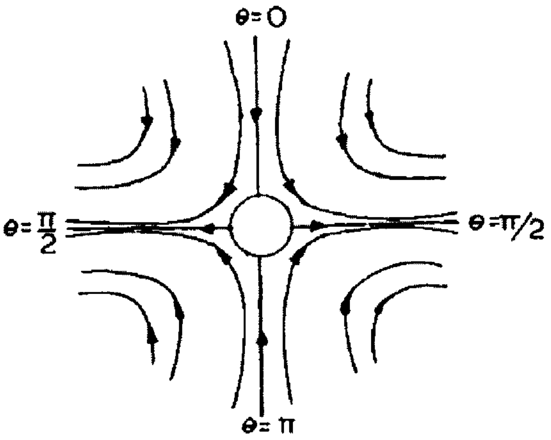

Figure 6-2: Secondary flow due to a rotating sphere in the meridional plane.

of *Re* from creeping flow to fully developed turbulent boundary-layer flow has been complied by Sawatzki [77].

The effect of confinement on a rotating sphere has been considered explicitly by [10], who obtained a Stokes solution to the problem of a sphere rotating about the longitudinal axis of circular cylindrical vessel filled to a finite depth with viscous incompressible fluid. Due to inherent geometrical symmetry of the problem, the streamlines lie in horizontal planes, and form there concentric circles with centers along the cylindrical axis as in the Stokes solution for rotating sphere in an unbounded medium. Experimental investigation of torque on a sphere in a rotating cylindrical vessel enclosed from both ends can be found in [63]. The secondary flow structure was also visualized, see figure 6-4.

The low and finite Reynolds number flow induced by two identical spheres rotating at same angular velocity about their line of centers, distance h apart, in an infinite fluid domain was studied by Davis et al [18]. Such a configuration generates in the meridional plane, a separation bubble that connects the two spheres and encloses a pair of counter-rotating toroidal vortices symmetrically disposed above and below the plane of symmetry, see figure 6-5. Using bipolar coordinates, authors obtained series solutions for predicting the structure of the separation bubble as a function of Re and the sphere separation distance h. In addition experiments were conducted to observe separation bubble in meridional plane and verify the theoretical predictions. For this two spheres were mounted on a rotating shaft in a circular cylinder enclosed from both bottom and top. Due to the confinement, in addition to the free standing bubble, two additional flow states were found, as shown in the figure 6-6).

6.1.2 Symmetry breaking

Here we argue that our experimental setup would produce qualitatively similar separation patterns as that of Davis et al [18], despite the fact that we do not have two

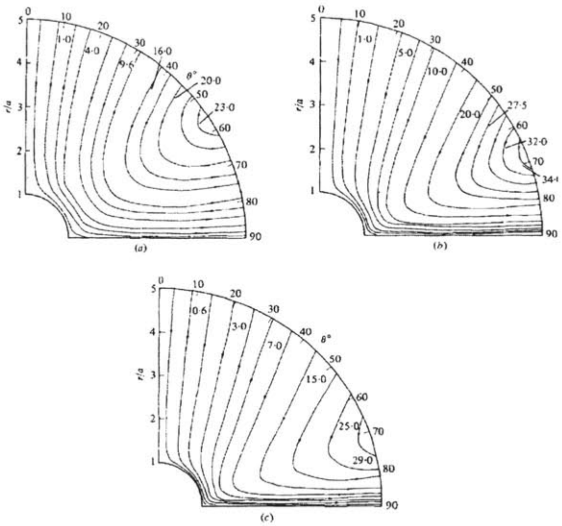

Figure 6-3: Streamlines for (a)Re = 10,(b) Re = 50 and (c)Re = 100 [21].

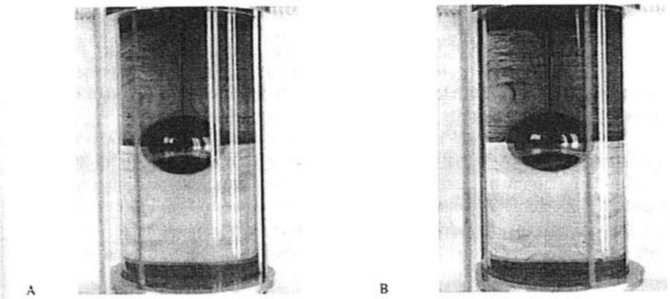

Figure 6-4: Experimental flow visualization of secondary flow pattern [63].

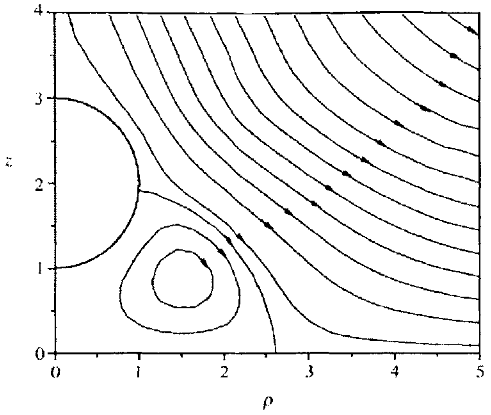

Figure 6-5: Streamline plot showing the separation bubble formed between two rotating sphere in an unbounded fluid domain. Due to symmetry only streamlines in one quadrant are shown [18].

rotating spheres. The main similarity to note is that the interface of the viscous and the heavy fluid acts like the horizontal free slip symmetry plane of the two sphere case. Hence, in our experimental setup the other sphere can be thought of as being virtually present in form of a reflection at the interface. Depending on the value of h, therefore we expect to generate flow patterns of either (a) or (b) type shown in the figure 6-6.

In the figure 6-7a), we sketch the recirculation zones in the meridional plane that correspond to symmetric flow with an isolated bubble, as shown in the figure 6-6 b) . By rotational symmetry, therefore the flow separates along a limit cycle as shown in the figure 6-7b).

6.2 Experimental Method

6.2.1 Physical Apparatus

The experiment comprised of a cylindrical acrylic vessel with radius $R = 10cm$, filled with viscous fluid (corn-syrup water mixture) over a layer of another immiscible heavy liquid (FC40). The cylindrical vessel was housed in another acrylic tank with a square cross-section which was filled with water. Supporting the acrylic vessel there was an aluminium support frame, which elevated the container $20cm$ from the ground level (see figure 6-8). In order to observe the vessel's circular cross section, a mirror was mounted underneath the aluminium support frame at 45 degree.

With the purpose of driving the fluid motion, a solid acrylic sphere with radius $a = 2.5cm$ was mounted at one of the end of a steel shaft and was positioned vertically in the vessel, along the axis of rotation of the cylindrical vessel. The shaft was hollow with external diameter $d_s = 2cm$ and was supported by two ball bearings to minimize

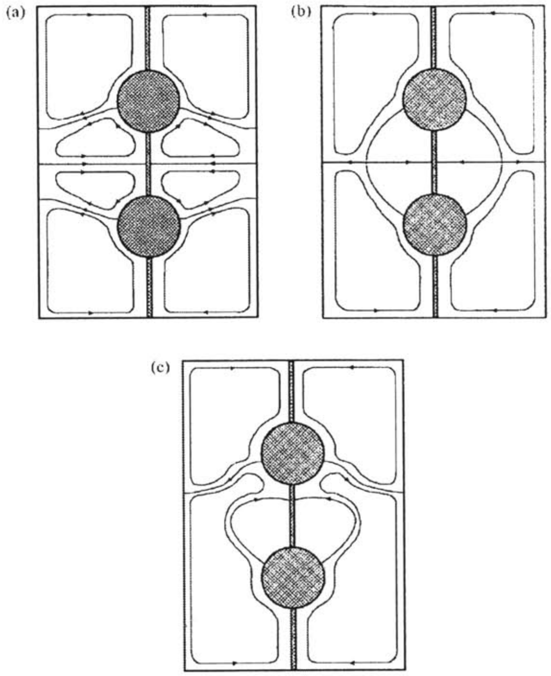

Figure 6-6: Schematic of the meridional flow patterns in a confined geometry: (a) symmetric flow with the bubble attached to the cylinder wall at low Re, (b) symmetric flow with an isolated bubble at moderate Reynolds number, typically Re $\preceq 10$, and (c) an asymmetric flow with the bubble attached to the lower cylinder at high Re [18].

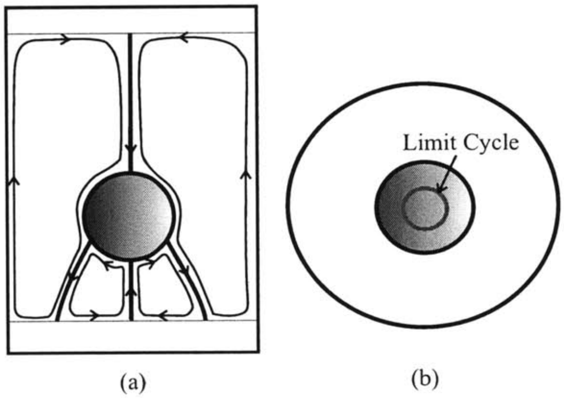

Figure 6-7: (a) Recirculation pattern in the meridional section for a rotating sphere confined in cylindrical vessel, and (b) Bottom view showing the limit cycle in red.

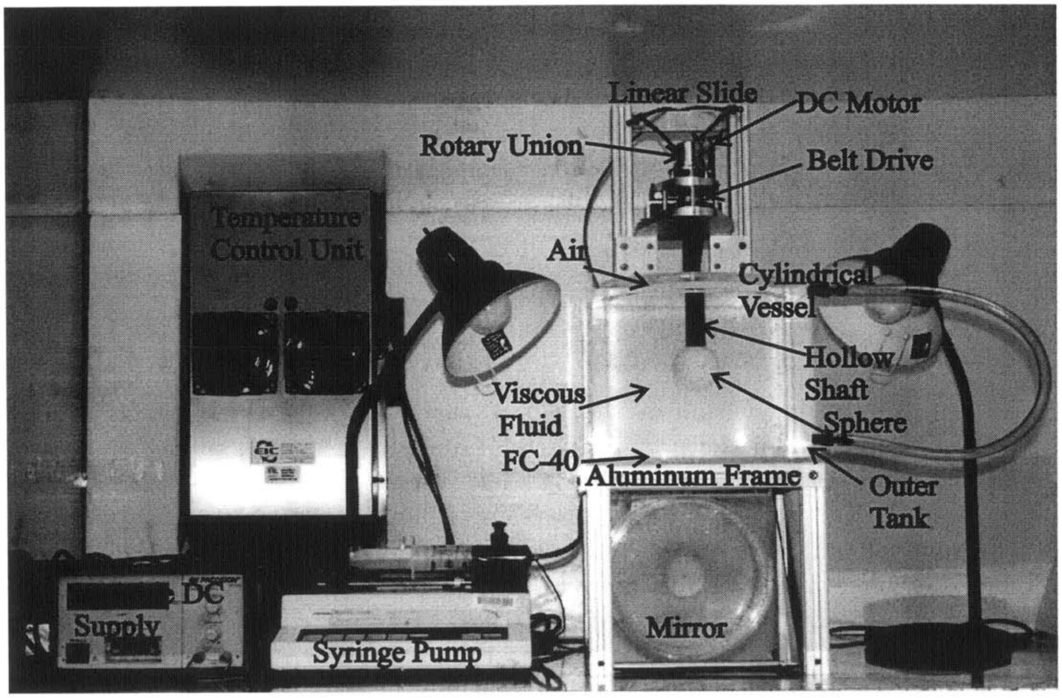

Figure 6-8: Experimental Apparatus.

lateral vibrations.

Rotation of the shaft was driven by a variable speed DC motor, through a belt drive. The rotation speed Ω was controlled by varying the input voltage to the motor through a variable voltage power supply. The shaft, bearing and motor assembly was mounted on an aluminium frame which was free to move along the aluminium support frame along a linear slide. By sliding the aluminium frame, the sphere was placed at different heights h relative to the interface during experimentation.

Four ports were drilled through the sphere for dye injection. Two ports were symmetrically placed near the south pole of the sphere. The location of other two ports was in the equatorial plane, at diametrically opposite positions. The ports were fed with dye by tubes that ran through the hollow shaft to the sphere. There were two tubes: one tube fed the two ports near the pole, while the other for the remaining two ports near the equator. The dye was injected externally through the tubes by a syringe pump. In order to allow dye transportation through the tubes while allowing rotation of shaft, a rotary union was used.

6.2.2 Fluid for experiments

In order to maintain a small Re, viscous fluids were used in the experiments. The experiments to visualize the fluid separation were run utilizing a corn syrup-water mixture. By using 400mL of water for every 1000mL of corn syrup, fluid with kinematic viscosity ν in the range $1 - 3 \times 10^{-2}\mathrm{m}^2/\mathrm{sec}$ (at temperature $T = 20°\mathrm{C}$) was generated. The vessel was not filled completely with corn syrup water mixture, leaving a thin layer of air between the lid and top interface of the mixture; leading to a free slip boundary condition.

In order to create free slip boundary condition at bottom interface of mixture as well, we filled the bottom of the vessel with a thin layer of FC40. FC40 is much heavier (specific gravity being 1.9) than corn syrup-water mixture, has viscosity close to that of water (around $2\times 10^{-4}\mathrm{m}^2/\mathrm{sec}$ at 25°C) and is immiscible with it.

6.2.3 Flow Visualization

Visualization of flow within the vessel was achieved through the injection of neutrally buoyant dye through the ports in the sphere, using a syringe pump. A mixture of fluid and liquid food dye was utilized. By mixing 10mL of the liquid dye with 100mL of the fluid (i.e. corn syrup mixture water mixture), the dye acquired a fluid form of density similar to the fluid density, thus minimizing buoyancy effects. Dye of two different colors were used for the two different sets of ports. Visualizations were done using both food dye and fluorescent dye.

When separation occurred the dyed fluid was drawn away from the spherical surface along a limit cycle into the bulk. The images of separation were captured using a CCD camera, looking up through the bottom of the vessel, via a 45 degree mirror. At the same time the camera also captured the dye evolution in the meridional section. Note that square tank filled with water reduced the optical distortion introduced by the cylindrical nature of the vessel. The visualizations are presented in next section.

6.3 Experimental Results and Discussion

Figures 6-9 and 6-10 show the dye evolution. Red dye that was released from the ports near the south pole of the sphere, spiraled outward towards the equator and separated along a closed curve in the southern hemisphere, forming a separation surface. The green dye that was injected from the ports located at the equator also spiraled towards this closed curve and eventually left the sphere wrapping itself around the separation surface, that had already been delineated by the red dye. The separation surface attached to the interface of corn syrup mixture and FC-40. Note that while the green dye was drawn into the bulk of the fluid after it reached this interface, the red dye remained confined to within the separation surface.

This behavior of dye confirms that the closed curve is an attracting limit cycle and indeed a separation line. In figure 6-11 we show a close up of the limit cycle as a dashed blue line, with the equator indicated by a black dashed line. This clearly shows the first experimental demonstration of $S4$ type separation pattern.

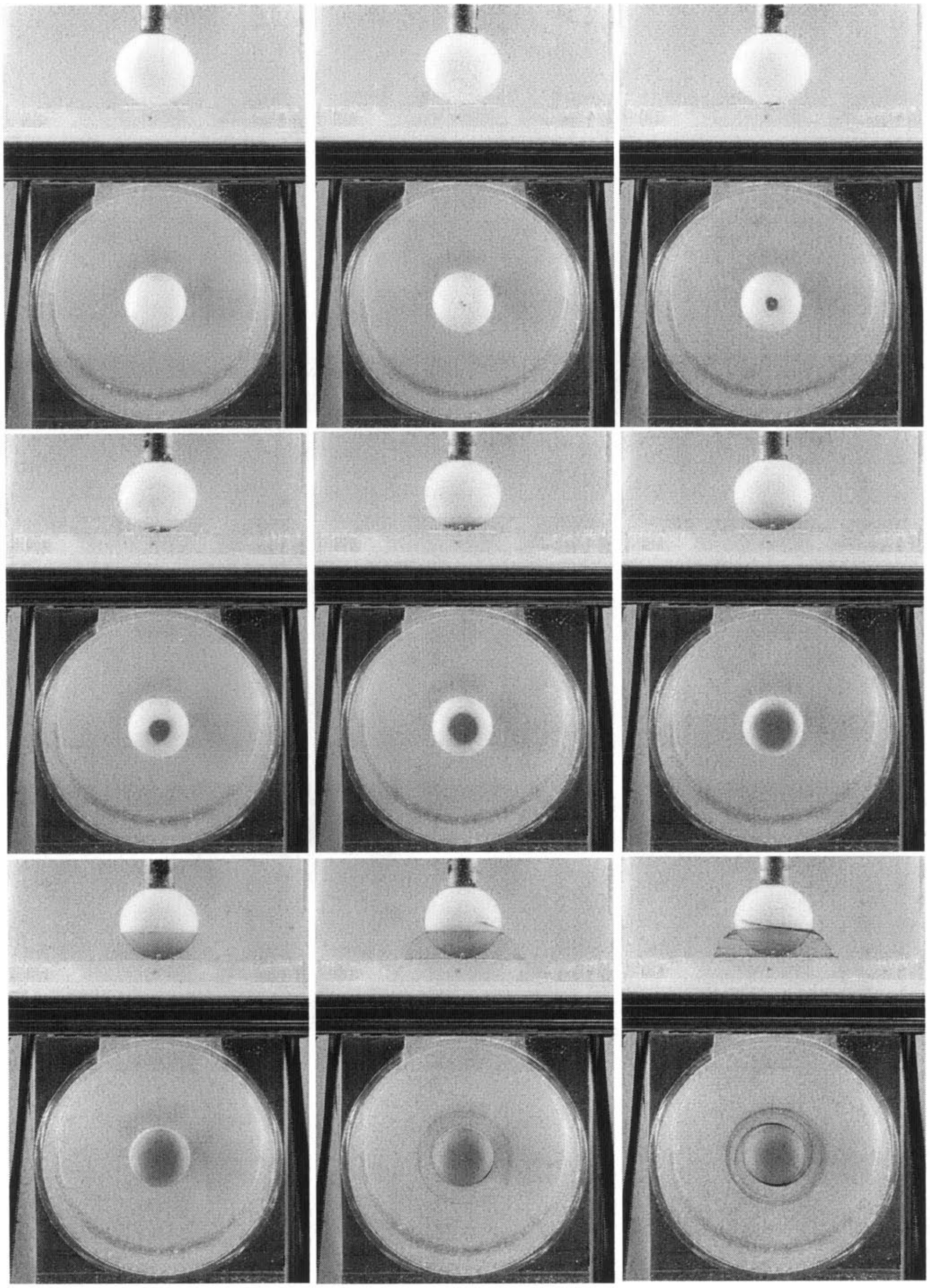

Figure 6-9: Dye evolution sequence at Reynolds No $Re = 12$.

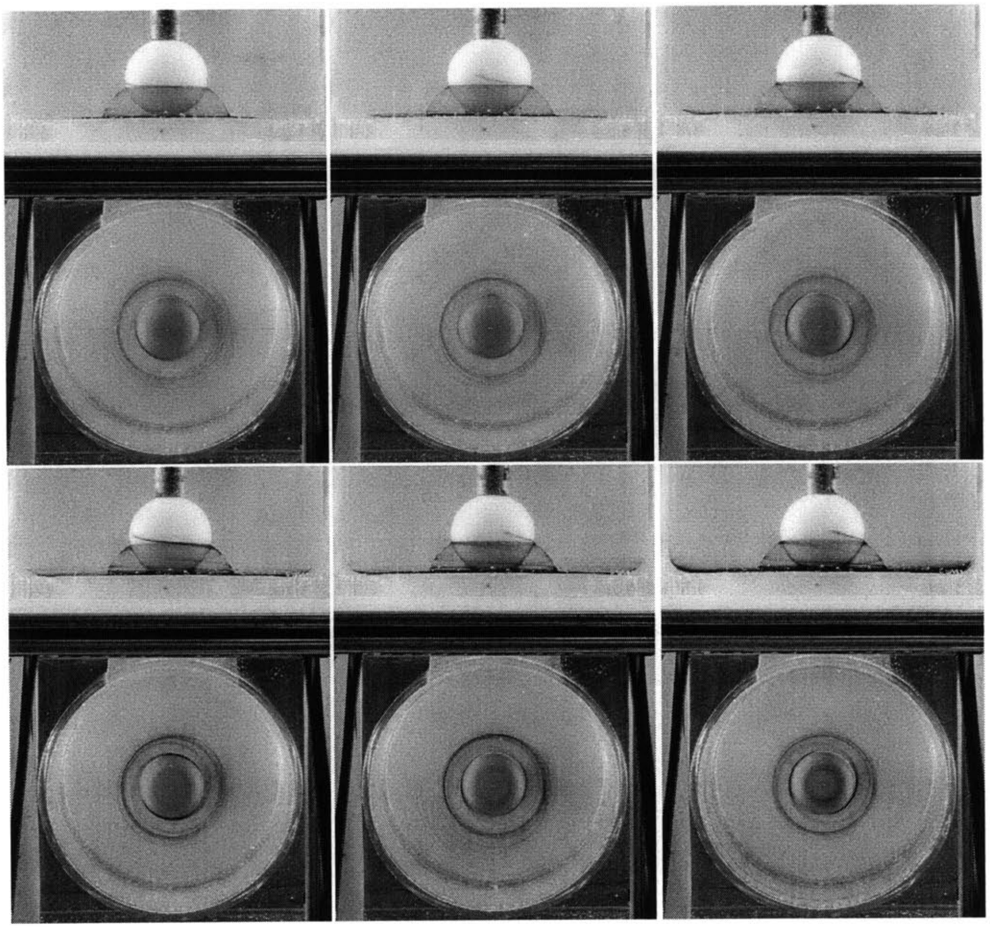

Figure 6-10: Same as figure 6-9, but for latter times.

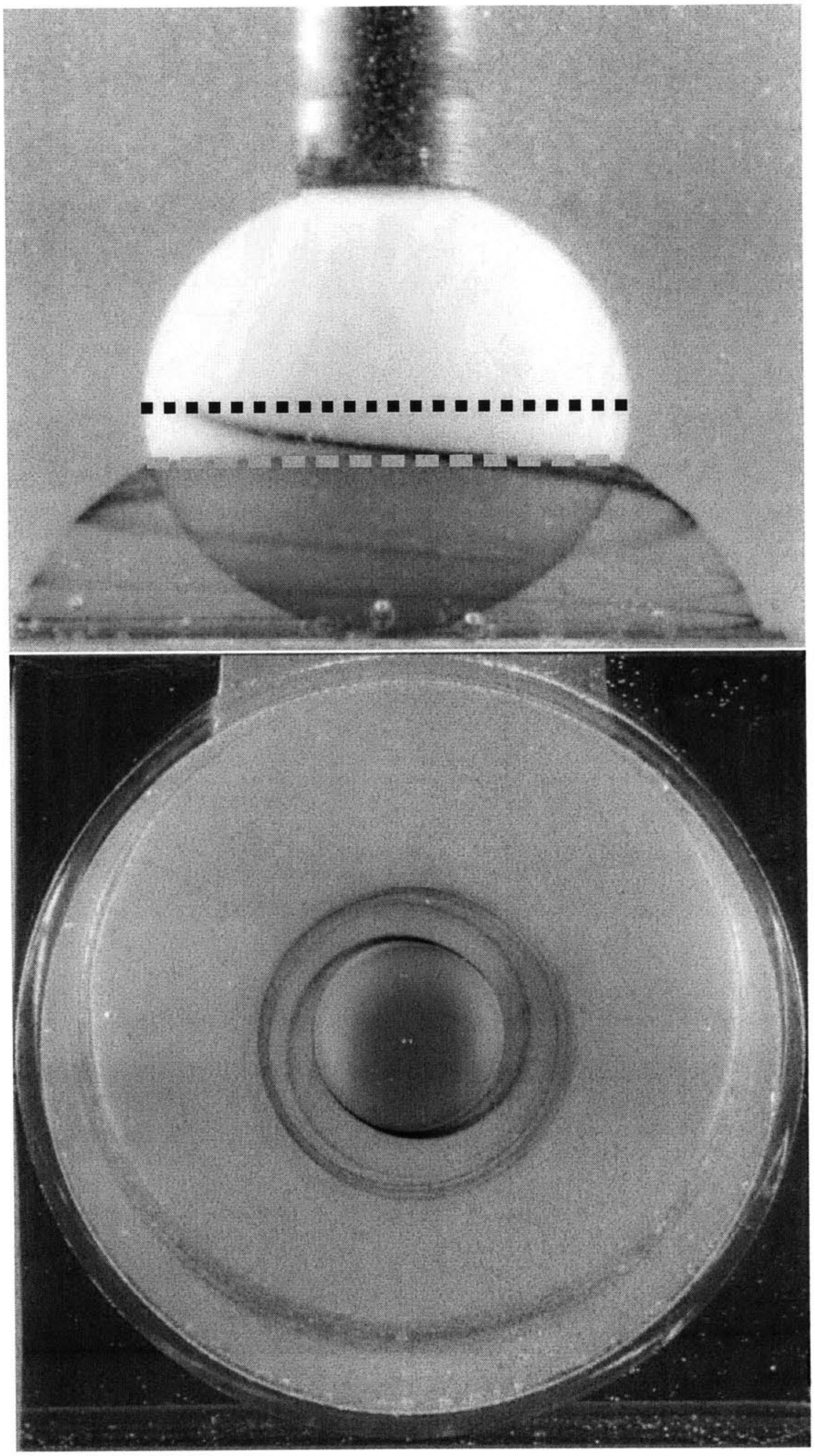

Figure 6-11: Close up of limit cycle shown as a blue dotted line. Also indicated is the location of the equator as a black dotted line.

Chapter 7

Moving Separation

Moving separation typically arises in turbulent fluid flows with slowly evolving mean. Often the slow mean component is introduced in the flow due to the motion of boundary, example being an accelerating airfoil. The material spike now forms at time varying location on the boundary. In simplest setting, this phenomenon can be observed experimentally by placing a cylinder in a two-dimensional crossflow of increasing speed [78], as shown in figure 7-1. Recall that we attributed moving spikes to finite time invariant manifolds in section 2.2.2. In this chapter we locate finite time manifolds in fluid flows with slow fast time scales by introducing a notion of *ghost manifolds*. Ghost manifolds emanate from a boundary layer with no unique extension to the boundary. The boundary layer is thin, hence the misleading perception that the ghost manifolds slide on the boundary. Still, the ghost manifolds turn out to have a virtual footprint on the boundary; this footprint can be detected and hence the spike formation can be predicted.

We summarize these findings in a numerically assisted analytic criterion for moving spikes that we derive using a combination of rescaling, dynamic averaging, topological invariant techniques and wavelet analysis. Our moving spike criterion translates to a criterion for moving separation when applied to flow around aerodynamic bodies. We first show this for 2D flows; extension to 3D flows follows immediately. We demonstrate the moving criterion in analytical and numerical examples of both 2D and 3D flow separation.

7.1 Motivation

In order to motivate the notion of *ghost manifold*, we begin by considering a two dimensional dynamical system of the form

$$\dot{\mathbf{x}} = \mathbf{v}(\mathbf{x}, \epsilon t, t), \tag{7.1}$$

where $\mathbf{x} = (x, y) \in U \subset \mathbb{R}^2$, $\mathbf{v} = (u, v)$, and $\epsilon \ll 1$ is a nonnegative small parameter. System (7.1) is therefore a non-autonomous system whose time dependence has two components, one is of $\mathcal{O}(1)$ and one is of $\mathcal{O}(\epsilon)$ speed.

Assume that system (7.1) admits a smooth compact two-dimensional manifold

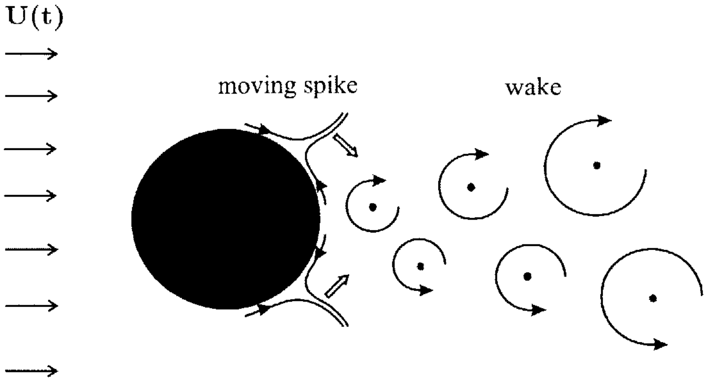

Figure 7-1: Wake behind a stationary cylinder in a two dimensional time varying crossflow. Also shown are material spikes that move towards the wake as Reynolds number increases.

$\mathcal{B}$ of fixed points that is independent of time. As an example, one can think of an unsteady fluid flow in which particle motions satisfy equation (7.1) with $\mathbf{v}$ denoting the velocity field of the fluid. In this case, any fixed no-slip boundary of the fluid is a time-independent critical manifold. By the form of (7.1), the fluid flow has a slowly evolving mean component as well as faster fluctuations.

Let $\mathbf{x}_b(s) = (x_b(s), y_b(s))$ be the arclength parametrization of $\mathcal{B}$ with s denoting the arclength that varies on a compact set I. The unit tangent and the outer unit normal to $\mathcal{B}$ will be denoted by $\mathbf{t}(s)$ and $\mathbf{n}(s)$, respectively. Then along $\mathcal{B}$, we have

$$\mathbf{v}(\mathbf{x}_b(s), \epsilon t, t) = 0, \quad \mathbf{n}^T(s)\nabla_{\mathbf{x}}\mathbf{v}(\mathbf{x}_b(s), \epsilon t, t)\mathbf{n}(s) = 0, \tag{7.2}$$

for all s and t. The second condition in (7.2) implies that the stretching rate normal to $\mathcal{B}$ vanishes identically along $\mathcal{B}$, which holds true for any flow that is locally incompressible along the critical manifold $\mathcal{B}$.

In order to separate the two time scales in the system (7.1) more explicitly, we introduce the phase variable

$$\phi = \epsilon t,$$

so that in extended phase space of the $(\mathbf{x}, \phi)$ variables, system (7.1) becomes

$$\begin{aligned} \dot{\mathbf{x}} &= \mathbf{v}(\mathbf{x}, \phi, t), \\ \dot{\phi} &= \epsilon. \end{aligned} \tag{7.3}$$

In the extended phase space, $\mathcal{B}$ shows up as an invariant slow manifold

$$\mathcal{S} = \{\ (\mathbf{x}_b(s), \phi) \mid s \in I,\ \phi \in \mathbb{R}\}, \tag{7.4}$$

with no motion in the $\mathbf{x}$-direction. and uniform slow motion in the ϕ-direction.

To focus on the dynamics near $\mathcal{S}$, we let

$$\mathbf{x}(s,\eta) = \mathbf{x}_b(s) + \eta\mathbf{n}(s),$$

where η is the distance from $\mathcal{S}$ along the normal $\mathbf{n}(s)$. After this transformation, system (7.3) can be written as

$$\begin{aligned} \dot{s} &= \tilde{u}(s,\eta,\phi,t), \\ \dot{\eta} &= \tilde{v}(s,\eta,\phi,t), \\ \dot{\phi} &= \epsilon, \end{aligned} \tag{7.5}$$

where

$$\begin{aligned} \tilde{u}(s,\eta,\phi,t) &= \frac{\mathbf{v}\left(\mathbf{x}_b(s) + \eta\mathbf{n}(s),\phi,t\right)\cdot\mathbf{t}(s)}{1-\eta\kappa(s)}, \\ \tilde{v}(s,\eta,\phi,t) &= \mathbf{v}\left(\mathbf{x}_b(s) + \eta\mathbf{n}(s),\phi,t\right)\cdot\mathbf{n}(s), \end{aligned} \tag{7.6}$$

with $\kappa(s) = x_b'(s)y_b''(s) - y_b'(s)x_b''(s)$ denoting the curvature of $\mathcal{B}$.

In the new coordinates (s,η,ϕ), the slow manifold $\mathcal{S}$ is simply given by $\eta = 0$, and the conditions (7.2) are equivalent to

$$\tilde{u}(s,0,\phi,t) = 0, \qquad \tilde{v}(s,0,\phi,t) = 0, \qquad \partial_\eta\tilde{v}(s,0,\phi,t) = 0.$$

Because of these conditions, we can rewrite $(\tilde{u},\tilde{v})$ as

$$\begin{aligned} \tilde{u}(s,\eta,\phi,t) &= \eta\int_0^1 \partial_\eta\tilde{u}(s,\eta p,\phi,t)\;dp, \\ \tilde{v}(s,\eta,\phi,t) &= \eta^2\int_0^1\int_0^1 \partial_\eta^2\tilde{v}(s,\eta pq,\phi,t)p\;dpdq. \end{aligned}$$

We introduce an additional blow-up of the normal coordinate near $\mathcal{S}$ by letting

$$\eta = \epsilon\tilde{\eta},$$

where $\epsilon \geq 0$ is a small parameter. Expanding in powers of ϵ and $\tilde{\eta}$, we obtain the dynamical system (7.5) in the form

$$\begin{aligned} \dot{s} &= \epsilon\tilde{\eta}\partial_\eta\tilde{u}(s,0,\phi,t) + \epsilon^2\tilde{\eta}^2\left[\frac{1}{2}\partial_\eta^2\tilde{u}(s,0,\phi,t) + \mathcal{O}(\tilde{\eta}\epsilon)\right], \\ \dot{\tilde{\eta}} &= \epsilon\tilde{\eta}^2\frac{1}{2}\partial_\eta^2\tilde{v}(s,0,\phi,t) + \epsilon^2\tilde{\eta}^3\left[\frac{1}{6}\partial_\eta^2\tilde{v}(s,0,\phi,t) + \mathcal{O}(\tilde{\eta}\epsilon)\right], \\ \dot{\phi} &= \epsilon, \end{aligned} \tag{7.7}$$

which can be thought of as a normal form of the original system (7.1) near $\mathcal{S}$ in the extended phase space.

7.2 Set-up and assumptions

Motivated by the normal formal (7.7), we now consider systems of the general form

$$\begin{aligned} \dot{\mathbf{x}} &= \epsilon \mathbf{f}(\mathbf{x}, \phi, t) + \epsilon^2 \mathbf{g}(\mathbf{x}, \phi, t; \epsilon), \\ \dot{\phi} &= \Delta\epsilon, \end{aligned} \tag{7.8}$$

where $\mathbf{x} = (x, z)$, $\epsilon \geq 0$ is a small parameter, and $\Delta \in [0, 1]$ is a constant that we shall ultimately set to one to obtain results relevant for the normal form (7.7) and hence for our original system (7.1).

The functions

$$\mathbf{f}(\mathbf{x}, \phi, t) = \begin{pmatrix} z f_1(x, \phi, t) \\ z^2 f_2(x, \phi, t) \end{pmatrix}, \qquad \mathbf{g}(\mathbf{x}, \phi, t; \epsilon) = \begin{pmatrix} z^2[g_1(x, \phi, t) + \mathcal{O}(z\epsilon)] \\ z^3[g_2(x, \phi, t) + \mathcal{O}(z\epsilon)] \end{pmatrix}, \tag{7.9}$$

and their derivatives are assumed to be uniformly bounded in time in a neighborhood of the invariant nonhyperbolic slow manifold

$$\mathcal{S} = \{(\mathbf{x}, \phi) \ : \ x \in I, \ z = 0, \ \phi \in \mathbb{R}\}.$$

We note that $z = \frac{y}{\epsilon}$ denotes a rescaled coordinate normal to $\mathcal{S}$.

In this general setting, we further assume the function $\mathbf{f}(\mathbf{x}, \phi, t)$ can be decomposed into a slowly evolving mean and fluctuations as follows:

$$\mathbf{f}(\mathbf{x}, \phi, t) = \mathbf{f}^0(\mathbf{x}, \phi) + \tilde{\mathbf{f}}(\mathbf{x}, \phi, t), \tag{7.10}$$

where

$$\begin{aligned} \lim_{T \to \infty} \frac{1}{T} \int_{t_0}^{t_0 - T} \tilde{\mathbf{f}}(\mathbf{x}, \phi, \tau)\, d\tau &= 0, \\ \limsup_{T \to \infty} \left| \int_{t_0}^{t_0 - T} \tilde{\mathbf{f}}(\mathbf{x}, \phi, \tau)\, d\tau \right| &< \infty, \\ \limsup_{T \to \infty} \left| \int_{t_0}^{t_0 - T} \nabla_{\mathbf{x}} \tilde{\mathbf{f}}(\mathbf{x}, \phi, \tau)\, d\tau \right| &< \infty, \end{aligned} \tag{7.11}$$

for any t_0. The fluctuating part $\tilde{\mathbf{f}}$ can be time-periodic or irregular in time. The lack of dependence of $\mathbf{f}^0$ explicitly on t creates a frequency gap between the mean and the fluctuations, as is typical in turbulent fluid flows [65].

7.3 Ghost manifold

7.3.1 Invariant manifolds in the $\Delta = 0$ limit

We now rewrite the decomposition (7.10) of system (7.8) as

$$\begin{aligned} \dot{\mathbf{x}} &= \epsilon[\mathbf{f}^0(\mathbf{x},\phi) + \tilde{\mathbf{f}}(\mathbf{x},\phi,t)] + \epsilon^2\mathbf{g}(\mathbf{x},\phi,t;\epsilon), \\ \dot{\phi} &= \epsilon\Delta. \end{aligned} \tag{7.12}$$

Therefore, up to $\mathcal{O}(\epsilon)$, the mean dynamics near the slow manifold $\mathcal{S}$ is governed by the system

$$\begin{aligned} \dot{\mathbf{x}} &= \epsilon\mathbf{f}^0(\mathbf{x},\phi), \\ \dot{\phi} &= \epsilon\Delta. \end{aligned} \tag{7.13}$$

Taking the $\Delta = 0$ limit, we obtain the equivalent system

$$\begin{aligned} \dot{x} &= zf_1^0(x,z,\phi), \\ \dot{z} &= z^2f_2^0(x,z,\phi), \\ \dot{\phi} &= 0, \end{aligned} \tag{7.14}$$

Observe that the manifold $\mathcal{S} = \{(x,z,\phi) \mid z = 0\}$ is a critical manifold (manifold of fixed points) for system (7.14). Localized pulse formation can be observed in system (7.14) along any smooth curve $\mathcal{C} \subset \mathcal{S}$ of the form

$$\mathcal{C} = \{\ (p\,(\phi)\,,0,\phi)\ \ :\ \phi \in \mathcal{I} \subset \mathbb{R}\}, \tag{7.15}$$

provided that

$$\begin{aligned} f_1^0(p(\phi),\phi) &= 0 \\ \sup_{\phi\in\mathcal{I}} \partial_x f_1^0(p(\phi),\phi) &< 0, \\ \inf_{\phi\in\mathcal{I}} f_2^0(p(\phi),\phi) &> 0. \end{aligned} \tag{7.16}$$

Indeed, if we rescale time via $\frac{d\tau}{dt} = \epsilon z(t)$ along trajectories of system (7.14), then conditions (7.16) render the set $\mathcal{C}$ a hyperbolic curve of fixed points with a two-dimensional unstable manifold $\mathcal{W}_0$ off the $\mathcal{S}$ plane, and with a two-dimensional stable manifold within the $\mathcal{S}$ plane. In forward time, $\mathcal{W}_0$ attracts nearby trajectories in the vicinity of $\mathcal{C}$, and forces them to eject from a neighborhood of $\mathcal{S}$. Passing back to the original time t, we therefore obtain a nonhyperbolic unstable manifold $\mathcal{W}_0$ emanating from the critical manifold $\mathcal{S}$ along the curve $\mathcal{C}$ (see Fig. 7-2)

For $\Delta > 0$, the manifolds $\mathcal{C}$ and $\mathcal{W}_0$ no longer remain invariant for system (7.13), in which the slow manifold $\mathcal{S}$ is now filled with ($x = const., z = 0$) invariant lines. Because of the uniform drift on these lines in the ϕ direction, there cannot be any other invariant set within $\mathcal{S}$ that is C^1-close $\mathcal{C}$ (unless $\mathcal{C}$ is itself a straight line).

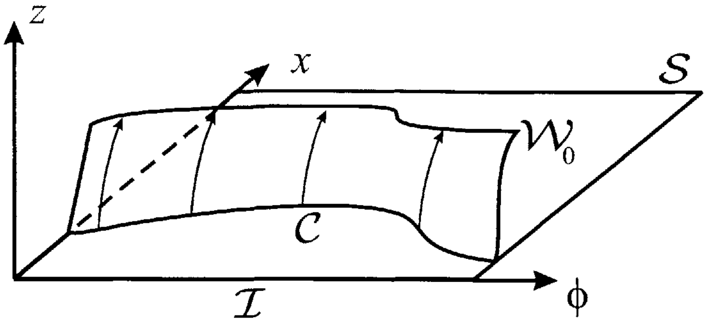

Figure 7-2: The geometry of the manifolds $\mathcal{S}$, $\mathcal{C}$ and $\mathcal{W}_0$ for $\Delta = 0$ under conditions (7.16).

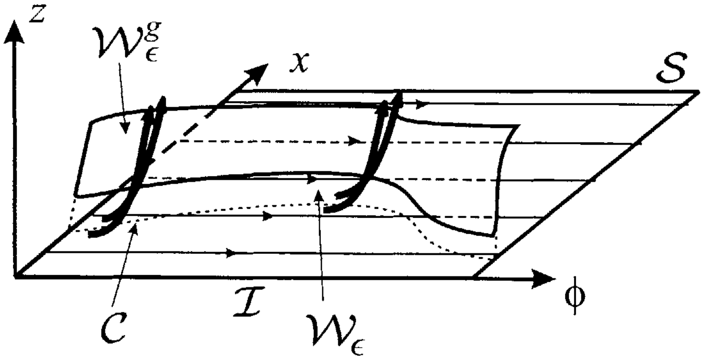

Figure 7-3: The geometry of the ghost manifold $\mathcal{W}_\epsilon^g$ for $\Delta > 0$.

Therefore, $\mathcal{C}$ typically has no smooth continuation for $\Delta > 0$. Still, numerical simulations indicate that trajectories of system (7.8) will continue to be ejected from the vicinity $\mathcal{S}$, forming spikes that appear to be moving along $\mathcal{C}$ as the phase variable ϕ (and hence time) increases. As we show below, this behavior is caused by a locally invariant piece $\mathcal{W}_\epsilon^g$ of the unstable manifold $\mathcal{W}_0$ that survives even for $\Delta = 1$ in system (7.8), as illustrated in Fig. 7-3. (By local invariance of a manifold we mean that trajectories can only leave the manifold through its boundary.)

The invariant manifold $\mathcal{W}_\epsilon^g$ lies off the slow manifold $\mathcal{S}$ and cannot be continued down to $\mathcal{S}$. We can therefore think of $\mathcal{W}_\epsilon^g$ as a locally invariant sheet that hovers over $\mathcal{S}$. For this reason, we shall refer to $\mathcal{W}_\epsilon^g$ as a *ghost manifold.*

7.3.2 Existence of a ghost manifold

In order to prove the existence of a ghost manifold $\mathcal{W}_\epsilon^g$ discussed above, we consider the modified version of system (7.12) of the form

$$\begin{aligned} \dot{\mathbf{x}} &= \epsilon[\mathbf{f}^0(\mathbf{x},\phi) + \tilde{\mathbf{f}}(\mathbf{x},\phi,t)] + \epsilon^2\mathbf{g}(\mathbf{x},\phi,t;\epsilon), \\ \dot{\phi} &= \epsilon\Delta M(z), \end{aligned} \tag{7.17}$$

where $M(z)$ is a C^∞ bump function (see, e.g., [12]) satisfying

$$M(z)\begin{cases} = 0 & z \leq \frac{1}{q}z^* \\ \in (0,1) & \frac{1}{q}z^* < z < z^* \\ = 1 & z \geq z^*. \end{cases} \tag{7.18}$$

The parameter $z^* > 0$ and $q > 1$ will be chosen later, see Appendix C.2 for details.

Note that the inclusion of the bump function in (7.17) makes no difference for $z \geq z^*$, but freezes the dynamics in the ϕ direction close to the slow manifold $\mathcal{S}$. As a result, $\mathcal{C}$ continues to be an invariant manifold for system (7.17) even for $\Delta > 0$. We shall construct an unstable manifold for $\mathcal{C}$ in the modified system (7.17) for $\Delta = 1$. We shall then argue that a subset of this unstable manifold will play the role of the ghost manifold $\mathcal{W}_\epsilon^g$ discussed above.

Applying averaging, topological invariant manifold techniques and scaling analysis, we prove in Appendix C.2 that under appropriate conditions, $\mathcal{W}_0$ perturbs into a nearby unstable manifold $\mathcal{W}_\epsilon^g$ for $\mathcal{C}$ in the modified system (7.17). Specifically, we have the following result:

Theorem 1 *Assume that there exists $\epsilon_0 > 0$ such that the conditions*

$$\begin{aligned} f_1^0(p(\phi),\phi) &= 0 \\ \sup_{\phi\in\mathcal{I}} \partial_x f_1^0(p(\phi),\phi) &< 0, \\ \inf_{\phi\in\mathcal{I}} f_2^0(p(\phi),\phi) &> 0, \\ \inf_{\phi\in\mathcal{I}} \left[f_2^0(p(\phi),\phi) - \partial_x f_1^0(p(\phi),\phi) - \epsilon\,|p'(\phi)|\right] &> 0, \end{aligned} \tag{7.19}$$

are satisfied for all $\phi \in \mathcal{I} = (-\infty, \epsilon t_0)$. Then, for all $\epsilon < \epsilon_0$ small enough and for $z^* = \frac{1}{\sqrt{\epsilon}}$, $q \approx 1$ and $\Delta = 1$, the modified system (7.17) admits an unstable manifold $\tilde{W}_\epsilon^\infty$ emanating from the curve $\mathcal{C}$.

The term $f_2^0(x,\phi) - \partial_x f_1^0(x,\phi)$ measures the rate of stretching normal to the slow manifold $\mathcal{S}$. The term $|p'(\phi)|$ is the speed at which $p(\phi)$ varies in the slow time scale. The fourth condition in (7.19) therefore requires that the rate of normal stretching along $p(\phi)$ should be larger than the speed of the leading-order spike location $p(\phi)$.

Since system (7.17) coincides with (7.12) for $z \geq z^*$, we obtain that a locally invariant subset of $\mathcal{W}^\infty$ also exists in system (7.12) in the form

$$\mathcal{W}_\epsilon^g = \mathcal{W}_\epsilon^\infty \bigcap \{\ (x,y,t)\ |\ y \geq y^*,\ t \leq t_0\}, \tag{7.20}$$

in the extended phase space (x, y, t) for the original system (7.3), where

$$y^* = \epsilon z^* = \sqrt{\epsilon}.$$

and $\mathcal{W}_\epsilon^\infty$ is the rescaled version of $\tilde{\mathcal{W}}_\epsilon^\infty$.

The locally invariant manifold $\mathcal{W}_\epsilon^g$ is the ghost manifold we sketched in Fig. 7-3. Its existence is guaranteed as long as conditions (7.19) hold on all available velocity data up to a present time t_0. If only finite-time velocity information is available up to t_0, the present construction of $\mathcal{W}_\epsilon^g$ can be combined with the finite-time invariant manifold approach used in [37].

As we show in Appendix C.3, second-order averaging can be used to obtain an approximation for the slope of $\mathcal{W}_\epsilon^\infty$ along $\mathcal{C}$. The resulting slope $s(\phi)$ of $\mathcal{W}_\epsilon^\infty$ relative to the normal $\mathbf{n}$ of $\mathcal{S}$ satisfies

$$s(\phi) = \frac{F^0(p(\phi), \phi)}{f_2^0(p(\phi), \phi) - \partial_x f_1^0(p(\phi), \phi)}, \tag{7.21}$$

for each $\phi \in \mathcal{I}$, where

$$\begin{aligned} F(x, \phi, t; t_0) &= g_1(x, t) + f_1(x, \phi, t) \int_{t_0}^{t} [f_2(x, \phi, \tau) - f_2^0(x, \phi)] d\tau \\ &+ [\partial_x f_1(x, \phi, t) - f_2^0(x, \phi)] \int_{t_0}^{t} f_1(x, \phi, \tau) d\tau. \end{aligned} \tag{7.22}$$

Formula (7.21) can be used to approximate the slope of $\mathcal{W}^g$ as well for small enough ϵ.

7.3.3 Dynamic averaging using wavelets

The application of Theorem 1 in section 7.3.2 requires the mean component $\mathbf{f}^0(\mathbf{x}, \epsilon t)$ of $\mathbf{f}(\mathbf{x}, \epsilon t, t)$ to be available. In applications, this time-varying mean component is not readily available and hence must be identified numerically. We denote the operation of extracting the mean of $\mathbf{f}(\mathbf{x}, \phi, t)$ by $\langle \cdot \rangle$, so that

$$\langle \mathbf{f} \rangle (\mathbf{x}, \phi) = \mathbf{f}^0(\mathbf{x}, \phi) = \langle \mathbf{f}(\mathbf{x}, \phi, t) \rangle. \tag{7.23}$$

Since we are concerned with extraction of the temporal mean, here we shall suppress the dependence of $\mathbf{f}$ on spatial variables.

The simplest approach to finding it would be finite-time averaging ([65]). In this approach, the mean operator is defined as

$$\langle f \rangle (\phi_0) = \frac{1}{2T_m(t_0)} \int_{t_0 - T_m(t_0)}^{t_0 + T_m(t_0)} f(\tau) d\tau,$$

where $T_m(t_0)$ is an appropriate time scale depending on the current time t_0 and $\phi_0 = \epsilon t_0$. There is no obvious choice for the averaging interval $T_m(t_0)$: one typically argues that $T_m(t_0)$ should be large in comparison with the characteristic periods of the fluctuating quantity $\tilde{\mathbf{f}}$, but small in comparison with the periods of the evolving mean $\langle \mathbf{f} \rangle$ in vicinity of the current time t_0. The result of this type of mean extraction will strongly depend on the choice of $T_m(t_0)$.

More powerful mean extraction methods have been developed for the purpose of signal processing. From a signal processing perspective, extraction of the mean of $\mathbf{f}$ is just the classical problem of *denoising*. Denoising seeks to provide a good approximation for signal from its noisy measurements. In our context, the noise is the high-frequency oscillatory component $\tilde{\mathbf{f}}(\mathbf{x}, \phi, t)$ with the signal of interest being $\mathbf{f}^0(\mathbf{x}, \phi)$.

One of the basic approaches to denoising is the generalized Fourier series technique. In such an analysis, the underlying function is expanded into an orthogonal series with the corresponding generalized Fourier coefficients estimated from the noisy data. By shrinking or truncating these coefficients and taking an inverse Fourier transform, a smoothed approximation to the underlying function is obtained.

For non-local basis functions (such as trigonometric functions), however, shrinking the Fourier coefficients will also affect the global shape of the reconstructed function and hence introduce unwanted artifacts. Therefore, classical Fourier-based techniques will have serious limitations for non-stationary and inhomogeneous signals [29] arising in applications such as turbulent fluid flows.

By contrast, wavelet-based smoothing methods provide a natural and flexible approach to the estimation of the true function from their noisy versions due to their ability to respond to local variations without allowing pathological behavior (see, e.g., [62], [17],[48]). We, therefore, propose wavelet-based denoising as an effective means to implement the averaging operator (7.23) numerically.

A brief review of wavelet analysis and wavelet based denosing can be found in section C.4 of Appendix C. We also refer the reader to [29] and the references cited therein for a description of wavelets for applications to fluid mechanics. In the numerical examples considered in section 7.4.3, we shall use Matlab's Wavelet Toolbox and its standard built-in denoising functions to carry out the averaging operation (7.23).

7.4 Moving separation in 2D

7.4.1 Physical set-up

In this section we discuss the application of Theorem 1 to moving flow separation or flow attachment on a no-slip boundary of a two dimensional unsteady fluid flow. Consider a 2D time-dependent velocity field $\mathbf{v}(\mathbf{x}, t) = (u(\mathbf{x}, t), v(\mathbf{x}, t))$ describing a fluid flow on a two-dimensional spatial domain parameterized by the coordinates $\mathbf{x} = (x, y)$. Assume that $\mathbf{v}$ and its derivatives are uniformly bounded in the vicinity of a no-slip boundary at $y = 0$, on which $\mathbf{v}$ satisfies

$$\mathbf{v}(x, 0, t) \equiv 0$$

for all times. We also assume that the flow satisfies the continuity equation

$$\rho_t + \nabla \cdot (\rho \mathbf{v}) = 0, \tag{7.24}$$

where $\rho\,(\mathbf{x}, t)$ denotes the fluid density. More general curved boundaries can also be treated as described in section 7.1.

The moving material spikes in such flows cannot be generated by classical unstable manifolds, since any unstable manifold would necessarily be tied to fixed points on the boundary We now discuss how ghost manifolds can be used to locate moving unsteady separation and attachment.

We start by assuming the presence of a slowly-varying mean component in the velocity field, which enable us to write the equation of particle motions as

$$\dot{\mathbf{x}} = \mathbf{v}(\mathbf{x}, \epsilon t, t) = (u(\mathbf{x}, \epsilon t, t), v(\mathbf{x}, \epsilon t, t)), \tag{7.25}$$

where $0 < \epsilon \ll 1$. We introduce the change of variables

$$y = \epsilon z e^{\int_{t_0}^{t} v_y(x,0,\epsilon\tau,\tau)\ d\tau}, \tag{7.26}$$

which transforms the particle motion (7.25) to the form (7.8) (cf. Kilic et al. [52] for details) with

$$\mathbf{f}(\mathbf{x}, \epsilon t, t) = \begin{pmatrix} zA(x, 0, \epsilon t, t) \\ z^2 C(x, 0, \epsilon t, t) \end{pmatrix}, \qquad \mathbf{g}(\mathbf{x}, \epsilon t, t; \epsilon) = \begin{pmatrix} z^2[A_y(x, 0, \epsilon t, t) + \mathcal{O}(z\epsilon)] \\ z^3[C_y(x, 0, \epsilon t, t) + \mathcal{O}(z\epsilon)] \end{pmatrix}, \tag{7.27}$$

and

$$\begin{aligned} A(x, z, \epsilon t, t) &= e^{\int_{t_0}^{t} v_y(x,0,\epsilon\tau,\tau) d\tau} u_y(x, z e^{\int_{t_0}^{t} v_y(x,0,\epsilon\tau,\tau) d\tau}, \epsilon t, t), \\ C(x, z, \epsilon t, t) &= \frac{1}{2} e^{\int_{t_0}^{t} v_y(x,0,\epsilon\tau,\tau) d\tau} v_{yy}(x, 0, \epsilon t, t) + O(z). \end{aligned} \tag{7.28}$$

We note that the conservation of mass condition (7.24) is crucial in obtaining the locally incompressible normal form (7.27).

We assume that $\mathbf{f}$ admits a decomposition

$$\mathbf{f}(\mathbf{x}, \phi, t) = \langle \mathbf{f} \rangle\,(\mathbf{x}, \phi) + \tilde{\mathbf{f}}(\mathbf{x}, \phi, t),$$

in the vicinity of the $z = 0$ boundary, where we have used the operator notation introduced in section 7.3.3. The fluctuating part of $\mathbf{f}$ is assumed to satisfy

$$\lim_{T \to \infty} \frac{1}{T} \int_{t_0}^{t_0 - T} \tilde{\mathbf{f}}(\mathbf{x}, \phi, \tau)\ d\tau = 0.$$

The above assumptions put us in the general framework considered in section 7.3.2. In the present context, a moving point $\mathbf{p}\,(\epsilon t)$ satisfying conditions (7.16) marks locations of zero shear for the mean component of $\mathbf{v}$. This is therefore the location of separation one would obtain by applying Prandtl's steady condition to the mean component of an unsteady flow at each time instant. This is to be contrasted with the widespread practice in the separation literature to apply Prandtl's condition instantaneously to the full velocity field $\mathbf{v}$. We shall see in examples how the latter procedure fails to identify the location of material spike formation correctly.

Theorem 1 asserts that applying Prandtl's criterion to the mean flow is correct as long as the motion of the Prandtl point $\mathbf{p}(\epsilon t)$ obtained in this fashion is not too fast (cf. last condition in (7.19)). In that case, there exists a ghost manifold $\mathcal{W}_\epsilon^g$ near the Prandtl point, generating a spike that co-moves with $\mathbf{p}(\epsilon t)$ near the no-slip boundary $y = 0$. In the extended phase space of the (x, y, ϕ) variables, for each $\phi \in \mathcal{I}$, we let

$$\mathcal{W}_\epsilon^g(t) = \mathcal{W}_\epsilon^g \bigcap \{(x, y, \phi) \mid \phi = \epsilon t,\ t \in (-\infty, t_0)\}, \tag{7.29}$$

be the intersection of $\mathcal{W}_\epsilon^g$ with the $\phi = const.$ plane. In the physical space (x, y), $\mathcal{W}_\epsilon^g(t)$ is then an attracting material line that attracts and ejects particles from the vicinity of the $y = 0$ boundary without having a point of attachment to that boundary. $\mathcal{W}_\epsilon^g(t)$ is therefore the center of a moving spike that can be predicted from its on-wall signature $\mathbf{p}(\epsilon t)$.

7.4.2 2D Moving separation and attachment criteria

We are now spell out the moving separation and attachment criteria that are obtained by applying Theorem 1 to a mass-conserving time-dependent velocity field satisfying the assumptions of section 7.4.1

Theorem 2 *Up to time t_0, moving separation due to a ghost manifold exists near the point $\mathbf{p}(\epsilon t) = (p(\epsilon t), 0)$ if for all $\phi \in \mathcal{I} = (-\infty, \epsilon t_0]$,*

$$\langle A \rangle (p(\phi), 0, \phi) = 0, \tag{7.30}$$

$$\sup_{\phi \in \mathcal{I}} \langle A_x \rangle (p(\phi), 0, \phi) < 0, \tag{7.31}$$

$$\inf_{\phi \in \mathcal{I}} \langle C \rangle (p(\phi), 0, \phi) > 0, \tag{7.32}$$

$$\inf_{\phi \in \mathcal{I}} \left[\langle C \rangle (p(\phi), 0, \phi) - \langle A_x \rangle (p(\phi), 0, \phi) - \epsilon |p'(\phi)| \right] > 0. \tag{7.33}$$

The last condition (7.33) in the above theorem is the only one that cannot be anticipated from an instantaneous application of Prandtl's steady result. This last condition states that for moving separation to occur near $\mathbf{p}(\epsilon t)$, particles should be ejected at a rate faster than the speed at which the separation point moves. A directly computable form of this condition can be obtained by differentiating (7.30) with respect to ϕ, which gives

$$p'(\phi) \langle A_x \rangle (p(\phi), 0, \phi) + \langle A_\phi \rangle (p(\phi), 0, \phi) = 0,$$

or, by (7.31),

$$p'(\phi) = -\frac{\langle A_\phi \rangle (p(\phi), 0, \phi)}{\langle A_x \rangle (p(\phi), 0, \phi)}.$$

This enables us to rewrite (7.33) as

$$\inf_{\phi\in\mathcal{I}} \left[\langle C\rangle (p(\phi),0,\phi) - \langle A_x\rangle (p(\phi),0,\phi) - \epsilon \left| \frac{\langle A_\phi\rangle (p(\phi),0,\phi)}{\langle A_x\rangle (p(\phi),0,\phi)} \right| \right] > 0.$$

From the formula (7.21), we conclude that the slope $s(t_0)$ of moving separation profile $\mathcal{W}_\epsilon^g(t_0)$ at t_0 is approximately given by

$$s(t_0) = \frac{\langle F\rangle (p(\epsilon t_0),0,\epsilon t_0)}{\langle C\rangle (p(\epsilon t_0),0,\epsilon t_0) - \langle A_x\rangle (p(\epsilon t_0),0,\epsilon t_0)}, \tag{7.34}$$

where

$$\begin{aligned} F(\mathbf{x},\phi,t;t_0) &= \frac{1}{2} e^{2\int_{t_0}^t v_y(x,0,\phi,\tau)d\tau} u_{yy}(\mathbf{x},\phi,t) + A(\mathbf{x},\phi,t)\int_{t_0}^t [C(\mathbf{x},\phi,\tau) - \langle C\rangle (\mathbf{x},\phi)]d\tau \\ &+ [A_x(\mathbf{x},\phi,t) - \langle C\rangle (\mathbf{x},\phi)] \int_{t_0}^t A(\mathbf{x},\phi,\tau)d\tau. \end{aligned} \tag{7.35}$$

Applying Theorem 1 in backward time, we obtain the following attachment criterion for moving attachment in unsteady flows satisfying the assumptions of section 7.4.1.

Theorem 3 *Starting from time* t_0*, moving attachment due to a ghost manifold exists near the point* $\mathbf{p}(\epsilon t) = (p(\epsilon t), 0)$ *if for all* $\phi \in \mathcal{I} = [\epsilon t_0, +\infty)$*,*

$$\begin{aligned} \langle A\rangle (p(\phi),0,\phi) &= 0, \\ \inf_{\phi\in\mathcal{I}} \langle A_x\rangle (p(\phi),0,\phi) &> 0, \\ \sup_{\phi\in\mathcal{I}} \langle C\rangle (p(\phi),0,\phi) &< 0, \\ \sup_{\phi\in\mathcal{I}} \left[\langle C\rangle (p(\phi),0,\phi) - \langle A_x\rangle (p(\phi),0,\phi) - \epsilon \left| \frac{\langle A_\phi\rangle (p(\phi),0,\phi)}{\langle A_x\rangle (p(\phi),0,\phi)} \right| \right] &< 0. \end{aligned}$$

The slope of moving attachment profile relative to the normal of the wall again satisfies formula (7.21). Note that to identify moving attachment, Theorem 3 requires the knowledge of future velocity data, which is typically not available.

7.4.3 Analytical and Numerical examples

In this section we analyze moving separation in analytical flow fields which model turbulent flows and flows over moving boundaries.

7.4.4 Separation bubble flow

In this section we revisit the unsteady bubble flow studied previously in the context of fixed unsteady flow separation in [39] and [52]. The general incompressible velocity field for the bubble model is given by

$$\begin{aligned} u(x,y,t) &= -y + 3y^2 + x^2y - \frac{2}{3}y^3 + \beta xyF(t), \\ v(x,y,t) &= -xy^2 - \frac{1}{2}\beta y^2 F(t), \end{aligned} \tag{7.36}$$

where $F(t)$ is any continuous function of time. Depending on the choice of $F(t)$, we can generate periodic, quasi-periodic or aperiodic time dependence for the velocity field.

In order to generate a flow with a time scale dichotomy, we take $F(t) = G(\phi) + H(\phi,t)$, where $H(\phi,t)$ satisfies

$$\lim_{T\to\infty} \frac{1}{T} \int_{t_0-T}^{t_0} H(\phi,t)dt = 0.$$

For a numerical demonstration of our main results, we consider two cases:

$$G(\phi) = a\sin(\phi), \qquad G(\phi) = a\log(\phi + b).$$

In both cases, we select

$$H(t) = (c + d\sin(\phi))r(t),$$

where $r(t)$ is a zero mean random variable with a normal distribution and unit variance. Such a time dependence models separation bubble with a well-defined slow mean growth, onto which substantial random oscillations are superimposed.

The velocity field (7.36) satisfies the hypothesis of section 7.1 and can be decomposed as

$$\mathbf{v}(\mathbf{x},t) = \mathbf{v}^0(\mathbf{x},\phi) + \tilde{\mathbf{v}}(\mathbf{x},\phi,t),$$

with the components

$$\mathbf{v}^0(\mathbf{x},\phi) = \begin{pmatrix} -y + 3y^2 + x^2y - \frac{2}{3}y^3 + \beta xyG(\phi) \\ -xy^2 - \frac{1}{2}\beta y^2 G(\phi) \end{pmatrix}, \qquad \tilde{\mathbf{v}}(\mathbf{x},\phi,t) = H(\phi,t)\begin{pmatrix} \beta xy \\ -\frac{1}{2}\beta y^2 \end{pmatrix}. \tag{7.37}$$

With A defined in (7.28), the mean $\langle A \rangle$ can be identified analytically as

$$\langle A \rangle (x,0,\phi) = x^2 + \beta x G(\phi) - 1.$$

Hence, the only candidate for a moving separation point is (cf. (7.30)-(7.32))

$$p(\phi) = -\frac{\beta G(\phi)}{2} - \sqrt{\frac{(\beta G(\phi))^2}{4} + 1}, \tag{7.38}$$

where

$$\langle A_x \rangle (p(\phi),0,\phi) = -\langle C \rangle (p(\phi),0,\phi) = -\sqrt{(\beta G(\phi))^2 + 4} \leq -2 < 0.$$

Furthermore, condition (7.33) takes the form

$$\begin{aligned} &\langle C\rangle\left(p(\phi),0,\phi\right)-\langle A_x\rangle\left(p(\phi),0,\phi\right)-\epsilon\left|\frac{\langle A_\phi\rangle\left(p(\phi),0,\phi\right)}{\langle A_x\rangle\left(p(\phi),0,\phi\right)}\right| \\ =\;& 3\sqrt{\frac{(\beta G(\phi))^2}{4}+1}-\epsilon\beta\left|\frac{G'(\phi)}{2}+\frac{\beta G(\phi)G'(\phi)}{\sqrt{\frac{(\beta G(\phi))^2}{4}+1}}\right|>0, \end{aligned}$$

which is satisfied for the parameters we have chosen.

The slope formula (7.34) takes the concrete form

$$s(\phi)=\frac{\langle F\rangle(\phi)}{3\sqrt{(\beta G(\phi))^2+4)}}, \tag{7.39}$$

where

$$F(t,\phi;t_0)=6+3\beta p(\phi)\left[2p(\phi)+\beta G(\phi)\right]\left[\int_{t_0}^{t}H(\phi,\tau)d\tau+\beta^2p(\phi)H(t)\int_{t_0}^{t}H(\phi,\tau)d\tau\right],$$

One has to numerically extract the slowly evolving mean of $F(t,\phi;t_0)$ at t_0, regarding it as a function of t and ϕ.

We computed the separation location function $p(\phi)$ identified (7.38), and drew a line of slope (7.39) relative to the wall normal at each point of the curve $p(\phi)$. The resulting line bundle is the green surface in Fig. 7-4 that shows numerically simulated spike formation in the extended phase space of the (x,y,ϕ) variables. Also shown are some past (black) and many current (red) positions of fluid particles launched closed to the $y=0$ no-slip wall.

We recall that the green surface is a visualization of W_ϵ^∞, the unstable manifold of an auxiliary adiabatic system we used in the proof of Theorem 1. Therefore, only an off-wall portion of W_ϵ^∞ will act as a ghost manifold that governs material spike formation. Indeed, it is evident from Fig. 7-4 that particles close to the boundary (shown in black) *intersect* W_ϵ^∞ transversely, and hence W_ϵ^∞ does not act as a locally invariant manifold in the immediate vicinity of the wall. Consequently, particles do not separate from the boundary along W_ϵ^∞ but are attracted to the upper portion of W_ϵ^∞. This upper portion is what we have referred to as the *ghost manifold* $\mathcal{W}_\epsilon^g$. The ghost manifold gives an accurate prediction for the location of the red spike, which changes as the slow phase variable $\phi=\epsilon t$ evolves in time.

Figure 7-5 shows the particle paths in the physical space (x,y) along with moving separation location and the linear approximation of the separation profile. Also shown in these plots as yellow circles are the instantaneous wall-shear zeros, which are often considered as separation locations in the aerodynamics literature. As Figure 7-5 shows, this practice is unjustified.

The second case we consider here is that of $G(\phi)=a\log(\phi+b)$, with $c\neq 0$ so that the $\tilde{\mathbf{v}}$ depends on the slow time scale as well. The snapshots of the particle separation are shown in the Fig. 7-6. Again, the ghost manifold we compute correctly predicts

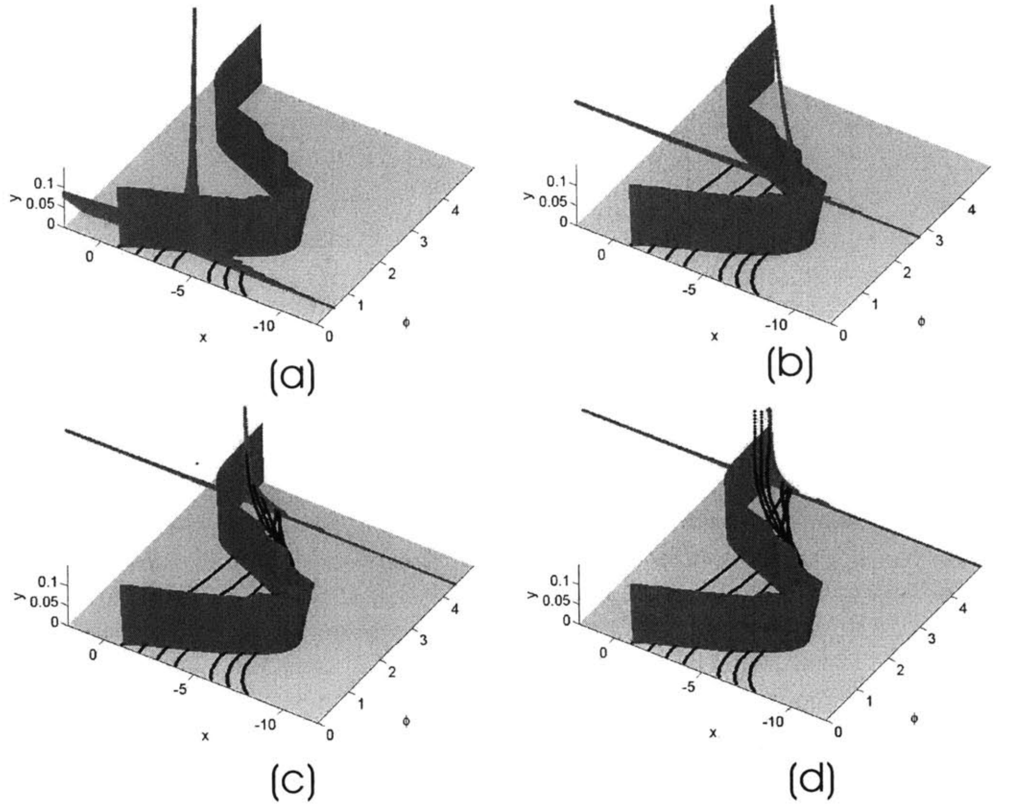

Figure 7-4: Separation geometry in the extended phase space (x, y, ϕ) associated with the separation bubble flow for the case $G(\phi) = a\sin(\phi t)$ and $H(\phi, t) = [c + d\sin(\epsilon t)]\, r(t)$ with $a = 2$, $c = 2$, $d = 0$, $\epsilon = 0.1$, $\beta = 4$. The subplots (a)-(d) correspond to the time instants $t = 5.50$, $t = 22.00$, $t = 38.50$, and $t = 44.00$.

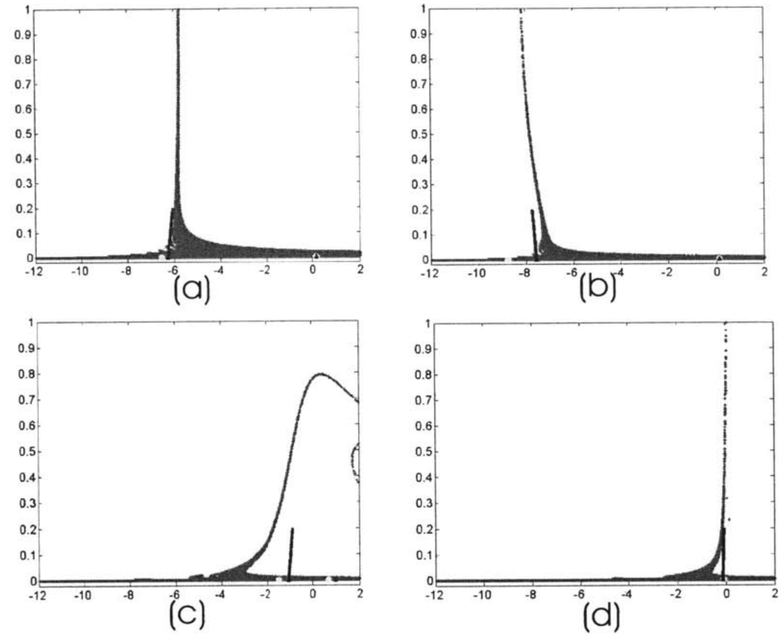

Figure 7-5: The blue triangles show moving separation and reattachment locations obtained from Theorem 2, while the yellow circles are the instantaneous wall-shear zeros. Also shown at the moving separation point is the linear approximation of the separation profile obtained from our slope formula. The subplots (a)-(d) correspond to times $t = 11.00$, $t = 21.80$, $t = 32.60$, and $t = 43.40$. The parameter values are the same as for the previous figure.

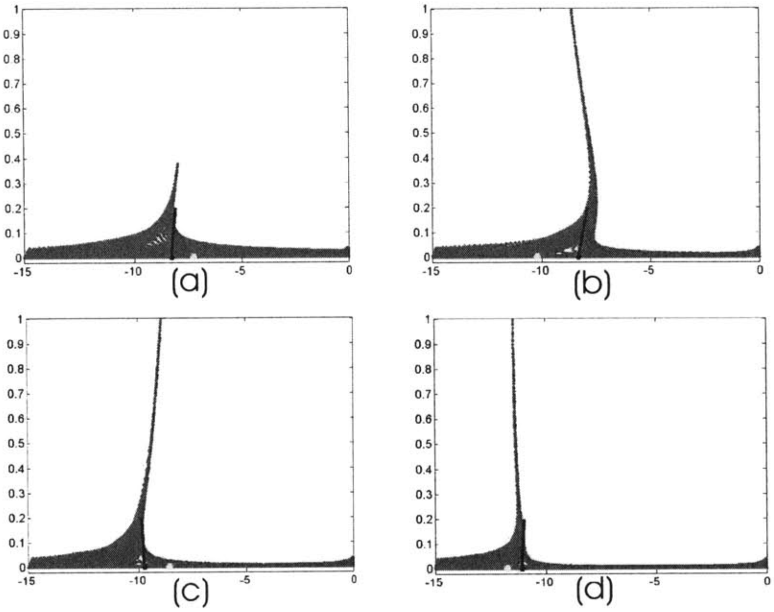

Figure 7-6: Same as Fig. 7-5, but for the case $G(t) = a\log(\epsilon t + b)$ and $H(\phi, t) = [c + d\sin(\epsilon t)]\, r(t)$ with $a = 1.5$, $b = 3$, $c = 2.25$, $d = 1.5$, $\epsilon = 0.1$, $\beta = 4$. The subplots (a)-(d) correspond to the times $t = 3.60$, $t = 21.60$, $t = 27.00$, and $t = 37.80$.

the location and orientation of the spike.

Separation over moving boundaries

Flows over moving wall is a paradigm for moving separation. In the context of steady flows over moving boundaries, it was realized for the first time independently by Moore, Rott and Sears that vanishing wall-shear and reversed flow are not necessarily a meaningful criteria for flow separation. Subsequently, Sear & Telinois [79] postulated a *MRS* model of unsteady separation, in which separation was defined as the instant when a singularity evolves in the solution of boundary-layer equations. In physical terms, this breakdown of the boundary layer solution indicates the first instant when a thin and passive shear layer adjacent to the wall starts to interact with the external flow and thereby separate from the surface.

As discussed by Sears & Telionis [79], the evolution of singularity in boundary layer solution $Re \to \infty$ delineates a definite time and location where the boundary layer separates from the surface and consequently an important tool for diagnostic tool for unsteady flows at finite Re. The authors further argued that separation would generally occur at a stream-wise location x_s, somewhere in the middle of the boundary layer where two MRS conditions are satisfied, namely i) *MRS I* - the stream-wise velocity vanishes in a frame of reference moving with the separation and (ii) *MRS II*- the vorticity $\omega = -\partial_y u$ vanishes at $x = x_s$.

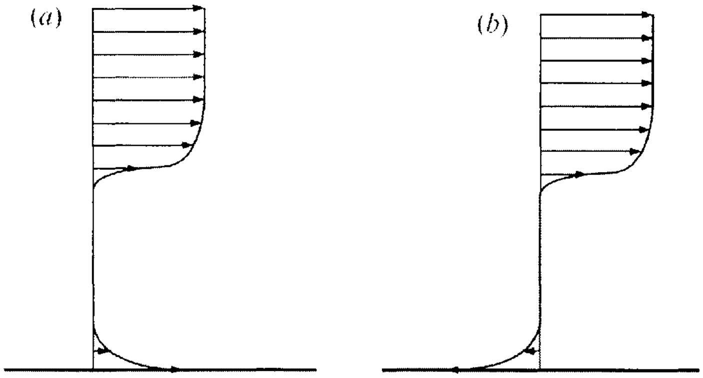

Figure 7-7: Velocity profile in frame comoving with separation point. a) Upstream-slipping separation b) Downstream-slipping separation, taken from [19]

Sears & Telionis [79] also identified two possible situations for which the streamwise velocity profiles as sketched in figure 7-7. In both cases the external mainstream flow is from left to right and the velocity profile at separation is sketched in a frame of reference of the moving separation point. Each case is described in terms of the relative motion of the separation singularity relative to the wall; in this nomenclature the situations in figures 7-7a) and b) are respectively referred to as *upstream-slipping* and *downstream-slipping* separation respectively. They also proposed an associated streamline patterns with saddle type singularity for both upstream and downstream slipping separation, which will discussed in next section.

There have been many studies to verify and refine MRS criteria. Most notable has been the work of Van Dommelen and coworkers [14]. As discussed by Van Dommelen, *MRS I* is less useful in establishing the location of separation since the speed of the separation structure is not know *a priori*; moreover it is essentially impossible to evaluate u_s in a conventional Eulerian formulation. To circumvent this problem, Van-Dommelen and Van-Dommelen & Shen recast the boundary layer equation in a Lagrangian coordinate system. In these coordinates the boundary layer momentum equation decouple from the continuity equation. Then by imposing the condition that the fluid-stretching in the wall-normal direction becomes infinitely large at the point of separation, Van-Dommelen obtained precise conditions for the singularity to develop in the unsteady boundary layer equations.

Van-Dommelen & Shen also carried out numerical simulation in the Lagrangian formulation for the boundary layer on an impulsively started cylinder. They established a separation singularity and found that the MRS conditions are satisfied at the separation point, which was determined to be of the upstream-slipping type. Furthermore it was established that the analytical structure of this type of singularity is substantially different from *Goldstein singularity* (type of separation singularity associated with steady boundary layer equations), as was conjectured previously by Sears & Telinois [79]. This singularity is now known as *Van-Dommelen* singularity.

Another interesting question to investigate is how the speed of the moving surface affects separation. For this, two model problems have been widely studied: the unsteady boundary layer developing on 1) an impulsively started rotating circular cylinder and 2) an infinite plane wall, induced by a vortex convected in a uniform flow above the surface. In first case the wall moves in the lab frame while in the latter case, the wall moves in a frame of reference fixed to the vortex. We would restrict our discussion to the cylinder problem, for the vortex problem the reader is referred to [22], [71]. The problem of a cylinder rotating in a uniform stream has been of historical interest since the wall moves in the direction of the external flow as well as counter to it on various portions of the cylinder. For a given *Re* number, it represents a family of problem involving a single parameter $q = \frac{r\Omega}{U}$, where r is the radius of cylinder, Ω is angular speed of cylinder and U is the free-stream velocity.

The case of very large rotation speed was first considered by Glauret [32] and Moore [66], who assumed that q is large enough so that separation is completely suppressed and found a steady-state solution describing an attached flow confined to thin ring ensheathing the rapidly rotating cylinder. Ece et. al. [27] used Eulerian coordinates to study the initial development of boundary layer on an impulsively started rotating cylinder for $0.05 \leq q \leq 10$. They were able to infer that unsteady separation is inhibited with increasing wall speed and noted the evolution of streamline patterns similar to those proposed by Sears and Telinois near the *MRS* point for both upstream- and downstream moving walls. Similar streamlines patterns have also been noticed in the flow visualization studies of Koromilas & Telinios [55] at a free-stream Reynolds number of 50. For $q \leq 2$ Shen & Wu [83] used Lagrangian coordinates and found a sharp eruptive response in the fourth quadrant in all cases ($q = 0.2, 1, 1.5$). It was determined that separation is delayed with increasing wall speed and is of the upstream-slipping type. For the range of rotation speed considered no downstream-slipping separation was observed.

A detailed study for both the model problems has been recently carried out by [19], to address two issues which were not clarified earlier: the minimum wall speed necessary to completely inhibit boundary-layer separation and to understand the changes in unsteady flow topology that occur with increasing wall speed. Even though the two problems have significantly different physical origins, it was found that the separation is eventually suppressed at a critical value of q, (which we shall denote by q_c) in a manner which emerges to be essentially the same.

For the rotating cylinder case q was varied in the range $1.5-2$. From the numerical study following conclusion were drawn

1. The time of unsteady separation t_s is delayed and the location of the unsteady separation x_s approaches the invicid stagnation point in the region of adverse pressure gradient as the surface speed increases. Both t_s and x_s appear to vary approximately linearly with surface speed q as a critical speed q_c is approached, whereupon separation is suppressed.

2. For both the model problems, a recirculation region develops in the flow at lower values of q. Subsequently, the unsteady separation singularity occurs just upstream of the recirculating region. At higher surface speeds, no recirculation is observed, but weak jet-like outflow pattern develops prior to the occurrence

of a considerably weakened separation singularity. The streamline pattern suggested by Sears & Telinois [79] and Koromilas & Telinois [55] as characterizing downstream-slipping separation was observed in the cylinder problem; however the results show that this flow pattern is not associated with unsteady separation. The separation singularity was always found to be confined to the bottom of the cylinder (in the fourth quadrant) where the mainstream flow is in same sense as the surface motion direction.

3. The magnitude of $U_e(x_s) - u_s$ which can be interpreted as the strength of separation, decreases with increasing surface speed, and the calculations indicated that the unsteady separation is suppressed at the critical value of surface speed where the magnitude of $U_e(x_s) - u_s$ becomes zero. For rotating cylinder $q_c = 1.91$, while for convective vortex problem the estimate of q_c was found to be 2.77.

4. In both the problems for all values of q less than q_c, the separation velocity profile corresponds to the upstream-slipping type; no evidence of downstream-slipping separation was found.

In order to evaluate above arguments, we consider an analytic model of a two-dimensional flow with a flat horizontal boundary that moves horizontally at speed U. Using the Perry-Chong procedure [72], we have derived a polynomial velocity field that is the solution of the Navier-Stokes equation up to fifth order in the distance from the moving wall. The velocity field is of the form

$$\begin{aligned} u(x,y,t) &= U + \alpha(t)y + y^2 + \beta(t)x^2y + \gamma(t)xy^2 - \frac{1}{3}\beta(t)y^3 + 15y^4 \\ &- x^3y^2 + \frac{1}{2}\left[\frac{1}{6}\alpha(t)\beta(t) + 1\right]xy^4 + \frac{1}{30}\alpha(t)\gamma(t)y^5, \\ v(x,y,t) &= -xy^2\beta(t) - \frac{1}{3}\gamma(t)y^3 + x^2y^3 - \frac{1}{10}\left[\frac{1}{6}\alpha(t)\beta(t) + 1\right]y^5, \end{aligned} \tag{7.40}$$

with U denoting the speed of the moving boundary at $y = 0$, and with the time-dependent parameters. $\alpha(t) < 0, \beta(t) > 0$ and $\gamma(t)$.

We first assume that the streamline patterns of the flow are constant, i.e., we fix the parameters $\alpha(t) = \alpha_0 < 0, \beta(t) = \beta_0 > 0$ and $\gamma(t) = \gamma_0$ in time. We show the relevant steady streamline geometries for upstream moving ($U < 0$) and downstream moving ($U > 0$) walls in Fig. 7-8a-c. Similar streamlines patterns were sketched by Sears and Tellionis [79], corresponding to upstream-slipping type and downstream-slipping separation. From these figures, it appears that particles separate from the boundary due to a saddle-type stagnation point in the interior of the flow, without any connection to on-wall flow quantities, as suggested by Sears and Tellionis. In order to analyze separation in the framework developed in this paper, we need to have a fixed boundary. To achieve this, we pass to a frame co-moving with the boundary by making the change of variables

$$\tilde{x} = x - Ut.$$

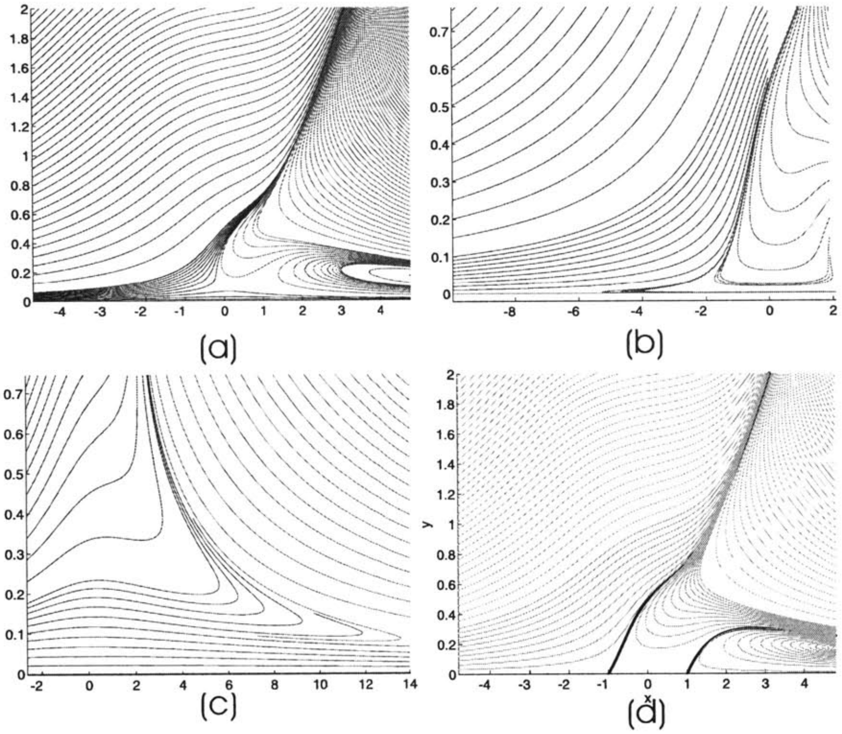

Figure 7-8: (a) Steady streamlines for downstream moving wall with $U = 0.1$, (b) Same for an upstream moving wall with $U = -0.1$ (c) Same for downstream moving wall $U = 3.1$ (d) Instantaneous streamline pattern at $t = 0$ in the frame comoving with the wall for $U = 0.1$. In all cases $\alpha_0 = -1, \beta_0 = 1$ and $\gamma_0 = -5$..

Dropping the tilde and introducing the phase variable $\phi = Ut$, we obtain an unsteady velocity field $\mathbf{v}_s$ in the co-moving frame with components

$$\begin{aligned} u_s(\mathbf{x},\phi) &= \alpha_0 y + y^2 + \beta_0 (x+\phi)^2 y + \gamma_0 (x+\phi) y^2 - \frac{1}{3}\beta_0 y^3 + 15y^4 \\ &- (x+\phi)^3 y^2 + \frac{1}{2}\left[\frac{1}{6}\alpha_0\beta_0 + 1\right](x+\phi)y^4 + \frac{1}{30}\alpha_0\gamma_0 y^5 \\ v_s(\mathbf{x},\phi) &= -(x+\phi)y^2\beta_0 - \frac{1}{3}\gamma_0 y^3 + (x+\phi)^2 y^3 - \frac{1}{10}\left[\frac{1}{6}\alpha_0\beta_0 + 1\right] y^5. \end{aligned} \tag{7.41}$$

Figure 7-8d shows the streamlines for the transformed velocity field $\mathbf{v}_s$ at $t = 0$. We observe two streamlines emanating from the wall: this means that the wall shear is zero in the moving frame at the points where these streamlines leave the wall. This suggests that contrary to the Sears-Tellionis argument, there may be on-wall signatures of moving separation near moving walls. This streamline pattern appears at $t = 0$ in the co-moving frame regardless of the wall-velocity U. For later times $t > 0$, this streamline pattern is of upstream-slipping type for a downstream moving wall ($U > 0$) and of downstream-slipping type for an upstream-moving wall ($U < 0$).

For the present flow, we have no fluctuation around the mean flow, and hence we have $\tilde{\mathbf{v}}_s(\mathbf{x},t) \equiv 0$ and $\mathbf{v}_s^0(\mathbf{x},\phi) \equiv \mathbf{v}_s(\mathbf{x},t)$, with U playing the role of ϵ. The zero wall shear point in the mean flow is given by

$$p(\phi) = -\delta - \phi, \qquad \delta = \sqrt{\frac{-\alpha_0}{\beta_0}}. \tag{7.42}$$

The conditions of Theorem 2 are satisfied whenever

$$\begin{aligned} \langle A_x \rangle (p(\phi),0,\phi) &= -2\beta_0\delta < 0, \\ \langle C \rangle (p(\phi),0,\phi) - \langle A_x \rangle (p(\phi),0,\phi) - \epsilon \left| \frac{\langle A_\phi \rangle (p(\phi),0,\phi)}{\langle A_x \rangle (p(\phi),0,\phi)} \right| &= 3\beta_0\delta - U > 0, \end{aligned}$$

which hold provided that

$$U < 3\beta_0\delta. \tag{7.43}$$

For $U < 0$ (upstream-moving wall), this last condition is always satisfied. Furthermore, by (7.34), the slope of the separation spike at any time t_0 is given by the constant value

$$s(t_0) = \frac{1 - \gamma_0\delta + \delta^3}{3\beta_0\delta}.$$

Figure 7-9 shows spike formation in the case of an upstream moving wall. Separation along the ghost manifold predicted by our theory is evident. The green streamline on the right generates attachment, as its endpoint satisfies the conditions of Theorem 3.

Figure 7-10 shows separating particle paths for a downstream-moving wall when the condition (7.43) is satisfied. In the case $U > 3\beta_0\delta$, Theorem 2 does not apply and hence we cannot predict whether or not $p(\phi)$ defined in (7.42) is a moving separation point.

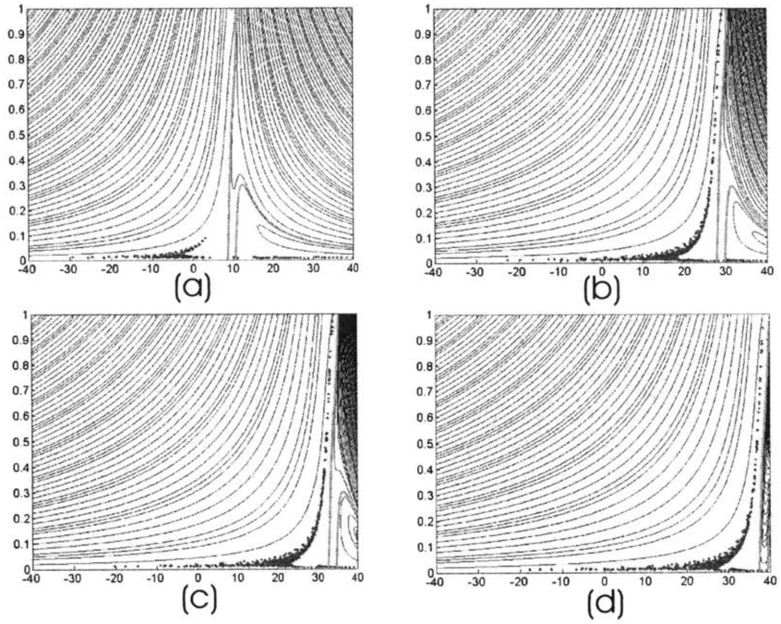

Figure 7-9: Upstream moving wall with $U = -3$, $\alpha_0 = -1$, $\beta_0 = 1$, $\gamma_0 = -5$, satisfying condition (7.43). For this flow the instantaneous wall shear zeros (computed in the frame moving with the wall) coincide with the moving separation and reattachment location. Also shown are the streamlines in blue and the separating and reattaching streamlines in green, along with their linear approximation in blue. The subplots (a)-(d) are taken at instants $t = 3.2$, $t = 6.4$, $t = 9.6$, and $t = 11.2$.

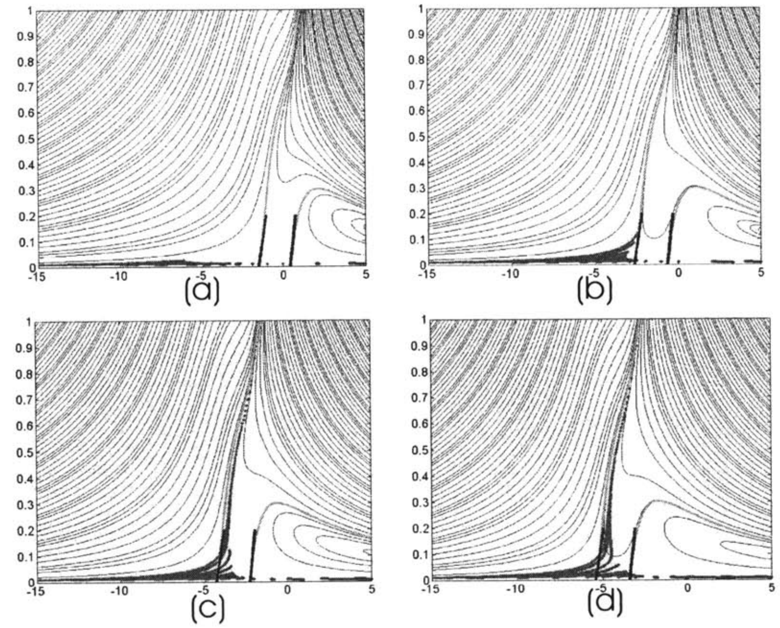

Figure 7-10: Downstream moving wall with $U = 0.1$, $\alpha_0 = -1$,$\beta_0 = 1$, $\gamma_0 = -5$,satisfying condition (7.43). For this flow, the instantaneous wall shear zeros coincide with the moving separation and reattachment location. Also shown are the streamlines in blue and the separating and reattaching streamlines in green, along with their linear approximation in blue.The subplots (a)-(d) correspond to $t = 5.50$,$t = 16.50$, $t = 33.00$, and $t = 44.00$.

Figure 7-11 shows the case of a fast-moving wall that violates (7.43). Note that particles do not separate from the vicinity of the wall despite the presence of instantaneous wall shear zeros at $p(\phi)$. Figure 7-8c shows the steady streamlines in the lab frame for this wall speed. A weak jet-like streamline pattern is evident in agreement with the findings of Degani [19], who found similar streamline patterns corresponding to separation inhibition.

For intermediate wall speeds satisfying condition (7.43), we observe a change in the scale of separation. Figure 7-12 shows small-scale separation for the wall speed $U = 1.2$. This underlines the fact that our separation criteria capture separation at all scales. While this universality is an advantage, it also a limitation: we cannot differentiate between local separation and large-scale boundary layer separation.

Flow past cylinder

In this section, we study separated flow past a stationary circular cylinder. There are two dimensionless parameters relevant to this flow, the Reynolds number $Re = 2U_m r/\nu$ and the Strouhal number $St = 2r/(U_m T)$, where r is the radius of cylinder,

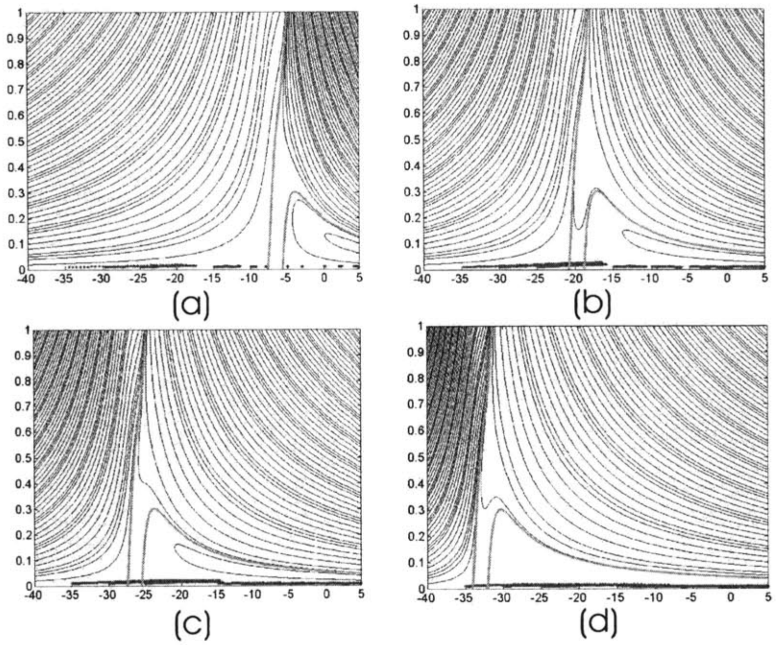

Figure 7-11: Same as figure 7-10, but with $U = 3.1$, so that the condition (7.43) is violated. The particles are released at same location as for the case of figure 7-10. As can be seen, though there is an initial upwelling, there is no pronounced separation. The subplots correspond to $t = 3.05$,$t = 9.15$,$t = 12.20$,$t = 15.25$.

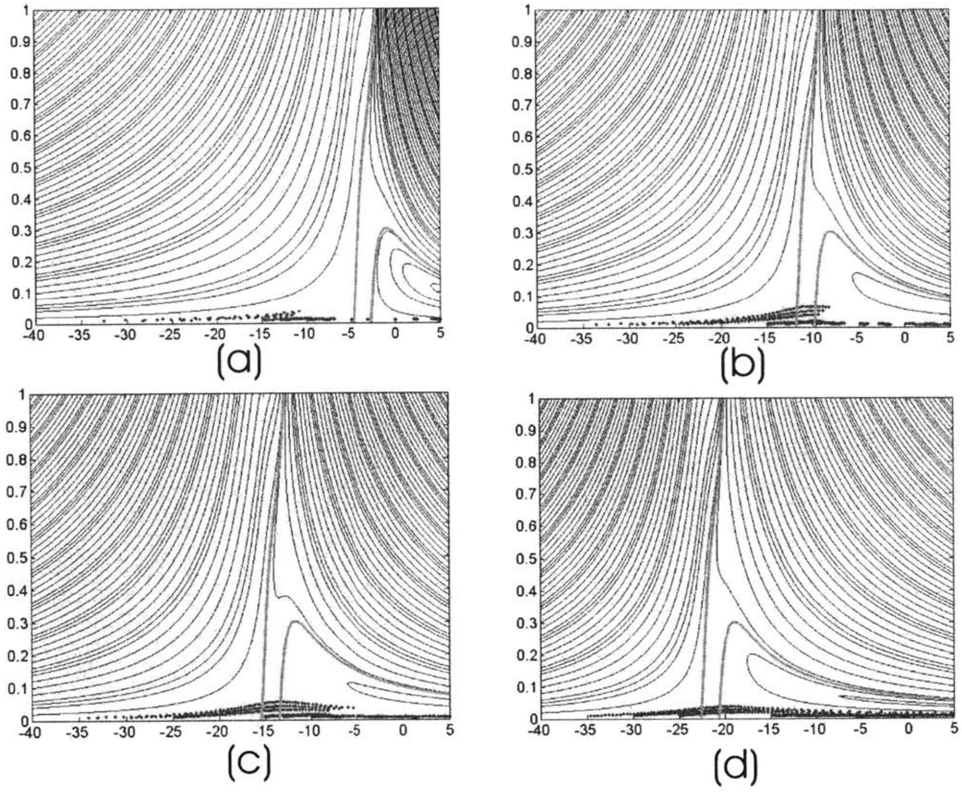

Figure 7-12: Same as figure 7-10, but with $U = 1.2$, for which condition (7.43) is satisfied. The particles are released from the same location as in the case of figure 7-10. While there is an upwelling suggesting small-scale separation, there is no pronounced spike formation. The subplots correspond to $t = 6$, $t = 9.0$, $t = 12.0$, and $t = 15.0$.

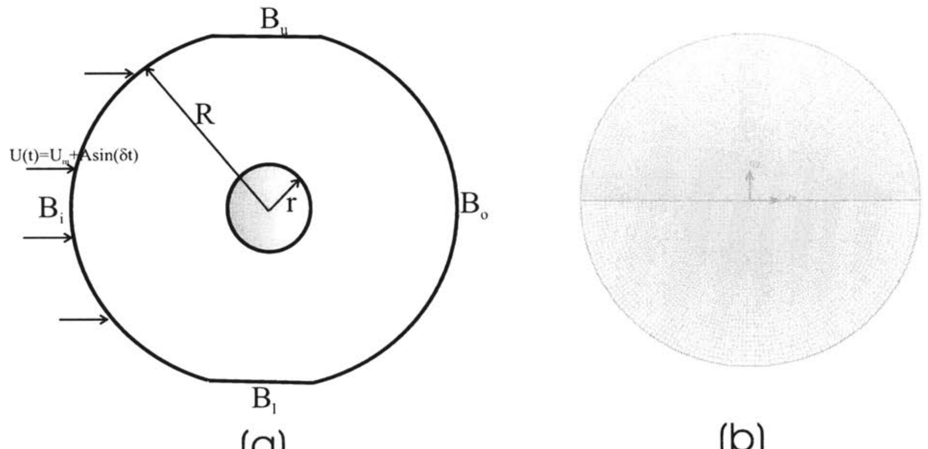

Figure 7-13: (a)Computational domain and (b) Mesh.

ν is the kinematic viscosity, U_m is the mean free stream velocity and T is the time period of von Kármán vortex shedding. The flow field inherits the periodicity of vortex shedding, which itself is a function of the Reynolds number. We introduce a slow time scale in the system by perturbing the free stream velocity U as

$$U(t) = U_m + A\sin(\epsilon t), \tag{7.44}$$

where ϵ is a small parameter such that $2\pi/\epsilon \gg T$.

We solve the two-dimensional unsteady Navier-Stokes equations

$$\begin{aligned} \partial_t \mathbf{u} + \mathbf{u}\cdot\nabla\mathbf{u} &= -\nabla p + \frac{1}{Re}\nabla^2\mathbf{u}, \\ \nabla\cdot\mathbf{u} &= 0, \end{aligned}$$

with p denoting the pressure. Figure 7-13 shows the computational domain and the reference frame, along with the O-type of mesh (generated by *GAMBIT*) used in our simulation. We use the spatial resolution recommended for this problem by [64]. The computational domain is partially bounded by two arcs of circle (B_i, B_o), one upstream of the cylinder and the other one downstream, both of same radius R. There are also two horizontal segments (B_u, B_l) connecting the arcs and containing sectors of 10° span. The inclusion of these segments defines the transition region between the inlet and outlet sections. For $R/(2r) > 75$, the solution is known to become independent of the location of the outer computational boundary ([64],[69]). For this reason we use $R/(2r) = 125$ in our simulation.

In the inflow section B_i, we use Dirichlet-type boundary condition with the free stream velocity given by (7.44). For the outflow boundary B_o, the diffusion flux in the direction normal to the exit surface is taken to be zero for all flow variables. On

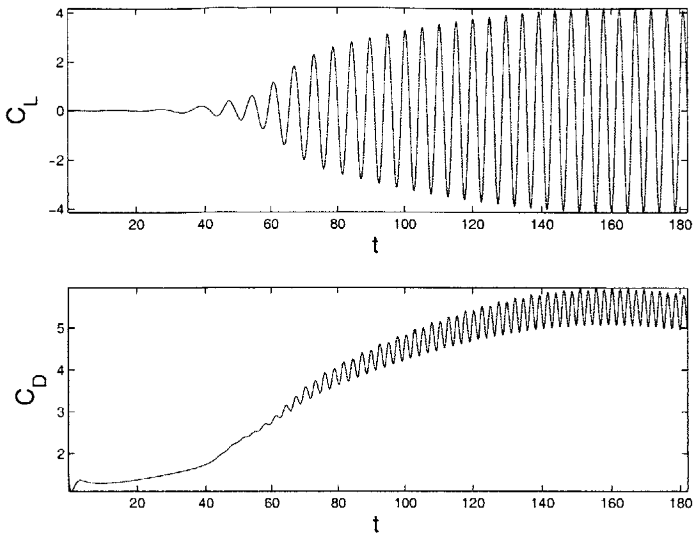

Figure 7-14: Time history of (a) Lift Coefficient (b) Drag coefficient

the horizontal segments B_u and B_l, zero normal velocity and zero normal gradient for all variables are prescribed. Finally, no-slip boundary condition is imposed on the cylinder. The initial condition for the computation is an impulsive start, i.e., at $t = 0$ the velocity field coincides with a potential flow past a stationary cylinder.

We used FLUENT to carry out the computation. The lift $C_L = L/\left(\frac{1}{2}\rho U^2 r\right)$ and drag $C_D = D/\left(\frac{1}{2}\rho U^2 r\right)$ coefficients (L and D are the lift and drag forces on the cylinder) are used as indicators of the convergence of the numerical solution. We set $U = 1m/s$, $r = 1m$, $A = 1m/s$, $\epsilon = 0.01/s$, $\rho = 1Kg/m^3$, and $\nu = 0.01\ m^2/s$, so that $Re = 200$ and $St \approx 0.2$. In this case, $T \approx 10s$ is the natural period of vortex shedding and $2\pi/\epsilon = 200\pi \gg T$. Figure 7-14 shows the time history of drag and lift coefficients; the presence of a slow time scale is evident from these plots.

In order to implement numerically the dynamic averaging, we used built-in functions of Matlab's Wavelet Toolbox. After trial and error, we found the *sym4* wavelet to be a good choice for a mother wavelet. Denoising was performed in the corresponding basis using a nonlinear multi-level soft thresholding, with the threshold value chosen based on the universal thresholding rule by Donoho & Johnstone [25]. Further details can be found in [35].

Numerical computation of $< A_\phi > (p(\phi, 0, \phi))$ in the condition (7.33) requires further attention. Since

$$\epsilon < A_\phi > (p(\phi), 0, \phi)) =< \epsilon A_\phi > (p(\phi), 0, \phi)) =< A >_t (\mathbf{x}, 0, \epsilon t)|_{\mathbf{x}=p(\epsilon t)}, \qquad (7.45)$$

one can numerically compute the condition (7.33) without the explicit knowledge of ϵ. To evaluate the time derivative, we used finite differencing. Figure 7-15 shows the predicted separation points along with the particle paths. Fixed separation occurs at

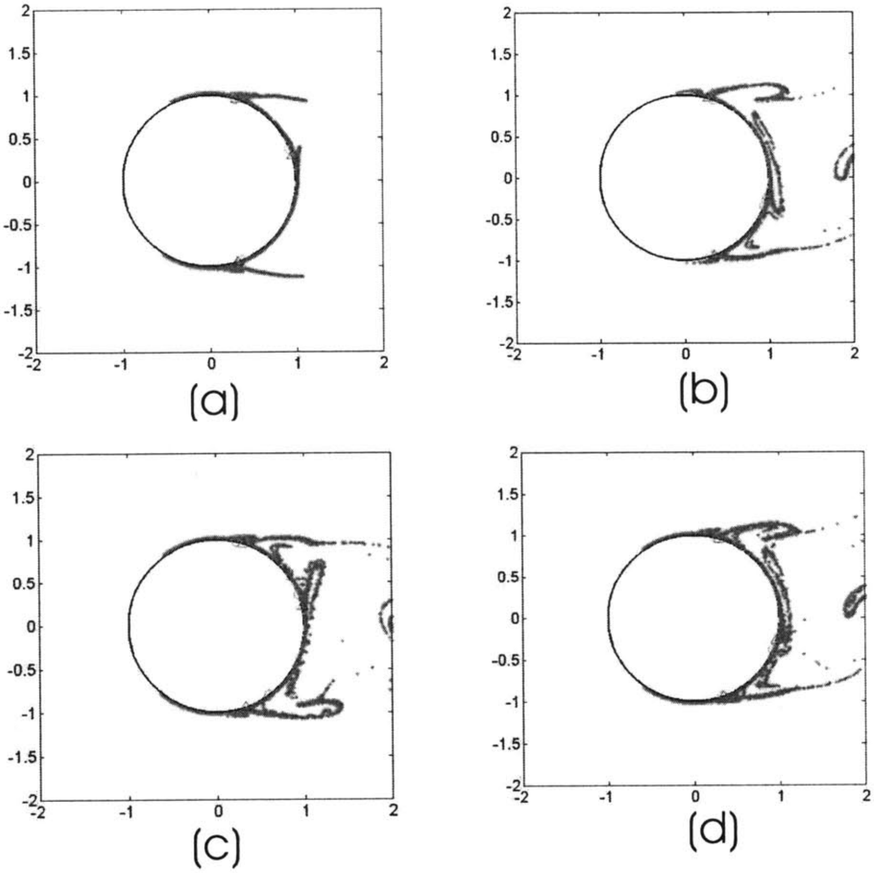

Figure 7-15: The blue triangles show separation locations from Theorem 2, while the megenta circles are the instantaneous wall-shear zeroes. The subplots (a)-(d) correspond to times $t = 135.275$, $t = 142.275$, $t = 145.075$, and $t = 151.375$.

the top and bottom of the cylinder, while moving separation is observed at the rear. Note that our moving separation criterion is also able to capture fixed separation locations, providing an unified approach to analyze separation in 2D unsteady fluid flows.

7.5 Moving Separation in 3D

In this section, we extend the notion of ghost manifold to three dimension fluid flows and deduce the moving separation criteria. We only present a brief outline of the analysis, as most of the details follow in a straightforward manner by extension of the ideas developed in Appendices B and C.

Using the canonical form (4.3) from chapter 4, it is straightforward to see that for the 3D velocity field $\mathbf{v}(\mathbf{x}, z, \phi, t)$ the particle motion in extended rescaled phase space (η, ϕ), satisfy

$$\begin{aligned} \dot{\eta} &= \epsilon \mathbf{f}(\eta, \phi, t) + \epsilon^2 \mathbf{g}(\eta, \phi, t; \epsilon), \\ \dot{\phi} &= \epsilon, \end{aligned} \tag{7.46}$$

where $\eta = (\mathbf{x}, \bar{z})$,

$$\mathbf{f} = \begin{pmatrix} \bar{z}\mathbf{A}_1(\mathbf{x}, 0, \phi, t) \\ \bar{z}^2 C_1(\mathbf{x}, 0, \phi, t) \end{pmatrix}, \qquad \mathbf{g} = \begin{pmatrix} \bar{z}^2[\partial_z \mathbf{A}_1(\mathbf{x}, 0, \phi, t) + \mathcal{O}(\bar{z}\epsilon)] \\ \bar{z}^3[\partial_z C_1(\mathbf{x}, 0, \phi, t) + \mathcal{O}(\bar{z}\epsilon)] \end{pmatrix}, \tag{7.47}$$

Associated with above system we consider a family of dynamical systems

$$\begin{aligned} \dot{\eta} &= \epsilon[< \mathbf{f} > (\eta, \phi) + \tilde{\mathbf{f}}(\eta, \phi, t)] + \epsilon^2 \mathbf{g}(\eta, \phi, t; \epsilon), \\ \dot{\phi} &= \epsilon \Delta, \end{aligned} \tag{7.48}$$

parameterized by $\Delta \in [0, 1]$. We have also assumed that $\mathbf{f}$ admits a decomposition of the form (7.10), with

$$\mathbf{f}^0(\eta, \phi) =< \mathbf{f} >= \begin{pmatrix} \bar{z} < \tau > (\mathbf{x}, \phi) \\ \bar{z}^2 < C > (\mathbf{x}, \phi) \end{pmatrix}, \tag{7.49}$$

where, $< \cdot >$ is the dynamic averaging operator notation introduced in the section (7.3.3). Hence, upto $\mathcal{O}(\epsilon)$, the particle dynamics is governed by

$$\begin{aligned} \dot{\eta} &= \epsilon < \mathbf{f} > (\eta, \phi), \\ \dot{\phi} &= \epsilon \Delta, \end{aligned} \tag{7.50}$$

and the separation patterns can be identified by analyzing its $\Delta = 0$ limit

$$\begin{aligned} \dot{\mathbf{x}} &= \epsilon \bar{z} < \tau > (\mathbf{x}, \phi), \\ \dot{\bar{z}} &= \epsilon \bar{z}^2 < C > (\mathbf{x}, \phi), \\ \dot{\phi} &= 0. \end{aligned} \tag{7.51}$$

As in 2D case, while these inferred separation patterns do not persist for the system (7.46), we show that under an additional speed condition (analogous to the last condition in (7.19)) there are corresponding ghost structures that lie off the no slip wall and continue to collect and eject fluid particles, leading to moving separation.

In order to establish this result, we consider the modified system (like for 2D case, c.f section 7.3.2)

$$\begin{aligned} \dot{\eta} &= \epsilon[< \mathbf{f} > (\eta, \phi) + \tilde{\mathbf{f}}(\eta, \phi, t)] + \epsilon^2 \mathbf{g}(\eta, \phi, t; \epsilon), \\ \dot{\phi} &= \epsilon \Delta M(\bar{z}), \end{aligned} \tag{7.52}$$

where, $M(\bar{z})$ is the bump function (see Eq. 7.18). Carrying out the dynamic averaging, as described in the Appendix C, one obtains the modified averaged equations

$$\begin{aligned} \dot{\xi} &= \epsilon < \mathbf{f} > (\xi, \phi) + \epsilon^2[\mathbf{f}^1(\xi, \phi, t) - \Delta\partial_\phi \mathbf{w} M(r)] + \mathcal{O}(\epsilon^3), \\ \dot{\phi} &= \epsilon\Delta M(r) + \mathcal{O}(\epsilon^2), \end{aligned} \tag{7.53}$$

where, $\xi = (\mathbf{q}, r)$, $\mathbf{f}^1$ is defined in Eq. (B.1) and

$$\mathbf{w}(\xi, \phi, t) = \int_{t_0}^{t} [\mathbf{f}(\xi, \phi, \tau) - < \mathbf{f} > (\xi, \phi)] d\tau. \tag{7.54}$$

Further making a change of variable

$$\mathbf{q} \to \mathbf{q} - \mathbf{p}(\phi), \tag{7.55}$$

where, $\mathbf{p}(\phi)$ is an arbitrary point on the boundary evolving at the slow time scale ϕ, we can express the above equations (7.53) as

$$\begin{aligned} \dot{\mathbf{q}} &= -\epsilon\Delta M(r)\mathbf{p}'(\phi) + \epsilon r[< \tau > (\mathbf{p}(\phi), \phi) + \nabla_{\mathbf{x}} < \tau > (\mathbf{p}(\phi), \phi).\mathbf{q}] + \mathcal{O}(\epsilon r|\mathbf{q}|) \\ &+ M(r)\mathcal{O}(\epsilon^2 r) + \mathcal{O}(\epsilon^2 r^2), \\ \dot{r} &= \epsilon r^2[< C > (\mathbf{p}(\phi), \phi) + \nabla_{\mathbf{x}} < C > (p(\phi), \phi).\mathbf{q}] + M(r)\mathcal{O}(\epsilon^2 r^2) + \mathcal{O}(\epsilon^2 r^3), \\ \dot{\phi} &= \epsilon\Delta M(r) + \mathcal{O}(\epsilon^2). \end{aligned} \tag{7.56}$$

Working with above set of equations (in place of Eq. (B.6)) in the extended phase space, and following the steps given in the Appendix B, one can deduce the following result

Moving separation point criteria Suppose that a point $\mathbf{p}(\phi)$ satisfies

$$\begin{aligned} < \tau > (\mathbf{p}(\phi), \phi) &= 0, \qquad \nabla_{\mathbf{x}} \cdot < \tau > (\mathbf{p}(\phi), \phi) < 0, \qquad \det \nabla_{\mathbf{x}} < \tau > (\mathbf{p}(\phi), \phi) > 0, \\ & < C > (\mathbf{p}(\phi), \phi) > 0, \end{aligned} \tag{7.57}$$

and

$$< C > (\mathbf{p}(\phi), \phi) - \nabla_{\mathbf{x}} \cdot < \tau > (\mathbf{p}(\phi), \phi) - \epsilon|\mathbf{p}'(\phi)| > 0, \tag{7.58}$$

for all $\phi \in \mathcal{I} = (-\infty, \phi_0]$, where $\phi_0 = \epsilon t_0$ and t_0 is the current time. Then $(\mathbf{x}, z) = (\mathbf{p}(\phi), 0)$ is a moving separation point for the velocity field $\mathbf{v}$.

Extension of above result to obtain an analogous speed condition for moving separation line is nontrivial and would be treated elsewhere.

Chapter 8

Open Separation

Open separation i.e., separation without wall-shear zeros at, atleast one end of the separation line was first observed by Wang [98]. The best known example of open separation occurs on a roundnosed body of revolution [98],[99],[15]. This form of separation is also known as *crossflow separation* due to the dominance of the circumferential pressure gradients in the separation process [101].

As discussed in the Introduction, the notion of open separation has been a contentious issue in flow separation community [15], since the time it was introduced. This notion directly challenged Lighthill's *closed separation paradigm* ([60]); according to which separation lines always starts from saddle-type wall-shear zeros and terminate at stable spirals or nodes. Tobak and Peake [94] used the terminology of global (closed) separation and local (open) separation to describe the two forms of separation.

Open separation having been confirmed by numerous experimental and numerical studies is now a well accepted phenomena. A convincing experimental support of open separation was first noted in Stetson's [85] testing of a blunt cone at 10° incidence. First computational evidence of open separation was obtained in a three-dimensional boundary layer solution by Wang et. al. [99]. A detailed experimental study of change in surface flow patterns from closed separation to open separation and vice versa, with varying geometrical configurations, Reynolds and Mach number, can be found in [100].

Despite these advances in characterizing flow separation, there has been a lack of a sound quantitative description of open separation patterns, like those observed over bodies of revolution (figure 2-4). The prime difficulty is the lack of a unique separation line and surface associated with such separation patterns, as was pointed out in section 2.2.3. This non-uniqueness has also been noted earlier in [42], [109], [101] and [108].

Despite this inherent difficultly, it is well-accepted in literature that it should be possible to create a definition for starting point of crossflow separation and identify the associated separation line. For instance taking a more practical viewpoint the VPI group ([101]) investigated several indicators and studied the correlations between those and the separation location determined from the flow visualizations. Measurement techniques for each indicator were then considered, this includes: oil flow visualization, laser Doppler velocimetry, surface pressure and magnitude and directional surface hot-film skin-friction measurements.

Based on this study it was concluded that hot-film skin-friction magnitude measurements is one of the most easiest and most accurate techniques: local skin-friction magnitude minima correlate well with separation line yet consistently on the further leeward side of the separation. It was also pointed out that while direction surface hot-film measurements provide data which have the potential to delineate global separation topology, there still remains the problem of algorithmically extracting separation line from other wall-shear lines.

As was discussed in the introduction (chapter 1), Wu et. al. ([108],[107]) proposed to examine closed and open separation within an unified framework. They circumvented the requirement for the separation line to initiate from the wall-shear singularity by defining it to be a wall-shear line which is a local maximizer of ϕ (see section A.6 for the definition) which is the product of upwelling and wall-shear line convergence. In this definition it was implicitly assumed that the maximizing curve is a always a wall-shear line which is not true in general (as was demonstrated in chapter 5). Moreover, in order to identify the initial point of an open separation line, they proposed an ad-hoc criteria. Citing numerical difficulties, Wu et. al. [108] were unable to convincingly validate this criteria in their example involving a flow past a prolate spheroid.

In this chapter we derive a quantitative criteria to best approximate crossflow separation. Recall, in chapter 2 we linked crossflow separation to pseudo manifolds associated with the attracting wall shear zero to which the crossflow separation line converges. The pseudo manifold is inherently non unique and so is its intersection with the boundary which is a candidate crossflow separation line. We detect the most influential candidate as a maximizing ridge of a boundary based scalar field.

The scalar field measures the cumulative upwelling along uniformly hyperbolic portion of wall shear trajectories that converge to the attracting wall shear zero. Therefore, the maximizing ridge of this scalar field identifies the curve on the boundary along which bulk of fluid particles break away and is therefore an ideal candidate for the crossflow separation line. Using differential invariant manifold technique we examine dynamical properties of the ridge in Appendix D, and establish that it indeed satisfies necessary criteria for being a crossflow separation line. This approach extends in a straightforward manner to unsteady flows using the techniques developed in chapter 4 and chapter 7.

Finally, we compare our criterion with that of Simpson et al. [101] and Wu et al. [108] in steady and unsteady flow models, and in a flow past a prolate spheroid at an angle of attack.

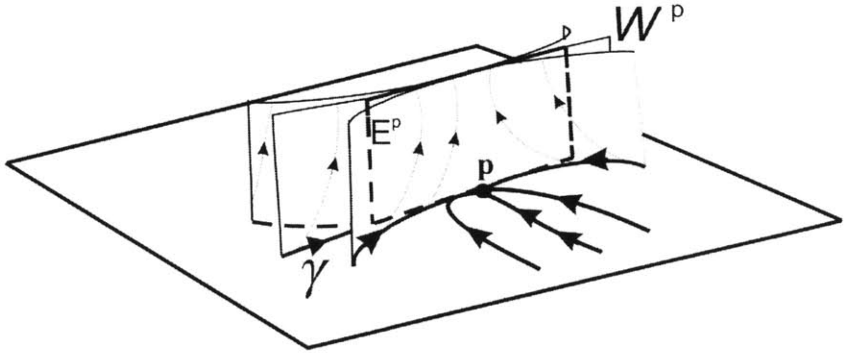

Figure 8-1: Pseudo manifolds near a stable node $\mathbf{p}$..

8.1 Pseudo manifolds

We first analyze crossflow separation in steady flows. Consider the stable node $\mathbf{p}$ of the steady rescaled system (3.10) (see section 3.1), so that

$$\mathbf{A}(\mathbf{p},0)=0,\qquad \det\nabla_{\mathbf{x}}\mathbf{A}(\mathbf{p},0)>0,\qquad \nabla_{\mathbf{x}}\cdot\mathbf{A}(\mathbf{p},0)<0,\qquad [\nabla_{\mathbf{x}}\cdot\mathbf{A}(\mathbf{p},0)]^2-4\det\nabla_{\mathbf{x}}\mathbf{A}(\mathbf{p},0)>0. \tag{8.1}$$

The eigenvalues $\lambda_1=-\lambda,\lambda_2=-\mu,\lambda_3=\nu$ of the linearized scaled flow

$$\begin{pmatrix}\mathbf{x}\\ z\end{pmatrix}=\begin{pmatrix}\nabla_{\mathbf{x}}\mathbf{A}(\mathbf{p},0) & \partial_z\mathbf{A}(\mathbf{p},0)\\ \mathbf{0} & C(\mathbf{p},0)\end{pmatrix}\begin{pmatrix}\mathbf{x}\\ z\end{pmatrix}. \tag{8.2}$$

at $\mathbf{p}$ satisfy

$$\lambda+\mu=\nabla_{\mathbf{x}}\cdot\mathbf{A}(\mathbf{p},0),\qquad \nu=C(\mathbf{p},0)=-\frac{1}{2}\nabla_{\mathbf{x}}\cdot\mathbf{A}(\mathbf{p},0), \tag{8.3}$$

where, $\lambda,\mu,\nu>0$. Without loss of generality we would assume $\lambda<\mu$. Let $\mathbf{e}_\lambda,\mathbf{e}_\mu$ and $\mathbf{e}_\nu$ be the eigenvectors corresponding to eigenvalues λ,μ and ν respectively. Consider the time reversed rescaled system

$$\mathbf{x}'=-\mathbf{A}(\mathbf{x},z),\qquad z'=-zC(\mathbf{x},z). \tag{8.4}$$

Choosing $a=(\lambda+\mu)/2>0$, we observe that

$$-\nu<0<\lambda<a<\mu. \tag{8.5}$$

Therefore, by *pseudo stable manifold* theorem (see Appendix D.1), there is invariant manifold $\mathcal{W}^p$ for system (8.4) which is nonlinear continuation of the subspace $E^p=\operatorname{span}\{\mathbf{e}_\lambda,\mathbf{e}_\mu\}$. We argue that the crossflow separation is a result of existence of the pseudo manifolds: these manifolds collect and eject fluid particles in the vicinity of the boundary. Since $a>0$, $\mathcal{W}^p$ is not guaranteed to be unique. As a result crossflow separation inherently admits a non-unique description in terms of invariant manifolds. Since each of the pseudo manifold is an invariant surface of the scaled flow (8.4), it intersects the $z = 0$ invariant plane along an invariant curve of (8.4). Hence, crossflow separation line is necessarily a union of wall shear trajectories, containing the node $\mathbf{p}$. This brings us to the fundamental question of crossflow separation: what distinguishes crossflow separation line, from other candidate wall shear lines.

8.2 Distinguishing properties of Crossflow Separation line

We argue that cross flow separation line has two distinguishing properties

i. It is *uniform hyperbolic*,

ii. It induces *maximal* upwelling of fluid particles in its vicinity.

These two properties are formalized below.

8.2.1 Uniform Hyperbolicity

We say that a wall-shear line γ is *uniform hyperbolic*, if for any $\mathbf{x}_0 \in \gamma$

$$S_{\perp}(s) < 0, \qquad C(\mathbf{x}(s, \mathbf{x}_0), 0) > 0, \tag{8.6}$$

where, recall

$$S_{\perp}(s) = \left. \frac{(\omega, (\nabla_{\mathbf{x}} \tau)\, \omega)}{|\omega|^2} \right|_{\mathbf{x}=\mathbf{x}(s,\mathbf{x}_0),\ z=0}, \tag{8.7}$$

measures the wall-shear stretching rate normal to γ and

$$C(\mathbf{x}(s, \mathbf{x}_0), 0) = \frac{1}{2} \partial^2_{zz} w(\mathbf{x}(s, \mathbf{x}_0), 0), \tag{8.8}$$

measures the rate of stretching normal to the boundary along γ. Uniform hyperbolicity is a stronger form of saddle type instability than *strong hyperbolicity*, a notion which was introduced in chapter 3 to describe 3D separation patterns which admit locally unique separation lines and separation surfaces.

In order to identify uniformly hyperbolic wall shear lines which contain the node $\mathbf{p}$, we consider an open connected neighborhood $\mathcal{O}$ of $\mathbf{p}$ such that

$$\mathcal{O} = \{ \mathbf{x} \in \mathbf{R}^2 | S_{\perp}(\mathbf{x}) < 0, C(\mathbf{x}, 0) > 0, \alpha(\mathbf{x}) = \mathbf{p} \}, \tag{8.9}$$

where, $\alpha(\mathbf{x})$ denotes the α-limit set of $\mathbf{x}$. Let $\overline{\mathcal{O}}$ be the closure of $\mathcal{O}$ in $\mathbf{R}^2$ with $\partial \mathcal{O}$ denoting its boundary. From the definition it is clear that the set $\overline{\mathcal{O}}$ contains $\{\mathbf{p}\}$ as the only invariant set of wall-shear field.

8.2.2 Scalar field & Ridge

Over any interval $\mathcal{I} \subset \mathbf{R}$, we associate with a wall-shear trajectory $\mathbf{x}(t; \mathbf{x}_0)$ a set

$$X(\mathcal{I}, \mathbf{x}_0) = \{\mathbf{x}(t; \mathbf{x}_0) | t \in \mathcal{I}\}. \tag{8.10}$$

Let $T_h(\mathbf{x}_0)$ be the first time, when $\mathbf{x}(t; \mathbf{x}_0)$ starting in $\mathcal{O}$ hits the boundary $\partial\mathcal{O}$ of $\overline{\mathcal{O}}$, i.e.

$$T_h(\mathbf{x}_0) = \sup\{t | X([-t, 0], \mathbf{x}_0) \subset \mathcal{O}, t \in \mathbf{R}^+\}. \tag{8.11}$$

We define a scalar field $\mathcal{C} : \mathcal{O} \setminus \mathbf{p} \to \mathbf{R}$

$$\mathcal{C}(\mathbf{x}_0) = \int_0^{T_h(\mathbf{x}_0)} C(\mathbf{x}(\tau; \mathbf{x}_0), 0) d\tau, \tag{8.12}$$

which measures the cumulative upwelling along $\mathbf{x}(t; \mathbf{x}_0)$, as it remains in the region $\mathcal{O}$. It is clear from the definition that

1. $\mathcal{C}$ is a non-negative function over $\overline{\mathcal{O}}$ i.e

   $$\mathcal{C}(\mathbf{x}_0) > 0, \forall \mathbf{x}_0 \in \mathcal{O}, \tag{8.13}$$

   such that

   $$\mathcal{C}(\mathbf{x}_0) \to 0, \mathbf{x}_0 \in \partial\mathcal{O}, \qquad \mathcal{C}(\mathbf{x}_0) \to \infty, \quad \text{as} \quad \mathbf{x}_0 \to \mathbf{p}. \tag{8.14}$$

2. For any $\mathbf{x}_0 \in \mathcal{O}$ and $\mathbf{x}_1, \mathbf{x}_2 \in X([-T_h(\mathbf{x}_m), \infty), \mathbf{x}_0)$ such that $\mathbf{x}(\bar{t}, \mathbf{x}_1) = \mathbf{x}_2$ for some $\bar{t} < 0$

   $$\mathcal{C}(\mathbf{x}_1) > \mathcal{C}(\mathbf{x}_2). \tag{8.15}$$

The maximizing curve or *ridge* of the scalar field $\mathcal{C}(\mathbf{x}_0)$ is an ideal candidate to define crossflow separation line, since in it's vicinity a bulk of fluid breaks away from the wall.

There exists many ways of defining ridge of a scalar field. The intuition behind these definitions is that along a ridge, one would expect:

1 to be locally at the highest point in the field transverse to the ridge and

2 at each point on the ridge the direction in which the topography decreases most rapidly should be *transverse* to the ridge.

Typically different definitions of a ridge differ in the reference direction they use for defining the *transverse* direction.

In this work we will use *second-derivative ridge* as the notion of the ridge, which is defined as follows [81]: A second-derivative ridge of a scalar field $\mathcal{C}$ is an injective curve $\mathbf{c} : (a, b) \to \mathcal{O}$ satisfying the following conditions for each $s \in (a, b)$

1. $\mathbf{c}(s)$ is a *gradient line* i.e. the tangent vector $\frac{d\mathbf{c}}{ds}$ to $\mathbf{c}(s)$ and the gradient $\nabla_{\mathbf{x}} \mathcal{C}(\mathbf{c}(s))$ are parallel.

2. The unit normal $\mathbf{n}(s)$ to the curve $\mathbf{c}(s)$ is an eigenvector corresponding to the minimum eigenvalue of the Hessian $H = \nabla_{\mathbf{x}}^2 \mathcal{C}(\mathbf{c}(s))$ such that

$$\Sigma(\mathbf{n}(s), \mathbf{n}(s)) = \min_{||\mathbf{u}||=1} H(\mathbf{u}, \mathbf{u}) < 0, \tag{8.16}$$

   where, Σ can be thought of as the bilinear form evaluated at the point $\mathbf{c}(s)$.

Let $\mathcal{R}(\mathbf{p})$ be a second-derivative ridge of $\mathcal{C}(\mathbf{x_0})$. There are two key properties of the ridge $\mathcal{R}(\mathbf{p})$, which makes it appropriate for describing crossflow separation.

8.2.3 Definition of Crossflow separation line

As a first proposition we show that for all practical purposes $\mathcal{R}(\mathbf{p})$ behaves as wall-shear trajectory. In order to establish this result, we examine the wall-shear trajectories which, in the eigenbasis $\{\mathbf{e}_\lambda \quad \mathbf{e}_\mu\}$ satisfy the ODE

$$\begin{aligned} \dot{x} &= -\lambda x + f(x,y), \\ \dot{y} &= -\mu y + g(x,y), \end{aligned} \tag{8.17}$$

where

$$\begin{pmatrix} f(\mathbf{x}) \\ g(\mathbf{x}) \end{pmatrix} = T^{-1}\mathbf{F}(T\mathbf{x}), \qquad T = [\mathbf{e}_\lambda \quad \mathbf{e}_\mu],$$

and

$$\mathbf{F}(\mathbf{x}) = \tau(\mathbf{x}) - \nabla_{\mathbf{x}}\tau(\mathbf{p})\mathbf{x} = \mathcal{O}(||\mathbf{x}||^2).$$

For a given $\delta > 0$, let $\mathcal{B}_{\alpha(\delta)} = [-\alpha(\delta), \alpha(\delta)] \times [-\alpha(\delta), \alpha(\delta)] \subset \mathbf{R}^2$ be a box centered at origin, such that

$$\min\{ \sup_{(x,y)\in\mathcal{B}_{\alpha(\delta)}} ||Df(x,y)||, \sup_{(x,y)\in\mathcal{B}_{\alpha(\delta)}} ||Dg(x,y)||\} \leq \frac{\delta}{3}. \tag{8.18}$$

Theorem Consider the portion of $\mathcal{R}(\mathbf{p})$ lying in the box $\mathcal{B}_\alpha$ i.e.

$$\mathcal{R}_\delta(\mathbf{p}) = \mathcal{R}(\mathbf{p}) \bigcap \mathcal{B}_{\alpha(\delta)}, \tag{8.19}$$

where,

$$\delta = \mu - \lambda. \tag{8.20}$$

Then for any given $\epsilon > 0$, there exists a $\mathbf{x}_m \in \mathcal{O}$ such that

$$D(X([-T_h(\mathbf{x}_m), \infty), \mathbf{x}_m), \mathcal{R}_\delta(\mathbf{p})) < \epsilon \tag{8.21}$$

where, D is the *Hasudorff metric.* Recall that given any two subsets $\mathcal{E}, \mathcal{F} \subset \mathbf{R}^2$, the *Hasudorff distance* $D(\mathcal{E}, \mathcal{F})$ between $\mathcal{E}$ and $\mathcal{F}$ is given by

$$D(\mathcal{E}, \mathcal{F}) = \sup_{\mathbf{y}\in\mathcal{E}} \inf_{\mathbf{x}\in\mathcal{F}} d(\mathbf{x}, \mathbf{y}), \tag{8.22}$$

where, $d(\mathbf{x}, \mathbf{y})$ is any Euclidian norm on $\mathbf{R}^2$.

Corollary:$\mathcal{R}(\mathbf{p})$ cannot terminate in the interior $\mathcal{O}$ and extends naturally to the boundary $\partial\mathcal{O}$ of $\overline{\mathcal{O}}$.

The proposition implies that $\mathcal{R}(\mathbf{p})$ behaves like a wall-shear trajectory over large region of interest which is proportional to difference between the two eigenvalues μ and λ corresponding to linearized wall-shear flow at the node $\mathbf{p}$. The corollary shows that $\mathcal{R}(\mathbf{p})$ has a well defined point of initiation. Therefore, we define crossflow separation line to be the ridge $\mathcal{R}(\mathbf{p})$.

8.2.4 Algorithm for crossflow separation line detection

I. Identify the open set $\mathcal{O}$ containing $\mathbf{p}$, the stable wall shear node of interest.

II. Compute the scalar field $\mathcal{C}(\mathbf{x}_0)$ over the set $\mathcal{O}$. For this the wall-shear ODE

$$\mathbf{x}' = \tau(\mathbf{x}), \tag{8.23}$$

is solved in backward time over a grid of initial conditions in $\mathcal{O}$ and the integral (8.12) is computed.

III. Determine the second-derivative ridge $\mathcal{R}(\mathbf{p})$ of $\mathcal{C}$. In order to numerically extract $\mathcal{R}(\mathbf{p})$ both the Hessian $\nabla^2_{\mathbf{x}}\mathcal{C}$ and the gradient field $\nabla_{\mathbf{x}}\mathcal{C}$ are determined. In case of a Cartesian grid, the Hessian is easily computed by finite differencing. Once the eigenvectors corresponding to the minimum eigenvalue direction of Hessian are computed, a scalar field can be formed by taking the inner product of these eigenvectors with the gradient field. The ridge can then be extracted by looking at the zero-valued level sets.

Remark 1 In order to find crossflow attachment line, identify an unstable node $\mathbf{p}$ and it's neighborhood $\mathcal{O}$, such that

$$\mathcal{O} = \{\mathbf{x} \in \mathbf{R}^2 | S_\perp(\mathbf{x}) > 0, C(\mathbf{x}, 0) < 0, \omega(\mathbf{x}) = \mathbf{p}\}. \tag{8.24}$$

Compute the scalar field $\mathcal{C}$

$$\mathcal{C}(\mathbf{x}_0) = -\int_0^{T_h(\mathbf{x}_0)} C(\mathbf{x}(\tau; \mathbf{x}_0), 0) d\tau, \tag{8.25}$$

where, T_h is given by

$$T_h(\mathbf{x}_0) = \sup\{t | X([0, t], \mathbf{x}_0) \subset \mathcal{O}, t \in \mathbf{R}^+\}. \tag{8.26}$$

To compute the integral in 8.25, the ODE 8.23 is solved for a grid of initial conditions in forward time. Following step III, extract the ridge $\mathcal{R}(\mathbf{p})$ of $\mathcal{C}$ containing $\mathbf{p}$. $\mathcal{R}(\mathbf{p})$ is the desired crossflow attachment line.

Remark 2 The algorithm given above for flat boundaries, carries over to curved moving boundaries in a straightforward manner by a framework developed in the Appendix E. This would be illustrated for prolate spheroid flow in section 8.4.

Remark 3 The above algorithm extends to the time-dependent velocity fields that possess a well-defined mean in time. The required modifications are described in next section.

8.3 Unsteady crossflow separation criteria

Recall that for the velocity field satisfying assumptions of chapter 4, there exists a coordinate system in which the particle motion near the boundary become

$$\dot{\zeta} = \epsilon \mathbf{v}^0(\zeta) + \mathcal{O}(\epsilon^2). \tag{8.27}$$

Since the $\mathcal{O}(\epsilon^2)$ term in (8.27) is uniformly bounded in time, the particle motion near the boundary is essentially governed by the steady velocity field

$$\mathbf{v}^0(\xi, \xi_3) = (\epsilon \xi_3 \overline{\tau}(\xi), \epsilon \xi_3^2 \overline{C}(\xi)). \tag{8.28}$$

Therefore one would expect, that the time-dependent perturbations of separation patterns found in the steady limit (8.28) would continue to act as organizing centers for flow separation in the unsteady flow as well. Indeed this was proved for separation patterns which admit locally unique separation line and surfaces (see chapter 4 for details). We argue that a similar result also carries over to cross flow separation in unsteady flows with finite mean component.

Let $\overline{\mathbf{p}}$ be a stable node of the averaged wall-shear field (4.10) so that it satisfies

$$\overline{\tau}(\overline{\mathbf{p}}) = 0, \quad \nabla_{\mathbf{x}} \cdot \overline{\tau}(\overline{\mathbf{p}}) < 0, \quad \mathrm{Det} \nabla_{\mathbf{x}} \overline{\tau}(\overline{\mathbf{p}}) > 0, \quad [\nabla_{\mathbf{x}} \cdot \overline{\tau}(\overline{\mathbf{p}})]^2 - 4 \mathrm{Det} \nabla_{\mathbf{x}} \overline{\tau}(\overline{\mathbf{p}}) > 0. \tag{8.29}$$

If in addition

$$\overline{C}(\overline{\mathbf{p}}) > 0, \tag{8.30}$$

then, based on the discussion in section (8.1) we infer the existence of pseudo unstable manifolds for $\overline{\mathbf{p}}$. Each of these pseudo manifolds contain the steady separation curve, which is the separating streamline from $\overline{\mathbf{p}}$. Under the conditions (8.29,8.30), this streamline perturbs to the time-dependent separation curve, while $\overline{\mathbf{p}}$ remains a *fixed separation point* (see Theorem 1 in section 4.2.2). Hence one would expect that time-dependent perturbations of the pseudo manifolds would continue to result in crossflow separation for the unsteady flow as well. By no-slip condition, the intersection of these time-dependent pseudo manifolds with the boundary cannot change in time and therefore the crossflow separation is fixed.

Thus, *fixed unsteady crossflow separation line* can be identified by applying the algorithm given in section 8.2.4 to the time averaged wall-shear field (4.10), with C replaced by its time-averaged counterpart $\overline{C}$ as defined in Eq. (4.12).

8.4 Numerical Verification

In this section we analyze crossflow separation in an analytic flow model and in numerical simulation. In both the cases we compare our crossflow separation criteria with that of Wu et. al. [108] and Simpson et. al. [101]. A brief summary of these criteria is given in the Appendix 3.12.

8.4.1 Analytical Example

In order to study the crossflow separation of type shown in figure 2-4, we consider an incompressible time-dependent analytical velocity field

$$\begin{aligned}
u &= (x+1)(d-x)z + cz^2 + \frac{1}{3}\left(2 + \frac{ab(1+ef)}{3}\right)z^3 + \frac{d(1-d)}{8}x^2z^2 + \frac{f(a-b)}{3}xz^3, \\
&+ \frac{(a-b)(1+ef)}{3}yz^3 \\
v &= (y-a)(y+b)(x+ey)(y+fx)z + cz^2 + \frac{ab(2e+f)}{3}z^3 + \frac{2(a-b)(1+ef)}{3}xz^3, \\
&+ \frac{(a-b)(e+6f)}{3}yz^3 \qquad (8.31) \\
w &= \frac{1-d}{2}z^2 + \left(1 + \frac{1+ef}{2ab}\right)xz^2 + abeyz^2 + \frac{f(a-b)}{2}x^2z^2 - fx^2yz^2 + \frac{3(a-b)e}{2}y^2z^2 \\
&+ (a-b)(1+ef)xyz^2 - 2ey^3z^2 - \frac{3(1+ef)}{2}xy^2z^2 + \frac{d(d-1)}{12}xz^3 + \frac{(b-a)(3e+f)}{6}z^4,
\end{aligned}$$

where, a, b, c, d, e, f are in general time-dependent parameters. This model has been derived from Navier-Strokes equations by using the perturbative procedure of Perry and Chong ([72]) as described in section A.5. In whatever follows we shall take a, b, c, d, e to be constants and $f(t)$ to be of the form

$$f(t) = \alpha + \beta r(t), \qquad (8.32)$$

where α, β are constants and

$$\lim_{T\to\infty} \frac{1}{T}\int_{t_0-T}^{t_0} r(t)dt = 0. \qquad (8.33)$$

Varying $r(t)$ in the model, we provide examples with different time dependence. Under the assumption (8.33), it is clear that the velocity field (8.31) admits a finite asymptotic average and the function $\Delta(\mathbf{x}, z, t)$ and its derivatives are uniformly bounded in time on bounded sets: thus our assumptions listed in section 4.1 are satisfied.

For this flow, the time-averaged wall-shear field and upwelling can be computed

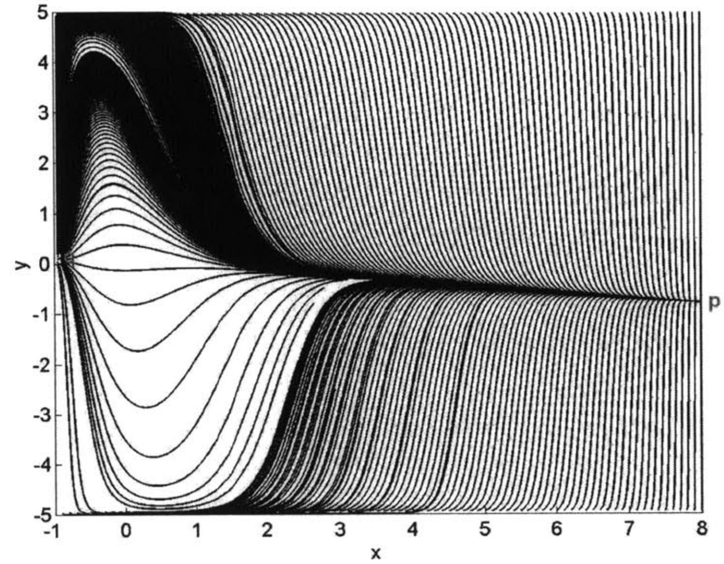

Figure 8-2: Time averaged wall shear trajectories for the time dependent analytical example. **p** is the stable node while **q** is the unstable node.

to be

$$\overline{\tau}(\mathbf{x}) = \begin{pmatrix} (x+1)(d-x) \\ (y-a)(y+b)(x+ey)(y+\alpha x) \end{pmatrix}, \tag{8.34}$$

$$\begin{aligned}\overline{C}(\mathbf{x}) &= \frac{1-d}{2} + \frac{1+e\alpha+2ab}{2ab}x + abey + \frac{\alpha(a-b)}{2}x^2 + (a-b)(1+e\alpha)xy + \frac{3(a-b)e}{2}y^2 \\ &- \alpha x^2 y - \frac{3(1+e\alpha)}{2}xy^2 - 2ey^3, \end{aligned} \tag{8.35}$$

respectively. Figure 8-2 shows the averaged wall-shear trajectories in the region of interest. This vector field has the required connection of the wall-shear trajectories between an unstable node at $\mathbf{q} = (-1, -b)$ and the stable node $\mathbf{p} = (d, -\alpha d)$. One can think of this model as obtained by straitening the round nosed body into locally an Euclidean plane. Hence, $y-$ axis corresponds to circumferential direction while $x-$ axis denotes the axis of the body.

Steady Case

By taking $\beta = 0$ in 8.32 we obtain a steady flow model. Following the algorithm given in section 8.2.4, we compute the scalar field $\mathcal{C}(x, y)$, which is shown in figure 8-3a) along with the associated ridge. Figure 8-3b)&c) shows the scalar fields $\mathcal{W}(x, y)$ and $\mathcal{S}(x, y)$ due to Wu. et. al. [108] and Simpson et. al. [101], respectively. Recall that $\mathcal{W}$ is the product of the wall vorticity line curvature and the strength of the wall-normal

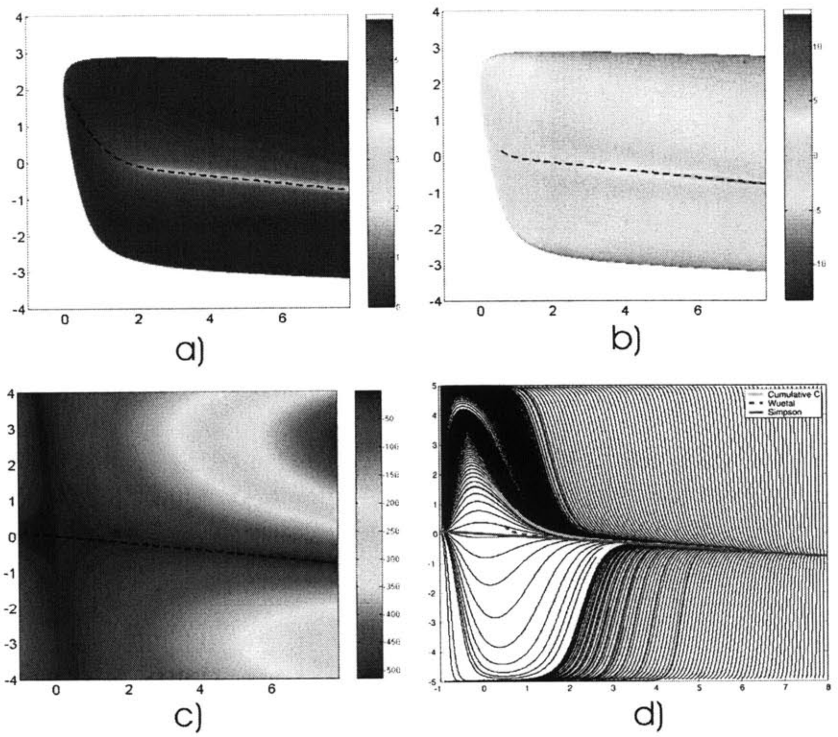

Figure 8-3: Scalar fields and ridges for the steady analytical example a) $\mathcal{C}(x, y)$, b)$\mathcal{W}(x, y)$ and c) $\mathcal{S}(x, y)$. In figure d) we show the comparison of the three predictions (red curve is ridge of $\mathcal{S}$, blue dashed curve is ridge of $\mathcal{W}$ and green curve is ridge of $\mathcal{C}$) along with the wall shear trajectories in black.

upwelling normalized by the wall-vorticity and $\mathcal{S}$ denotes the wall-shear magnitude. The ridge of $\mathcal{W}$ shown as a dotted curve in the figure 8-3b) is determined based on the condition (A.67). The ridge of $\mathcal{S}$ is obtained by looking at the circumferential minima of $\mathcal{S}(x, y)$ for each x location. The ridges of the scalar fields $\mathcal{C}$, $\mathcal{W}$ and $\mathcal{S}$ lead to distinct crossflow separation lines. For a direct comparison these separation lines have been plotted together in the figure 8-3d) along with the wall-shear trajectories and in figure 8-4a) along with the streamlines.

In the vicinity of node **p** all the separation lines capture the separation location very well. However, the separation line based on $\mathcal{S}$ continues from **p** to **q**, failing to locate the point of initiation of the crossflow separation. On the other hand separation lines derived from the scalar fields $\mathcal{W}$ and $\mathcal{C}$ terminate at distinct locations. In order to investigate which of these terminal points better approximates separation initiation location, we plot in figure 8-4b) the streamlines starting very close to the wall in the vicinity of these points. Clearly, the predictions based on $\mathcal{C}$ is able to capture the point of initiation of crossflow separation more accurately than due to Wu et. al.

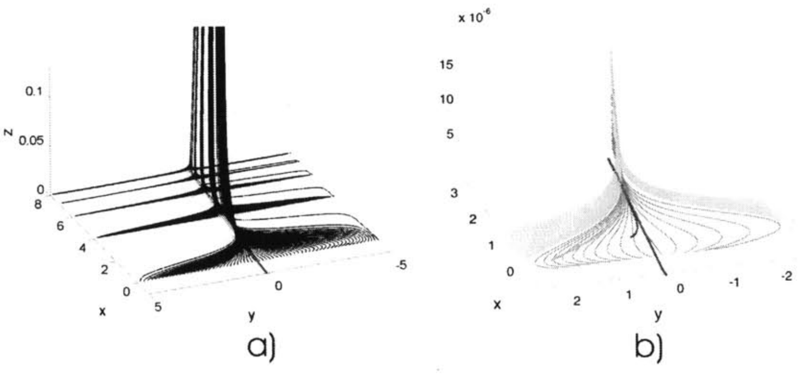

Figure 8-4: Steady analytical example (a)Validation of the separation line prediction with the streamline behavior (red curve is ridge of $\mathcal{S}$, blue curve is ridge of $\mathcal{W}$ and green curve is ridge of $\mathcal{C}$). (b) Same as (a) but with streamlines shown close to the wall.

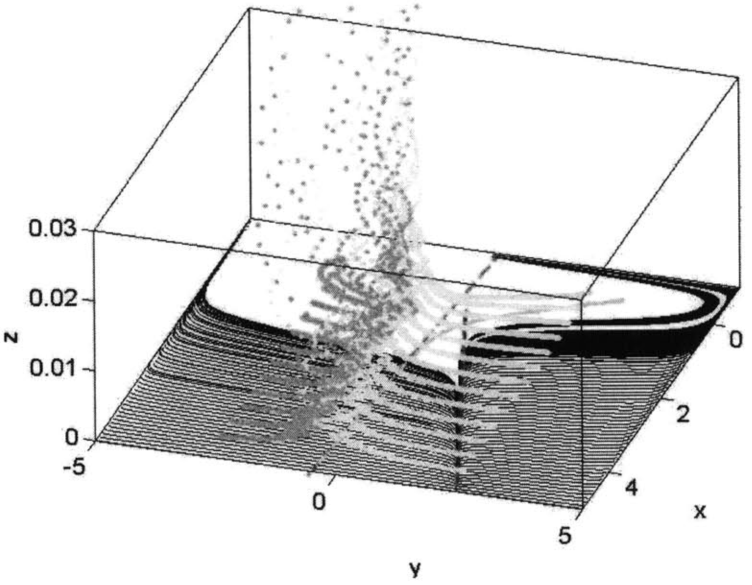

Figure 8-5: Crossflow separation prediction for the analytical example with periodic time dependence. Red curve is ridge of $\mathcal{S}$, blue curve is ridge of $\mathcal{W}$ and green curve is ridge of $\mathcal{C}$ and the black curves denote the instantaneous wall shear trajectories. Also shown in magenta and blue are the particle paths.

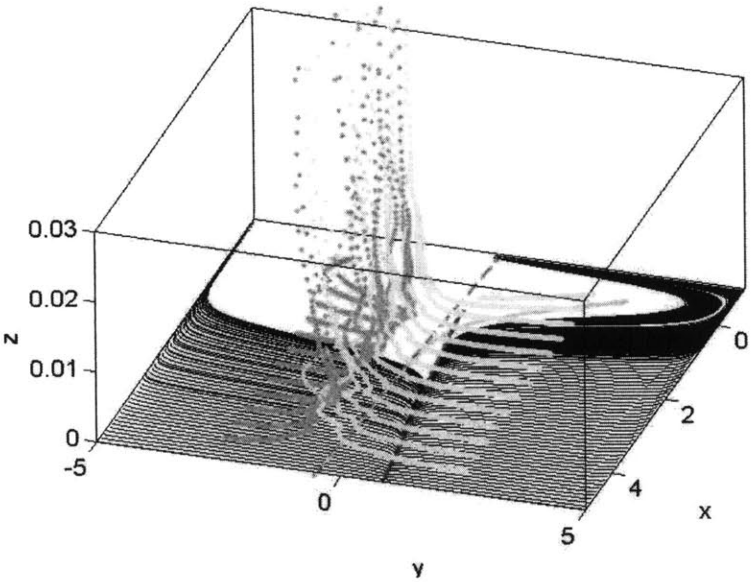

Figure 8-6: Same as figure 8-5 but with aperiodic time dependence for the analytical example.

Time-dependent Case

Figures 8-5 and 8-6 shows the predictions for the periodic and turbulent time dependence, respectively. In order to mimic turbulent flow conditions we have taken $r(t)$ to be a zero mean random variable with normal distribution. Because, $r(t)$ is zero mean, its integral is bounded, and it satisfies 8.33.

It is evident from these figures that the crossflow separation line (blue curve) based on Wu et. al. criteria is completely misleading, while that due to Simpson et. al. (red curve) fails to get the correct initial location of the separation line.

8.4.2 Prolate Spheroid

Despite its simple geometry spheroid flows are the arctypes of flows around airborne and underwater vehicles at incidence or in maneuvering. They exhibit rich variety of complex three-dimensional turbulent shear flows, featuring: stagnation flow, highly three-dimensional boundary layer under the influence of strong pressure gradients and streamline curvature, formation and evolution of free-vortex sheet and ensuing stream-wise vortices. Most importantly spheroid flows is a paradigm for studying crossflow separation as was mentioned in the introduction.

For numerical study, we consider a 6 : 1 prolate-spheroid at an angle of attack $\alpha = 20$. The flow is taken to be incompressible and the Reynolds number Re_L based on the freestream velocity U_0 and the body length L is 4.2×10^6. This geometry and

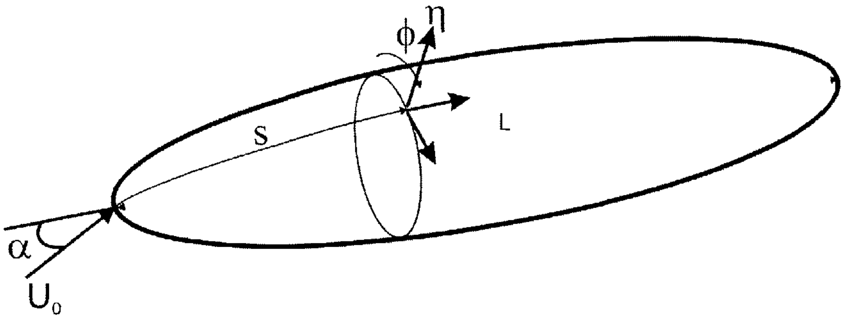

Figure 8-7: (s, ϕ, η) curvilinear coordinate system introduced to study separation on prolate spheroid.

flow conditions, agree with the experiments conducted by VPI group [101].

Simulating flow past spheroid at incline is numerically challenging. Several approaches have been employed in past including: Reduced Navier Stokes simulation [98], Large Eddy Simulation (LES) [80], Reynolds Averaged Navier Stokes Simulation (RANS) [54] and full Navier Stokes simulations. For the current work, the simulation have been carried out in *FLUENT*, a commercially available CFD software.

FLUENT implements a *finite-volume based* RANS solver for the computation with several engineering turbulence models. Based on the recommendations given in [54], *KO*-2 model which is a revised version of $k - \omega$ *Wilcox* model, has been used for the closure. For near-wall treatment *law-of-wall* and related hypothesis are used (see [54] for details).

The coordinate system adopted in this study is such that the positive x-axis is in the streamwise direction, y points to the upward vertical direction, and the $x - y$ plane makes the vertical symmetrical plane. The origin of the coordinate system is placed at the centroid of the spheroid. The symmetry of the geometry and the flow allows us to model only a half of the domain. Thus, the domain consists of the body surface, upstream/far-field inlet, vertical plane of the symmetry and exit boundary. On the wall no-slip boundary condition is used, on the inlet boundary, freestream conditions are specified and on the exit boundary, the solutions variables are extrapolated. In order to apply the algorithm given in section 8.2.4 to spheroid flow, we introduce an orthogonal curvilinear coordinate system (s, ϕ, η) (see Fig. 8-7), where: s is the *arc-length* parametrization of the ellipse (which is the curve of revolution for prolate spheroid), ϕ is the *circumferential* angle and η is the distance measured normal to the spheroid surface. The details are given in Appendix A.6, where we also summarize the crossflow separation criteria due to Wu et. al. [108] and Simpson et. al. [101] in (s, ϕ, η) coordinates. Figure 8-8a) shows the wall-shear trajectories in (s, ϕ) coordinates; due to symmetry ϕ is varied only over $[-\pi/2, \pi/2]$) (see figure 8-8b) for a complete view). The presence of primary separation line, a secondary separation line and a weak attachment line mediating the two separation line, is evident from this figure. Figure 8-9a) and b) show the scalar field C computed

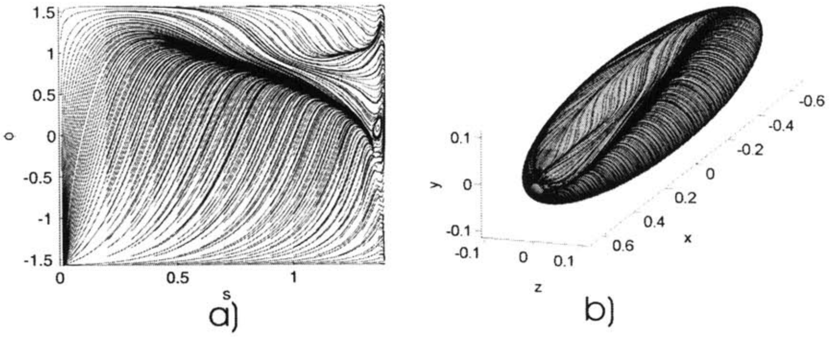

Figure 8-8: a) Wall shear trajectories over prolate spheroid in (s, ϕ) coordinates b) Wall shear trajectories shown on the prolate spheroid.

in backward and forward time along with the crossflow separation and attachment lines respectively as extracted ridges. In figure 8-9c) and d) are shown the scalar fields $\mathcal{W}$ and $\mathcal{S}$, respectively. These different criteria are compared in the figure 8-9e). Again all the predictions are identical near the nodal point of separation, with a slight difference in their point of initiation. Due to numerical difficulties we are not able to convincingly validate the crossflow separation location with streamlines (shown in figure 8-10).

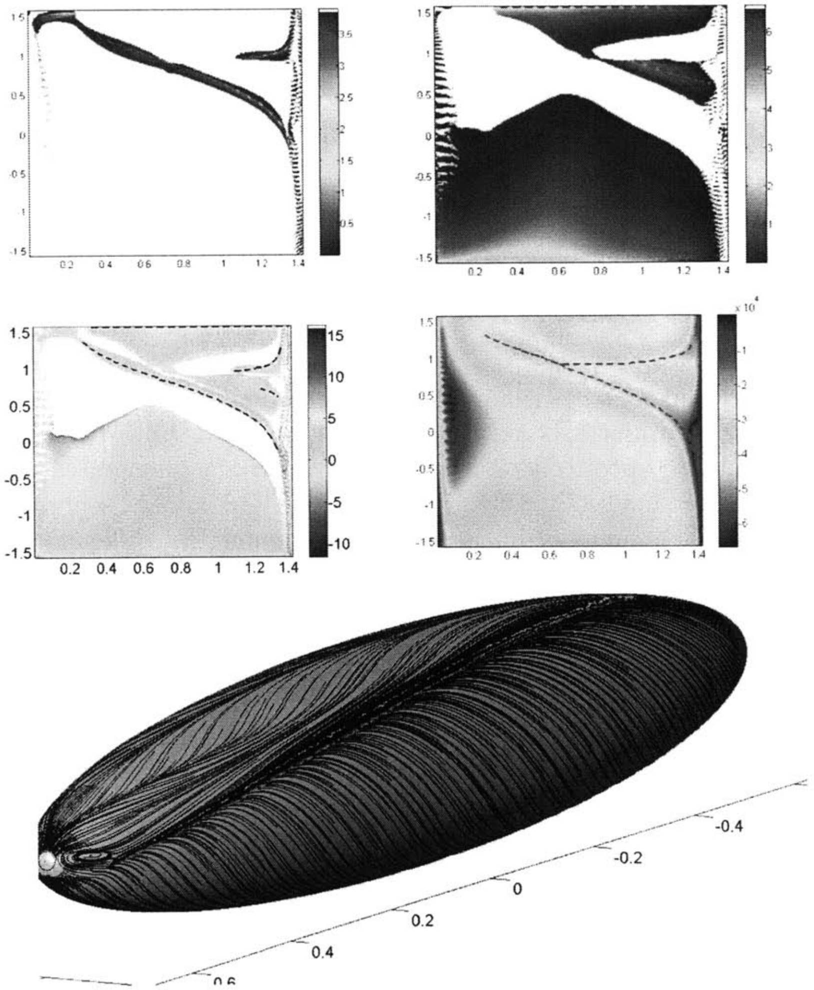

Figure 8-9: Ridges of a) Cumulative $\mathcal{C}$ for separation b) Cumulative $\mathcal{C}$ for attachment c) Scalar field $\mathcal{W}$ d) Scalar field $\mathcal{S}$ for prolate spheroid flow. Figure e) Predictions based on different criteria along with wall shear trajectories on the spheroid. The green curve is separation line and blue curve is attachment line based on scalar field $\mathcal{C}$, red curves correspond to ridges of $\mathcal{W}$ and magenta curves are the ridges of $\mathcal{S}$.

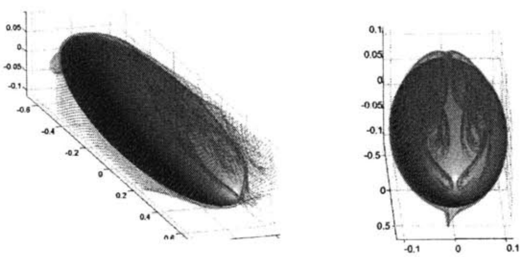

(a) (b)

Figure 8-10: a) Streamlines for prolate spheroid flow, b) Same as a) but a different view.

Chapter 9

Closure

9.1 Contributions

Using concepts from nonlinear dynamical systems theory, we have obtained a complete classification of physically observable separation and attachment patterns in steady and unsteady 3D fluid flows. We derived exact criteria to locate such patterns, which are phrased in Eulerian (lab-frame based) quantities, though our approach stems from the Lagrangian ideas. We also obtained exact formulae for locally approximating the shape of these patterns. Some notable features of our results include:

1) they are applicable to general unsteady velocity field which satisfies no slip condition and is mass conserving,
2) cover both laminar and turbulent fluid flows,
3) can detect both small-scale recirculation and large scale boundary layer separation,
4) only uses quantities computed from distributed wall-shear, wall-density and pressure measurements along the boundary.

We have verified these criteria in analytic flow models, numerical simulations of important benchmark problems and in experiments. Our analysis follows a well-defined wall-based algorithm, thus the present study of problems provides a practical recipe to uncover the geometry of three-dimensional separated flows in arbitrary flow domains.

9.2 Future Work

In addition, our work opens up opportunities to address other important related problems, which are listed below:

1) Quantitative investigation of the effect of the location and shape of separation/attachment on the unsteady hydrodynamic forces generated on a boundary

in 2D/3D flows. For example in 2D flows, separation theory when coupled with wake models [75], should lead to useful estimates of drag and lift forces. A significant challenge however is to get a handle on the global separation geometry from the wall-based measurements.

2) The wall-based separation criteria opens the door to a variety of approaches to active control of aerodynamic separation location and separation geometry, as demonstrated in two-dimensional context [2],[59]. By combining the low order models of wall-shear and pressure evolution on the boundary like those derived in [53] or Proper Orthogonal Decomposition models [7] with the 3D extension of analytic approach of [2], it seems feasible to derive feedback laws for 3D separation control. Some challenges in this approach include: modeling the interaction of actuator flow like synthetic jets with the background flow and guaranteeing controller stability in presence of inherent delays in the system.

3) Despite lack of a complete theory, separation on slip boundaries enjoys wide interest, examples being: boundary-current separation in oceanic flows, wake formation behind moving bubbles, recirculation in microfluidic devices, and lift generation on free-flying insects. Slip separation in 2D unsteady flows has been recently considered [58]. Using appropriate modifications and extensions of the techniques used in this work, it seems feasible to generalize the results of [58] to 3D unsteady free-slip flows. A particular challenge is the lack of exact solution to equations of variation along trajectories on a slip boundary.

4) Another problem that naturally follows is separation of particles of non zero volume near no-slip and slip boundaries. In 2D incompressible flows for e.g. the motion of neutrally buoyant particles can be analyzed in a 4D phase space [6]. In order to tackle such questions, separation theory has to be generalized to higher dimensions. A recent progress in this direction for studying mixing in fluid flows can be found in [41].

Appendix A

Appendix: Steady Separation

A.1 Proof of separation-line criterion

We first identify S-type and R-type strong hyperbolicity by analyzing the linearization of the scaled flow (3.10) along wall shear trajectories. We then use invariant manifold theory to deduce the emergence of a robust separation or attachment surface from strongly hyperbolic trajectories.

A.1.1 Linearized scaled flow along a wall shear trajectory

The linearized scaled flow (3.10) along a wall shear trajectory $\mathbf{x}(s, \mathbf{x}_0)$ satisfies

$$\begin{pmatrix} \xi' \\ \eta' \end{pmatrix} = \begin{pmatrix} \nabla_{\mathbf{x}}\mathbf{A}(\mathbf{x}(s, \mathbf{x}_0), 0) & \partial_z \mathbf{A}(\mathbf{x}(s, \mathbf{x}_0), 0) \\ \mathbf{0} & C(\mathbf{x}(s, \mathbf{x}_0), 0) \end{pmatrix} \begin{pmatrix} \xi \\ \eta \end{pmatrix}. \tag{A.1}$$

This linear system immediately yields the solution component

$$\eta(s) = \eta_0 e^{\int_0^s C(\mathbf{x}(r;\mathbf{x}_0),0)\, dr}, \tag{A.2}$$

which enables us to re-write the ξ-component of (A.1) as

$$\xi' = \nabla_{\mathbf{x}}\mathbf{A}(\mathbf{x}(s; \mathbf{x}_0), 0)\xi + \eta_0 \partial_z \mathbf{A}(\mathbf{x}(s; \mathbf{x}_0), 0) e^{\int_0^s C(\mathbf{x}(r;\mathbf{x}_0),0)\, dr}, \tag{A.3}$$

a two-dimensional inhomogeneous system of linear ODEs.

Observing that $\mathbf{A}(\mathbf{x}(s; \mathbf{x}_0), 0)$ is a solution of the homogeneous part of (A.3), we introduce the change of coordinates

$$\xi = \mathbf{T}(s)\rho, \qquad \mathbf{T}(s) = \left[\frac{\mathbf{A}(\mathbf{x}(s; \mathbf{x}_0), 0)}{|\mathbf{A}(\mathbf{x}(s; \mathbf{x}_0), 0)|}, \frac{\mathbf{A}^{\perp}(\mathbf{x}(s; \mathbf{x}_0), 0)}{|\mathbf{A}^{\perp}(\mathbf{x}(s; \mathbf{x}_0), 0)|} \right],$$

$$\mathbf{A}^{\perp}(\mathbf{x}(s; \mathbf{x}_0), 0) = \mathbf{J}\mathbf{A}(\mathbf{x}(s; \mathbf{x}_0)), \qquad \mathbf{J} = \begin{pmatrix} 0 & -1 \\ 1 & 0 \end{pmatrix}.$$

This coordinate change transforms (A.3) to the form

$$\rho' = \mathbf{R}(s)\rho + \eta_0 \mathbf{T}^T(s)\partial_z \mathbf{A}(\mathbf{x}(s;\mathbf{x}_0),0)e^{\int_0^s C(\mathbf{x}(r;\mathbf{x}_0),0)\ dr}, \tag{A.4}$$

where, as found by Haller & Iacono (2003) in a similar calculation, we have

$$\begin{aligned} \mathbf{R}(s) &= \begin{pmatrix} S_{\|}(s) & a(s) \\ 0 & S_{\perp}(s) \end{pmatrix}, \qquad a(s) = \left.\frac{\mathbf{A}\cdot\left([\nabla_{\mathbf{x}}\mathbf{A}]\,\mathbf{A}^{\perp} - \left[\nabla_{\mathbf{x}}\mathbf{A}^{\perp}\right]\mathbf{A}\right)}{|\mathbf{A}|^2}\right|_{\mathbf{x}=\mathbf{x}(s,\mathbf{x}_0),\ z=0}, \\ S_{\|}(s) &= \left.\frac{\mathbf{A}\cdot\left([\nabla_{\mathbf{x}}\mathbf{A}]\,\mathbf{A}\right)}{|\mathbf{A}|^2}\right|_{\mathbf{x}=\mathbf{x}(s,\mathbf{x}_0),\ z=0}, \qquad S_{\perp}(s) = \left.\frac{\mathbf{A}^{\perp}\cdot\left([\nabla_{\mathbf{x}}\mathbf{A}]\,\mathbf{A}^{\perp}\right)}{|\mathbf{A}^{\perp}|^2}\right|_{\mathbf{x}=\mathbf{x}(s,\mathbf{x}_0),\ z=0}. \end{aligned} \tag{A.5}$$

Because $\mathbf{R}(s)$ is upper diagonal, we can solve (A.4) explicitly to obtain

$$\rho(s) = \mathbf{\Psi}(s,0)\rho_0 + \eta_0 \int_{s_0}^{s} \mathbf{\Psi}(s,q)\mathbf{T}^T(q)\partial_z \mathbf{A}(\mathbf{x}(q;\mathbf{x}_0),0)e^{\int_0^q C(\mathbf{x}(r;\mathbf{x}_0),0)\ dr}dq,$$

with the matrix

$$\mathbf{\Psi}(s,s_0) = \begin{pmatrix} e^{\int_{s_0}^s S_{\|}(r)\ dr} & \int_{s_0}^s e^{\int_q^s S_{\|}(r)\ dr + \int_{s_0}^q S_{\perp}(r)\ dr} a(q)\ dq \\ 0 & e^{\int_0^s S_{\perp}(r)\ dr} \end{pmatrix}. \tag{A.6}$$

Thus, by (A.2) and (A.6), the solution of (A.1) takes the following form in the (ρ,η) coordinates:

$$\begin{pmatrix} \rho(s) \\ \eta(s) \end{pmatrix} = \mathbf{\Phi}(s)\begin{pmatrix} \rho_0 \\ \eta_0 \end{pmatrix}, \tag{A.7}$$

with

$$\begin{aligned} \mathbf{\Phi}(s) &= \begin{pmatrix} e^{\int_0^s S_{\|}(r)\ dr} & \int_0^s e^{\int_q^s S_{\|}(r)\ dr + \int_0^q S_{\perp}(r)\ dr} a(q)\ dq & d_1(s) \\ 0 & e^{\int_0^s S_{\perp}(r)\ dr} & d_2(s) \\ 0 & 0 & e^{\int_0^s C(\mathbf{x}(r;\mathbf{x}_0),0)\ dr} \end{pmatrix}, \\ \begin{pmatrix} d_1(s) \\ d_2(s) \end{pmatrix} &= \int_0^s \mathbf{\Psi}(s,q)\mathbf{T}^T(q)\partial_z \mathbf{A}(\mathbf{x}(q;\mathbf{x}_0),0)e^{\int_0^q C(\mathbf{x}(r;\mathbf{x}_0),0)\ dr}dq. \end{aligned} \tag{A.8}$$

For later use, we compute $d_2(s)$ to find

$$d_2(s) = \int_0^s e^{\int_q^s S_{\perp}(r)\ dr + \int_0^q C(\mathbf{x}(r;\mathbf{x}_0),0)\ dr} \left.\frac{\partial_z^2 w\cdot\omega}{2|\omega|}\right|_{\mathbf{x}=\mathbf{x}(q,\mathbf{x}_0),\ z=0} dq. \tag{A.9}$$

A.1.2 Strong S-hyperbolicity of wall shear trajectories

Here we give a precise mathematical definition of strong S-hyperbolicity. Strong R-hyperbolicity can be defined similarly by reversing the direction of the rescaled time s.

Consider a wall shear line γ, and let $\mathbf{x}(s;\mathbf{x}_0)$ be the wall shear trajectory starting from $\mathbf{x}_0 \in \gamma$ at $s = 0$. We say that γ is *strongly S-hyperbolic* with the stable subbundle $\{\eta = 0\}$ and with an unstable subbundle off the $\{\eta = 0\}$ plane, if the following hold:

(1) For any $\mathbf{x}_0$ and for any solution $(\rho_1(s), \rho_2(s), 0)$ of (A.1) that is initially orthogonal to γ, the solution component $\rho_2(s)$ decays to zero exponentially as $s \to \infty$, and grows exponentially as $s \to -\infty$.

(2) For any $\mathbf{x}_0$, there exists a unique one-dimensional subspace

$$N^u(\mathbf{x}_0) = \left\{k \cdot \left(0, \rho_2^0, \eta^0\right) \;\middle|\; k \in \mathbb{R},\ \eta^0 > 0,\ \left|\left(0, \rho_2^0, \eta^0\right)\right| = 1\right\},$$

such that for any solution $(\rho(s), \eta(s))$ with $(\rho(0), \eta(0)) \in N^u(\mathbf{x}_0)$, the orthogonal projection $\Pi_s\left[(\rho(s), \eta(s))\right]$ of $(\rho(s), \eta(s))$ onto the $\{\rho_1 = 0\}$ plane decays to zero exponentially as $s \to -\infty$ and grows exponentially as $s \to +\infty$.

(3) The subspace family $\operatorname{span}\{N^u(\ \cdot\ ), (1, 0, 0)\}$ is invariant under the linearized scaled flow, i.e., $\Pi_s\left[\boldsymbol{\Phi}(s) N^u(\mathbf{x}_0)\right] \subset N^u\left(\mathbf{x}\left(s; \mathbf{x}_0\right)\right)$ for any $s \in \mathbb{R}$. Furthermore, the angle $\theta\left(\mathbf{x}\left(s; \mathbf{x}_0\right)\right)$ between $N^u\left(\mathbf{x}\left(s; \mathbf{x}_0\right)\right)$ and the normal of the $\{\eta = 0\}$ plane is uniformly bounded for any s (i.e., $N^u\left(\mathbf{x}\left(s; \mathbf{x}_0\right)\right)$ does not approach the $z = 0$ boundary asymptotically).

We show the geometry of properties (2) and (3) in figure A-1.

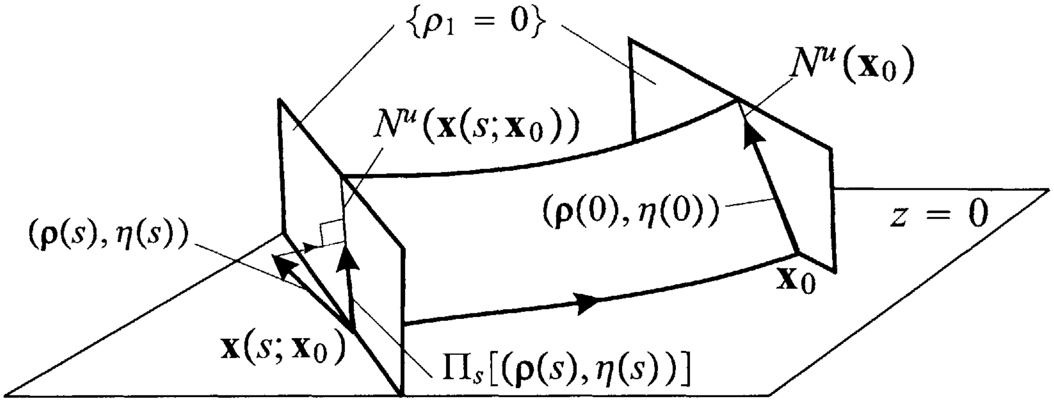

Figure A-1: Properties of the subspace family $N^u(\ \cdot\ )$.

A.1.3 Growth and decay rates along wall shear trajectories

We now compute all growth and decay rates needed to identify strong S-hyperbolicity. First, we note that by (A.7) and (A.8), property (1) above is equivalent to

$$\limsup_{s \to \infty} \frac{1}{s} \int_0^s S_\perp(r)\, dr < 0, \qquad \limsup_{s \to -\infty} \frac{1}{s} \int_0^s S_\perp(r)\, dr < 0. \tag{A.10}$$

To examine properties (2)-(3), consider a unit vector

$$\mathbf{r}^0(\mathbf{x}_0) = \begin{pmatrix} 0 \\ \rho_2^0 \\ \eta^0 \end{pmatrix} = \begin{pmatrix} 0 \\ \sin\theta(\mathbf{x}_0) \\ \cos\theta(\mathbf{x}_0) \end{pmatrix}, \qquad \cos\theta(\mathbf{x}_0) > 0,$$

in the $\{\rho_1 = 0\}$ plane. Noting that

$$\mathbf{\Phi}(s)\mathbf{r}^0(\mathbf{x}_0) = \begin{pmatrix} \sin\theta(\mathbf{x}_0) \int_0^s e^{\int_q^s S_{\parallel}(r)\ dr + \int_0^q S_{\perp}(r)\ dr} a(q)\ dq + \cos\theta(\mathbf{x}_0) d_1(s) \\ \sin\theta(\mathbf{x}_0) e^{\int_0^s S_{\perp}(r)\ dr} + \cos\theta(\mathbf{x}_0) d_2(s) \\ \cos\theta(\mathbf{x}_0) e^{\int_0^s C(\mathbf{x}(r;\mathbf{x}_0),0)\ dr} \end{pmatrix}, \quad \text{(A.11)}$$

we express property (3) as

$$\begin{aligned} \left[\sin\theta(\mathbf{x}_0) e^{\int_0^s S_{\perp}(r)\ dr} + \cos\theta(\mathbf{x}_0) d_2(s)\right] &= \tan\theta\left(\mathbf{x}(s;\mathbf{x}_0)\right) \left[\cos\theta(\mathbf{x}_0) e^{\int_0^s C(\mathbf{x}(r;\mathbf{x}_0),0)\ dr}\right], \\ \limsup_{s\in\mathbb{R}} \left|\tan\theta\left(\mathbf{x}(s;\mathbf{x}_0)\right)\right| &< \infty. \end{aligned} \quad \text{(A.12)}$$

The orthogonal projection of $\mathbf{\Phi}(s)\mathbf{r}^0(\mathbf{x}_0)$ onto the $\{\rho_1 = 0\}$ has length

$$\begin{aligned} &\sqrt{\left[\sin\theta(\mathbf{x}_0) e^{\int_0^s S_{\perp}(r)\ dr} + \cos\theta(\mathbf{x}_0) d_2(s)\right]^2 + \left[\cos\theta(\mathbf{x}_0) e^{\int_0^s C(\mathbf{x}(r;\mathbf{x}_0),0)\ dr}\right]^2} \\ = &\left|\sqrt{1 + \tan^2\theta\left(\mathbf{x}(s;\mathbf{x}_0)\right)} \cos\theta(\mathbf{x}_0) e^{\int_0^s C(\mathbf{x}(r;\mathbf{x}_0),0)\ dr}\right|. \end{aligned} \quad \text{(A.13)}$$

Based on (A.7), (A.8), (A.12) and (A.13), properties (2) and (3) can be expressed as

$$\begin{aligned} \limsup_{s\to-\infty} \frac{1}{s} \log\left[\cos\theta(\mathbf{x}_0) e^{\int_0^s C(\mathbf{x}(r;\mathbf{x}_0),0)\ dr}\right] &> 0, \\ \limsup_{s\to-\infty} \frac{1}{s} \log\left[\sqrt{1 + \tan^2\theta\left(\mathbf{x}(s;\mathbf{x}_0)\right)} \cos\theta(\mathbf{x}_0) e^{\int_0^s C(\mathbf{x}(r;\mathbf{x}_0),0)\ dr}\right] &> 0 \\ \limsup_{s\to\infty} \frac{1}{s} \log\left[\cos\theta(\mathbf{x}_0) e^{\int_0^s C(\mathbf{x}(r;\mathbf{x}_0),0)\ dr}\right] &> 0, \\ \limsup_{s\in\mathbb{R}} \left|\tan\theta\left(\mathbf{x}(s;\mathbf{x}_0)\right)\right| &< \infty, \end{aligned} \quad \text{(A.14)}$$

which is in turn equivalent to the set of conditions

$$\begin{aligned} \limsup_{s\to-\infty} \frac{1}{s} \int_0^s C(\mathbf{x}(r;\mathbf{x}_0),0)\ dr &> 0, \\ \limsup_{s\to\infty} \frac{1}{s} \int_0^s C(\mathbf{x}(r;\mathbf{x}_0),0)\ dr &> 0, \\ \limsup_{\mathbf{x}_0\in\gamma} \left|\tan\theta\left(\mathbf{x}_0\right)\right| &< \infty. \end{aligned} \quad \text{(A.15)}$$

A.1.4 Separation slope

We shall now argue that the third condition in (A.15) already follows from (A.10) and from the remaining two conditions in (A.15). As a side result, we obtain an expression for the angle between the separation surface and the local wall normal.

Recall that under conditions (A.15), the second component of $\mathbf{\Phi}(s)\mathbf{r}^0(\mathbf{x}_0)$ decays exponentially to zero as $s \to -\infty$:

$$\limsup_{s\to-\infty} \frac{1}{s} \log \left| \sin\theta(\mathbf{x}_0) e^{\int_0^s S_\perp(r)\,dr} + \cos\theta(\mathbf{x}_0) d_2(s) \right| > 0. \tag{A.16}$$

Equivalently, for all $s < 0$ with large enough $|s|$, we have

$$0 < K_1 \leq \frac{1}{s} \log \left| \sin\theta(\mathbf{x}_0) e^{\int_0^s S_\perp(r)\,dr} + \cos\theta(\mathbf{x}_0) d_2(s) \right|, \tag{A.17}$$

where the constant $K_1 > 0$ can be selected arbitrarily small. For $s < 0$, we can rewrite (A.17) as

$$\frac{e^{K_1 s}}{e^{\int_0^s S_\perp(r)\,dr}} \geq \left| \sin\theta(\mathbf{x}_0) + \cos\theta(\mathbf{x}_0) \frac{d_2(s)}{e^{\int_0^s S_\perp(r)\,dr}} \right|.$$

Taking the limit $s \to -\infty$ on both sides of this last inequality, using the second inequality in (A.10), and selecting

$$0 < K_1 < -\limsup_{s\to-\infty} \frac{1}{s} \int_0^s S_\perp(r)\,dr,$$

we obtain $\tan\theta(\mathbf{x}_0) = -\lim_{s\to-\infty} \left[d_2(s) / \exp \int_0^s S_\perp(r)\,dr \right]$, i.e.,

$$\tan\theta(\mathbf{x}_0) = \int_{-\infty}^{0} e^{\int_0^s [C(\mathbf{x}(r;\mathbf{x}_0),0) - S_\perp(r)]\,dr} \left. \frac{\partial_z^2 \mathbf{u} \cdot \omega}{2|\omega|} \right|_{\mathbf{x}=\mathbf{x}(s,\mathbf{x}_0),\ z=0} ds. \tag{A.18}$$

Now, by the boundedness of $\mathbf{x}(s, \mathbf{x}_0)$, the second factor in the integrand in (A.18) is uniformly bounded. Also, by the second inequality in (A.10) and by the first inequality in (A.15), the first factor in the integrand in (A.18) decays exponentially in q with an exponent that is uniformly bounded in $\mathbf{x}_0$.

From the above, we conclude that (A.18) always gives a $\tan\theta(\mathbf{x}_0)$ value that is well-defined and uniformly bounded in $\mathbf{x}_0$ whenever the second inequality in (A.10) and the first inequality in (A.15) hold. Selecting the $\theta(\mathbf{x}_0)$ defined by (A.18) and proceeding backward through the steps leading from (A.16) to (A.18), we find that the second component of $\mathbf{\Phi}(s)\mathbf{r}^0(\mathbf{x}_0)$ always decays exponentially to zero if the second inequality in (A.10) and the first inequality in (A.15) hold. Thus, the third condition in (A.15) is superfluous.

A.1.5 Quantitative separation and attachment criteria

The discussion above implies that the strong S-hyperbolicity conditions in (A.10) and (A.15) can be summarized as

$$\begin{aligned}
\limsup_{s\to+\infty}\frac{1}{s}\int_0^s S_\perp(r)\,dr &< 0, & \limsup_{s\to-\infty}\frac{1}{s}\int_0^s S_\perp(r)\,dr &< 0,\\
\limsup_{s\to+\infty}\frac{1}{s}\int_0^s C(\mathbf{x}(r;\mathbf{x}_0),0)\,dr &> 0, & \limsup_{s\to-\infty}\frac{1}{s}\int_0^s C(\mathbf{x}(r;\mathbf{x}_0),0)\,dr &> 0.
\end{aligned} \tag{A.19}$$

With the constants

$$\begin{aligned}
n_+ &= \limsup_{s\to+\infty}\frac{1}{s}\int_0^s S_\perp(r)\,dr, & n_- &= \limsup_{s\to-\infty}\frac{1}{s}\int_0^s S_\perp(r)\,dr,\\
w_+ &= \limsup_{s\to+\infty}\frac{1}{s}\int_0^s C(\mathbf{x}(r;\mathbf{x}_0),0)\,dr, & w_- &= \limsup_{s\to-\infty}\frac{1}{s}\int_0^s C(\mathbf{x}(r;\mathbf{x}_0),0)\,dr,
\end{aligned}$$

the separation conditions (A.19) take the simple form

$$n_\pm < 0, \qquad w_\pm > 0. \tag{A.20}$$

For *attachment lines*, we obtain an analogous criterion by reversing time in all our arguments; this leads to the attachment conditions

$$n_\pm > 0, \qquad w_\pm < 0. \tag{A.21}$$

A.1.6 Qualitative separation and attachment criteria

Robust separation- and attachment lines

We recall that the α-limit set of a wall shear trajectory $\mathbf{x}\,(s;\mathbf{x}_0)$ is the set of points visited arbitrarily closely by $\mathbf{x}\,(s;\mathbf{x}_0)$ as $s \to -\infty$. The α-limit set is always invariant, i.e., consists of a set of full trajectories. If γ is bounded, then its α-limit set is guaranteed to be nonempty, closed and connected (see, e.g., Guckenheimer & Holmes 1983).

We also recall that the ω-limit set of $\mathbf{x}\,(s;\mathbf{x}_0)$ is defined as the α-limit set of $\mathbf{x}\,(-s;\mathbf{x}_0)$, i.e., the set of points visited arbitrarily closely by $\mathbf{x}\,(s;\mathbf{x}_0)$ as $s \to +\infty$.The properties of ω-limit sets are identical to those listed above for α-limit sets. By the Poincaré-Bendixson theory, the α- and ω-limit set of a bounded planar trajectory is either a fixed point, a set of fixed points connected by wall shear trajectories, or a limit cycle (see, e.g., Guckenheimer & Holmes 1983).

As a consequence, the α-limit set for a strongly S-hyperbolic wall shear trajectory $\mathbf{x}\,(s;\mathbf{x}_0)$ cannot be a stable invariant set because $\mathbf{x}\,(s;\mathbf{x}_0)$ approaches the α-limit set it in backward time. Furthermore, the α-limit set cannot be an unstable node, unstable spiral, or unstable limit cycle distinct from $\mathbf{x}(s;\mathbf{x}_0)$; in each such case, $\mathbf{x}(s;\mathbf{x}_0)$ would attract nearby wall shear trajectories as $s \to -\infty$.

Therefore, the only possible α-limit set for a bounded strongly S-hyperbolic wall shear trajectory $\mathbf{x}(s;\mathbf{x}_0)$ is a saddle-type wall shear zero or an unstable limit cycle coinciding with $\mathbf{x}(s;\mathbf{x}_0)$. Both the saddle and the limit cycle must be structurally stable, i.e., robust under small perturbations to the flow (see property (v) in our requirements for separation in section 2.2.1). Saddles and limit cycles are known to be structurally stable if they are *nondegenerate*, i.e., attract nearby wall shear trajectories at an exponential rate as $s \to -\infty$.

The ω-limit set of a bounded strongly S-hyperbolic wall shear trajectory $\mathbf{x}(s;\mathbf{x}_0)$ can only be a stable node, a stable spiral, an attracting limit cycle, an attracting curve of fixed points with wall shear trajectories connecting them. For any other ω-limit set, $\mathbf{x}(s;\mathbf{x}_0)$ would not attract all infinitesimally close trajectories of (3.10) in the $z = 0$ plane.

The last two of the above ω-limit sets – sets of zeros and zeros connected by trajectories – are structurally unstable, i.e., can be dramatically altered by arbitrary small perturbations to the flow. For this reason, we have to exclude them as possible ω-limit sets for a separation line by the robustness requirement (v) of section 2.2.1.

The requirement of robustness also implies the following: if the ω-limit set of a wall shear trajectory $\mathbf{x}(s;\mathbf{x}_0)$ in a separation line is a stable node, then the node must have unequal negative eigenvalues and $\mathbf{x}(s;\mathbf{x}_0)$ must be tangent to the eigenvector corresponding to the larger eigenvalue. Figure A-2 shows how equal eigenvalues and tangency to the eigenvector with the smaller eigenvalue leads to a structurally unstable separation line.

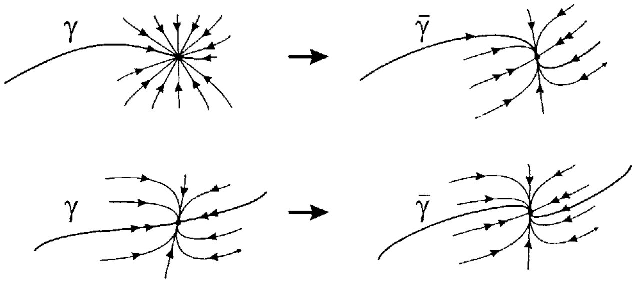

Figure A-2: The effect of small perturbations on wall shear lines asymptotic to a degenerate stable node (improper node). Also, the effect of small perturbations on a wall shear line tangent to the weaker eigenvector of a nondegenerate node (proper node).

The remaining two possible ω-limit sets – stable spirals and stable limit cycles – are structurally stable, as long as they are nondegenerate, i.e., attract nearby wall shear trajectories at an exponential rate as $s \to \infty$.

Based on the above discussion, the only possible separation lines are those listed in (S1)-(S4) of section 3.4. Reversing the direction of time in our arguments, we obtain that the only possible attachment lines are those listed in (R1)-(R4) of section 3.4.

Separation and attachment surfaces

Having identified the only possible candidates for separation and attachment lines, we now give additional conditions under which such candidates are actual separation or attachment lines, i.e., are contained in separation or attachment surfaces emanating from the wall.

Conditions on α-limit sets Assume that the α-limit set of a strongly S-hyperbolic wall shear trajectory $\mathbf{x}(s;\mathbf{x}_0)$ is a nondegenerate saddle-type wall shear zero $\mathbf{p}$. Then $\mathbf{p}$ is a saddle-type fixed point for the rescaled flow (3.10) with two eigenvectors in the $z=0$ plane. The trajectory $\mathbf{x}(s;\mathbf{x}_0)$ is tangent to the eigenvector corresponding to a positive eigenvalue; the other eigenvector of $\mathbf{p}$–corresponding to a negative eigenvalue–is transverse to γ in the $z=0$ plane.

Because the trajectory $\mathbf{x}(s;\mathbf{x}_0)$ is strongly S-hyperbolic, we know that

$$w_- = \limsup_{s\to-\infty} \frac{1}{s}\int_0^s C(\mathbf{x}(r;\mathbf{x}_0),0)\ dr > 0 \tag{A.22}$$

must hold by (A.20). Since $\mathbf{x}(s;\mathbf{x}_0)$ tends to $\mathbf{p}$ exponentially fast in s, we have

$$w_- = \operatorname{sign}\ C(\mathbf{p},0) = \operatorname{sign}\ \partial_z^2 w(\mathbf{p},0),$$

which, by (A.22), implies

$$\partial_z^2 w(\mathbf{p},0) > 0. \tag{A.23}$$

Assume now that the α-limit set of a strongly S-hyperbolic $\mathbf{x}(s;\mathbf{x}_0)$ is a nondegenerate unstable limit cycle that coincides with $\mathbf{x}(s;\mathbf{x}_0)$. If T denotes the period of the limit cycle, then the strong S-hyperbolicity condition (A.22) implies

$$\begin{aligned} w_- &= \limsup_{s\to-\infty} \frac{1}{s}\int_0^s C(\mathbf{x}(r;\mathbf{x}_0),0)\ dr \\ &= \limsup_{n\to-\infty} \frac{1}{nT}\left[n\int_0^T C(\mathbf{x}(r;\mathbf{x}_0),0)\ dr\right] \\ &= \frac{1}{2T}\int_0^T \partial_z^2 w(\mathbf{x}(s;\mathbf{x}_0),0)\ ds > 0, \end{aligned}$$

or, equivalently,

$$\int_\Gamma \partial_z^2 w\ ds > 0. \tag{A.24}$$

Conditions on ω-limit sets Assume that the ω-limit set of a strongly S-hyperbolic wall shear trajectory $\mathbf{x}(s;\mathbf{x}_0)$ is a nondegenerate spiral-type or node-type wall shear zero $\mathbf{q}$. Then repeating the argument leading to condition (A.23), we find that $w_+ > 0$ implies

$$\partial_z^2 w(\mathbf{q},0) > 0.$$

Assume now that the ω-limit set of a strongly S-hyperbolic $\mathbf{x}(s;\mathbf{x}_0)$ is a nondegenerate stable limit cycle Γ. Again, repeating the argument leading to (A.24), we find that $w_+ > 0$ implies

$$\int_\Gamma \partial_z^2 w \, ds > 0.$$

Existence of a separation surface Assume that the α-limit set of a strongly S-hyperbolic wall shear trajectory $\mathbf{x}(s;\mathbf{x}_0)$ is a nondegenerate saddle-type wall shear zero $\mathbf{p}$. We have seen that $\mathbf{p}$ must satisfy condition (A.23), which means that the linearized rescaled flow must have a second positive eigenvalue with the corresponding eigenvector off the $z = 0$ plane.

By the stable manifold theorem (see, e.g., Guckenheimer & Holmes 1983), the scaled flow (3.10) has a unique continuously differentiable two-dimensional unstable manifold $W^u(\mathbf{p})$, containing trajectories of (3.10) that are backward-asymptotic to $\mathbf{p}$. $W^u(\mathbf{p})$ is also known to be tangent to the plane $E^u(\mathbf{p})$ spanned by the eigenvectors corresponding to the two positive eigenvalues of the saddle $\mathbf{p}$.

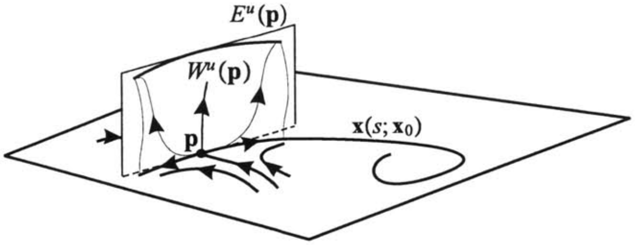

Figure A-3: The construction of the separation surface as the two-dimensional unstable manifold of the saddle $\mathbf{p}$.

Now $\mathbf{x}(s;\mathbf{x}_0)$ is backward-asymptotic to $\mathbf{p}$, hence $\mathbf{x}(s;\mathbf{x}_0)$ is contained in $W^u(\mathbf{p})$. But $\mathbf{x}(s;\mathbf{x}_0)$ is also contained in the invariant plane $z = 0$, thus $W^u(\mathbf{p})$ must intersect the $z = 0$ plane all along $\mathbf{x}(s;\mathbf{x}_0)$.

Along the intersection, $W^u(\mathbf{p})$ remains transverse to the $z = 0$ plane. Indeed, the linearized flow map of (A.8) is a diffeomorphism, and hence cannot map linearly independent vectors into linearly dependent vectors along $\mathbf{x}(s;\mathbf{x}_0)$. Also, under the action of the linearized scaled flow (A.1), off-wall vectors tangent to $W^u(\mathbf{p})$ along $\mathbf{x}(s;\mathbf{x}_0)$ will converge to the off-plane unstable eigenvector of $\mathbf{p}$, and hence remain bounded away from the $z = 0$ plane. Thus, the angle between $W^u(\mathbf{p})$ and the wall normal at $\mathbf{x}_0$ is precisely $\theta(\mathbf{x}_0)$, as computed in (A.18). We conclude that $\mathcal{S} = W^u(\mathbf{p})$ satisfies properties (i)-(iv) of a separation surface with slope (A.18).

Assume now that the α-limit set of a strongly S-hyperbolic wall shear trajectory $\mathbf{x}(s;\mathbf{x}_0)$ is a nondegenerate unstable limit cycle Γ that coincides with $\mathbf{x}(s;\mathbf{x}_0)$. Then condition (A.24) and the formula for (A.8) imply that $\boldsymbol{\Phi}(T)$, the linearized period-T map (Poincaré map) along Γ for the scaled flow, has an eigenvector off the $z = 0$ plane with eigenvalue

$$e^{\frac{1}{2}\int_\Gamma \partial_z^2 w \, ds} > 1.$$

Since Γ is a nondegenerate stable limit cycle in the $z = 0$ plane, $\mathbf{\Phi}(T)$ must also have an eigenvalue of modulus less than one with the corresponding eigenvector transverse to Γ in the $z = 0$ plane.

The stable manifold theorem for maps (see, e.g., Guckenheimer & Holmes 1983) then implies the existence of a unique and continuously differentiable one-dimensional unstable manifold for $\mathbf{\Phi}(T)$, which means a two-dimensional unstable manifold $W^u(\Gamma)$ for Γ. Again, only vectors tangent to $W^u(\Gamma)$ along Γ remain bounded away from $z = 0$ plane in backward time under the linearized flow (A.1). Consequently, the angle between $W^u(\Gamma)$ and the wall normal at $\mathbf{x}_0$ is precisely $\theta(\mathbf{x}_0)$, as computed in (A.18). We conclude that the surface $\mathcal{S} = W^u(\Gamma)$ satisfies all properties (i)-(iv) of a separation surface with slope (A.18)

The separation criteria (S1)-(S4) of section 3.4 simply summarize the results of this appendix. Reversing the direction of the scaled time s, we obtain the attachment criteria (R1)-(R4) of section 3.4.

A.1.7 Tangential separation is not robust

The existence of a tangential separation curve is equivalent to the unboundedness of the first expression in (3.28). Since the wall-pressure gradient is uniformly bounded in a regular steady Navier-Stokes flow, the first expression in (3.28) can only be unbounded if the matrix

$$-2\nabla_{\mathbf{x}}\tau(\mathbf{p}) + \nabla_{\mathbf{x}} \cdot \tau(\mathbf{p})\,\mathbf{I} \tag{A.25}$$

becomes singular. That is the case if and only if $\nabla_{\mathbf{x}} \cdot \tau(\mathbf{p})/2$ is a multiplicity-two eigenvalue of the wall-shear Jacobian $\nabla_{\mathbf{x}}\tau(\mathbf{p})$.

Out of all possible wall-shear zeros that can generate separation, only nonhyperbolic fixed points and improper stable nodes can have repeated eigenvalues. Nonhyperbolic fixed points, however, will disappear under generic small perturbations. Improper stable nodes do not disappear, but become proper nodes or spirals under small perturbations. As a result, all robust separation curves must be transverse to the boundary.

The existence of a tangential separation surface is equivalent to the unboundedness of the improper integral in the second expression in (3.28). Note, however, that the first factor in this improper integral decays exponentially, and the second factor is uniformly bounded whenever the separation line is bounded. Tangential separation, therefore, could only occur if the separation line started from a nonhyperbolic fixed point or a nonhyperbolic limit cycle of the wall-shear field. Again, such objects are not robust under perturbations.

A.2 Nondegeneracy of separation and attachment lines

The qualitative conditions (S1)-(S4) and (R1)-(R4) determine four possible separation and four possible attachment patterns. To identify such patterns in applications, we must also verify the inequalities (A.20) and (A.21), which represent nondegeneracy conditions for the saddles, nodes, spirals, and limit cycles to which the separation lines asymptote. For completeness, we now list the corresponding nondegeneracy conditions for all cases.

We shall use the characteristic equation

$$\lambda^2 - \nabla_{\mathbf{x}} \cdot \tau(\bar{\mathbf{x}})\lambda + \det \nabla_{\mathbf{x}}\tau(\bar{\mathbf{x}}) = 0 \tag{A.26}$$

associated with the wall shear Jacobian $\nabla_{\mathbf{x}}\tau(\bar{\mathbf{x}})$. We shall also use wall shear trajectories $\mathbf{x}(s)$ that solve the ODE $\mathbf{x}' = \tau(\mathbf{x})$.

(S1) $\mathbf{x}(s)$ originates from a *saddle* $\mathbf{p}$ and ends in a *stable spiral* $\mathbf{q}$.

(a) $n_+ < 0$: $\mathbf{q}$ attracts nearby wall shear trajectories at an asymptotic exponential rate if the Jacobian $\nabla_{\mathbf{x}}\tau(\mathbf{p})$ has eigenvalues with negative real parts, i.e., (A.26) has roots with $\mathrm{Re}\lambda_i < 0$ for $\bar{\mathbf{x}} = \mathbf{q}$. That is precisely the case if

$$\nabla_{\mathbf{x}} \cdot \tau(\mathbf{q}) < 0, \qquad [\nabla_{\mathbf{x}} \cdot \tau(\mathbf{q})]^2 < 4 \det \nabla_{\mathbf{x}}\tau(\mathbf{q}). \tag{A.27}$$

(b) $w_+ > 0$: This condition simplifies to $C(\mathbf{q}, 0) > 0$, which requires

$$\partial_z^2 w(\mathbf{q}, 0) > 0. \tag{A.28}$$

(c) $n_- < 0$: This condition holds if $\mathbf{p}$ is a nondegenerate saddle, i.e., by (A.26),

$$\det \nabla_{\mathbf{x}}\tau(\mathbf{p}) < 0. \tag{A.29}$$

(d) $w_- > 0$: This condition simplifies to $C(\mathbf{p}, 0) > 0$, which requires

$$\partial_z^2 w(\mathbf{p}, 0) > 0. \tag{A.30}$$

(S2) $\mathbf{x}(s)$ originates from a *saddle* $\mathbf{p}$ and ends in a *stable node* $\mathbf{q}$.

(a) $n_+ < 0$: $\nabla_{\mathbf{x}}\tau(\mathbf{q})$ must have unequal negative eigenvalues, i.e., by (A.26), we must have

$$\nabla_{\mathbf{x}} \cdot \tau(\mathbf{q}) < 0, \qquad [\nabla_{\mathbf{x}} \cdot \tau(\mathbf{q})]^2 > 4 \det \nabla_{\mathbf{x}}\tau(\mathbf{q}). \tag{A.31}$$

(b) $w_+ > 0$: Same as (A.28).

(c) The eigenvector corresponding to the smaller eigenvalue of $\nabla_{\mathbf{x}}\tau(\mathbf{q})$ is

$$\mathbf{e}(\mathbf{q}) = \left(-2\partial_y\tau_x(\mathbf{q})\ ,\ 2\partial_x\tau_y(\mathbf{q}) - \nabla_{\mathbf{x}}\cdot\tau(\mathbf{q}) + \sqrt{[\nabla_{\mathbf{x}}\cdot\tau(\mathbf{q})]^2 - 4\det\nabla_{\mathbf{x}}\tau(\mathbf{q})}\right).$$

As we discussed earlier (cf. figure A-2), $\mathbf{x}(s)$ cannot be tangent to $\mathbf{e}(\mathbf{q})$, thus we must have

$$\mathbf{e}(\mathbf{q}) \times \lim_{s\to\infty}\frac{\tau(\mathbf{x}(s))}{|\tau(\mathbf{x}(s))|} \neq \mathbf{0}. \tag{A.32}$$

(d) $n_- < 0$: Same as (A.29).

(e) $w_- > 0$: Same as (A.30).

(S3) $\mathbf{x}(s)$ originates from a *saddle* $\mathbf{p}$ and spirals onto a *stable limit cycle* Γ.

(a) $n_+ < 0$: The limit cycle must attract nearby wall shear trajectories at an exponential rate. That is the case if the average normal strain rate along Γ is negative, i.e., $\int_\Gamma S_\perp(s)\,ds < 0$. Using the definition of $S_\perp(s)$, we therefore obtain

$$\int_\Gamma \frac{\omega\cdot(\nabla_{\mathbf{x}}\tau\omega)}{|\omega|^2}\,ds < 0. \tag{A.33}$$

(b) $w_+ > 0$: The limit cycle should be of saddle-type, i.e., must repel nearby off-wall trajectories of the scaled flow (3.10) at an exponential rate. That is the case if the average of $C(\mathbf{x},0) > 0$ along Γ is positive, i.e.,

$$\int_\Gamma \partial_z^2 w\,ds > 0. \tag{A.34}$$

(c) $n_- < 0$: Same as (A.29).

(d) $w_- > 0$: Same as (A.30).

$\mathbf{x}(s)$ is a *stable limit cycle* Γ.

(a) $n_+ < 0$: Same a (A.33).

(b) $w_+ > 0$: Same as (A.34).

(c) $n_- < 0$: Holds whenever (A.33) is satisfied ($n_- = n_+$).

(d) $w_- > 0$: Holds whenever (A.34) is satisfied ($w_- = w_+$).

The corresponding nondegeneracy conditions for attachment patterns are obtained from identical arguments in backward time. We only list the results:

(R1) $\mathbf{x}(s)$ originates from an *unstable spiral* $\mathbf{p}$ and ends in a *saddle* $\mathbf{q}$.

(a) $n_- > 0$: Equivalent to

$$\nabla_{\mathbf{x}} \cdot \tau(\mathbf{q}) > 0, \qquad [\nabla_{\mathbf{x}} \cdot \tau(\mathbf{q})]^2 < 4 \det \nabla_{\mathbf{x}} \tau(\mathbf{q}). \tag{A.35}$$

(b) $w_- < 0$: Equivalent to

$$\partial_z^2 w\,(\mathbf{p}, 0) < 0. \tag{A.36}$$

(c) $n_+ > 0$: Equivalent to

$$\det \nabla_{\mathbf{x}} \tau(\mathbf{q}) < 0. \tag{A.37}$$

(d) $w_+ < 0$: Equivalent to

$$\partial_z^2 w\,(\mathbf{q}, 0) < 0. \tag{A.38}$$

(R2) $\mathbf{x}(s)$ originates from an *unstable node* $\mathbf{p}$ and ends in a *saddle* $\mathbf{q}$.

(a) $n_- > 0$: Equivalent to

$$\nabla_{\mathbf{x}} \cdot \tau(\mathbf{q}) > 0, \qquad [\nabla_{\mathbf{x}} \cdot \tau(\mathbf{q})]^2 > 4 \det \nabla_{\mathbf{x}} \tau(\mathbf{q}). \tag{A.39}$$

(b) $w_- < 0$: Same as (A.36).

(c) With the vector

$$\mathbf{e}(\mathbf{p}) = \left(-2\partial_y \tau_x(\mathbf{p})\ ,\ 2\partial_x \tau_y(\mathbf{p}) - \nabla_{\mathbf{x}} \cdot \tau(\mathbf{p}) - \sqrt{[\nabla_{\mathbf{x}} \cdot \tau(\mathbf{p})]^2 - 4 \det \nabla_{\mathbf{x}} \tau(\mathbf{p})} \right),$$

we must have

$$\mathbf{e}(\mathbf{p}) \times \lim_{s \to -\infty} \frac{\tau\left(\mathbf{x}(s)\right)}{\left|\tau\left(\mathbf{x}(s)\right)\right|} \neq \mathbf{0}. \tag{A.40}$$

(d) $n_+ > 0$: Same as (A.37).

(e) $w_+ > 0$: Same a (A.38).

(R3) $\mathbf{x}(s)$ spirals off an *unstable limit cycle* Γ and ends in a *saddle* $\mathbf{q}$.

(a) $n_- > 0$: Equivalent to

$$\int_\Gamma \frac{\omega \cdot (\nabla_{\mathbf{x}} \tau \omega)}{|\omega|^2}\, ds > 0. \tag{A.41}$$

(b) $w_- < 0$: Equivalent to

$$\int_\Gamma \partial_z^2 w \; ds < 0. \tag{A.42}$$

(c) $n_+ > 0$: Same as (A.37).
(d) $w_+ > 0$: Same a (A.38).

(R4) $\mathbf{x}(s)$ is an *unstable limit cycle* Γ.

(a) $n_- > 0$: Same as (A.41).
(b) $w_- < 0$: Same as (A.42).
(c) $n_+ > 0$: Holds whenever (A.41) is satisfied.
(d) $w_+ > 0$: Holds whenever (A.42) is satisfied.

A.3 Separation at corners

Using the form given in Eq. 3.32 for the velocity field and introducing the rescaled time s through the relation $ds/dt = x(t)z(t)$, we find that streamlines satisfy

$$\frac{d}{ds}(x, y, z) = (xA, B, zC). \tag{A.43}$$

A point $\mathbf{p} = (0, p)$ in the $z = 0$ plane is a fixed point for Eq. A.43 if

$$B(\mathbf{p}, 0) = 0. \tag{A.44}$$

To understand the topology of limiting streamlines near $(\mathbf{p}, 0)$, we linearize Eq. A.43 at $(\mathbf{p}, 0)$. The linearization of the scaled velocity field (Eq. A.43) at $(\mathbf{p}, 0)$ admits the coefficient matrix

$$\mathbf{M}(\mathbf{p}) = \begin{pmatrix} A(\mathbf{p},0) & 0 & 0 \\ \partial_x B(\mathbf{p},0) & \partial_y B(\mathbf{p},0) & \partial_z B(\mathbf{p},0) \\ 0 & 0 & C(\mathbf{p},0) \end{pmatrix}. \tag{A.45}$$

Restricted to the $z = 0$ plane, the eigenvalues of $\mathbf{M}(\mathbf{p})$ are

$$A(\mathbf{p}, 0) = \partial^3_{xxz} u(\mathbf{p}, 0), \qquad \partial_y B(\mathbf{p}, 0) = \partial^3_{xyz} v(\mathbf{p}, 0), \tag{A.46}$$

thus $\mathbf{p}$ can only be a saddle or a node for the rescaled Eq. A.43 within the $z = 0$ plane.

From the characteristic Eq. A.45, we find that $\mathbf{p}$ is a nondegenerate node within the $z = 0$ plane in Eq. A.43 if

$$[A(\mathbf{p}, 0) + \partial_y B(\mathbf{p}, 0)]^2 > 4A(\mathbf{p}, 0)\partial_y B(\mathbf{p}, 0) > 0, \tag{A.47}$$

whereas $\mathbf{p}$ is a nondegenerate saddle within the $z = 0$ plane if

$$A(\mathbf{p}, 0)\partial_y B(\mathbf{p}, 0) < 0. \tag{A.48}$$

Combining Eqns. A.47 and A.48 with Eq. A.46 gives the nondegeneray conditions in Eqns. 3.35 and 3.36.

Using the form in Eq. 3.32 for the velocity field in the continuity equation (Eq. 3.1), we obtain

$$\nabla\rho \cdot (x^2zA, xzB, xz^2C) + \rho xz[2A + x\partial_x A + \partial_y B + 2C + z\partial_z C] = 0,$$

or, equivalently,

$$\nabla\rho \cdot (xA, B, zC) + \rho[2A + x\partial_x A + \partial_y B + 2C + z\partial_z C] = 0. \tag{A.49}$$

By Eq. A.44, at the equilibrium $\mathbf{p}$, Eq. A.49 reduces to

$$2A(\mathbf{p}, 0) + \partial_y B(\mathbf{p}, 0) + 2C(\mathbf{p}, 0) = 0, \tag{A.50}$$

which is equivalent to Eq. 3.34 by Eq. A.46.

A.4 Simplification of slope formula along limit cycle

Consider a limit cycle Γ which is a separation line and therefore satisfies

$$\int_\Gamma C(\mathbf{x}(s, \mathbf{x}_0))ds > 0, \qquad \int_\Gamma S_\perp(s)ds < 0. \tag{A.51}$$

To obtain a simplification of slope formula (3.28) along Γ, we introduce

$$F(s) = e^{\int_0^s P(r)\, dr} R(s), \tag{A.52}$$

where

$$P(s) = C(\mathbf{x}(s, \mathbf{x}_0)) - \overline{S}_\perp(s), \qquad R(s) = \frac{\partial_z^2 \mathbf{u} \cdot \omega}{2|\omega|}|_{\mathbf{x}=\mathbf{x}(s,\mathbf{x}_0),\ z=0}. \tag{A.53}$$

By periodicity of Γ, $\mathbf{x}(s, \mathbf{x}_0) = \mathbf{x}(s + T, \mathbf{x}_0)$, hence $P(s)$ and $R(s)$ are also periodic functions with the same period. Then

$$\begin{aligned} F(s+T) &= e^{\int_0^{s+T} P(r)\, dr} R(s+T) = e^{\int_0^T P(r)\, dr} e^{\int_T^{s+T} P(r)\, dr} R(s) \\ &= e^{\int_0^T P(r)\, dr} e^{\int_0^s P(r)\, dr} R(s) = e^{\int_0^T P(r)\, dr} F(s), \end{aligned} \tag{A.54}$$

and hence for any integer n

$$F(s+nT) = K^n F(s),$$

where

$$K = e^{\int_0^T P(r)\,dr}. \qquad \text{(A.55)}$$

The slope formula (3.28) can be expressed in terms of function F as

$$\begin{aligned}
\tan\tilde{\theta}(\xi_0, t_0) &= \lim_{n\to\infty}\int_{-nT}^{0} F(s)ds = \lim_{n\to\infty}\left[\int_{-nT}^{-(n-1)T} F(s)ds + \int_{-(n-1)T}^{-(n-2)T} F(s)ds + \cdots \int_{-T}^{0} F(s)d\right. \\
&= \lim_{n\to\infty}\left[\int_0^T F(s-nT)ds + \int_0^T F(s-(n-1)T)ds + \cdots \int_0^T F(s-T)ds\right], \\
&= \int_0^T F(s)ds \lim_{n\to\infty}\left[K^{-n} + K^{-(n-1)} + \cdots K^{-1}\right], \\
&= \frac{\int_0^T F(s)ds}{K}\left[1 + \frac{1}{K} + \frac{1}{K^2}\cdots\right], \qquad \text{(A.}
\end{aligned}$$

where we have used (A.4). The above series converges since $K > 1$, by strong hyperbolicity of Γ (A.51) and we obtain

$$\tan\tilde{\theta}(\xi_0, t_0) = \frac{\int_0^T F(s)ds}{K-1}. \qquad \text{(A.57)}$$

Substituting the expressions (A.52) and (A.55) for F and K respectively we get the simplified formula (3.31).

A.5 Flow Models

A.5.1 The Perry-Chong procedure

We seek the velocity field $\mathbf{u}(\mathbf{x}) = (u_1(\mathbf{x}), u_2(\mathbf{x}), u_3(\mathbf{x}))$, with $\mathbf{x} \equiv (x_1, x_2, x_3)$,$x_3 > 0$, as a Taylor-expansion at the boundary point $\mathbf{x} = \mathbf{0}$:

$$u_i = A_i + \sum_{j=1}^{3} A_{ij}x_j + \sum_{j,k=1}^{3} A_{ijk}x_jx_k + \sum_{j,k,l=1}^{3} A_{ijkl}x_jx_kx_l + \sum_{j,k,l,m=1}^{3} A_{ijklm}x_jx_kx_lx_m + \ldots, \qquad \text{(A.58)}$$

with dots referring to terms of higher order. A_i, A_{ij}, A_{ijk}, and A_{ijkl} are symmetric tensors in all their indices except for the first one. The total number of independent coefficients is 105.

Perry & Chong (1986) find relations among $A_{ij\ldots}$ by forcing (A.58) to satisfy the continuity equation (3.1), the no-slip boundary conditions on the boundary $x_3 = 0$, and the vorticity transport equations up to cubic order in x_i. For $\rho = 1\ kg/m^3$, this procedure yields

$$\begin{aligned}
A_{1233} &= A_{2133}, \qquad A_{1333} = -2A_{1113} - A_{1223} - A_{2123}, \\
A_{2333} &= -A_{2113} - A_{1123} - 2A_{2223}, \qquad A_{11233} = A_{21133}, \\
A_{11333} &= -2A_{11113} - A_{11223} - A_{21123}, \qquad A_{12233} = A_{21233} \\
A_{12333} &= -2A_{11123} - A_{12223} - A_{21223}, \\
A_{11133} &= -\frac{A_{223}A_{13}}{24\nu} - \frac{A_{23}A_{123}}{12\nu} - \frac{A_{13}A_{113}}{24\nu} - \frac{A_{21233} + A_{12233} + A_{13333}}{2}, \\
A_{22333} &= -A_{21123} - 2A_{22223} - A_{11223}, \quad A_{21333} = -A_{21113} - 2A_{21223} - A_{11123}, \\
A_{22233} &= -\frac{A_{113}A_{23}}{24\nu} + \frac{A_{13}A_{213}}{12\nu} + \frac{A_{23}A_{223}}{24\nu} - \frac{A_{21133} + A_{11233} + A_{23333}}{2}.
\end{aligned} \tag{A.59}$$

The above relations – combined with the continuity equations and the no-slip condition on the wall – reduce the total number of unknown coefficients to 29. These remaining coefficients can be determined by prescribing local features of the wall shear field

$$\begin{aligned}
\tau_1(x_1, x_2) &= a_1 + b_1x_1 + c_1x_2 + d_1x_1^2 + e_1x_1x_2 + f_1x_2^2 \\
&+ g_1x_1^3 + h_1x_1^2x_2 + i_1x_1x_2^2 + j_1x_2^3 \\
\tau_2(x_1, x_2) &= a_2 + b_2x_1 + c_2x_2 + d_2x_1^2 + e_2x_1x_2 + f_2x_2^2 \\
&+ g_2x_1^3 + h_2x_1^2x_2 + i_2x_1x_2^2 + j_2x_2^3.
\end{aligned}$$

Equating $\partial_{x_3}(u_1, u_2)|_{x_3=0}$, with (τ_1, τ_2), we obtain

$$\begin{aligned}
A_{13} &= a_1, & A_{113} &= \frac{b_1}{2}, & A_{123} &= \frac{c_1}{2}, & & \\
A_{1113} &= \frac{d_1}{3}, & A_{1123} &= \frac{e_1}{6}, & A_{1223} &= \frac{f_1}{3}, & & \\
A_{11113} &= \frac{g_1}{4}, & A_{11123} &= \frac{h_1}{12}, & A_{11223} &= \frac{i_1}{12}, & A_{12223} &= \frac{j_1}{4}, \\
A_{23} &= a_2, & A_{213} &= \frac{b_2}{2}, & A_{223} &= \frac{c_2}{2}, & & \\
A_{2113} &= \frac{d_2}{3}, & A_{2123} &= \frac{e_2}{6}, & A_{2223} &= \frac{f_2}{3}, & & \\
A_{21113} &= \frac{g_2}{4}, & A_{21123} &= \frac{h_2}{12}, & A_{21223} &= \frac{i_2}{12}, & A_{22223} &= \frac{j_2}{4}.
\end{aligned} \tag{A.60}$$

This leaves nine free coefficients: A_{133}, A_{233}, A_{2133} A_{1133}, A_{2233}, A_{13333}, A_{21133}, A_{21233} and A_{23333}. By choosing these parameters appropriately, we can create various flow patterns near the boundary.

A.5.2 Model with linear wall shear field

Consider a linear wall shear field

$$\begin{aligned}\tau_1(x_1, x_2) &= a_1 + b_1 x_1 + c_1 x_2, \\ \tau_2(x_1, x_2) &= a_2 + b_2 x_1 + c_2 x_2,\end{aligned}$$

which has a unique zero if $b_1 c_2 - b_2 c_1 \neq 0$. By (A.59) and (A.60), we obtain the corresponding velocity field

$$\begin{aligned}u_1 &= a_1 x_3 + b_1 x_1 x_3 + c_1 x_2 x_3 + x_3^2 \left[A_{133} + A_{1133} x_1 + A_{1233} x_2\right], \\ u_2 &= a_2 x_3 + b_2 x_1 x_3 + c_2 x_2 x_3 + x_3^2 \left[A_{233} + A_{1233} x_1 + A_{2233} x_2\right], \\ u_3 &= -\frac{b_1 + c_2}{2} x_3^2 - \frac{A_{1133} + A_{2233}}{3} x_3^3, \end{aligned} \qquad \text{(A.61)}$$

with nine free parameters. For simplicity, we take $a_1 = a_2 = 0$, which places the wall shear zero at the origin. In addition, we let $A_{133} = \alpha$, $A_{233} = \beta$, $A_{1133} = A_{2233} = \delta$ and $A_{1233} = 0$. The parameters α, β, and δ then determine the type and the direction of the separation or attachment at the point $x_1 = x_2 = 0$.

A.5.3 Model with unbounded separatrix in the wall shear field

Consider the skin friction field

$$\begin{aligned}\tau_1(x_1, x_2) &= a x_1, \\ \tau_2(x_1, x_2) &= -b x_2 + c x_1^2,\end{aligned}$$

For $a, b > 0$, this wall shear field has a unique saddle-type zero at the origin. The unstable manifold of the saddle is the x_2 axis; the stable manifold of the saddle has an unbounded parabola-type shape.

We set A_{133}, A_{2133},A_{233}, A_{2233}, A_{13333}, A_{21133}, A_{21233} and A_{23333} equal to zero and let $A_{1133} = -d$. Then (A.59)-(A.60) give the velocity field (5.3) with all the remaining coefficients obtained from the equations (A.59)-(A.60).

A.5.4 Model with separation bubble

We now consider a quadratic wall shear field

$$\begin{aligned}\tau_1(x_1, x_2) &= (x_1/a)^2 + (x_2/b)^2 - 1, \\ \tau_2(x_1, x_2) &= -(c x_1 + d) x_2,\end{aligned}$$

which has a pair of zeros symmetric to the x_1 axis, and another pair symmetric to the x_2 axis. The first pair of zeros are saddles, whereas the second pair are typically spirals. Such a zero distribution is the typical on-wall signature of a separation bubble.

Using (A.59)-(A.60) and letting $A_{133} = \alpha$, $A_{233} = \beta$, $A_{1133} = A_{2233} = \delta$ and $A_{1233} = 0$, we obtain the corresponding velocity field (5.6).

A.5.5 Model with stable limit cycle in the wall shear field

Consider the skin friction field

$$\begin{aligned}\tau_1(x_1, x_2) &= \mu x_1 + x_2 - x_1^3 - x_1 x_2^2, \\ \tau_2(x_1, x_2) &= -x_1 + \mu x_2 - x_2 x_1^2 - x_2^3.\end{aligned}$$

Passing to polar coordinates reveals that for $\mu > 0$, this wall shear field has an attracting limit cycle at $x_1^2 + x_2^2 = \mu$, which encircles an unstable spiral at the origin. The limit cycle is created in a supercritical Hopf bifurcation as μ is varied from negative to positive values. For simplicity, we choose all remaining free coefficients in (A.59)-(A.60) to be zero, which yields the velocity field (5.8).

As we show in section 5.1.4, the above example exhibits open separation along the limit cycle, with a separation surface that is orthogonal to the $z = 0$ plane. Exploiting the cylindrical symmetry of the model, we can also find a higher-order approximation to the separation surface as follows.

We transform the velocity field (5.8) to cylindrical coordinates to obtain the rescaled equations of motion

$$\begin{aligned}\dot{r} &= \mu r - r^3 + \frac{8}{3} z^2, \\ \dot{\theta} &= -1, \\ \dot{z} &= -\mu z + 2 z r^2 - \frac{4}{3} z^3.\end{aligned}$$

Due to rotational symmetry in θ, the (r, z) subsystem

$$\begin{aligned}\dot{r} &= \mu r - r^3 + \frac{8}{3} z^2, \\ \dot{z} &= -\mu z + 2 z r^2 - \frac{4}{3} z^3, \end{aligned} \tag{A.62}$$

decouples from the full scaled flow and can be analyzed separately.

The limit cycle Γ appears in (A.62) as a saddle-type fixed point $(\bar{r}, \bar{z}) = (\sqrt{\mu}, 0)$. The separation surface emanating from Γ is then the unstable manifold of $(\bar{r}, \bar{z})$, which we seek in the form

$$r = f(z) = \sqrt{\mu} + a z^2 + \mathcal{O}(z^3). \tag{A.63}$$

Using the invariance of the unstable manifold, we differentiate both sides of (A.63) in time and use (A.62) to obtain

$$f(z) = \sqrt{\mu} + \frac{8}{3(7 - 3\mu)} z^2,$$

which gives

$$x^2 + y^2 - \frac{16\sqrt{\mu}}{3(7-3\mu)} z^2 = \mu + \mathcal{O}(z^4), \tag{A.64}$$

a quadratic approximation for the separation surface.

A.5.6 Model with homoclinic bifurcation in the wall shear field

The quadratic wall shear field

$$\begin{aligned} \tau_1(x_1, x_2) &= x_2, \\ \tau_2(x_1, x_2) &= x_1 + \mu x_2 - x_1^2 - x_1 x_2, \end{aligned}$$

is one of the simplest possible vector fields that admit a homoclinic bifurcation as the parameter μ is varied through zero (see Khalil 2002). The homoclinic bifurcation involves the creation and destruction of an orbit that connects a saddle point at $(x_1, x_2) = (0, 0)$ to itself.

The τ-field also admits another fixed point $(x_1, x_2) = (0, 1)$, which undergoes a supercritical Hopf bifurcation as μ is varied through zero. For a range of parameters, the attracting limit cycle created by the Hopf bifurcation also attracts the unstable manifold of the saddle point, creating a connection between the saddle and the limit cycle. For simplicity, we again choose all remaining free coefficients in (A.59)-(A.60) to be zero, which yields the velocity field (5.10).

A.6 Vorticity-based separation theory

Here we summarize the vorticity-based incompressible separation theory of Wu et al. [108]. We express their results in our notation for comparison with our theory.

Let the $\mathbf{x}^{\perp}(s; \mathbf{x}_0)$ be a trajectory of the wall-vorticity field $\omega(\mathbf{x})$. Let $\mathbf{e}(s)$ and $\mathbf{n}(s)$ be the unit tangent and the unit normal to $\mathbf{x}^{\perp}(s)$ so that

$$\mathbf{e}(s) = \frac{\mathbf{A}^{\perp}(\mathbf{x}^{\perp}(s; \mathbf{x}_0), 0)}{|\mathbf{A}^{\perp}(\mathbf{x}^{\perp}(s; \mathbf{x}_0), 0)|}, \qquad \mathbf{n}(s) = \frac{\mathbf{A}(\mathbf{x}^{\perp}(s; \mathbf{x}_0), 0)}{|\mathbf{A}(\mathbf{x}^{\perp}(s; \mathbf{x}_0), 0)|}.$$

The curvature $\kappa_2(s)$ of $\mathbf{x}^{\perp}(s; \mathbf{x}_0)$ satisfies

$$\mathbf{e}' = \kappa_2 \mathbf{n}, \tag{A.65}$$

thus,

$$\begin{aligned} \kappa_2(s) &= \left(\frac{d}{ds} \frac{\mathbf{A}^{\perp}}{\sqrt{\mathbf{A} \cdot \mathbf{A}}} \right) \cdot \mathbf{n} = \left(\frac{(\nabla_{\mathbf{x}} \mathbf{A}^{\perp}) \, \mathbf{A}^{\perp}}{\sqrt{\mathbf{A} \cdot \mathbf{A}}} - \frac{\frac{d}{ds} \mathbf{A} \cdot \mathbf{A}}{\sqrt{\mathbf{A} \cdot \mathbf{A}}^3} \mathbf{A}^{\perp} \right) \cdot \frac{\mathbf{A}}{|\mathbf{A}(\mathbf{x}^{\perp}(s), 0)|} \\ &= \frac{\mathbf{A} \cdot \left(\left[\nabla_{\mathbf{x}} \mathbf{A}^{\perp} \right] \mathbf{A}^{\perp} \right)}{\sqrt{\mathbf{A} \cdot \mathbf{A}}^3} = \frac{\mathbf{A} \cdot \left(\left[\nabla_{\mathbf{x}} \mathbf{J} \mathbf{A} \right] \mathbf{A}^{\perp} \right)}{\sqrt{\mathbf{A} \cdot \mathbf{A}}^3} = -\frac{\mathbf{A}^{\perp} \cdot \left(\left[\nabla_{\mathbf{x}} \mathbf{A} \right] \mathbf{A}^{\perp} \right)}{|\mathbf{A}^{\perp}|^3}. \end{aligned}$$

We conclude that at any point $\mathbf{x}_0$,

$$\kappa_2 = -S_{\perp}/\left|\mathbf{A}\right|. \tag{A.66}$$

Furthermore, along a wall shear trajectory $\mathbf{x}(s;\mathbf{x}_0)$, we have

$$\begin{aligned}\eta_1(s) &= \frac{d}{ds}\log\left|\mathbf{A}\left(\mathbf{x}(s;\mathbf{x}_0),0\right)\right| = \frac{1}{\left|\mathbf{A}\right|}\frac{2\frac{d}{ds}\mathbf{A}\cdot\mathbf{A}}{2\sqrt{\mathbf{A}\cdot\mathbf{A}}} \\ &= \frac{\mathbf{A}\cdot\left(\left[\nabla_{\mathbf{x}}\mathbf{A}\right]\mathbf{A}\right)}{\left|\mathbf{A}\right|^3},\end{aligned}$$

thus at any point $\mathbf{x}_0$, we have

$$\eta_1 = S_{\|}/\left|\mathbf{A}\right|. \tag{A.67}$$

Wu et al. ([108]) require that in a separation zone, wall shear trajectories should converge and the flow should develop an upwelling. They find that these two requirements are equivalent to

$$\kappa_2 > 0, \qquad \kappa_2\left(\kappa_2 - \eta_1\right) > 0,$$

which, by (A.66) and (A.67), can be rewritten as

$$S_{\perp} < 0, \qquad S_{\perp} + S_{\|} < 0. \tag{A.68}$$

For attachment lines, the analogous criteria are

$$S_{\perp} > 0, \qquad S_{\perp} + S_{\|} > 0.$$

Wu et al. [108] also propose that in addition to satisfying (A.66)-(A.67), a separation line must also be a local maximizing curve (*ridge*) for the scalar field

$$\varphi = \kappa_2\left(\kappa_2 - \eta_1\right) = S_{\perp}\left(S_{\perp} + S_{\|}\right)/\left|\mathbf{A}\right|^2 = S_{\perp}\left(S_{\perp} + S_{\|}\right)/\left|\omega\right|^2,$$

which is the product of the τ-line curvature and the strength of the wall-normal upwelling normalized by the wall-vorticity. Thus, Wu et al. propose that the separation line must be a portion of a wall shear line satisfying

$$\nabla_{\mathbf{x}}\varphi\cdot\omega = 0, \qquad \omega^T\left[\nabla^2_{\mathbf{x}}\varphi\right]\omega < 0. \tag{A.69}$$

Wu et al. also state that (A.68)-(A.69) may be satisfied over an entire wall shear line (closed separation) or on part of a wall shear trajectory (open separation).

Note, however, that unless the φ-field is degenerate, (A.69) defines ridges that are not wall shear lines. Indeed, along any wall shear trajectory $\mathbf{x}(s;\mathbf{x}_0)$,

$$\frac{d}{ds}\left\{\nabla_{\mathbf{x}}\varphi\left(\mathbf{x}(s;\mathbf{x}_0)\right)\cdot\omega\left(\mathbf{x}(s;\mathbf{x}_0)\right)\right\} = \frac{1}{\rho\nu}\left\{\omega^T\left[\nabla^2_{\mathbf{x}}\varphi\right] + \left(\nabla_{\mathbf{x}}\varphi\right)^T\left[\nabla_{\mathbf{x}}\omega\right]\right\}\cdot\tau\Big|_{\mathbf{x}(s;\mathbf{x}_0)} \neq 0,$$

unless $\tau\left(\mathbf{x}(s;\mathbf{x}_0)\right) \equiv 0$ *or* $\tau\left(\mathbf{x}\right)$ is linear, in which case $\nabla^2_{\mathbf{x}}\varphi \equiv \mathbf{0}$ and $\nabla_{\mathbf{x}}\omega \equiv \mathbf{0}$. Thus, away from wall shear zeros, the trajectories of a nondegenerate wall shear field do not coincide with the ridges of φ.

We conclude that (A.69) fails to capture either open or closed separation lines unless the τ-field is degenerate. Indeed, the vorticity-based separation theory fails to identify the correct separation line in all of our examples of section 5.1, even though it provides a close approximation near wall shear zeros. Citing numerical difficulties, Wu et al. [108] were unable to validate (A.69) in their example involving a flow past a prolate spheroid. Nevertheless, their example appears to admit a large near-linear domain for the τ-field, thus an exact numerical evaluation of (A.69) may give a good approximation for the separation line.

Finally, Wu et al. [108] propose that for incompressible Navier-Stokes flows, the separation angle defined in figure (2-5) satisfies

$$\tan\theta_\omega(\mathbf{x}_0) = \left.\frac{\partial_2 p}{|\tau|\left(3\kappa_2 - \eta_1\right)}\right|_{\mathbf{x}=\mathbf{x}_0,\ z=0}, \tag{A.70}$$

where ∂_2 denotes the derivative in the direction of ω and p denotes the pressure. Noting that

$$\partial_2 p = \frac{\left(\nabla_{\mathbf{x}} p, \omega\right)}{|\omega|},$$

and using (A.66)-(A.67), we rewrite (A.70) to obtain

$$\tan\theta_\omega(\mathbf{x}_0) = \left.\frac{\nabla_{\mathbf{x}} p\cdot\omega}{|\tau|\left(-3S_\perp - S_{||}\right)}\right|_{\mathbf{x}=\mathbf{x}_0,z=0} = -\frac{1}{\rho\nu}\left.\frac{\nabla_{\mathbf{x}} p\cdot\omega}{|\omega|\left(3S_\perp + S_{||}\right)}\right|_{\mathbf{x}=\mathbf{x}_0,z=0}. \tag{A.71}$$

To see the connection between this vorticity-based slope-approximation and the true separation slope $\tan\theta(\mathbf{x}_0)$ obtained in (3.28), assume that $\mathbf{x}(s,\mathbf{x}_0)\equiv\mathbf{x}_0$ holds, i.e., $\mathbf{x}_0$ is a zero of the wall shear field. Then the exact slope formula (3.28) can be evaluated as

$$\begin{aligned}\tan\theta(\mathbf{x}_0) &= \frac{1}{\nu\rho}\int_{-\infty}^{0} e^{-\frac{1}{2}\left[3S_\perp(\mathbf{x}_0)+S_{||}(\mathbf{x}_0)\right]s}\,\frac{\nabla_{\mathbf{x}} p(\mathbf{x}_0,0)\cdot\omega(\mathbf{x}_0)}{2|\omega(\mathbf{x}_0)|}ds \\ &= -\frac{1}{\rho\nu}\left.\frac{\nabla_{\mathbf{x}} p\cdot\omega}{|\omega|\left(3S_\perp + S_{||}\right)}\right|_{\mathbf{x}=\mathbf{x}_0,z=0} = \tan\theta_\omega(\mathbf{x}_0).\end{aligned} \tag{A.72}$$

Thus, $\tan\theta(\mathbf{x}_0)$ and $\tan\theta_\omega(\mathbf{x}_0)$ are equal at wall shear zeros, but differ at other points in nondegenerate fluid flows. Indeed, (3.28) and (A.71) only agree throughout γ if the wall shear field is linear and $\nabla_{\mathbf{x}} p\cdot\omega/|\omega|$ in constant along γ.

Appendix B

Appendix: Fixed Unsteady Separation

B.1 Averaged equations

To derive the first-order averaged equation (4.5) from (4.3), we introduce the near-identity change of variables

$$\eta = \zeta + \epsilon \mathbf{w}(\zeta, t),$$

leading to

$$\begin{aligned}
\dot{\eta} &= \dot{\zeta} + \epsilon \nabla_\zeta \mathbf{w}(\zeta, t)\dot{\zeta} + \epsilon \partial_t \mathbf{w}(\zeta, t) \\
&= \epsilon \mathbf{f}(\zeta + \epsilon \mathbf{w}(\zeta, t), t) + \epsilon^2 \mathbf{g}(\zeta + \epsilon \mathbf{w}(\zeta, t), t; \epsilon) \\
&= \epsilon \mathbf{f}(\zeta, t) + \epsilon^2 [\nabla_\zeta \mathbf{f}(\zeta, t)\mathbf{w}(\zeta, t) + \mathbf{g}(\zeta, t; 0)] + \mathcal{O}(\epsilon^3).
\end{aligned}$$

Rearranging gives

$$\dot{\zeta} = (\mathbf{I} + \epsilon \nabla_\zeta \mathbf{w}(\zeta, t))^{-1} \left\{ \epsilon \left[\mathbf{f}(\zeta, t) - \partial_t \mathbf{w}(\zeta, t) \right] + \epsilon^2 [\nabla_\zeta \mathbf{f}(\zeta, t)\mathbf{w}(\zeta, t) + \mathbf{g}(\zeta, t; 0)] + \mathcal{O}(\epsilon^3) \right\}.$$

For small ϵ, we have the expansion

$$(\mathbf{I} + \epsilon \nabla_\zeta \mathbf{w}(\zeta, t))^{-1} = \mathbf{I} - \epsilon \nabla_\zeta \mathbf{w}(\zeta, t) + \mathcal{O}(\epsilon^2),$$

which gives

$$\begin{aligned}
\dot{\zeta} &= \epsilon \left[\mathbf{f}(\zeta, t) - \partial_t \mathbf{w}(\zeta, t) \right] \\
&\quad + \epsilon^2 \left[\nabla_\zeta \mathbf{f}(\zeta, t)\mathbf{w}(\zeta, t) + \mathbf{g}(\zeta, t; 0) + \nabla_\zeta \mathbf{w}(\zeta, t)\partial_t \mathbf{w}(\zeta, t) - \nabla_\zeta \mathbf{w}(\zeta, t)\mathbf{f}(\zeta, t) \right] + \mathcal{O}(\epsilon^3).
\end{aligned}$$

Choosing

$$\mathbf{w}(\zeta, t) = \int_{t_0}^{t} [\mathbf{f}(\zeta, t) - \overline{\mathbf{f}}(\zeta)] d\tau, \qquad \overline{\mathbf{f}}(\zeta) = \lim_{T \to \infty} \frac{1}{T} \int_{t_0 - T}^{t_0} \mathbf{f}(\zeta, \tau) d\tau,$$

for a given t_0, we obtain the first-order averaged normal form

$$\dot{\zeta} = \epsilon\overline{\mathbf{f}}(\zeta) + \epsilon^2\mathbf{f}^1(\zeta, t) + \mathcal{O}(\epsilon^3),$$

where

$$\begin{aligned} \mathbf{f}^1(\zeta, t) &= \nabla_\zeta\mathbf{f}(\zeta, t)\mathbf{w}(\zeta, t) + \mathbf{g}(\zeta, t; 0) + \nabla_\zeta\mathbf{w}(\zeta, t)\partial_t\mathbf{w}(\zeta, t) - \nabla_\zeta\mathbf{w}(\zeta, t)\mathbf{f}(\zeta, t), \\ &= \nabla_\zeta\mathbf{f}(\zeta, t)\mathbf{w}(\zeta, t) + \mathbf{g}(\zeta, t; 0) - \nabla_\zeta\mathbf{w}(\zeta, t)\overline{\mathbf{f}}(\zeta). \end{aligned}$$

With $\zeta = (\mathbf{q}, p)$ and

$$\begin{aligned} \overline{\tau}(\mathbf{q}) &= \lim_{T\to\infty}\frac{1}{T}\int_{t_0-T}^{t_0}\mathbf{A}_1(\mathbf{q}, 0, \tau)d\tau, \qquad \phi(\mathbf{q}, t; t_0) = \int_{t_0}^{t}[\mathbf{A}_1(\mathbf{q}, 0, t) - \overline{\tau}(\mathbf{q})]d\tau, \\ \overline{C}(\mathbf{q}) &= \lim_{T\to\infty}\frac{1}{T}\int_{t_0-T}^{t_0}C_1(\mathbf{q}, 0, \tau)d\tau, \qquad \psi(\mathbf{q}, t; t_0) = \int_{t_0}^{t}[C_1(\mathbf{q}, 0, t) - \overline{C}(\mathbf{q})]d\tau, \end{aligned}$$

we can express $\overline{\mathbf{f}}$ as

$$\overline{\mathbf{f}}(\zeta) = \begin{pmatrix} p\overline{\tau}(\mathbf{q}) \\ p^2\overline{C}(\mathbf{q}) \end{pmatrix}.$$

Similarly we can express $\mathbf{f}^1$ as

$$\mathbf{f}^1(\zeta, t) = \begin{pmatrix} p^2\mathbf{F}(\mathbf{q}, t) \\ p^3G(\mathbf{q}, t) \end{pmatrix}, \tag{B.1}$$

where

$$\begin{aligned} \mathbf{F}(\mathbf{q}, t) &= (\nabla_\mathbf{x}\mathbf{A}_1(\mathbf{q}, 0, t) - \overline{C}\mathbf{I})\phi + \mathbf{A}_1(\mathbf{q}, 0, t)\psi + \partial_z\mathbf{A}_1(\mathbf{q}, 0, t) - \nabla_\mathbf{x}\phi\overline{\tau}, \\ G(\mathbf{q}, t) &= \nabla_\mathbf{x}C_1(\mathbf{q}, 0, t) \cdot \phi + 2(C_1(\mathbf{q}, 0, t) - \overline{C})\psi + \partial_z C_1(\mathbf{q}, 0, t) - \nabla_\mathbf{x}\psi \cdot \overline{\tau}, \end{aligned}$$

with $\cdot$ denoting the standard inner product.

The second-order averaged form is obtained in a similar manner. Specifically, we eliminate the time dependence in $\mathbf{f}^1$ by introducing the change of variables

$$\zeta = \xi + \epsilon^2\mathbf{h}(\xi, t), \quad \mathbf{h}(\xi, t) = \int_{t_0}^{t}[\mathbf{f}^1(\xi, t) - \overline{\mathbf{f}}^1(\xi)]d\tau.$$

We follow the same procedure as above to obtain

$$\dot{\xi} = \epsilon\overline{\mathbf{f}}(\xi) + \epsilon^2\overline{\mathbf{f}}^1(\xi) + \mathcal{O}(\epsilon^3), \tag{B.2}$$

where

$$\overline{\mathbf{f}}^1(\xi) = \lim_{T\to\infty}\frac{1}{T}\int_{t_0-T}^{t_0}\mathbf{f}^1(\xi, \tau)d\tau = \begin{pmatrix} s^2\overline{F}(\mathbf{r}) \\ s^3\overline{G}(\mathbf{r}) \end{pmatrix},$$

with $\xi = (\mathbf{r}, s)$ and

$$\overline{\mathbf{F}} = \lim_{T\to\infty} \frac{1}{T} \int_{t_0-T}^{t_0} \mathbf{F}(\mathbf{r}, \tau)d\tau, \qquad \overline{G} = \lim_{T\to\infty} \frac{1}{T} \int_{t_0-T}^{t_0} G(\mathbf{r}, \tau)d\tau.$$

In component form, we can rewrite (B.2) as

$$\begin{aligned} \dot{\mathbf{r}} &= \epsilon s[\overline{\tau}(\mathbf{r}) + s\epsilon\overline{\mathbf{F}}(\mathbf{r})] + \mathcal{O}(\epsilon^3), \\ \dot{s} &= \epsilon s^2[\overline{C}(\mathbf{r}) + s\epsilon\overline{G}(\mathbf{r})] + \mathcal{O}(\epsilon^3). \end{aligned} \tag{B.3}$$

B.2 Persistence of separation patterns in the full flow

In this appendix, we prove Theorem 1 of section 4.2.2 and Theorem 2 of section 4.2.3. The proof relies on topological invariant manifold techniques that we apply on a case-by-case basis.

B.2.1 Persistence of separation curves: node and spiral

For system (4.13), the point $(\mathbf{p}, 0)$ is a separation point if and only if (cf. chapter 3)

$$\overline{\tau}(\mathbf{p}) = 0, \qquad \nabla_{\mathbf{x}} \cdot \overline{\tau}(\mathbf{p}) < 0, \qquad \det\nabla_{\mathbf{x}}\overline{\tau}(\mathbf{p}) > 0, \qquad \overline{C}(\mathbf{p}) > 0, \tag{B.4}$$

Here we show that under the same conditions, the unstable manifold emanating from $\mathbf{p}$ persists in the full system (4.5). This result is not obvious because the no-slip boundary conditions make the unstable manifold degenerate (nonhyperbolic), and hence its survival under small perturbations is not guaranteed by classic dynamical systems results.

Recall that the first-order averaged normal form (4.5) in the component form $\zeta = (\mathbf{q}, p)$ is given by

$$\begin{aligned} \dot{\mathbf{q}} &= \epsilon p\overline{\tau}(\mathbf{q}) + \epsilon^2 p^2 \mathbf{n}_1(\mathbf{q}, p, \epsilon, t), \\ \dot{p} &= \epsilon p^2 \overline{C}(\mathbf{q}) + \epsilon^2 p^3 n_2(\mathbf{q}, p, \epsilon, t), \end{aligned} \tag{B.5}$$

where the $\mathcal{O}(\epsilon^2)$ terms are bounded by our assumptions. By making the change of coordinates $\mathbf{q} \longrightarrow \mathbf{q} - \mathbf{x}_0$, where $\mathbf{x}_0$ is any point on the boundary, we transform the first-order averaged equations (B.5) to the form

$$\begin{aligned} \dot{\mathbf{q}} &= \epsilon p\overline{\tau}(\mathbf{x}_0) + \epsilon p\nabla_{\mathbf{x}}\overline{\tau}(\mathbf{x}_0) \cdot \mathbf{q} + \epsilon p[\mathbf{m}_1(\mathbf{q}, p, \epsilon, t)q_1^2 + \mathbf{m}_2(\mathbf{q}, p, \epsilon, t)q_1 q_2 + \mathbf{m}_3(\mathbf{q}, p, \epsilon, t)q_2^2], \\ &+ \epsilon^2 p^2 \mathbf{m}_4(\mathbf{q}, p, \epsilon, t), \\ \dot{p} &= \epsilon p^2 \overline{C}(\mathbf{x}_0) + \epsilon^2 p^3 m_5(\mathbf{q}, p, \epsilon, t) + \epsilon p^2 \mathbf{q} \cdot \mathbf{m}_6(\mathbf{q}, p, \epsilon, t), \end{aligned} \tag{B.6}$$

where $\mathbf{m}_i$ are appropriate smooth functions that are uniformly bounded in their arguments, notably in t.

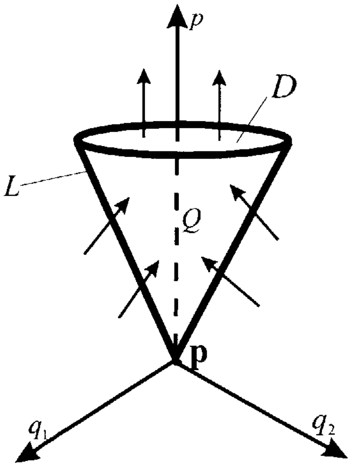

Figure B-1: Geometry of the set Q.

Choosing $\mathbf{x}_0 = \mathbf{p}$ in (B.6), we obtain

$$\begin{aligned} \dot{\mathbf{q}} &= \epsilon p \nabla_{\mathbf{x}} \overline{\tau}(\mathbf{p}) \cdot \mathbf{q} + \epsilon p [\mathbf{m}_1(\mathbf{q}, p, \epsilon, t) q_1^2 + \mathbf{m}_2(\mathbf{q}, p, \epsilon, t) q_1 q_2 + \mathbf{m}_3(\mathbf{q}, p, \epsilon, t) q_2^2] \\ &\quad + \epsilon^2 p^2 \mathbf{m}_1(\mathbf{q}, p, \epsilon, t), \\ \dot{p} &= \epsilon p^2 \overline{C}(\mathbf{p}) + \epsilon^2 p^3 m_5(\mathbf{q}, p, \epsilon, t) + \epsilon p^2 \mathbf{q} \cdot \mathbf{m}_6(\mathbf{q}, p, \epsilon, t), \end{aligned} \tag{B.7}$$

as transformed equations of motion for fluid particles near $\mathbf{p}$.

Consider the solid cone

$$Q = \{(\mathbf{q}, p) \mid |\mathbf{q}| \leq \alpha p, \quad 0 \leq p \leq \beta\},$$

where α and β are positive constants to be selected below (figure B-1). The lateral surface L of this cone is

$$L = \{(\mathbf{q}, p) \in Q \mid \ |\mathbf{q}| = \alpha p\}, \tag{B.8}$$

which can be parameterized by $q_1 = \alpha p \cos(\theta)$, $q_2 = \alpha p \sin(\theta)$, where $\theta \in [0, 2\pi)$ and $\alpha = \tan(\psi)$ with ψ denoting the half-angle of the cone. The outward unit normal $\mathbf{n}$ to Q can be written as

$$\mathbf{n} = \frac{1}{\sqrt{1+\alpha^2}} \begin{pmatrix} \cos(\theta) \\ \sin(\theta) \\ -\alpha \end{pmatrix}. \tag{B.9}$$

Finally, the top disk D of the cone can be described as

$$D = \{(\mathbf{q}, p) \in Q \mid p = \beta\}. \tag{B.10}$$

Restricted to the disk D, the particle equations of motion become

$$\begin{aligned}
\dot{p}|_{p=\beta} &= \epsilon\beta^2\left[\overline{C}(\mathbf{p}) + \epsilon\beta m_5(\mathbf{q},\beta,\epsilon,t) + \mathbf{q}\cdot\mathbf{m}_6(\mathbf{q},\beta,\epsilon,t)\right], \\
&\geq \epsilon\beta^2[\overline{C}(\mathbf{p}) - \epsilon p|m_5(\mathbf{q},p,\epsilon,t)| - |\,\mathbf{q}|\cdot|m_6(\mathbf{q},p,\epsilon,t)|] \geq \epsilon\beta^2\frac{\overline{C}(\mathbf{p})}{2} > 0,
\end{aligned}$$

provided that we choose ϵ and β appropriately small. Therefore, solutions intersecting the D leave Q immediately if $\overline{C}(\mathbf{p}) > 0$ and ϵ and β are small enough.

Now consider the L boundary of the cone Q, for which $\mathbf{q} = \alpha p\mathbf{e}$, where $\mathbf{e} = (\cos\theta, \sin\theta)^T$, and hence

$$\begin{aligned}
\dot{\mathbf{q}}|_{\mathbf{q}=\alpha p\mathbf{e}} &= \epsilon p^2\{\alpha\nabla_{\mathbf{x}}\overline{\tau}(\mathbf{p})\mathbf{e} + p\alpha^2[\mathbf{m}_1(\alpha p\mathbf{e},p,\epsilon,t)\cos^2(\theta) \\
&+ \mathbf{m}_2(\alpha p\mathbf{e},p,\epsilon,t)\cos(\theta)\sin(\theta) + \mathbf{m}_3(\alpha p\mathbf{e},p,\epsilon,t)\sin^2(\theta)] + \epsilon\mathbf{m}_4(\alpha p\mathbf{e},z,\epsilon,t)\}, \\
\dot{p}|_{\mathbf{q}=\alpha p^n\mathbf{e}} &= \epsilon p^2\left[\overline{C}(\mathbf{p}) + \epsilon p m_5(\alpha p\mathbf{e},p,\epsilon,t) + \alpha p\mathbf{e}\cdot\mathbf{m}_6(\alpha p\mathbf{e},p,\epsilon,t)\right].
\end{aligned}$$

The flow enters the cone on this surface, provided

$$\mathbf{n}\cdot(\dot{\mathbf{q}},\dot{p}) < 0, \tag{B.11}$$

everywhere on the surface. This is the case if

$$\alpha\dot{p}|_{\alpha p\mathbf{e}} > \dot{\mathbf{q}}|_{\alpha p\mathbf{e}}\cdot\mathbf{e} \text{ for any } \theta \text{ and } 0 < p \leq \beta,$$

or, equivalently,

$$\begin{gathered}
\alpha\left[\overline{C}(\mathbf{p}) - \mathbf{e}\cdot\nabla_{\mathbf{x}}\overline{\tau}(\mathbf{p})\mathbf{e}\right] + \epsilon\alpha p m_5 - \epsilon\mathbf{m}_4\cdot\mathbf{e} \\
+p\alpha^2[\mathbf{e}\cdot\mathbf{m}_6 - \mathbf{m}_1\cdot\mathbf{e}\cos^2(\theta) + \mathbf{m}_2\cdot\mathbf{e}\cos(\theta)\sin(\theta) + \mathbf{m}_3\cdot\mathbf{e}\sin^2(\theta)] > 0
\end{gathered}$$

for any θ and for all $0 < p \leq \beta$. By choosing $\alpha = 1$, and setting ϵ and β sufficiently small, we can make the above inequality satisfied provided that

$$\overline{C}(\mathbf{p}) - \lambda_{\max}[\nabla_{\mathbf{x}}\overline{\tau}(\mathbf{p})] > 0, \tag{B.12}$$

where $\lambda_{\max}[\nabla_{\mathbf{x}}\overline{\tau}(\mathbf{p})]$ is the maximum singular value of the Jacobian of the wall-shear field evaluated at the separation point $\mathbf{p}$. The second and third inequalities in (B.4) imply $\lambda_{\max}[\nabla_{\mathbf{x}}\overline{\tau}(\mathbf{p})] < 0$. This, along with the last inequality in (B.4), implies that condition (B.12) is always satisfied. From this we conclude that solutions intersecting the L boundary of the cone Q enter Q immediately.

(a) Solutions staying in Q in backward time converge to $\mathbf{p}$ We next examine the asymptotic behavior of solutions staying in the cone for all backward times, from which we shall later conclude the existence of an unstable manifold for $\mathbf{p}$.

Consider an initial position $(\mathbf{q}_0, p_0) \in Q$ at t_0, and denote the trajectory starting from this initial position by $(\mathbf{q}(t), p(t))$. Integration of

$$\dot{p}(t) = \epsilon p(t)^2\left[\overline{C}(\mathbf{p}) + \epsilon p m_5(\mathbf{q},p,\epsilon,t) + \mathbf{q}\cdot\mathbf{m}_6(\mathbf{q},p,\epsilon,t)\right]_{(\mathbf{q}(t),p(t))}, \tag{B.13}$$

gives

$$p(t) = \frac{p_0}{1 + \epsilon p_0 \int_t^{t_0} \left[\overline{C}(\mathbf{p}) + \epsilon p(\tau) m_5(\mathbf{q}, p, \epsilon, \tau) + \mathbf{q} \cdot \mathbf{m}_6(\mathbf{q}, p, \epsilon, \tau)\right] \, d\tau}. \tag{B.14}$$

If the trajectory starting from $(\mathbf{q}_0, p_0)$ stays in Q for all backward times, equation (B.14) holds for *all* $t \leq t_0$. Choosing ϵ and β appropriately small then leads to the estimate

$$\begin{aligned} p(t) &\leq \frac{p_0}{1 + \epsilon p_0 \int_t^{t_0} \left[\overline{C}(\mathbf{p}) - \epsilon p |m_5(\mathbf{q}, p, \epsilon, t)| - |\,\mathbf{q}| \cdot |m_6(\mathbf{q}, p, \epsilon, t)|\right] d\tau} \\ &\leq \frac{p_0}{1 + \frac{\epsilon p_0}{2} \overline{C}(\mathbf{p})(t_0 - t)}. \end{aligned}$$

This allows us to conclude that

$$\lim_{t \to -\infty} p(t) = 0.$$

In other words, trajectories that never leave Q in backward time will necessarily converge to the $p = 0$ boundary of the cone Q. By the definition of Q, however, this convergence in the p direction implies

$$\lim_{t \to -\infty} \mathbf{q}(t) = 0.$$

(b) All solutions leave Q in forward time For any $p_0 > 0$, consider an initial position $(\mathbf{q}_0, p_0) \in Q$ at time t_0; denote the trajectory starting from this initial position by $(\mathbf{q}(t), p(t))$. In forward time, the trajectory cannot leave the cone through L. We show that the p coordinate grows and reaches β in a uniform finite time for any given $p_0 > 0$. Hence, the trajectory must exit the cone through D.

By our discussion in (a), along the trajectory starting from $(\mathbf{q}_0, p_0)$, we have

$$p(t) \geq \frac{p_0}{1 - \epsilon p_0 \int_{t_0}^{t} \left[\overline{C}(\mathbf{p}) - \epsilon p |m_5(\mathbf{q}, p, \epsilon, t)| - |\,\mathbf{q}| \cdot |m_6(\mathbf{q}, p, \epsilon, t)|\right] d\tau} \geq \frac{p_0}{1 - \epsilon p_0 \frac{\overline{C}(\mathrm{p})}{2}(t - t_0)},$$

which holds for $t > t_0$ while the trajectory stays in Q in forward time. Then, if $p_0 \neq 0$, then the relation $p(t) \leq \beta$ is violated at times

$$t > t_0 + \frac{2}{\epsilon \overline{C}(\mathbf{p})} \left[\frac{1}{p_0} - \frac{1}{\beta}\right]. \tag{B.15}$$

Thus, the trajectory has to leave the cone through D.

(c) There exist solutions that stay in Q for all backward times To prove that there are solutions that stay in Q for all backward times, we follow the argument

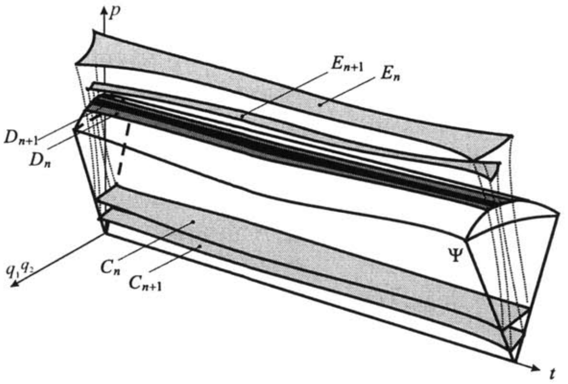

Figure B-2: The cylinders C_n, D_n and E_n shown schematically in the extended phase space.

developed by Haller [39]. In the extended phase space of the $(\mathbf{q}, p, t)$ variables, let

$$\Psi = Q \times \mathbb{R}, \qquad \mathcal{L} = L \times \mathbb{R}, \qquad \mathcal{D} = D \times \mathbb{R}. \tag{B.16}$$

Consider an infinite sequence of closed curves $\{C_n\}_{n=1}^{\infty}$ with $C_n \in L$ such that each C_n encircles the p axis, and $\lim_{n\to\infty} C_n = 0$. In the extended phase space, each family of circles, C_n appears as an infinite cylinder

$$\mathcal{C}_n = \{(\mathbf{q}, p, t) \mid \mathbf{q} \in C_n, t \in \mathbb{R}\}, \tag{B.17}$$

as shown in figure B-2.

By our discussion in subsection (b) above, we conclude that there exists a finite time $T_n > 0$ (8.11), such that at time $t + T_n$, all solutions $(\mathbf{q}, p, t)$ starting from the cylinder $\mathcal{C}_n$ are outside Q. At time T_n, the image of the cylinder C_n under the flow map is E_n, as shown in the figure B-2. All trajectories evolving from $\mathcal{C}_n$ in forward time intersect the boundary of $\mathcal{D}$ forming another cylinder D_n, as shown in figure B-2. Similarly, the cylinder $\mathcal{C}_{n+1}$ gives rise to a cylinder $D_{n+1} \subset D_n$ on the boundary of $\mathcal{D}$. By construction, any solutions starting from $D_n \setminus D_{n+1}$ exits $\mathcal{C}$ somewhere between the circles C_n and C_{n+1} in backward time. The infinite sequence of cylinders, $D_1 \supset D_2 \supset \cdots$, is a nested sequence of non-empty closed set, and hence

$$D^{\infty} = \cap_{n\geq 1} D_n, \tag{B.18}$$

is a nonempty curve by Cantor's theorem. Observe that a point $(\mathbf{q}^*, p^*, t^*) \in D^{\infty}$ will never exit Q in backward time because there is no index N for which $(\mathbf{q}^*, p^*, t^*) \in D_N \setminus D_{N+1}$. For any time t^*, therefore, we have found an initial condition $(\mathbf{q}^*, p^*)$ such that the corresponding solution $(\mathbf{q}^*(t), p^*(t))$ stays in Q for all $t \leq t^*$.

(d) Existence of unstable manifold From (a) above, we obtain that $(\mathbf{q}^*(t), p^*(t))$ converges to the origin (the tip of the cone Q) in backward time. Thus, we have shown that there is a nonempty set of initial fluid particle positions W^∞ that stay in Q for all backward times. By definition, W^∞ is an invariant set that is necessarily smooth in t because it is composed of fluid trajectories that are smooth in t. We, therefore, conclude that all trajectories in W^∞ converge to $p = \mathbf{q} = 0$ in backward time, thus W^∞ is an unstable manifold for $(\mathbf{p}, 0)$.

By reversing the time direction in all the above arguments, we conclude the persistence of a attachment profile (stable manifold) under the conditions

$$\overline{\tau}(\mathbf{p}) = 0, \qquad \nabla_{\mathbf{x}} \cdot \overline{\tau}(\mathbf{p}) > 0, \qquad \det \nabla_{\mathbf{x}} \overline{\tau}(\mathbf{p}) > 0, \qquad \overline{C}(\mathbf{p}) < 0,$$

and hence (4.19) follows.

B.2.2 Persistence of separation surfaces: saddle connections and limit cycles

Consider a bounded wall-shear line γ of the time averaged wall-shear field $\overline{\tau}$. As shown in chapter 3, γ is separation line for the averaged steady velocity fields if

(S1) γ originates from a saddle $\mathbf{p}$ with $\overline{C}(\mathbf{p}) > 0$ and ends at a stable spiral $\mathbf{q}$ with $\overline{C}(\mathbf{q}) > 0$.

(S2) γ originates from a saddle $\mathbf{p}$ with $\overline{C}(\mathbf{p}) > 0$ and ends at a stable node $\mathbf{q}$ with $\overline{C}(\mathbf{q}) > 0$. Also, γ is tangent to the direction of weaker attraction at $\mathbf{q}$.

(S3) γ originates from a saddle $\mathbf{p}$ with $\overline{C}(\mathbf{p}) > 0$ and spirals onto a stable limit cycle Γ with $\int_\Gamma \overline{C} ds > 0$.

(S4) γ is a stable limit cycle with $\int_\gamma \overline{C} ds > 0$.

Similarly, γ is a attachment line if

(R1) γ originates at a unstable spiral $\mathbf{p}$ with $\overline{C}(\mathbf{p}) < 0$ and ends at a saddle $\mathbf{q}$ with $\overline{C}(\mathbf{q}) < 0$.

(R2) γ originates at a unstable node $\mathbf{p}$ with $\overline{C}(\mathbf{p}) < 0$ and ends at a saddle $\mathbf{q}$ with $\overline{C}(\mathbf{q}) < 0$. Also, γ is tangent to the direction of weaker repulsion at $\mathbf{p}$.

(R3) γ spirals off from an unstable limit cycle Γ with $\int_\Gamma \overline{C} ds < 0$ and ends at a saddle $\mathbf{q}$ with $\overline{C}(\mathbf{q}) < 0$.

(R4) γ is a unstable limit cycle with $\int_\gamma \overline{C} ds < 0$.

Below we show that under the stronger pointwise assumptions

$$\overline{S}_\perp(\mathbf{x}) - \overline{C}(\mathbf{x}) < 0, \qquad \overline{C}(\mathbf{x}) > 0, \tag{B.19}$$

on all points $\mathbf{x}$ in γ, the four basic separation patterns (S1)-(S4) inferred based on the steady limit (4.13) persist in the full flow (4.5). Under the assumptions

$$\overline{S}_{\perp}(\mathbf{x}) - \overline{C}(\mathbf{x}) > 0, \qquad \overline{C}(\mathbf{x}) < 0, \qquad \forall \mathbf{x} \in \gamma, \tag{B.20}$$

similar conclusion hold for the four basic attachment patterns (R1)-(R4), leading to the results discussed in section 4.2.3.

The proof of above results relies on *Wasewsky principle*, which we recall briefly for convenience following the formulation given by Conley (1970).

The Wasewsky principle

Suppose Ω is an open set in $\mathbb{R}^n$, $f : \Omega \to \mathbb{R}^n$ is a continuous map, and let

$$\phi \colon \mathbf{x}_0 \mapsto \mathbf{x}\,(t; \mathbf{x}_0)$$

(with $\mathbf{x}\,(0; \mathbf{x}_0) = \mathbf{x}_0$) be the flow map of the ordinary differential equation

$$\dot{\mathbf{x}} = f(\mathbf{x}). \tag{B.21}$$

We shall denote the *closure* of W in Ω by $\bar{W}$ and define

$$\Phi(\mathbf{x}, \mathcal{I}) = \{\phi(\mathbf{x}, t) |\ t \in \mathcal{I}\},$$

where $\mathcal{I} \subset \mathbb{R}$.

Let $W \subset \Omega$ be any set and consider the sets

$$\begin{aligned} W^{ev} &= \{\mathbf{x} \in W |\ \phi(\mathbf{x}, t) \notin W \quad \text{for some,} \quad t > 0\}, \\ W^{im} &= \{\mathbf{x} \in W |\ \Phi(\mathbf{x}, [0, t]) \not\subset W, \forall t > 0\}. \end{aligned}$$

W is called a forward time *Wasewsky* set if the following conditions are satisfied

(1) If $\mathbf{x} \in W$ and $\Phi(\mathbf{x}, [0, t]) \subset \bar{W}$, then $\Phi(\mathbf{x}, [0, t]) \subset W$,

(2) W^{im} is closed relative to W^{ev}.

The *Wasewsky principle* states the following: If W is a Wasewsky set then W^{im} is a strong deformation retract of W^{ev}, and W^{ev} is open relative to W.

An important quantity introduced in the proof of the above result is the time map $\tau : W^{ev} \to \mathbf{R}$, defined as

$$\tau(\mathbf{x}) = \sup\{t \geq 0 | \Phi([0, t], \mathbf{x}) \subset W\}.$$

By the definition of W^{ev}, $\tau(\mathbf{x})$ is finite, and by continuity of the flow, we have $\Phi(\mathbf{x}, [0, \tau(\mathbf{x})]) \subset \bar{W}$. Thus, by property (1) above, we have $\phi(\mathbf{x}, \tau(\mathbf{x})) \in W$. Now from the definition of τ, $\phi(\tau(\mathbf{x}), \mathbf{x}) \in W^{im}$ and $\tau(\mathbf{x}) = 0$ for $\mathbf{x} \in W^{im}$. This leads to the following corollary.

Corollary: The *Wasewsky map* $\Gamma : W^{ev} \to W^{im}$ defined as

$$\Gamma(\mathbf{x}) = \phi(\mathbf{x}, \tau(\mathbf{x})), \tag{B.22}$$

is continuous. It is this last corollary of the Wasewsky principle that we shall use below in our arguments.

Transformed equations of motion

We begin our persistence proof by introducing new coordinates along a separation line γ identified from the first-order averaged normal form. At any point $\mathbf{x} = \mathbf{x}(s, \mathbf{x}_0) \in \gamma$, the unit tangent $\mathbf{t}(s)$ and the unit normal $\mathbf{n}(s)$ to γ are given by

$$\mathbf{t}(s) = \frac{\overline{\tau}}{|\overline{\tau}|}|_{\mathbf{x}(s,\mathbf{x}_0)}, \qquad \mathbf{n}(s) = \frac{\overline{\omega}}{|\overline{\omega}|}|_{\mathbf{x}(s,\mathbf{x}_0)}, \tag{B.23}$$

respectively, where $\mathbf{x}(s, \mathbf{x}_0)$ is the wall–shear trajectory with $\mathbf{x}(0, \mathbf{x}_0) = \mathbf{x}_0$. Let $(x(s_p), y(s_p)) \in \mathbf{x}(s, x_0)$. We change coordinates through

$$\begin{pmatrix} \mathbf{q} \\ p \end{pmatrix} = T_p \begin{pmatrix} \eta_1 \\ \eta_2 \\ \eta_3 \end{pmatrix}, \tag{B.24}$$

with

$$T_p = \begin{pmatrix} \mathbf{t}(s_p) & \mathbf{n}(s_p) & \mathbf{0} \\ 0 & 0 & 1 \end{pmatrix}, \tag{B.25}$$

to obtain from (B.6) the new equations of particle motion

$$\begin{aligned}
\dot{\eta}_1 &= \epsilon\eta_3|\overline{\tau}(x(s_p), y(s_p))| + \epsilon\eta_3\eta_1\overline{S}_{||}((x(s_p), y(s_p))) + \epsilon\eta_3\eta_2\overline{S}_{|\perp}((x(s_p), y(s_p))), \\
&+ \epsilon\eta_3[h_1(\eta, \epsilon, t)\eta_1^2 + h_2(\eta, \epsilon, t)\eta_1\eta_2 + h_3(\eta, \epsilon, t)\eta_2^2] + \epsilon^2\eta_3^2 h_4(\eta, \epsilon, t), \qquad \text{(B.26)} \\
\dot{\eta}_2 &= \epsilon\eta_3\eta_1\overline{S}_{\perp|}((x(s_p), y(s_p))) + \epsilon\eta_3\eta_2\overline{S}_{\perp}((x(s_p), y(s_p))) \\
&\quad + \epsilon\eta_3[h_5(\eta, \epsilon, t)\eta_1^2 + h_6(\eta, \epsilon, t)\eta_1\eta_2 + h_7(\eta, \epsilon, t)\eta_2^2] + \epsilon^2\eta_3^2 h_8(\eta, \epsilon, t), \qquad \text{(B.27)} \\
\dot{\eta}_3 &= \epsilon\eta_3^2[\overline{C}(x(s_p), y(s_p)) + \epsilon\eta_3 h_9(\eta, \epsilon, t) + \eta_1 h_{10}(\eta, \epsilon, t) + \eta_2 h_{11}(\eta, \epsilon, t)]. \qquad \text{(B.28)}
\end{aligned}$$

In the above equations, $h_i(\eta, \epsilon, t)$ are appropriate smooth and bounded functions in all the arguments and

$$\begin{aligned}
\overline{S}_{||}(x(s_p), y(s_p)) &= <\mathbf{t}, \nabla_{\mathbf{x}}\overline{\tau}\mathbf{t}> |_{\mathbf{x}=(x(s_p),y(s_p))}, \\
\overline{S}_{\perp}(x(s_p), y(s_p)) &= <\mathbf{n}, \nabla_{\mathbf{x}}\overline{\tau}\mathbf{n}> |_{\mathbf{x}=(x(s_p),y(s_p))}, \\
\overline{S}_{|\perp}(x(s_p), y(s_p)) &= <\mathbf{t}, \nabla_{\mathbf{x}}\overline{\tau}\mathbf{n}> |_{\mathbf{x}=(x(s_p),y(s_p))}, \\
\overline{S}_{\perp|}(x(s_p), y(s_p)) &= <\mathbf{n}, \nabla_{\mathbf{x}}\overline{\tau}\mathbf{t}> |_{\mathbf{x}=(x(s_p),y(s_p))}.
\end{aligned}$$

Persistence of separation surface near a saddle

Consider a nondegenerate saddle $(\mathbf{p}, 0)$ of the time averaged wall shear-field; it will satisfy

$$\overline{\tau}(\mathbf{p}) = 0, \qquad \det\nabla_{\mathbf{x}}\overline{\tau}(\mathbf{p}) < 0, \qquad \overline{C}(\mathbf{p}) > 0.$$

Let $\mathbf{x}_1(s), s \in \mathcal{I}_1 = [-s_-, 0]$ and $\mathbf{x}_2(s), s \in \mathcal{I}_2 = [0, s_+]$ be the two branches of the unstable manifold in the vicinity of $\mathbf{p}$ such that $\mathbf{x}_1(0) = \mathbf{x}_2(0) = \mathbf{p}$, where $s_- > 0$ and $s_+ > 0$ are to be chosen later. Define

$$\gamma_v = \mathbf{x}_1(s) \cup \mathbf{x}_2(s), \qquad s \in \mathcal{I} = \mathcal{I}_1 \cup \mathcal{I}_2,$$

which is just a subset of the separation line in the vicinity of $\mathbf{p}$. We construct a cone section along γ parameterized by $s_p \in \mathcal{I}$ as follows:

$$Q_{s_p} = \{(\eta_1, \eta_2, \eta_3) \mid \eta_1 = 0, |\eta_2| \leq \eta_3, \quad 0 \leq \eta_3 \leq \beta(s_p)\},$$

where $\beta(s)$ is a positive continuous function to be selected below (see figure B-3). The lateral side L_{s_p} of Q_{s_p} is given by

$$L_{s_p} = \{(\eta_1, \eta_2, \eta_3) \in Q_{s_p} || \eta_2| = \eta_3\}.$$

The top of the cone will be denoted by D_{s_p}

$$D_{s_p} = \{(\eta_1, \eta_2, \eta_3) \in Q_{s_p} | \eta_3 = \beta(s_p)\}.$$

Along the boundary D_{s_p} of the cone, the inequality

$$\begin{aligned} \dot{\eta}_3|_{\{\eta \in D_{s_p}\}} &= \epsilon\beta^2(s_p)[\overline{C}(x(s_p), y(s_p)) + \epsilon\beta(s_p)h_9(\eta, \epsilon, t) + \eta_2 h_{11}(\eta, \epsilon, t)] \\ &\geq \epsilon\beta^2(s_p)\frac{\overline{C}(x(s_p), y(s_p))}{2} > 0, \end{aligned} \tag{B.29}$$

holds, provided that we choose ϵ and $\beta(s_p)$ sufficiently small (using $\eta_2 \in Q_{s_p}$, which implies $|\eta_2| < \eta_3$). Therefore, solutions intersecting the D_{s_p} boundary of Q_{s_p} leave Q_{s_p} immediately.

The flow enters Q_{s_p} along the L_{s_p} boundary if

$$\dot{\eta}_2|_{\{\eta \in L_{s_p}\}} - \dot{\eta}_3|_{\{\eta \in L_{s_p}\}} < 0. \tag{B.30}$$

Since

$$\begin{aligned} \dot{\eta}_2|_{\{\eta \in L_{s_p}\}} &= \epsilon\eta_3^2[\overline{S}_\perp(x(s_p), y(s_p)) + \eta_3 h_7(\eta, \epsilon, t) + \epsilon h_8(\eta, \epsilon, t)], \\ \dot{\eta}_3|_{\{\eta \in L_{s_p}\}} &= \epsilon\eta_3^2\left[\overline{C}(x(s_p), y(s_p)) + \epsilon\eta_3 h_9(\eta, \epsilon, t) + \eta_3 h_{11}(\eta, \epsilon, t)\right], \end{aligned}$$

for (B.30) to be true, we must have

$$[\overline{S}_\perp(x(s_p), y(s_p)) - \overline{C}(x(s_p), y(s_p))] + \eta_3 f_1(\eta_3, \epsilon, t) + \epsilon f_2(\eta_3, \epsilon, t) < 0, \tag{B.31}$$

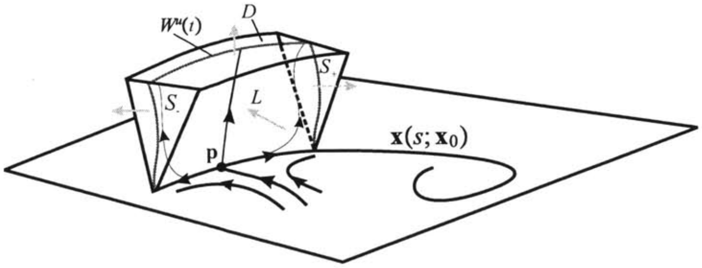

Figure B-3: Wasewsky set near a saddle.

where $f_i, i = 1, 2$ are smooth bounded functions. Since $\overline{S}_\perp(x(s_p), y(s_p)) - \overline{C}(x(s_p), y(s_p)) < 0$, the inequality (B.31) can be satisfied by choosing ϵ and $\beta(s_p)$ sufficiently small as before. Since $\mathcal{I}$ is compact, we can choose

$$\beta(s) \equiv \min_{s_p \in \mathcal{I}} \beta(s_p) = \beta,$$

so that inequalities (B.29) and (B.31) are satisfied for all $s_p \in \mathcal{I}$.

We define a cone bundle ψ along γ by letting

$$\psi = \bigcup_{s \in \mathcal{I}} Q_s.$$

The boundary of ψ is formed by the following sets (see figure B-3):

$$D = \bigcup_{s \in \mathcal{I}} D_s, \qquad L = \bigcup_{s \in \mathcal{I}} L_s, \qquad S_+ = Q_{s_+}, \qquad S_- = Q_{s_-}. \tag{B.32}$$

The flow exits ψ along, say, S_+ provided

$$\dot{\eta_1}\big|_{\eta \in S_+} = \epsilon\eta_3[|\overline{\tau}(\gamma(s_+))| + \eta_2\overline{S}_{|\perp}((x(s_p), y(s_p))) + \eta_2^2 h_3(\eta, \epsilon, t) + \epsilon\eta_3 h_4(\eta, \epsilon, t)] > 0.$$

This last inequality can be satisfied by choosing β sufficiently small. Similar conclusion holds for S_-.

From the above analysis, we conclude that solutions intersecting the $L - \gamma$ boundary of ψ enter ψ immediately, and those that intersect D and the $S_\pm$ boundary leave ψ immediately.

We now fix the origin of our coordinate system at $\mathbf{p}$, so that in $(x(s_p), y(s_p)) = \mathbf{p}$ in the equations of motion (B.26)-(B.28).

(a) Solutions staying in ψ in backward time converge to γ Consider an initial position $(\eta_{10}, \eta_{20}, \eta_{30}) \in \psi$ at t_0 and denote the trajectory emanating from this initial position by $(\eta_1(t), \eta_2(t), \eta_3(t))$. Integration of

$$\dot{\eta_3} = \epsilon\eta_3^2[\overline{C}(\mathbf{p}) + \epsilon\eta_3 h_9(\eta, \epsilon, t) + \eta_1 h_{10}(\eta, \epsilon, t) + \eta_2 h_{11}(\eta, \epsilon, t)],$$

along the trajectory gives

$$\frac{\eta_{30}}{\eta_3(t)} = 1 + \epsilon\eta_{30}\int_t^{t_0} \left[\overline{C}(\mathbf{p}) + \epsilon\eta_3 h_9(\eta,\epsilon,t) + \eta_1 h_{10}(\eta,\epsilon,t) + \eta_2 h_{11}(\eta,\epsilon,t)\right] d\tau. \quad (B.33)$$

Since the trajectory stays in ψ for all backward times, equation (B.33) holds for *all* $t \leq t_0$,. By choosing s_- and s_+ sufficiently small, we can bound $\eta_1(t)$ and $\eta_2(t)$ to arbitrary small values leading to the estimate

$$1+\epsilon\eta_{30}\int_t^{t_0} \left[\overline{C}(\mathbf{p}) + \epsilon\eta_3 h_9(\eta,\epsilon,t) + \eta_1 h_{10}(\eta,\epsilon,t) + \eta_2 h_{11}(\eta,\epsilon,t)\right] d\tau > 1+\epsilon\eta_{30}\int_t^{t_0} \frac{\overline{C}(\mathbf{p})}{2} d\tau. \quad (B.34)$$

Then (B.33) and (B.34) imply

$$\eta_3(t) \leq \frac{\eta_{30}}{1+\epsilon\eta_{30}\frac{\overline{C}(\mathbf{p})}{2}(t_0 - t)}.$$

This allows us to conclude that

$$\lim_{t\to-\infty} \eta_3(t) = 0.$$

In other words, trajectories that never leave ψ in backward time will necessarily converge to the $\eta_3 = 0$ boundary of the cone ψ.

(b) There exists solutions that stay in ψ for all backward times We now show that there are non-zero solutions that stay in ψ for all $t \leq t_0$. We first note that the set

$$\Psi = \{(\eta,t) | \eta \in \psi, t \in \mathbb{R}\}, \quad (B.35)$$

has the following properties:

(i) On the boundary component

$$\partial\Psi^1 = \{(\eta,t) \in \Psi | \eta \in D \cup S_+ \cup S_-\}, \quad (B.36)$$

of Ψ, the vector field $(\dot{\eta}, \dot{t})$ points strictly inwards in backward time.

(ii) On the boundary component

$$\partial\Psi^2 = \{(\eta,t) \in \Psi | \eta \in L - \gamma_v\}, \quad (B.37)$$

of Ψ, the vector field $(\dot{\eta}, \dot{t})$ points strictly outwards in backward time.

(iii) The remaining boundary component $\partial\Psi^3 = \Psi - \partial\Psi^1 - \partial\Psi^2$ of Ψ is just the invariant piece of the plane (γ_v, t) in the (η, t) space.

(iv) As a consequence of (i)-(iii), the set of points immediately leaving Ψ in backward time is $W^{im} = \partial\Psi^2$.

(v) Let W^{ev} denote the set of points eventually leaving Ψ in backward time. By definition, $W^{im} \subset W^{ev}$. Because $\partial\Psi^3$ is not in W^{ev}, we conclude that W^{im} is relatively closed in W^{ev}, i.e., any Cauchy sequence in W^{im} that does not have a limit in W^{im} will not have a limit W^{ev} either.

(vi) Ψ is a closed set in the (η, t) space.

The properties (iv)-(vi) of Ψ are the defining properties of a backward time Wasewsky set (see section B.2.2). Recall that for any Wasewsky set, the Wasewsky map given by (B.22) is continuous.

Suppose now that all non-zero solutions leave Ψ eventually in backward time. Then $W^{ev} = \Psi - \partial\Psi^3$, and hence $\Gamma(\Psi - \partial\Psi^3) = \partial\Psi^2$. But a continuous map Γ cannot map a connected set $\Psi - \partial\Psi^3$ into a disconnected set $\partial\Psi^2$, thus we obtain a contradiction. Therefore, there exist solutions that stay in ψ for all backward times, and these solutions converge to the $\xi = 0$ as $t \to -\infty$. This proves the existence of the unstable manifold $W^u(t)$ for γ_v.

The unstable manifold $W^u(t)$ cannot be one-dimensional, because that would make W^{ev} a connected set, thereby violating the continuity of the Wasewsky map (B.22). But $W^u(t)$ cannot be three-dimensional either, because that would violate the local volume–preserving property of the flow map (infinitesimal volumes tangent to $W^u(t)$ at the wall would shrink to zero in backward time, violating local incompressibility at the wall). Thus, $W^u(t)$ must be a connected two-dimensional set depending smoothly on t.

Persistence of separation surfaces base at limit cycles

Let the trajectory $\mathbf{x}(s, \mathbf{x}_0)$ be contained in a limit cycle $\Gamma(s)$ of the averaged wall-shear field; assume that $\Gamma(s)$ has period T. Following the construction in section B.2.2, we define a cone section along $\Gamma(s)$

$$Q_{s_p} = \{(\eta_1, \eta_2, \eta_3) \mid \eta_1 = 0, |\eta_2| \le \eta_3, \quad 0 \le \eta_3 \le \beta(s_p)\},$$

where $\beta(s)$ is a positive continuous functions to be selected below (figure B-4). The lateral side L_{s_p} of this cone is

$$L_{s_p} = \{(\eta_1, \eta_2, \eta_3) \in Q_{s_p} || \eta_2| = \eta_3\},$$

and the top D_{s_p} is given by

$$D_{s_p} = \{(\eta_1, \eta_2, \eta_3) \in Q_{s_p} | \eta_3 = \beta(s_p)\}.$$

Based on an argument similar to the one given in section B.2.2, we conclude that there exists $\beta(s_p) > 0$ and ϵ sufficiently small such that

$$\dot{\eta}_3|_{\{\eta \in D_{s_p}\}} > 0,$$

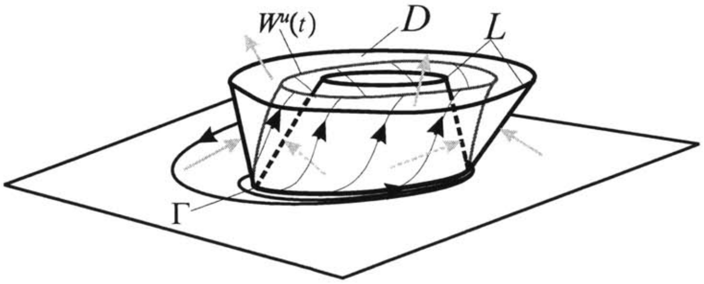

Figure B-4: Wasewski set for limit cycle.

and

$$\dot{\eta}_2|_{\{\eta\in L_{s_p}\}} - \dot{\eta}_3|_{\{\eta\in L_{s_p}\}} < 0, \tag{B.38}$$

for all s_p. Choosing

$$\beta(s) \equiv \min_{s_p\in\mathcal{I}} \beta(s_p) = \beta,$$

we define a cone bundle ψ on $\Gamma(s)$

$$\psi = \bigcup_{s\in\mathcal{I}} Q_s.$$

Again, the boundary of ψ is formed by the following sets

$$D = \bigcup_{s\in\mathcal{I}} D_s, \qquad L = \bigcup_{s\in\mathcal{I}} L_s. \tag{B.39}$$

With these ingredients, an estimate similar to the one used in section B.2.2 shows that solutions staying in ψ in backward time converge to Γ. We can then again invoke the Wasewsky principle to conclude that there exist solutions that stay in ψ forever in backward time. Then, following the arguments given in section B.2.2, we again conclude the existence of a two-dimensional unstable manifold for Γ.

B.3 Separation at corners

Recall that if the flow admits a corner at the intersection of the $z = 0$ and $x = 0$ planes, then by the no-slip condition along these two planes, the velocity field can be written as (see section 3.6)

$$\mathbf{v}(\mathbf{x}, z, t) = (xzA, xzB, xzC), \tag{B.40}$$

where

$$
\begin{aligned}
A(\mathbf{x}, z, t) &= \int_0^1 \int_0^1 \partial_{xz}^2 u(rx, y, sz, t) dr ds, \\
B(\mathbf{x}, z, t) &= \int_0^1 \int_0^1 \partial_{xz}^2 v(rx, y, sz, t)\ dr ds, \\
C(\mathbf{x}, z, t) &= \int_0^1 \int_0^1 \partial_{xz}^2 w(rx, y, sz, t) dr ds.
\end{aligned}
\tag{B.41}
$$

After the change of coordinates

$$
\begin{aligned}
x &= \bar{x} E_x(y, \bar{z}, t), \quad E_x(y, \bar{z}, t) = e^{\int_{t_0}^t \bar{z} E_z(\bar{x}, y, \tau) A(0, y, \bar{z} E_z(\bar{x}, y, \tau) d\tau}, \\
z &= \bar{z} E_z(\bar{x}, y, t), \quad E_z(\bar{x}, y, t) = e^{\int_{t_0}^t \bar{x} E_x(y, \bar{z}, \tau) C(\bar{x} E_x(y, \bar{z}, \tau), y, 0, \tau) d\tau},
\end{aligned}
$$

the x–component of the equations of motion becomes

$$
\dot{x} = (\dot{\bar{x}} + \bar{x}\bar{z} E_z A(0, y, \bar{z} E_z)) E_x = \bar{x}\bar{z} E_x E_z A(\bar{x} E_x(y, \bar{z}, t), y, \bar{z} E_z(\bar{x}, y, t), t),
$$

or, equivalently,

$$
\begin{aligned}
\dot{\bar{x}} &= \bar{x}\bar{z} E_z [A(\bar{x} E_x(y, \bar{z}, t), y, \bar{z} E_z(\bar{x}, y, t), t) - A(0, y, \bar{z} E_z)] \\
&= \bar{x}^2 \bar{z} E_x E_z [\partial_x A(0, y, \bar{z} E_z(\bar{x}, y, t), t) + \mathcal{O}(\bar{x})].
\end{aligned}
$$

The $\bar{z}$-component of the equations of motion is similar, with the role of $\bar{x}$ and $\bar{z}$ interchanged. The full set of transformed equations of motion are of the form

$$
\begin{aligned}
\dot{\bar{x}} &= \bar{x}^2 \bar{z} A_1(\bar{x}, y, \bar{z}, t), \\
\dot{y} &= \bar{x}\bar{z} B_1(\bar{x}, y, \bar{z}, t), \\
\dot{\bar{z}} &= \bar{x}\bar{z}^2 C_1(\bar{x}, y, \bar{z}, t),
\end{aligned}
$$

where

$$
\begin{aligned}
A_1(\bar{x}, y, \bar{z}, t) &= E_x E_z [\partial_x A(0, y, \bar{z} E_z(\bar{x}, y, t), t) + \mathcal{O}(\bar{x})], \\
B_1(\bar{x}, y, \bar{z}, t) &= E_x E_z B(\bar{x} E_x(y, \bar{z}, t), y, \bar{z} E_z(\bar{z}, y, t), t), \\
C_1(\bar{z}, y, \bar{z}, t) &= E_x E_z [\partial_z C(\bar{x} E_x(y, \bar{z}, t), y, 0, t) + \mathcal{O}(\bar{z})].
\end{aligned}
$$

Rescaling $\bar{z} \to \epsilon \bar{z}$ in order to focus on the dynamics near the $z = 0$ boundary, we obtain

$$
\dot{\eta} = \epsilon \mathbf{f}(\eta, t) + \epsilon^2 \mathbf{g}(\eta, t; \epsilon), \tag{B.42}
$$

where $\eta = (\bar{x}, y, \bar{z})$ and

$$
\mathbf{f} = \begin{pmatrix} \bar{x}^2 \bar{z} A_1(\bar{x}, y, 0, t) \\ \bar{x}\bar{z} B_1(\bar{x}, y, 0, t) \\ \bar{x}\bar{z}^2 C_1(\bar{x}, y, 0, t) \end{pmatrix}, \qquad \mathbf{g} = \begin{pmatrix} \bar{x}^2 \bar{z}^2 [\partial_{\bar{z}} A_1(0, y, 0, t) + \mathcal{O}(\epsilon \bar{z}^2)] \\ \bar{x}\bar{z}^2 [\partial_{\bar{z}} B_1(\bar{x}, y, 0, t) + \mathcal{O}(\epsilon \bar{z}^2)] \\ \bar{x}\bar{z}^3 [\partial_{\bar{z}} C_1(\bar{x}, y, 0, t) + \mathcal{O}(\epsilon \bar{z}^2)] \end{pmatrix}.
$$

We isolate the mean of f via the averaging transformation

$$\eta = \zeta + \epsilon \mathbf{w}(\zeta, t), \quad \mathbf{w}(\zeta, t) = \int_{t_0}^{t} [\mathbf{f}(\ \zeta, \tau) - \overline{\mathbf{f}}(\zeta)] d\tau, \quad \overline{\mathbf{f}}(\zeta) = \lim_{T \to \infty} \frac{1}{T} \int_{t_0 - T}^{t_0} \mathbf{f}(\zeta, \tau) d\tau, \tag{B.43}$$

which transform (B.42) to the first-order averaged normal form

$$\dot{\zeta} = \epsilon \overline{\mathbf{f}}(\zeta) + \mathcal{O}(\epsilon^2), \tag{B.44}$$

which is analogous to (4.5). The steady limit of (B.44) in component form is then given by (4.22).

B.4 Refined separation slope estimate

In order to obtain a refined estimate for the slope of separation curves and surfaces, we apply the slope formulae for steady separation derived in chapter 3 to the steady limit

$$\begin{aligned} \dot{\mathbf{r}} &= \epsilon s[\overline{\tau}(\mathbf{r}) + s\epsilon \overline{\mathbf{F}}(\mathbf{r})], \\ \dot{s} &= \epsilon s^2[\overline{C}(\mathbf{r}) + s\epsilon \overline{G}(\mathbf{r})], \end{aligned} \tag{B.45}$$

of the second-order averaged system (B.3). First note that at $t = t_0$, we have $z = \tilde{z}$, therefore

$$(\mathbf{r}, s) = (\mathbf{q}, p) + \mathcal{O}(\epsilon^2) = (\mathbf{x}, z/\epsilon) + \mathcal{O}(\epsilon).$$

In the $(\mathbf{x}, z)$ coordinates, therefore, the slope of a separation or attachment curve at the point $(\mathbf{p}, 0)$ is given by

$$\mathbf{g}_0 = -\left[\nabla_{\mathbf{x}} \overline{\tau}(\mathbf{p}) - \mathbf{I}\overline{C}(\mathbf{p})\right]^{-1} \overline{\mathbf{F}}(\mathbf{p}). \tag{B.46}$$

Note that

$$\begin{aligned} \lim_{T \to \infty} \frac{1}{T} \int_{t_0 - T}^{t_0} \mathbf{A}_1(\mathbf{q}, 0, \tau) \psi d\tau &= \lim_{T \to \infty} \frac{1}{T} \left\{ [\phi\psi]_{t_0 - T}^{t_0} - \int_{t_0 - T}^{t_0} \phi [C_1(\mathbf{q}, 0, \tau) - \overline{C}] d\tau \right\} \\ &= -\lim_{T \to \infty} \frac{1}{T} \left\{ \int_{t_0 - T}^{t_0} \phi [C_1(\mathbf{q}, 0, \tau) - \overline{C}] d\tau \right\}, \end{aligned}$$

where, we have used $\overline{\tau}(\mathbf{p}) = 0$ and the uniform boundedness of ϕ and ψ. We thus obtain the following simplified form of $\overline{F}$ at the separation point:

$$\overline{\mathbf{F}}(\mathbf{p}) = \lim_{T \to \infty} \frac{1}{T} \int_{t_0 - T}^{t_0} [\partial_{\tilde{z}} \mathbf{A}_1(\mathbf{q}, 0, t) + (\nabla_{\mathbf{x}} \mathbf{A}_1(\mathbf{p}, 0, \tau) - C_1(\mathbf{p}, 0, \tau)\mathbf{I}) \int_{t_0}^{\tau} \mathbf{A}_1(\mathbf{p}, 0, s) ds] d\tau.$$

Substituting this relation into (B.46), we obtain the desired separation slope formula (4.27).

Applying the results of chapter 3 to the steady flow (B.45), we obtain that the slope of the separation surface at a point $\mathbf{x}_0$ of a separation line γ at time t_0 is given by

$$\tan(\theta(\mathbf{x}_0, t_0)) = -\lim_{s \to -\infty} \int_0^s e^{\int_0^q [\overline{C}(\mathbf{x}(r,\mathbf{x}_0)) - \overline{S}_\perp(r)]dr} \frac{\overline{\mathbf{F}} \cdot \overline{\omega}}{|\overline{\omega}|} |_{\mathbf{x}=\mathbf{x}(q,\mathbf{x}_0)} dq. \tag{B.47}$$

Similarly, a attachment surface's slope satisfies

$$\tan(\theta(\mathbf{x}_0, t_0)) = -\lim_{s \to \infty} \int_0^s e^{\int_0^q [\overline{C}(\mathbf{x}(r,\mathbf{x}_0)) - \overline{S}_\perp(r)]dr} \frac{\overline{\mathbf{F}} \cdot \overline{\omega}}{|\overline{\omega}|} |_{\mathbf{x}=\mathbf{x}(q,\mathbf{x}_0)} dq. \tag{B.48}$$

The quantity $\overline{\mathbf{F}} \cdot \overline{\omega}$ appearing in the above slope formulae can be further simplified to

$$\begin{aligned}
\overline{\mathbf{F}} \cdot \overline{\omega} &= \lim_{T \to \infty} \frac{1}{T} \int_{t_0 - T}^{t_0} \mathbf{F}(\mathbf{r}, \tau) \cdot \overline{\omega} d\tau \\
&= \lim_{T \to \infty} \frac{1}{T} \int_{t_0 - T}^{t_0} \{\overline{\omega} \cdot ([\nabla_{\mathbf{x}} \mathbf{A}_1 - \overline{C}\mathbf{I}]\phi), + \psi \mathbf{A}_1 \cdot \overline{\omega} + \partial_{\bar{z}} \mathbf{A}_1 \cdot \overline{\omega} - \overline{\omega} \cdot (\nabla_{\mathbf{x}} \phi \overline{\tau})\} \, d\tau.
\end{aligned}$$

Note that

$$\begin{aligned}
\lim_{T \to \infty} \frac{1}{T} \int_{t_0 - T}^{t_0} \psi \mathbf{A}_1(\mathbf{q}, 0, \tau) \cdot \overline{\omega} d\tau &= \lim_{T \to \infty} \frac{1}{T} \left\{ [\psi \phi \cdot \overline{\omega}]_{t_0 - T}^{t_0} - \int_{t_0 - T}^{t_0} [C_1(\mathbf{q}, 0, \tau) - \overline{C}]\phi \cdot \overline{\omega} d\tau \right\} \\
&= -\lim_{T \to \infty} \frac{1}{T} \left\{ \int_{t_0 - T}^{t_0} [C_1(\mathbf{q}, 0, \tau) - \overline{C}]\phi \cdot \overline{\omega} d\tau \right\},
\end{aligned}$$

where, we have used the identity $\overline{\tau} \cdot \overline{\omega} = 0$; we have also used the uniform boundedness of ϕ and ψ. As a consequence, we obtain

$$\begin{aligned}
\overline{\mathbf{F}} \cdot \overline{\omega} &= \lim_{T \to \infty} \frac{1}{T} \int_{t_0 - T}^{t_0} \mathbf{F}(\mathbf{r}, \tau) \cdot \overline{\omega} d\tau \\
&= \lim_{T \to \infty} \frac{1}{T} \int_{t_0 - T}^{t_0} \left\{ \partial_{\bar{z}} \mathbf{A}_1 \cdot \overline{\omega} + \overline{\omega} \cdot ([\nabla_{\mathbf{x}} \mathbf{A}_1 - C_1 \mathbf{I}] \int_{t_0}^{\tau} [\mathbf{A}_1 - \overline{\tau}] dp) \right. \\
&\quad \left. - \overline{\omega} \cdot (\int_{t_0}^{\tau} [\nabla_{\mathbf{x}} \mathbf{A}_1 - \nabla_{\mathbf{x}} \overline{\tau}] dp \overline{\tau}) \right\} d\tau,
\end{aligned}$$

which makes (B.47) and (B.48) equivalent to the slope formulae given in (4.28) and (4.29).

Appendix C

Appendix: Moving Separation

C.1 Averaging the modified system

To prove Theorem 1, we first observe that the fluctuations embodied by $\tilde{\mathbf{f}}$ in equation (7.17) can be transformed to higher-order terms by an appropriate version of the classical method of averaging. Specifically, we seek a near-identity transformation of the form

$$\mathbf{x} = \xi + \epsilon \mathbf{w}(\xi, \phi, t), \quad \xi = (\xi, \lambda),$$

where $\mathbf{w} = (w_1, w_2)$ is a uniformly bounded function to be determined. Substitution into (7.17) gives

$$\begin{aligned}
\dot{\mathbf{x}} &= \dot{\xi} + \epsilon \nabla_\xi \mathbf{w} \dot{\xi} + \epsilon \partial_\phi \mathbf{w} \dot{\phi} + \epsilon \partial_t \mathbf{w} \\
&= \epsilon \mathbf{f}(\xi + \epsilon \mathbf{w}, \phi, t) + \epsilon^2 \mathbf{g}(\xi + \epsilon \mathbf{w}, \phi, t; \epsilon) + \mathcal{O}(\epsilon^3) \\
&= \epsilon \mathbf{f}(\xi, \phi, t) + \epsilon^2 [\, \mathbf{g}(\xi, \phi, t; 0) + \nabla_{\mathbf{x}} \mathbf{f}(\xi, \phi, t) \mathbf{w}] + \mathcal{O}(\epsilon^3). \qquad \text{(C.1)}
\end{aligned}$$

From the transformed equation (C.1), we obtain

$$[\mathbf{I} + \epsilon \nabla_\xi \mathbf{w}] \dot{\xi} = \epsilon [\mathbf{f} - \partial_t \mathbf{w}] + \epsilon^2 \left[\mathbf{g}(\xi, \phi, t; 0) + \nabla_{\mathbf{x}} \mathbf{f}(\xi, \phi, t) \mathbf{w} - \Delta M(\lambda) \partial_\phi \mathbf{w} \right] + \mathcal{O}(\epsilon^3).$$

If $||\nabla_\xi \mathbf{w}||$ remains uniformly bounded for all $t \leq t_0$, then for small enough ϵ, we can write

$$[\mathbf{I} + \epsilon \nabla_\xi \mathbf{w}]^{-1} = \mathbf{I} - \epsilon \nabla_\xi \mathbf{w} + \mathcal{O}(\epsilon^2), \qquad \text{(C.2)}$$

from which we obtain

$$\begin{aligned}
\dot{\xi} &= [\mathbf{I} + \epsilon \nabla_\xi \mathbf{w}]^{-1} \left\{ \epsilon [\mathbf{f} - \partial_t \mathbf{w}] + \epsilon^2 [\, \mathbf{g}(\xi, \phi, t; 0) + \nabla_{\mathbf{x}} \mathbf{f}(\xi, \phi, t) \mathbf{w} - \Delta M(\lambda) \partial_\phi \mathbf{w}] + \mathcal{O}(\epsilon^3) \right\}, \\
&= \epsilon [\mathbf{f} - \partial_t \mathbf{w}] + \epsilon^2 \left[\mathbf{g}(\xi, \phi, t; 0) + \nabla_{\mathbf{x}} \mathbf{f}(\xi, \phi, t) \mathbf{w} - \Delta M(\lambda) \partial_\phi \mathbf{w} - \nabla_\xi \mathbf{w} (\mathbf{f} - \partial_t \mathbf{w}) \right] + \mathcal{O}(\epsilon^3).
\end{aligned}$$

By choosing

$$\mathbf{w}(\xi, \phi, t) = \begin{pmatrix} w_1(\xi, \phi, t) \\ w_2(\xi, \phi, t) \end{pmatrix} \int_{t_0}^{t} [\mathbf{f}(\xi, \phi, \tau) - \mathbf{f}^0(\xi, \phi)] d\tau, \qquad \text{(C.3)}$$

we ensure the uniform boundedness of $\mathbf{w}$ and $||\nabla_\xi \mathbf{w}||$ (cf. assumption (7.11)), and obtain the first-order averaged form of (7.17) as

$$\begin{aligned}
\dot{\xi} &= \epsilon \mathbf{f}^0(\xi,\phi) + \epsilon^2[\mathbf{F}(\xi,\phi,t) - \Delta\partial_\phi \mathbf{w} M(\lambda)] + \mathcal{O}(\epsilon^3), \\
\dot{\phi} &= M(\lambda + \epsilon w_2) = \epsilon\Delta M(\lambda) + \mathcal{O}(\epsilon^2),
\end{aligned} \tag{C.4}$$

where

$$\mathbf{F}(\xi,\phi,t) = \begin{pmatrix} \lambda^2 F(\xi,\phi,t) \\ \lambda^3 G(\xi,\phi,t) \end{pmatrix} = \mathbf{g}(\xi,\phi,t;0) + (\nabla_\mathbf{x}\mathbf{f})\,\mathbf{w} - (\nabla_\xi \mathbf{w})\,\mathbf{f}^0, \tag{C.5}$$

with

$$\begin{aligned}
F(\xi,\phi,t) &= g_1(\xi,\phi,t) + [\partial_x f_1(\xi,\phi,t) - f_2^0(\xi,\phi)]\varphi + f_1(\xi,\phi,t)\psi - f_1^0(\xi,\phi)\partial_\xi\varphi, \\
G(\xi,\phi,t) &= g_2(\xi,\phi,t) + 2[f_2(\xi,\phi,t) - f_2^0(\xi,\phi)]\psi + \partial_x f_2(\xi,\phi,t)\varphi - f_1^0(\xi,\phi)\partial_\xi\psi, \\
\varphi(\xi,\phi,t) &= \int_{t_0}^t [f_1(\xi,\phi,\tau) - f_1^0(\xi,\phi)]d\tau, \quad \psi(\xi,\phi,t) = \int_{t_0}^t [f_2(\xi,\phi,\tau) - f_2^0(\xi,\phi)]d\tau, \\
\mathbf{w}(\xi,\phi,t) &= \begin{pmatrix} w_1 \\ w_2 \end{pmatrix} = \begin{pmatrix} \lambda\varphi(\xi,\phi,t) \\ \lambda^2\psi(\xi,\phi,t) \end{pmatrix}.
\end{aligned}$$

C.2 Unstable manifold for system 7.17

The first-order averaged equations (C.4) can be written as

$$\begin{aligned}
\dot{\xi} &= \epsilon\lambda[f_1^0(\xi,\phi) + \mathcal{O}(\epsilon\lambda)] + \mathcal{O}(\epsilon^2\lambda) + \mathcal{O}(\epsilon^3\lambda^3), \\
\dot{\lambda} &= \epsilon\lambda^2[f_2^0(\xi,\phi) + \mathcal{O}(\epsilon\lambda)] + \mathcal{O}(\epsilon^2\lambda^2) + \mathcal{O}(\epsilon^3\lambda^4), \\
\dot{\phi} &= \epsilon\Delta M(\lambda).
\end{aligned} \tag{C.6}$$

We introduce the change of coordinates

$$\zeta = \xi - p(\phi),$$

with $p(\phi)$ satisfying (7.16), the new equations of motion become

$$\begin{aligned}
\dot{\zeta} &= -\epsilon\Delta p'(\phi)M(\lambda) + \epsilon\lambda[\zeta\partial_x f_1^0(p(\phi),\phi) + \mathcal{O}(\epsilon\lambda) + \mathcal{O}(\zeta^2)] + \mathcal{O}(\epsilon^2\lambda) + \mathcal{O}(\epsilon^3\lambda^3), \\
\dot{\lambda} &= \epsilon\lambda^2[f_2^0(p(\phi),\phi) + \mathcal{O}(\epsilon\lambda) + \mathcal{O}(\zeta)] + \mathcal{O}(\epsilon^2\lambda^2) + \mathcal{O}(\epsilon^3\lambda^4), \\
\dot{\phi} &= \epsilon\Delta M(\lambda).
\end{aligned} \tag{C.7}$$

We also define the wedge-shaped set

$$W = \{(\zeta,\lambda,\phi) \mid \ |\zeta| \le \lambda, \quad \lambda \in [0, h(\phi)], \quad \phi \in \mathcal{I}\}, \tag{C.8}$$

along the curve $\mathcal{C}$, where the ϕ-dependent height, $h(\phi)$, of W is yet to be chosen.

Note that W is bounded by the surfaces

$$\begin{aligned} S^+ &= \{(\zeta,\lambda,\phi) \mid \zeta = \lambda, \quad \lambda \in [0,h(\phi)], \quad \phi \in \mathcal{I}\}, \\ S^- &= \{(\zeta,\lambda,\phi) \mid \zeta = -\lambda, \quad \lambda \in [0,h(\phi)], \quad \phi \in \mathcal{I}\}, \\ T &= \{(\zeta,h(\phi),\phi) \mid |\zeta| \le h(\phi), \ \phi \in \mathcal{I}\}, \\ L &= \{(\zeta,\lambda,\phi_0) \mid |\zeta| \le \lambda, \quad \lambda \in [0,h(\phi_0)]\}. \end{aligned}$$

We observe the following:

1. Along $S^{\pm}$, the outer normal to W is given by $\mathbf{n}_{S^{\pm}} = \frac{1}{\sqrt{2}}(\pm 1,-1,0)$ and hence on $S^{\pm}$, the right-hand-side $\mathbf{v}^m$ of system (C.7) satisfies

$$\mathbf{v}^m \cdot \mathbf{n}_{S^{\pm}}|_{S^{\pm}} = \pm\epsilon\Delta p'(\phi)M(\lambda) + \epsilon\lambda^2\{[\partial_x f_1^0(p(\phi),\phi) - f_2^0(p(\phi),\phi)] + \mathcal{O}(\epsilon) + \mathcal{O}(\lambda)\}.$$

   - For $z^* \le \lambda \le h(\phi)$, we have

$$\begin{aligned} \mathbf{v}^m \cdot \mathbf{n}_{S^{\pm}}|_{S^{\pm}} &= \pm\epsilon\Delta p'(\phi) + \epsilon\lambda^2\left[\partial_x f_1^0(p(\phi),\phi) - f_2^0(p(\phi),\phi)\right] + \mathcal{O}(\epsilon\lambda) \\ &< \epsilon\Delta\,|p'(\phi)| + \epsilon(z^*)^2\left[\partial_x f_1^0(p(\phi),\phi) - f_2^0(p(\phi),\phi)\right] + \epsilon h(\phi)K_1 \end{aligned}$$

   Fixing

$$\Delta = 1, \qquad z^* = \frac{1}{\sqrt{\epsilon}}, \tag{C.9}$$

   we obtain, under the condition (7.19),

$$\begin{aligned} \mathbf{v}^m \cdot \mathbf{n}_{S^{\pm}}|_{S^{\pm}} &< -\left[f_2^0(p(\phi),\phi) - \partial_x f_1^0(p(\phi),\phi) - \epsilon\,|p'(\phi)|\right] + \epsilon h(\phi)K_1 \\ &< 0, \end{aligned} \tag{C.10}$$

   for all $\phi \in \mathcal{I}$, appropriate $K_1 > 0$ and

$$h(\phi) \le H_1 = \frac{\inf_{\phi\in\mathcal{I}}\left[f_2^0(p(\phi),\phi) - \partial_x f_1^0(p(\phi),\phi) - \epsilon\,|p'(\phi)|\right]}{2\epsilon K_1} = \frac{C_1}{2\epsilon K_1}, \tag{C.11}$$

   provided that

$$z^* = \left\{\frac{1}{\epsilon}\right\}^{\frac{1}{2}} < h(\phi) \le H_1 = \frac{C_1}{2\epsilon K_1}, \tag{C.12}$$

   or

$$\sqrt{\epsilon} < \frac{C_1}{2K_1} \Longrightarrow \epsilon \le \left\{\frac{C_1}{2K_1}\right\}^2. \tag{C.13}$$

   - For $\frac{z^*}{q} < \lambda < z^*$, following the above steps and using (C.9) , we again obtain

$$\begin{aligned} \mathbf{v}^m \cdot \mathbf{n}_{S^\pm}|_{S^\pm} &= \pm\epsilon p'(\phi)M(\lambda) + \epsilon\lambda^2\left[\partial_x f_1^0(p(\phi),\phi) - f_2^0(p(\phi),\phi)\right] + \mathcal{O}(\epsilon\lambda) \\ &< \epsilon\,|p'(\phi)| + \epsilon(\frac{z^*}{q})^2\left[\partial_x f_1^0(p(\phi),\phi) - f_2^0(p(\phi),\phi)\right] + \mathcal{O}(\epsilon\lambda) \\ &< -\left\{\frac{1}{q^2}\left[f_2^0(p(\phi),\phi) - \partial_x f_1^0(p(\phi),\phi)\right] - \epsilon\,|p'(\phi)|\right\} + \epsilon h(\phi)K_2 \\ &< 0, \end{aligned} \tag{C.14}$$

for appropriate $K_2 > 0$ and $q = 1 + \delta$ with $0 < \delta \ll 1$, provided that ϵ and $h(\phi)$ is small enough.

- For $0 < \lambda \le \frac{z^*}{q}$, we obtain similarly from (7.19) that

$$\begin{aligned} \mathbf{v}^m \cdot \mathbf{n}_{S^\pm}|_{S^\pm} &< -\epsilon\lambda^2\{[f_2^0(p(\phi),\phi) - \partial_x f_1^0(p(\phi),\phi)] + \mathcal{O}(\epsilon) + \mathcal{O}(\lambda)\} \\ &< -\epsilon\lambda^2\{[f_2^0(p(\phi),\phi) - \partial_x f_1^0(p(\phi),\phi)] + \epsilon K_3 + h(\phi)K_4\} \\ &< 0, \end{aligned} \tag{C.15}$$

for appropriate $K_3, K_4 > 0$ provided that ϵ and $h(\phi)$ are small enough.

2. Along the boundary segment T of W, the outer normal is given by $\mathbf{n}_T = (0,0,1)$, and

$$\begin{aligned} \mathbf{v}^m \cdot \mathbf{n}_T|_T &= \epsilon h^2(\phi)[f_2^0(p(\phi),\phi) + \mathcal{O}(\epsilon h(\phi)) + \mathcal{O}(\zeta)], \\ &> \epsilon h^2(\phi)[f_2^0(p(\phi),\phi) - \epsilon h(\phi)K_2 - h(\phi)K_3] \\ &> 0, \end{aligned} \tag{C.16}$$

for appropriate $K_2, K_3 > 0$, and small enough $\epsilon > 0$ and h_ϕ.

3. Along L, the outer normal is given by $\mathbf{n}_L = (0,0,1)$, and hence, by (C.9), we have

$$\mathbf{v}^m \cdot \mathbf{n}_L|_L = \epsilon M(\lambda + \epsilon w_2) \ge 0. \tag{C.17}$$

We fix now $h(\phi) = h > 0$, $\epsilon > 0$ small enough so that estimates (C.10)-(C.17) for system (C.7) all hold for all $\phi \in \mathcal{I} = (-\infty, \phi_0)$, where $\phi_0 = \epsilon t_0$. We then rewrite (C.7) as an autonomous dynamical system on the extended phase space of the $(\zeta, \lambda, \phi, t)$ variables as follows:

$$\begin{aligned} \dot\zeta &= -\epsilon\Delta p'(\phi)M(\lambda) + \epsilon\lambda[\zeta\partial_x f_1^0(p(\phi),\phi) + \mathcal{O}(\epsilon\lambda) + \mathcal{O}(\zeta^2)] + \mathcal{O}(\epsilon^2\lambda) + \mathcal{O}(\epsilon^3\lambda^3), \\ \dot\lambda &= \epsilon\lambda^2[f_2^0(p(\phi),\phi) + \mathcal{O}(\epsilon\lambda) + \mathcal{O}(\zeta)] + \mathcal{O}(\epsilon^2\lambda^2) + \mathcal{O}(\epsilon^3\lambda^4), \\ \dot\phi &= \epsilon\Delta M(\lambda), \\ \dot t &= 1. \end{aligned}$$

For this system, we define the set

$$\mathcal{W} = W \times (-\infty, t_0),$$

the extension of the cone W defined in (C.8).

Observe that by estimates (C.10)-(B.8), the set of initial conditions $(\zeta_0, \lambda_0, \phi_0, t_0)$ that immediately leave $\mathcal{W}$ in *backward* time is given by

$$\mathcal{W}^{im} = \left\{(\zeta, \lambda, \phi, t) \in \mathcal{W} \mid \lambda > 0\,, \quad (\zeta, \lambda, \phi) \in S^+ \cup S^-\right\}, \tag{C.18}$$

which is a union of the two disjoint components $(S^+ \cap \{\lambda > 0\}) \times (-\infty, t_0]$ and $(S^- \cap \{\lambda > 0\}) \times (-\infty, t_0]$.

Assume that $\mathcal{W}^{ev} = \mathcal{W}$, i.e., all the initial conditions eventually leave $\mathcal{W}$ in backward time. Then $\mathcal{W}$ qualifies as a backward time Wasewski set (see section B.2.2), since

1. $\mathrm{cl}(\mathcal{W}) = \mathcal{W}$,
2. $\mathcal{W}^{im}$ is a relatively closed subset of $\mathcal{W}^{ev}$. Indeed, Cauchy sequences in $\mathcal{W}^{im}$ that converge to $\mathcal{C}$ (given by $\zeta = 0,\ \lambda = 0$), have their limit points outside $\mathcal{W}^{im}$ and $\mathcal{W}^{ev}$. All other sequences in $\mathcal{W}^{im}$ converge to points within $\mathcal{W}^{im}$ and those points are in $\mathcal{W}^{ev}$, since $\mathcal{W}^{im} \subset \mathcal{W}^{im}$ by definition.

Thus, by the Wasewski principle, the *Wasweski map* Γ defined in (B.22) is continuous, which is a contradiction, because Γ maps the connected set $\mathcal{W}^{ev}$ into the disconnected set $\mathcal{W}^{im}$. Therefore, we conclude that $\mathcal{W}^{ev} \neq \mathcal{W}$ and there exists a nonempty set $\tilde{\mathcal{W}}_\epsilon^\infty$ of solutions which stay in $\mathcal{W}$ for all backward times, i.e.. for $(-\infty, t_0]$. Also

1. $\tilde{\mathcal{W}}_\epsilon^\infty$ is a two dimensional set,
2. $\tilde{\mathcal{W}}_\epsilon^\infty$ extends to the top boundary $T \times (-\infty, t_0)$ of the Wasewki set, $\mathcal{W}$, and
3. $\tilde{\mathcal{W}}_\epsilon^\infty$ is necessarily smooth in t, because it is composed of trajectories that are smooth in t.

Next we want to argue that all solutions in $\tilde{\mathcal{W}}_\epsilon^\infty$ tend to $\zeta = \lambda = 0$ in backward time. Consider a specific initial condition $(\zeta_0, \lambda_0, \phi_0, t_0) \in \tilde{\mathcal{W}}_\epsilon^\infty$, and denote the trajectory emanating from this initial position by $(\zeta(t), \lambda(t), \phi(t))$. Along this trajectory, the λ-component of system (C.7) can be re-written as

$$\dot{\lambda} = \epsilon\lambda^2[f_2^0(p(\phi), \phi) + \zeta m_1(\zeta, \lambda, \phi, t) + \epsilon m_2(\zeta, \lambda, \phi, t)], \tag{C.19}$$

for some appropriate smooth functions m_1 and m_2. Direct integration gives

$$\begin{aligned}
\lambda(t) \quad &= \quad \frac{\lambda_0}{1 + \epsilon\lambda_0 \int_t^{t_0} [f_2^0(p(\phi), \phi) + \zeta m_1(\zeta, \lambda, \phi, \tau) + \epsilon m_2(\zeta, \lambda, \phi, t)]\, d\tau}, \\
&\leq \quad \frac{\lambda_0}{1 + \epsilon\lambda_0 \int_t^{t_0} [f_2^0(p(\phi), \phi) - H|m_1(\zeta, \lambda, \phi, \tau)| - \epsilon|m_2(\zeta, \lambda, \phi, t)|]\, d\tau},
\end{aligned}$$

with H being a uniform upper bound for $h(\phi)$. The above inequality holds for all $t \in (-\infty, t_0]$, because the trajectory we consider stays in $\mathcal{W}$ for all backward times.

Making ϵ and H small enough, the uniform boundedness of $m_k(\zeta, \lambda, \phi, \tau)$ leads to the estimate

$$\lambda(t) \leq \frac{\lambda_0}{1 + \frac{1}{2}\epsilon\lambda_0 \int_t^{t_0} \inf_{\phi\in\mathcal{I}} f_2^0(p(\phi), \phi)\; d\tau} = \frac{\lambda_0}{1 + \epsilon\lambda_0 c_2(t_0 - t)/2},$$

which implies that

$$\lim_{t\to-\infty} \lambda(t) = 0.$$

Therefore, trajectories that never leave $\mathcal{W}$ in backward time will necessary converge to the $\lambda = 0$ boundary of $\mathcal{W}$. By definition of $\mathcal{W}$, however, this convergence in the λ direction implies

$$\lim_{t\to-\infty} \zeta(t) = 0.$$

We therefore conclude that all trajectories in $\tilde{\mathcal{W}}_\epsilon^\infty$ converge to the set $\lambda = \zeta = 0$ (i.e., the curve $\mathcal{C}$) in backward time, thus $\tilde{\mathcal{W}}_\epsilon^\infty$ is an unstable manifold for $\mathcal{C}$ for all $t \leq t_0$.

C.3 Slope of the unstable manifold for $\Delta = 0$

In this section we determine a slope formula that can be used to linearly approximate $\mathcal{W}_\epsilon^\infty$. By the structure of the steady adiabatic limit (7.14) of first order averaged normal form (C.4), we obtain $(x, y) = (p(\phi), y)$ as a first order approximation for $\mathcal{W}_\epsilon^\infty$. Following the approach developed in [52] for fixed unsteady separation in fluid flows, the approximation for $\mathcal{W}_\epsilon^\infty$ can be refined by a second order averaging.

As in case of first-order averaging, we eliminate the oscillatory part of $\mathbf{F}$ in equation (C.4) by seeking a near-identity coordinate change of the form

$$\xi = \eta + \epsilon^2\mathbf{h}(\eta, \phi, t), \qquad \eta = (\eta, \mu),$$

where, $\mathbf{h} = (h_1, h_2)$ is a uniformly bounded function to be specified later. The above coordinate applied to system (C.4) with $\Delta = 0$ gives

$$\begin{aligned} \dot{\xi} &= \dot{\eta} + \epsilon^2\left(\nabla_\eta \mathbf{h}\right)\dot{\eta} + \epsilon^2\left(\partial_\phi \mathbf{h}\right)\dot{\phi} + \epsilon^2\partial_t\mathbf{h}, \\ &= \epsilon\mathbf{f}^0(\eta + \epsilon^2\mathbf{h}, \phi) + \epsilon^2\mathbf{F}(\eta + \epsilon^2\mathbf{h}, \phi, t) + \mathcal{O}(\epsilon^3), \\ &= \epsilon\mathbf{f}^0(\eta, \phi) + \epsilon^2\mathbf{F}(\eta, \phi, t) + \mathcal{O}(\epsilon^3), \end{aligned} \tag{C.20}$$

leading to

$$[\mathbf{I} + \epsilon^2\nabla_\eta\mathbf{h}]\dot{\eta} = \epsilon\mathbf{f}^0(\eta, \phi) + \epsilon^2[\mathbf{F}(\eta, \phi, t - \partial_t\mathbf{h}] + \mathcal{O}(\epsilon^3). \tag{C.21}$$

If $||\nabla_\eta\mathbf{h}||$ remains uniformly bounded for all $t \leq t_0$, then for small enough ϵ, the operator $[\mathbf{I} + \epsilon^2\nabla_\eta\mathbf{h}]$ is invertible, and hence (C.21) can be written as

$$\begin{aligned} \dot{\eta} &= [\mathbf{I} + \epsilon^2\nabla_\eta\mathbf{h}]^{-1}\left\{\epsilon\mathbf{f}^0(\eta, \phi) + \epsilon^2[\mathbf{F}(\eta, \phi, t) - \partial_t\mathbf{h}] + \mathcal{O}(\epsilon^3)\right\}, \qquad \text{(C.22)} \\ &= \epsilon\mathbf{f}^0(\eta, \phi) + \epsilon^2[\mathbf{F}(\eta, \phi, t) - \partial_t\mathbf{h}] + \mathcal{O}(\epsilon^3). \end{aligned}$$

We recall that we have set $\Delta = 0$, therefore $\phi = const.$ by (C.4).

Assume that $\mathbf{F}$ (C.5) admits a decomposition of the form

$$\mathbf{F}(\xi,\phi,t) = \mathbf{F}^0(\xi,\phi) + \tilde{\mathbf{F}}(\xi,\phi,t), \quad \lim_{T\to\infty}\frac{1}{T}\int_{t_0-T}^{t_0}\tilde{\mathbf{F}}(\xi,\phi,t)dt = 0,$$

Then by choosing

$$\mathbf{h}(\eta,\phi,t) = \int_{t_0}^{t}\left[\mathbf{F}(\eta,\phi,t) - \mathbf{F}^0(\eta,\phi)\right] d\tau, \tag{C.23}$$

we obtain from (C.22) the second-order averaged normal form

$$\begin{aligned} \dot{\eta} &= \epsilon\mu\left[f_1^0(\eta,\phi) + \epsilon\mu F^0(\eta,\phi)\right] + \mathcal{O}(\epsilon^3), \\ \dot{\mu} &= \epsilon\mu^2\left[f_2^0(\eta,\phi) + \epsilon\mu G^0(\eta,\phi)\right] + \mathcal{O}(\epsilon^3), \end{aligned}$$

Rescaling time by letting $d\tau/dt = \epsilon\mu(t)$ and ignoring higher-order terms, we obtain the system

$$\begin{aligned} \eta' &= f_1^0(\eta,\phi) + \epsilon\mu F^0(\eta,\phi), \\ \mu' &= \mu\left[f_2^0(\eta,\phi) + \epsilon\mu G^0(\eta,\phi)\right], \end{aligned}$$

Under the conditions of Theorem 1, the above system has an hyperbolic fixed point $(p(\phi),0)$ for every constant $\phi \in \mathcal{I}$ with an associated one dimensional unstable manifold. The unstable manifold at $\phi \in \mathcal{I}$ is tangent to the unstable eigenvector

$$\mathbf{e}(\phi) = \begin{pmatrix} \epsilon F^0(p(\phi),\phi) \\ f_2^0(p(\phi),\phi) - \partial_x f_1^0(p(\phi),\phi) \end{pmatrix}, \tag{C.24}$$

Recalling that

$$(\eta,\mu) = (\xi,\lambda) + \mathcal{O}(\epsilon^2) = (x,z) + \mathcal{O}(\epsilon) = (x,y/\epsilon) + \mathcal{O}(\epsilon),$$

we find from (C.24) that the slope of $\mathcal{W}_\epsilon^\infty$ relative to the normal of $\mathcal{S}$ becomes 7.21.

C.4 Review of Wavelet Analysis

Before going into the details of wavelet based denoising, we first briefly review *multi-resolution analysis* (see for e.g. [62], [17],[48]), essential to the development of the denoising operation.

C.4.1 Multi resolution analysis

Consider the space $\mathcal{L}^2(\mathbf{R})$ of square integrable functions $f(t) : \mathbf{R} \to \mathbf{R}$

$$\mathcal{L}^2(\mathbf{R}) = \{f(t) | \int_{\mathbf{R}} |f(t)|^2 dt < \infty\}, \tag{C.25}$$

with standard inner product $< \cdot, \cdot >$

$$< f(t), g(t) >= \int_{\mathbf{R}} f(t)g(t)dt. \tag{C.26}$$

A *multiresolution analysis* (or approximation) of $\mathcal{L}^2(\mathbf{R})$ consists of a nested sequence of closed subspaces V_j, $j \in Z$ of $\mathcal{L}^2(\mathbf{R})$

$$\cdots \subset V_{-2} \subset V_{-1} \subset V_0 \subset V_1 \subset V_2 \subset \cdots , \tag{C.27}$$

such that

$$\bigcap_{j \in Z} V_j = 0, \qquad \overline{\bigcup_{j \in Z} V_j} = \mathcal{L}^2(R), \tag{C.28}$$

V_j are scale and shift invariant

$$f(t) \in V_{j-1} \Leftrightarrow f(2t) \in V_j, \qquad f(t) \in V_j \Leftrightarrow f(t - 2^j k) \in V_j, \tag{C.29}$$

and there exists a *scaling function* $\phi(t) \in V_0$ whose integer translates span V_0

$$V_0 = \{f \in \mathcal{L}^2(\mathbf{R}) | f(t) = \sum_{k \in Z} \alpha_k \phi(t - k), \alpha_k \in \mathbf{R}\}. \tag{C.30}$$

The function $\phi(t)$ has to satisfy the two-scale difference equation

$$\phi(t) = \sqrt{2} \sum_{k \in Z} h_k \phi(2t - k), \tag{C.31}$$

for some coefficients $h_k \in \mathbf{R}$ which are known as the *filter coefficients*. The family $\{\phi_{jk}\}$, where

$$\phi_{jk}(t) = 2^{j/2} \phi(2^j t - k), \qquad j, k \in Z, \tag{C.32}$$

then forms an orthonormal basis of V_j. Defining W_j as the orthogonal complement of V_j in V_{j+1}, gives rise to a sequence $\{W_j | j \in Z\}$ of closed mutually orthogonal subspaces of $\mathcal{L}^2(R)$, such that each W_j is a dilate of W_0, and their direct sum is $\mathcal{L}^2(R)$ i.e.

$$\mathcal{L}^2(R) = \bigoplus_{j \in Z} W_j. \tag{C.33}$$

The space W_0 is spanned by integer translates of *mother wavelets* $\psi(t)$ that is related to the scaling function $\phi(t)$ through the equation

$$\psi(t) = \sqrt{2} \sum_{k \in Z} (-1)^k h_{1-k} \phi(2t - k). \tag{C.34}$$

In this way one obtains a wavelet system which is an infinite collection of translated and scaled versions of the mother wavelet $\psi(t)$

$$\psi_{jk}(t) = 2^{j/2} \psi(2^j t - k), \qquad i, j \in Z, \tag{C.35}$$

such that $\{\psi_{jk}, j, k \in Z\}$ is an orthonormal basis of $\mathcal{L}^2(R)$. Therefore any $f \in \mathcal{L}^2(R)$ can be represented as

$$f(t) = \sum_{j \in Z} \sum_{k \in Z} w_{jk} \psi_{jk}(t) = \sum_{k \in Z} c_{j_0 k} \phi_{j_0 k}(t) + \sum_{j=j_0}^{\infty} \sum_{j \in Z} w_{jk} \psi_{jk}(t), \tag{C.36}$$

with $c_{j_0 k} = \langle f, \phi_{j_0 k} \rangle$ and $w_{jk} = \langle f, \phi_{jk} \rangle$ and is referred to as the *discrete wavelet transform* of $f(t)$. Here j_0 represents a *coarse* level of approximation. The first part of (C.36) is the projection of f onto the coarse approximating space V_{j_0} and the second part represents the details. This equation demonstrates that any function $f(t) \in \mathcal{L}^2(\mathbf{R})$ may be represented as a series of successive approximations in the wavelet expansion. The first approximation is achieved by the scaling functions ϕ is a kind of smoothing. The parts which cannot be represented with sufficient accuracy in this way, can be approximated further by wavelets ψ with increasing resolutional levels allowing finer and finer gradation.

Through a careful choice of filter coefficients h_k, wavelet functions with desirable properties can be constructed. It is possible to construct, finite-length sequences of filter coefficients satisfying all of the axioms of multiresolution analysis, resulting in compactly supported ϕ and ψ that have time-frequency localization. This localization allows parsimonious representation for a wide set of different functions in wavelet series, which is the key to their powerful approximating capability.

In many practical situations, the function to be represented as a wavelet series may be defined only over a finite interval and only sampled values of $f(t)$ may be known. Several extensions are available to handle these constraints [62]. Analogous to *Fast Fourier Transform*, there is *Mallat's* fast algorithm [62], which allows *Discrete Wavelet Transform* and *Inverse Discrete Wavelet Transform* to be performed efficiently.

C.4.2 Wavelet based denoising

Consider a function $f \in \mathcal{L}^2(\mathbf{R})$ that is observed in a noisy form as $X(t)$ such that

$$X(t) = f(t) + W(t), \tag{C.37}$$

where, $W(t)$ is a zero mean Gaussian white noise with variance σ_w^2. The first step in denoising is to decompose $X(t)$ into an orthogonal wavelet series

$$X(t) = \sum_{k \in Z}^{\infty} c_{j_0 k} \phi_{j_0 k}(t) + \sum_{j=j_0}^{\infty} \sum_{k \in Z} \tilde{w}_{jk} \psi_{jk}(t), \tag{C.38}$$

where, $\tilde{w}_{jk}$ can be thought as the wavelets coefficients of f contaminated with noise. The sparseness of the wavelet expansion makes it reasonable to assume that essentially only a few *large* wavelet coefficients contain information about the underlying function f, while *small* coefficients can be attributed to the noise which uniformly contaminates all coefficients.

An approximate wavelet representation of the underlying function f can then be obtained by retaining the *significant* large coefficients and setting all others equal to zero. Thresholding the wavelet coefficients $\tilde{w}_{jk}$ and reconstructing the corresponding signal can be represented as an averaging operator $<>$ as

$$f(t) \approx < X(t) >= \sum_{k \in Z}^{\infty} c_{j_0 k} \phi_{j_0 k}(t) + \sum_{j=j_0}^{\infty} \sum_{k \in Z} \rho_T(\tilde{w}_{jk}) \psi_{jk}(t), \tag{C.39}$$

where, ρ_T is a threshold function. Depending on the choice of ρ_T, there are two basic approaches to denoising: *linear estimation* and *nonlinear estimation.* A good review of these can be found in [1], [3].

Following the standard generalized Fourier methodology, in linear estimation by wavelets, the thresholding function is given by

$$\rho_T(\tilde{w}_{ij}) = \begin{matrix} \tilde{w}_{ij} & i \leq M, \\ 0 & i > M, \end{matrix} \tag{C.40}$$

i.e. all coefficients in the first M coarsest levels are considered significant and all coefficients at higher resolution levels are neglected. The performance of the truncated wavelet estimator clearly depends on an appropriate choice of M. Too small M will result in an oversmoothed estimator, whereas setting M large simply reproduces the data.

Such truncated estimators however face difficulties in estimating inhomogeneous functions with bursts and intermittency like those arise in turbulent flows. Accurate approximation of the bursts will require high-level terms and as a result a large value of M, while the corresponding oscillating terms will damage the estimate in smooth regions. In essence, linear estimation does not use the local nature of wavelet series and as a result suffers from similar problems as the use of a Fourier sine and cosine basis.

In contrast to the linear wavelet estimators, a nonlinear wavelet estimator is based on selective reconstruction of empirical wavelet coefficients. Nonlinear thresholding of wavelet coefficients has been proposed by Donoho and Johnstone [25] to denoise signals corrupted by a *Gaussian noise* and it has been later generalized to *correlated* and *non Gaussian noises* [96],[97]. For the noisy signal which has been transformed into wavelet coefficient space, only the coefficients whose modulus is above a given threshold value are kept, and the denoised signal is obtained using an inverse wavelet transform.

Thresholding function Thresholding essentially allows the data itself to decide which coefficients are significant and to exploit the local nature of wavelet bases. The *hard thresholding* is a *keep or kill rule* and is given by

$$\rho_T(\tilde{w}_{jk}) = \tilde{w}_{jk} \mathcal{I}(|\tilde{w}_{jk}| > T), \tag{C.41}$$

where, $\mathcal{I}$ is an indicator function. On the other hand, the *soft thresholding* defined by

$$\rho_T(\tilde{w}_{jk}) = \tilde{w}_{jk} \max(0, |\tilde{w}_{jk}| - T), \tag{C.42}$$

is a *shrink or kill rule.* The hard thresholding results in larger variance while soft thresholding has a larger bias. To compromise the trade-off between variance and bias, a *firm thresholding* can be used which offers some advantages over both the hard and soft variants. However, this has a drawback in that it requires two threshold values, thus making the estimation procedure for the threshold values more computationally expensive.

Threshold selection Clearly, an appropriate choice of the threshold value T is fundamental to the effectiveness of the procedure described in the previous section. Too large threshold might *cut off* important parts of the true function underlying the noisy data, whereas too small a threshold retains noise in the selective reconstruction. Donoho and Johnstone proposed an universal threshold

$$T_D = \sigma_w \sqrt{2 \log N}, \tag{C.43}$$

with σ_w being the noise variance and is to be replaced by suitable its estimate $\hat{\sigma_w}$ derived from data when it is unknown and N is the length of the data set. Despite the simplicity of such a threshold, for both hard and soft thresholding the resulting nonlinear wavelet estimator is asymptotically near-minimax in terms of mean square error.

Moreover, for inhomogeneous functions it outperforms any linear estimator, including the truncated and shrunk wavelet estimators as discussed earlier. Whilst having important asymptotic properties, the universal threshold depends on the data only through the σ_w (or its estimate). Otherwise, it essentially ignores the data and cannot be tuned to a specific problem at hand. In fact, for large samples T_D will remove with high probability all the noise in the reconstruction, but part of the real signal might also be lost. As a result, the universal threshold does not compromise between signal and noise and tends to oversmooth in practice.

In view of above various alternative data-adaptive thresholding rules have been developed. For example Donoho and Johnstone proposed a *SureShrink* thresholding rule based on minimizing *Stein's unbiased risk estimate.* Other variants exist, which for e.g. are based on *multiple hypotheses testing* and *Bayesian* approaches (see [95]). Further modifications of the basic thresholding scheme include, *level dependent* and *block thresholding.* In the first case, different thresholds are used on different levels, while in the second the coefficients are thresholded in blocks rather than individually. Both modifications imply better asymptotic properties of the resulting wavelet estimators.

Estimation of noise variance In order to determine the threshold T_D, the unknown variance of the noise has to be estimated. The standard method commonly used is the *Median Absolute Deviation* (MAD), which estimates the level of the noise from the median of the modulus of wavelet coefficients at the smallest scale [95]. An alternate technique is a recursive algorithm proposed in [5].

Appendix D

Appendix: Crossflow separation

D.1 Pseudo stable manifold theorem

The pseudo stable manifold theorem is a generalization of stable manifold theorem [36]. It can be used to obtain a characterization of internal structure of stable and unstable manifolds associated with hyperbolic invariant sets. For instance, stable manifolds contain invariant submanifolds (like strong stable manifold) in which the initial conditions converge faster than a prescribed exponential rate.

We recall pseudo stable manifold theorem for a fixed point $\mathbf{p}$ of a dynamical system

$$\dot{\mathbf{x}} = f(\mathbf{x}), \tag{D.1}$$

where, $\mathbf{x} \in \mathbf{R}^n$ and f is of class C^r with $r > 1$. Assume that there exits a splitting of the tangent space $T_p\mathbf{R}^n = E_1 \oplus E_2$ such that for some $a \in \mathbf{R}$, the real parts of the eigenvalues of $Df(\mathbf{p})|E_1$ are smaller than a and the real part of the eigenvalues of $Df(\mathbf{p})|E_2$ are larger than a. Then there exits a locally invariant C^1 manifold $\mathcal{W}$ that is tangent to the subspace E_1. In general, $\mathcal{W}$ is neither unique nor of class C^r.

D.2 Proof of Proposition I

D.2.1 Modified Wall-shear field

We shall denote by $C^0(\mathbf{R}^n, \mathbf{R}^m)$ the space of continuous functions $f : \mathbf{R}^n \to \mathbf{R}^m$ and

$$\mathcal{C}^0(\mathbf{R}^n, \mathbf{R}^m) = \{f \in C^0(\mathbf{R}^n, \mathbf{R}^m), ||f||_0 = \sup_{\mathbf{x} \in \mathbf{R}^n} ||f(\mathbf{x})|| < \infty\}, \tag{D.2}$$

where, $||(x_1, \cdots, x_m)|| = \sum_{i=1}^m |x_i|$ is the norm used on $\mathbf{R}^m$. There exists smooth *bump function* $\gamma(x, y) \in \mathcal{C}^0(\mathbf{R}^2, \mathbf{R})$ (see [12]) such that

1. $\gamma(x, y) \equiv 1$ for $(x, y) \in \mathcal{B}_{\frac{\alpha(\delta)}{3}}$.

2. $\gamma(x, y) \equiv 0$ for $(x, y) \in \mathbf{R}^2 \setminus \mathcal{B}_{\alpha(\delta)}$

3. $||\gamma||_0 = 1$, $\nabla_{\mathbf{x}}\gamma(x,y) \in \mathcal{C}^0(\mathbf{R}^2, \mathbf{R})$ and $||\nabla_{\mathbf{x}}\gamma||_0 \leq \frac{2}{\alpha(\delta)}$,

where, $\alpha(\delta)$ above is as defined in section 8.2.3. From now on we would drop the dependence of α on δ for brevity.

Defining $F(x,y) = f(x,y)\gamma(x,y)$ and $G(x,y) = g(x,y)\gamma(x,y)$ we get a *modified* system

$$\begin{aligned} \dot{x} &= -\lambda x + F(x,y), \\ \dot{y} &= -\mu y + G(x,y), \end{aligned} \tag{D.3}$$

which agrees with the system (8.17) on the set $\mathcal{B}_{\alpha/3}$.

Using the mean value theorem we get

$$\sup_{(x,y)\in\mathcal{B}_\alpha} ||f(x,y)|| < \frac{\delta\alpha}{3}, \qquad \sup_{(x,y)\in\mathcal{B}_\alpha} ||g(x,y)|| < \frac{\delta\alpha}{3}.$$

and therefore

$$\begin{aligned} ||\nabla_{\mathbf{x}}F||_0 &= \sup_{(x,y)\in\mathbf{R}^2} ||\nabla_{\mathbf{x}}F(x,y)|| \\ &= \sup_{(x,y)\in\mathcal{B}_\alpha} ||\nabla_{\mathbf{x}}(\gamma(x,y)f(x,y))|| \\ &< \sup_{(x,y)\in\mathcal{B}_\alpha} ||\nabla_{\mathbf{x}}f(x,y)|| + ||\nabla_{\mathbf{x}}\gamma||_0 \sup_{(x,y)\in\mathcal{B}_\alpha} ||f(x,y)|| \\ &< \frac{\delta}{3} + \frac{2}{\alpha}\frac{\delta\alpha}{3} < \delta, \end{aligned} \tag{D.4}$$

with similar estimate for $||\nabla_{\mathbf{x}}G||_0$. Also, $F(0,0) = G(0,0) = 0$, $\nabla_{\mathbf{x}}F(0,0) = \nabla_{\mathbf{x}}G(0,0) = 0$ and $F, G \in \mathcal{C}^1(\mathbf{R}^2, \mathbf{R})$. By *Mean Value* theorem, F satisfies

$$||F(x_2,y_2) - F(x_1,y_1)|| \leq \delta\left(|x_2 - x_1| + |y_2 - y_1|\right), \tag{D.5}$$

with similar inequality for G. Hence, F and G are globally *Lipsitz*.

D.2.2 Integral Equations

For $0 < \epsilon < 1$ and $\mu, K > 0$ we introduce the space

$$\mathcal{B}_{\epsilon,K}((-\infty,0],\mathbf{R}^2) = \{\phi(t) = (\phi_1(t),\phi_2(t)) : \phi_1,\phi_2 \in \mathcal{C}^0((-\infty,0],\mathbf{R}), \phi_1(0) = \alpha, ||\phi||_\epsilon \leq K\}, \tag{D.6}$$

where, the norm $||\cdot||_\epsilon$ is defined as

$$||\phi||_\epsilon = \sup_{t\leq 0} ||\phi(t)||e^{\epsilon\mu t}, \tag{D.7}$$

We show that $\mathcal{B}_{\epsilon,K}((-\infty,0],\mathbf{R}^2)$ is *complete metric* space. First consider the space

$$\mathcal{B}_{\epsilon,\infty}((-\infty,0],\mathbf{R}^2)=\{\phi(t)=(\phi_1(t),\phi_2(t)):\phi_1,\phi_2\in\mathcal{C}^0((-\infty,0],\mathbf{R}),\phi_1(0)=0,||\phi||_\epsilon<\infty\},\tag{D.8}$$

and take a Cauchy sequence $\{\phi_n\}_{n\in\mathcal{N}}\subset\mathcal{B}_{\epsilon,\infty}((-\infty,0],\mathbf{R}^2)$. There exists integer J such that for $m,n>J$ and any $\tilde{\delta}>0$ and any $t\leq 0$

$$||\phi_n-\phi_m||_\epsilon<\tilde{\delta}e^{\epsilon\mu t}\tag{D.9}$$

or

$$||\phi_n(t)-\phi_m(t)||<\tilde{\delta}.\tag{D.10}$$

Hence for any fixed t, $\{\phi_n(t)\}_{n\in\mathcal{N}}$ is Cauchy sequence in $\mathbf{R}^2$ and so converges to say $\phi(t)$. Moreover, the above inequality shows that this convergence is uniform on compact subsets $K=[t_1,t_2]\subset(-\infty,0]$, hence $\phi(t)$ is a continuous function. Moreover $\phi_1(0)=\alpha$, concluding that $\mathcal{B}_{\epsilon,\infty}((-\infty,0],\mathbf{R}^2)$ is complete metric space. Since $\mathcal{B}_{\epsilon,K}((-\infty,0],\mathbf{R}^2)$ is closed subset of $\mathcal{B}_{\epsilon,\infty}((-\infty,0],\mathbf{R}^2)$, it is a complete metric space.

We want to determine an negatively invariant set for the system (D.3) as set of initial condition defined by

$$\mathcal{W}_\epsilon=\{\mathbf{w}_0\in\mathbf{R}^2:\phi(t;\mathbf{w}_0)\in\mathcal{B}_{\epsilon,K}((-\infty,0],\mathbf{R}^2)\},\tag{D.11}$$

where, $\phi(t;\mathbf{w}_0)$ is solution of the system (D.3) with initial condition $\mathbf{w}_0$. Note that $\mathbf{w}_0=(0,0)\in\mathcal{W}_\epsilon$.

Let $\phi(t)=(\phi_1(t),\phi_2(t))\in\mathcal{W}_\epsilon$, then it satisfies for $t\leq 0$

$$\begin{aligned}\dot{\phi}_1&=-\lambda\phi_1(t)+F(\phi(t)),\\ \dot{\phi}_2&=-\mu\phi_2(t)+G(\phi(t)).\end{aligned}\tag{D.12}$$

Equivalently the integral equations are true

$$\begin{aligned}\phi_1(t)e^{\lambda t}&=w_{01}+\int_0^t e^{\lambda\tau}F(\phi(\tau))d\tau,\\ \phi_2(t)e^{\mu t}&=\phi_2(\tilde{t})e^{\mu\tilde{t}}+\int_{\tilde{t}}^t e^{\mu\tau}G(\phi(\tau))d\tau,\end{aligned}$$

where, we have taken $\phi_1(0)=w_{01}$. Since for any $\tilde{t}<0$ $(\phi_1(\tilde{t}),\phi_2(\tilde{t}))\in\mathcal{W}_\epsilon$

$$\limsup_{\tilde{t}\to-\infty}|\phi_2(\tilde{t})e^{\mu\tilde{t}}|=\limsup_{t\to-\infty}e^{\mu(1-\epsilon)\tilde{t}}|\phi_2(\tilde{t})|e^{\mu\epsilon\tilde{t}}\leq\lim_{\tilde{t}\to-\infty}e^{\mu(1-\epsilon)\tilde{t}}K=0,$$

we get from (D.15)

$$\phi_2(t)=\int_{-\infty}^t e^{\mu(\tau-t)}G(\phi(\tau))d\tau$$

Hence $\phi(t) \in \mathcal{W}_\epsilon$ iff

$$\begin{aligned}
\phi_1(t) &= w_{01}e^{-\lambda t} + \int_0^t e^{\lambda(\tau-t)}F(\phi(\tau))d\tau, \\
\phi_2(t) &= \int_{-\infty}^t e^{\mu(\tau-t)}G(\phi(\tau))d\tau. \qquad \text{(D.13)}
\end{aligned}$$

We next show that for every $|w_{01}| \le \alpha$, where recall that α depends on δ (see section 8.2.3), we can determine $\phi(t)$ satisfying the above integral equations, under appropriate restrictions on ϵ and δ. Hence we can construct a piece of $\mathcal{W}_\epsilon$ as

$$\mathcal{W}_\epsilon^\alpha = \{(w_{01}, w_{02}) : w_{02} = \int_{-\infty}^0 e^{\mu\tau}G(\phi(\tau; w_{01}, w_{02}))d\tau, |w_{01}| \le \alpha\}. \qquad \text{(D.14)}$$

D.2.3 Contraction Mapping

We show next that for appropriate choice of α, ϵ, K and δ then the *Lyapunov-Perron Operator* $\mathcal{F}$ defined by

$$\mathcal{F}(\phi)(t) = \begin{pmatrix} w_{01}e^{-\lambda t} + \int_0^t e^{\lambda(\tau-t)}F(\phi(\tau))d\tau, \\ \int_{-\infty}^t e^{\mu(\tau-t)}G(\phi(\tau))d\tau \end{pmatrix},$$

is a contraction mapping on the complete metric space $\mathcal{B}_{\epsilon,K}((-\infty, 0], \mathbf{R}^2)$ for any $|w_{01}| \le \alpha$.

We first prove that the range of $\mathcal{F}$ is $\mathcal{B}_{\epsilon,K}((-\infty, 0], \mathbf{R}^2)$. Let $\psi(t) = (\psi_1(t), \psi_2(t)) = \mathcal{F}(\phi(t))$, then

$$\begin{aligned}
||\psi(t)|| &\le |w_{01}|e^{-\lambda t} + \int_0^t e^{\lambda(\tau-t)}||F(\phi(\tau))||d\tau + \int_{-\infty}^t e^{\mu(\tau-t)}||G(\phi(\tau))||d\tau \\
&\le \alpha e^{-\lambda t} + \delta\left[\int_0^t e^{\lambda(\tau-t)}||\phi(\tau)||d\tau + \int_{-\infty}^t e^{\mu(\tau-t)}||\phi(\tau)||d\tau\right].
\end{aligned}$$

and for $t \le 0$

$$\begin{aligned}
|\psi(t)|e^{\epsilon\mu t} &\le \alpha e^{(\epsilon\mu-\lambda)t} + \delta\left[e^{-(\lambda-\epsilon\mu)t}\int_0^t e^{\lambda\tau}e^{-\epsilon\mu\tau}||\phi||_\epsilon d\tau + e^{-\mu(1-\epsilon)t}\int_{-\infty}^t e^{\mu\tau}e^{-\epsilon\mu\tau}||\phi||_\epsilon d\tau\right] \\
&\le \alpha e^{(\epsilon\mu-\lambda)t} + \delta\left[e^{-(\lambda-\epsilon\mu)t}\int_0^t e^{(\lambda-\epsilon\mu)\tau}K d\tau + e^{-\mu(1-\epsilon)t}\int_{-\infty}^t e^{\mu(1-\epsilon)\tau}K d\tau\right] \\
&\le \alpha e^{(\epsilon\mu-\lambda)t} + \delta K\left[e^{-(\lambda-\epsilon\mu)t}\frac{e^{(\lambda-\epsilon\mu)t}-1}{(\lambda-\epsilon\mu)} + e^{-\mu(1-\epsilon)t}\frac{e^{\mu(1-\epsilon)t}}{(1-\epsilon)\mu}\right] \\
&\le \alpha e^{(\epsilon\mu-\lambda)t} + \delta K\left[\frac{1-e^{(\epsilon\mu-\lambda)t}}{(\lambda-\epsilon\mu)} + \frac{1}{(1-\epsilon)\mu}\right].
\end{aligned}$$

For $\epsilon > \frac{\lambda}{\mu}$, we get the estimate

$$\sup_{t\leq 0}\left[\alpha e^{(\epsilon\mu-\lambda)t} + \delta K\left[\frac{e^{(\epsilon\mu-\lambda)t}-1}{(\epsilon\mu-\lambda)} + \frac{1}{(1-\epsilon)\mu}\right]\right] = \alpha + \frac{\delta K}{\mu(1-\epsilon)}. \tag{D.15}$$

If we can satisfy

$$\alpha + \frac{\delta K}{\mu(1-\epsilon)} \leq K, \tag{D.16}$$

then

$$\sup_{t\leq 0}||\psi(t)||e^{\epsilon\mu t} \leq K,$$

which implies that $\psi(t) \in \mathcal{B}_{\epsilon,K}((-\infty,0],\mathbf{R}^2)$.

Next consider $\phi(t), \psi(t) \in \mathcal{B}_{\epsilon,K}((-\infty,0],\mathbf{R}^2)$, then following similar steps as above

$$\begin{aligned}||\mathcal{F}(\phi)(t) - \mathcal{F}(\psi)(t)|| &\leq \int_0^t e^{\lambda(\tau-t)}||F(\phi(\tau)) - F(\psi)(\tau)||d\tau \\ &+ \int_{-\infty}^t e^{\mu(\tau-t)}||G(\phi(\tau)) - G(\psi)(\tau)||d\tau \\ &\leq \delta\left[\int_0^t e^{\lambda(\tau-t)}||\phi(\tau)-\psi(\tau)||d\tau + \int_{-\infty}^t e^{\mu(\tau-t)}||\phi(\tau)-\psi(\tau)||d\tau\right],\end{aligned}$$

and for $t \leq 0$

$$\begin{aligned}||\mathcal{F}(\phi)(t) - \mathcal{F}(\psi)(t)||e^{\epsilon\mu t} &\leq \delta\left[e^{-(\lambda-\epsilon\mu)t}\int_0^t e^{\lambda\tau}e^{-\epsilon\mu\tau}||\phi-\psi||_\epsilon d\tau\right] \\ &+ \delta e^{-\mu(1-\epsilon)t}\int_{-\infty}^t e^{\mu\tau}e^{-\epsilon\mu\tau}||\phi-\psi||_\epsilon d\tau \\ &\leq \delta\left[\frac{e^{(\epsilon\mu-\lambda)t}-1}{(\epsilon\mu-\lambda)} + \frac{1}{(1-\epsilon)\mu}\right]||\phi-\psi||_\epsilon,\end{aligned}$$

and thus

$$||\mathcal{F}(\phi) - \mathcal{F}(\psi)||_\epsilon = \sup_{t\leq 0}||\mathcal{F}(\phi)(t) - \mathcal{F}(\psi)(t)||e^{\epsilon\mu t} \leq C||\phi-\psi||_\epsilon.$$

If

$$C = \delta\sup_{t\leq 0}\left[\frac{e^{(\epsilon\mu-\lambda)t}-1}{(\epsilon\mu-\lambda)} + \frac{1}{(1-\epsilon)\mu}\right] = \frac{\delta}{\mu(1-\epsilon)} < 1, \tag{D.17}$$

then $\mathcal{F}$ is a contraction mapping on $\mathcal{B}_{\epsilon,K}((-\infty,0],\mathbf{R}^2)$.

Hence, by *fixed point theorem* we conclude the existence of an unique $\phi(t) \in \mathcal{B}_{\epsilon,K}((-\infty,0],\mathbf{R}^2)$ satisfying the integral equations (D.13), provided the inequalities

$$\alpha + \frac{\delta K}{\mu(1-\epsilon)} \leq K, \quad \frac{\delta}{\mu(1-\epsilon)} < 1, \tag{D.18}$$

are satisfied for a particular choice of $\delta, K, \alpha(\delta)$ and $\frac{\lambda}{\mu} < \epsilon < 1$. The second inequality gives

$$\frac{\lambda}{\mu} < \epsilon < 1 - \frac{\delta}{\mu}, \tag{D.19}$$

or

$$\delta < \mu - \lambda, \tag{D.20}$$

which can be satisfied for the choice of $\alpha = \alpha(\delta)$ as defined in section 8.2.3. The first inequality hold true provided we choose K such that

$$K > \frac{\alpha(\delta)}{(1 - \frac{\delta}{\mu(1-\epsilon)})}. \tag{D.21}$$

Then the contraction mapping argument given in previous section works and we infer the existence of $\mathcal{W}_\epsilon^\alpha$.

Remarks

1. ϵ can be chosen arbitrary close to $\frac{\lambda}{\mu}$ so that $\epsilon\mu \sim \lambda$ and the solutions initiating in $\mathcal{W}_\epsilon^\alpha$, grow in backward time at slowest possible rate λ.

2. The bound δ is directly proportional to the difference $\mu - \lambda$, hence if $\mu \gg \lambda$ then the region in which the $\mathcal{W}_\epsilon^\alpha$ can be constructed can be made large.

D.2.4 Ridge for modified system

In the previous section, we have showed the existence of an invariant set $\mathcal{W}_\epsilon^\alpha$ for the modified wall-shear field, such that solutions starting in it grows in backward time, at the least exponential rate compared to any other solution starting in the neighborhood. We next show that this property of $\mathcal{W}_\epsilon^\alpha$ renders it to be a ridge of the scalar field . Moreover it shows that the ridge of that scalar field is in fact a wall-shear trajectory.

The divergence of the vector field $\tau_m(\mathbf{x})$ associated with the modified system (D.3), is given by

$$\nabla_{\mathbf{x}} \cdot \tau_m(\mathbf{x}) = -(\lambda + \mu) + \partial_x F(x, y) + \partial_y G(x, y). \tag{D.22}$$

Note that for $\mathbf{x} \in \mathbf{R}^2 \setminus \mathcal{B}_\alpha$, $\nabla_{\mathbf{x}} \cdot \tau_m(\mathbf{x}) = -(\lambda + \mu)$ and thus is uniform in this region.

Using the expression for $\nabla_{\mathbf{x}} \cdot \tau_m$ (D.22), we can express the scalar field (8.12)

$$\mathcal{C}_m(\mathbf{x}_0) = -\int_0^{T_h(\mathbf{x}_0)} \nabla_{\mathbf{x}} \cdot \tau_m(\mathbf{x}(\tau; \mathbf{x}_0)) d\tau = (\lambda + \mu) T_h(\mathbf{x}_0) - \int_0^{T_h(\mathbf{x}_0)} [\partial_x F(\mathbf{x}(\tau; \mathbf{x}_0)) + \partial_y G(\mathbf{x}(\tau; \mathbf{x}_0))] d\tau \tag{D.23}$$

Since $||DF||_0 < \delta < \mu - \lambda$ and $||DG||_0 < \delta < \mu - \lambda$, we can estimate the above integral as

$$\mathcal{C}_m(\mathbf{x}_0) = T_h(\mathbf{x}_0)(\lambda + \mu) + \mathcal{O}([\mu - \lambda]). \tag{D.24}$$

Hence, the value of scalar field $\mathcal{C}_m(\mathbf{x}_0)$ at $\mathbf{x}_0$ is proportional to the time $T_h(\mathbf{x}_0)$.

We want to show that the *ridge* of $\mathcal{C}_m$ coincides with $\mathcal{W}_\epsilon^\alpha$. For this first consider the linear part of the system (D.3)

$$\begin{aligned} \dot{x} &= -\lambda x \\ \dot{y} &= -\mu y, \end{aligned} \tag{D.25}$$

It can be easily verified that for the above system $\mathcal{W}_\epsilon^\alpha = \mathcal{W}^L$ where

$$\mathcal{W}^L = \{(x,0) | x \in \mathbf{R}\}, \tag{D.26}$$

and can be thought of as an image of the curve $\mathbf{c}(x) = (x, 0)$ defined over $\mathbf{R}$. We show that $\mathbf{c}(x) = (x, 0)$ is a second-derivative ridge of the scalar field $\mathcal{C}_L$

$$\mathcal{C}_L(\mathbf{x}_0) = T_L(\mathbf{x}_0)(\lambda + \mu), \tag{D.27}$$

where, $T_L(\mathbf{x}_0)$ is the time it takes for the solution starting at $\mathbf{x}_0$ to intersect a circle of radius r encircling origin. Here r is chosen so that $\mathcal{B}_r \supset \mathcal{B}_\alpha$ and $T_L(\mathbf{x}_0)$ satisfies

$$x_0^2 e^{2\lambda T_L(\mathbf{x}_0)} + y_0^2 e^{2\mu T_L(\mathbf{x}_0)} = r^2, \tag{D.28}$$

By implicit differentiation we see that $\forall x \neq 0$

$$\nabla_{\mathbf{x}} \mathcal{C}_L(\mathbf{c}(x)) = \begin{pmatrix} -\frac{(\lambda+\mu)}{\lambda x} \\ 0 \end{pmatrix}, \qquad H(x) = \nabla_{\mathbf{x}}^2 \mathcal{C}_L(\mathbf{c}(x)) = (\lambda+\mu) \begin{pmatrix} \frac{1}{\lambda x^2} & 0 \\ 0 & -\frac{e^{2T_L(\mathbf{c}(x))(\mu-\lambda)}}{\lambda x^2} \end{pmatrix}. \tag{D.29}$$

and for $\mathbf{n} = (0, 1)^T$

$$\Sigma(\mathbf{n}, \mathbf{n}) = \min_{||\mathbf{u}||=1} \mathbf{u}^T H(x) \mathbf{u} - -\frac{(\lambda + \mu) e^{2T_L(\mathbf{c}(x))(\mu-\lambda)}}{\lambda x^2} < 0. \tag{D.30}$$

Since $\nabla_{\mathbf{x}} \mathcal{C}_L(\mathbf{c}(x))$ is parallel to $\frac{d\mathbf{c}(x)}{dx}$ and $\mathbf{n}$ is the normal to $\mathbf{c}(x)$ for all $x \in \mathbf{R}$, $\mathbf{c}(x)$ is a second derivative ridge of $\mathcal{C}_L$.

In order to show that $\mathcal{W}_\epsilon^\alpha$ is a second-derivative ridge of $\mathcal{C}_m$, note that $\mathcal{C}_m$ can be viewed as a perturbation to the scalar field $\mathcal{C}_L$, so that

$$\mathcal{C}_m = \mathcal{C}_L + \mathcal{O}([\mu - \lambda]). \tag{D.31}$$

By uniqueness of $\mathcal{W}_\epsilon^\alpha$, $\mathcal{W}^L$ perturbs to $\mathcal{W}_\epsilon^\alpha$. So far we have argued that the ridge of $\mathcal{C}_m$ computed for the modified system (D.3) coincides with $\mathcal{W}_\epsilon^\alpha$. Since the scalar field $\mathcal{C}_m$ coincides with $\mathcal{C}$ computed for the original system (8.17) in the region $\mathcal{B}_\alpha$, this portion of ridge coincides with that of the ridge of $\mathcal{C}$.

D.3 Other Crossflow separation criteria

Prolate spheroid is a body of revolution, obtained by rotating the ellipse

$$\frac{x^2}{a^2} + \frac{z^2}{b^2} = 1, \tag{D.32}$$

about the x-axis, with $a > b$. In the arc length parametrization, ellipse can be represented as

$$x(s) = a\cos(l(s)), \qquad r(s) = b\sin(l(s)), \tag{D.33}$$

where, s is arc length

$$s(t) = \int_0^t \sqrt{a^2 \sin^2 q + b^2 \cos^2 q}\,dq, \tag{D.34}$$

and $t = l(s)$ is the inverse of above function. By introducing η which measures the distance from the wall, along the wall normal, we obtain a curvilinear coordinate system (s, ϕ, η) with the transformation

$$\begin{pmatrix} x(s,\phi,\eta) \\ y(s,\phi,\eta) \\ z(s,\phi,\eta) \end{pmatrix} = \begin{pmatrix} F(s,\phi,\eta) \\ G(s,\phi,\eta) \\ H(s,\phi,\eta) \end{pmatrix} = \begin{pmatrix} x(s) \\ r(s)\sin(\phi) \\ r(s)\cos(\phi) \end{pmatrix} + \mathbf{n}\eta, \tag{D.35}$$

where, $\mathbf{n}$ is the outer unit wall normal

$$\mathbf{n} = \begin{pmatrix} -r'(s) \\ x'(s)\sin(\phi) \\ x'(s)\cos(\phi) \end{pmatrix}. \tag{D.36}$$

The unit coordinate vectors are

$$\mathbf{e}_1 = \frac{1}{h_1}\begin{pmatrix} x'(s) - r''(s)\eta \\ (r'(s) + x''(s)\eta)\sin(\phi) \\ (r'(s) + x''(s)\eta)\cos(\phi) \end{pmatrix}, \qquad \mathbf{e}_2 = \frac{1}{h_2}\begin{pmatrix} 0 \\ (r(s) + x'(s)\eta)\cos(\phi) \\ -(r(s) + x'(s)\eta)\sin(\phi) \end{pmatrix}, \qquad \mathbf{e}_3 = \mathbf{n}, \tag{D.37}$$

with the scale factors

$$h_1(s,\phi,\eta) = 1 - \kappa(s)\eta, \qquad h_2(s,\phi,\eta) = r(s) + x'(s)\eta, \qquad h_3(s,\phi,\eta) = 1 \tag{D.38}$$

where, $\kappa(s) = x'(s)r''(s) - r'(s)x''(s)$ is the curvature of the curve of revolution (ellipse in this case). The coordinate system is orthogonal since $\mathbf{e}_i \cdot \mathbf{e}_j = 0$ for $i \neq j$, $i, j = 1, 2, 3$.

The velocity field $\mathbf{v}$ in these coordinates can be expressed as

$$\mathbf{v} = u_1\mathbf{e}_1 + u_2\mathbf{e}_2 + u_3\mathbf{e}_3. \tag{D.39}$$

As the spheroid surface is given by $\eta = 0$, the wall-shear field becomes

$$\tau(s,\phi) = \partial_\eta u_1(s,\phi,0)\mathbf{e}_1 + \partial_\eta u_2(s,\phi,0)\mathbf{e}_2. \tag{D.40}$$

The wall shear trajectories $\xi(\tau; s_0, \phi_0) = (s(\tau; s_0, \phi_0), \phi(\tau; s_0, \phi_0))$ satisfy the ODE

$$s' = \partial_\eta u_1(s,\phi,0), \qquad \phi' = \frac{1}{r(s)}\partial_\eta u_2(s,\phi,0), \tag{D.41}$$

and $S_\perp$ computed along $\xi(\tau; s_0, \phi_0)$ takes the form

$$S_\perp(\tau) = \left.\frac{(\tilde{\omega}, J\tilde{\omega})}{|\tilde{\omega}|^2}\right|_{\xi=\xi(\tau,\xi_0)}, \tag{D.42}$$

where

$$J(s,\phi) = \begin{pmatrix} \partial^2_{s\eta}u_1(s,\phi,0) & \partial^2_{\phi\eta}u_1(s,\phi,0) \\ \frac{\partial^2_{s\eta}u_2(s,\phi,0)}{r(s)} - \frac{\partial_\eta u_2(s,\phi,0)r'(s)}{r^2(s)} & \frac{\partial^2_{\phi\eta}u_2(s,\phi,0)}{r(s)}. \end{pmatrix}, \tag{D.43}$$

and $\tilde{\omega}(s,\phi)$ is a vector

$$\tilde{\omega}(s,\phi) = -\frac{1}{r(s)}\partial_\eta u_2(s,\phi,0)\mathbf{e}_1 + \partial_\eta u_1(s,\phi,0)\mathbf{e}_2, \tag{D.44}$$

whose components are the contravaraint components of the wall vortcity field

$$\omega(s,\phi) = -\partial_\eta u_2(s,\phi,0)\mathbf{e}_1 + \partial_\eta u_1(s,\phi,0)\mathbf{e}_2. \tag{D.45}$$

Using incompressibility, the scalar field $\mathcal{C}(s,\phi)$ can be expressed as

$$\mathcal{C}(s,\phi) = \frac{1}{2}\partial^2_\eta u_3(s,\phi,0,t) = -\frac{1}{2}\left[\partial^2_{s\eta}u_1(s,\phi,0,t) + \frac{\partial^2_{\phi\eta}u_2(s,\phi,0,t)}{r(s)} + \frac{r'(s)}{r(s)}\partial_s u_1(s,\phi,0,t)\right].$$

D.3.1 Wall-shear based criteria

According to Simpson et. al. [101], the crossflow separation line is the curve formed by circumferential minima of the wall-shear magnitude. For fixed s, let $p(s)$ be a point which locally minimizes the scalar field $\mathcal{S}(s,\phi)$

$$\mathcal{S}(s,\phi) = |\tau(s,\phi)|. \tag{D.46}$$

Note that for fixed s, $\mathcal{S}(s,\phi)$ is a continuous function over a compact set $[0, 2\pi]$ and therefore attains an absolute minima and a maxima. As a result, $p(s)$ is defined for every $s \in [0, s_m]$. Then according to Simpson et. al., the crossflow separation line is the curve $\xi(s) = \{(s, p(s)) | s \in [0, s_m]\}$.

D.3.2 Wall vorticity based criteria

Recall from section A.6, Wu et al. [108] proposed that the separation line must be a local maximizing curve (*ridge*) for the scalar field

$$\mathcal{W} = \kappa_2 \left(\kappa_2 - \eta_1\right), \tag{D.47}$$

where, in (s, ϕ) coordinates κ_2 and η_1 are given by

$$\kappa_2 = -S_\perp / \left|\tilde{\omega}\right|, \qquad \eta_1 = \log\left|\omega\right|. \tag{D.48}$$

More precisely open separation line is obtained as a curve satisfying

$$\nabla_{\mathbf{x}}\mathcal{W} \cdot \omega = 0, \qquad \omega^T \left[\nabla^2_{\mathbf{x}}\mathcal{W}\right] \omega < 0. \tag{D.49}$$

with

$$\nabla_{\mathbf{x}} = \mathbf{e}_1 \frac{\partial}{\partial s} + \mathbf{e}_2 \frac{1}{r(s)} \frac{\partial}{\partial \phi}, \tag{D.50}$$

being the gradient and $\nabla^2_{\mathbf{x}}$ the corresponding Hessian.

Appendix E

Appendix: Separation Theory in Curvilinear Coordinates

In this Appendix we formulate separation theory in general curvilinear coordinate system.

E.1 Curvilinear coordinate system

In a steady inertial frame (x, y, z) introduce a time-dependent change of coordinates

$$x^i = x^i(x, y, z, t), \qquad i = 1, 2, 3 \tag{E.1}$$

$$\tau = t. \tag{E.2}$$

We shall assume the transformation to be invertible so that

$$x = F(x^1, x^2, x^3, \tau), \quad y = G(x^1, x^2, x^3, \tau), \quad z = H(x^1, x^2, x^3, \tau), \quad t = \tau \tag{E.3}$$

In an curvilinear coordinate system (x^1, x^2, x^3), one can introduce, two sets of base vectors: *covariant base vectors* $\mathbf{a}_i$

$$\mathbf{a}_i = \partial_{x^i}\mathbf{r}, \tag{E.4}$$

and *contravariant base vectors*

$$\mathbf{a}^j = \nabla x^i \tag{E.5}$$

so that

$$\mathbf{a}_i \cdot \mathbf{a}^j = 0. \tag{E.6}$$

Note that for a concise representation of the formulae, we have used the tensor index notation, with the summation convention in effect when one upper and one lower index in a term or in a product are same, e.g. $\mathbf{u} = u^i\mathbf{a}_i$.

Thus, any vector $\mathbf{v}$ can be expressed as

$$\mathbf{v} = v^i\mathbf{a}_i = v_i\mathbf{a}^i, \tag{E.7}$$

where, v^i and v_i are called *contravariant components* and *covariant components* of $\mathbf{v}$, respectively. The physical components V_i are defined by

$$V_i = v^i \sqrt{g_{ii}} = \sqrt{g_{ii}} g^{ij} v_j, \tag{E.8}$$

where no sum is implied on the index i.

Using the two types of base vectors we can form the scalars

$$g_{ij} = \mathbf{a}_i \cdot \mathbf{a}_j, \tag{E.9}$$

$$g^{ij} = \mathbf{a}^i \cdot \mathbf{a}^j. \tag{E.10}$$

which are the *fundamental metric* components of the space in which the curvilinear coordinates have been introduced. These scalars are related by

$$g_{ij} g^{jk} = \delta_i^k, \tag{E.11}$$

leading to

$$g^{ij} = (g_{rs} g_{mn} - g_{rn} g_{ms})/g, \qquad g_{ij} = g(g^{rs} g^{mn} - g^{rn} g^{ms}), \tag{E.12}$$

where

$$g = \det g_{ij}. \tag{E.13}$$

The covariant components of the differentiation of the base vectors $\mathbf{a}_i$ is given by

$$\partial_{x^j} \mathbf{a}_i = [ij, k] \mathbf{a}^k, \tag{E.14}$$

where, $[ij, k]$ are *Christoffel* symbols of *first-kind*

$$[ij, k] = \frac{1}{2} \left[\partial_{x^j} g_{ik} + \partial_{x^i} g_{jk} - \partial_{x^k} g_{ij} \right]. \tag{E.15}$$

The contravariant components of the differentiation of the base vectors $\mathbf{a}_i$ are known as *Christoffel* symbols of *second-kind* and denoted by Γ_{ij}^m, so that

$$\partial_{x^j} \mathbf{a}_i = \Gamma_{ij}^m \mathbf{a}_m. \tag{E.16}$$

Γ_{ij}^m is related to $[ij, k]$ by

$$\Gamma_{ij}^m = g^{mk} [ij, k]. \tag{E.17}$$

In terms of Γ_{ij}^m, for any vector $\mathbf{v} = v^i \mathbf{a}_i$, we get

$$\partial_{x^i} \mathbf{v} = v_{,i}^k \mathbf{a}_k, \tag{E.18}$$

where, the components

$$v_{,i}^k = \partial_{x^i} v^k + v^r \Gamma_{ir}^k, \tag{E.19}$$

are known as *covariant derivatives* of the contravariant components.

E.1.1 Particle equations of motion

Consider a coordinate system

$$\mathbf{r} = \mathbf{\Phi}(x^1, x^2, t) + \mathbf{n}(x^1, x^2, t)x^3, \tag{E.20}$$

where, x^3 is the distance measured normal to the boundary. In such a system, body surface is simply given by

$$x^3 = 0, \tag{E.21}$$

for all times t. We shall distinguish the coordinates parallel to the boundary by denoting them as $\xi = (x^1, x^2)$, while $\eta = x^3$ would refer to component normal to the boundary.

In the coordinates (E.20) the velocity vector $\mathbf{u}$ can be expressed as

$$\mathbf{u} = u^1\mathbf{a}_1 + u^2\mathbf{a}_2 + u^3\mathbf{a}_3, \tag{E.22}$$

where $\mathbf{a}_i$ are the *covariant* base vectors associated with the system (ξ, η) and u^i are the *contravariant* components.

The fluid velocity $\mathbf{v} = v^i\mathbf{a}_i$ relative to the moving frame is

$$\mathbf{v} = \mathbf{u} + \mathbf{w}, \tag{E.23}$$

where

$$\mathbf{w} = \mathbf{a}_i\partial_t x^i, \tag{E.24}$$

is the absolute velocity of the moving frame. Assume the following

1. On the boundary, the velocity field $\mathbf{u}$ satisfies no-slip condition

   $$\mathbf{u}(\mathbf{r}_{\mathcal{B}}, t) = -\mathbf{w}(\mathbf{r}_{\mathcal{B}}, t), \qquad \forall \mathbf{r}_{\mathcal{B}} \in \mathcal{B}(t). \tag{E.25}$$

   In the moving frame, above condition can be expressed as

   $$\mathbf{v}(\xi, 0, t) = 0. \tag{E.26}$$

2. The velocity field $\mathbf{u}$ is mass conserving. As a result with no sinks or sources present on the boundary, $\mathbf{v}$ satisfies the continuity equation

   $$\partial_t[\rho\sqrt{g}] + \partial_{x^i}[\rho\sqrt{g}v^i] = 0, \tag{E.27}$$

   where, g is the determinant of the *metric tensor*.

3. The density ρ and it's on-wall gradient on the boundary remains bounded from below and from above for all times. By virtue of (E.26), the continuity equation (E.27) on the $\eta = 0$ boundary simplifies to

   $$\partial_t[\rho(\xi, 0, t)\sqrt{g(\xi, 0, t)}] + \rho(\xi, 0, t)\sqrt{g(\xi, 0, t)}\partial_\eta v^3(\xi, 0, t) = 0. \tag{E.28}$$

Integrating above equation in time, we get

$$\rho(\xi,0,t)\sqrt{g(\xi,0,t)} = \rho(\xi,0,t_0)\sqrt{g(\xi,0,t_0)}e^{\int_{t_0}^{t}\partial_\eta v^3(\xi,0,s)ds}. \tag{E.29}$$

Hence the requirement of bounded density and bounded density gradients on the boundary is kinematically equivalent to

$$|\int_{t_0}^{t}\partial_\eta v^3(\xi,0,s)ds| < K, \quad |\int_{t_0}^{t}\partial^2_{x^1\eta}v^3(\xi,0,s)ds| < K, \quad ,|\int_{t_0}^{t}\partial^2_{x^2\eta}v^3(\xi,0,s)ds| < K, \quad \forall t \tag{E.30}$$

where, K is a positive constant. For incompressible flows since $\partial_\eta v^3(\xi,0,t)\equiv 0$ (see section E.1.2), the condition (2.6) is automatically satisfied.

In the (ξ,η) coordinates the particle equations of motion satisfy

$$\frac{dx^i}{dt} = v^i(x^1,x^2,x^3,t), \qquad i=1,2,3. \tag{E.31}$$

As for the flat boundaries (see chapter 2), by introducing the transformation (which is well behaved under the conditions (2.6))

$$\eta \longrightarrow \eta e^{\int_{t_0}^{t}\partial_\eta v^3(\xi,0,s)ds}, \tag{E.32}$$

the particle motion (E.31) can be expressed as

$$\begin{aligned} \dot{\xi} &= \eta\tilde{\mathbf{A}}(\xi,\eta,t), \\ \dot{\eta} &= \eta^2\tilde{C}(\xi,\eta,t), \end{aligned} \tag{E.33}$$

where

$$\begin{aligned} \tilde{\mathbf{A}}(\xi,\eta,t) &= e^{\int_{t_0}^{t}\partial_\eta v^3(\xi,0,\tau)d\tau}\mathbf{A}(\xi,\eta e^{\int_{t_0}^{t}\partial_\eta v^3(\xi,0,\tau)d\tau},t), \\ \tilde{C}(\xi,\eta,t) &= \frac{1}{2}e^{\int_{t_0}^{t}\partial_\eta v^3(\xi,0,\tau)d\tau}\partial^2_\eta v^3(\xi,0,t) + \mathcal{O}(\eta), \end{aligned}$$

with $\mathbf{A} = (A_1, A_2)$ and

$$A_1(\xi,\eta,t) = \int_0^1 \partial_\eta v^1(\xi,s\eta,t)ds, \quad A_2(\xi,\eta,t) = \int_0^1 \partial_\eta v^2(\xi,s\eta,t)ds. \tag{E.34}$$

With the particle equations of motion in canonical form (E.33) the separation theory developed in chapters 3, 4, 7 and 8 extend to curved moving boundaries.

E.1.2 Normal derivatives in terms of pressure and wall shear gradients

Examination of slope formulae reveals that their computation requires the knowledge of on wall second order normal derivatives, namely: $\partial^2_\eta v^1(\xi,0,t)$, $\partial^2_\eta v^2(\xi,0,t)$ and

$\partial_\eta^2 v^3(\xi, 0, t)$. It is often difficult to obtain these derivatives directly experimentally or even numerically. For incompressible flows, using restrictions of the continuity and the Navier Stokes equations on the boundary, these derivatives can be expressed in terms of on wall derivatives of the wall shear field $\tau(\xi, 0, t)$ and the pressure field $p(\xi, 0, t)$. We would restrict our discussion to incompressible flows.

Evaluating the incompressible continuity equation

$$\partial_{x^i}[\rho\sqrt{g}v^i] = 0, \tag{E.35}$$

on the $\eta = 0$ boundary shows that

$$\partial_\eta v^3(\xi, 0, t) \equiv 0. \tag{E.36}$$

As a result, the velocity field $\mathbf{v}$ can be expressed in the form

$$\mathbf{v} = \eta A_1 \mathbf{a}_1 + \eta A_2 \mathbf{a}_2 + \eta^2 C \mathbf{n}, \tag{E.37}$$

where, A_1, A_2 are given by (E.34) and

$$C(\xi, \eta, t) \quad = \quad \int_0^1 \int_0^1 \partial_\eta^2 v^3(\xi, sp\eta, t) s ds dp. \tag{E.38}$$

Substituting the above form of $\mathbf{v}$ in the equation (E.35), we get

$$\eta\partial_{x^1}[\sqrt{g}A_1] + \eta\partial_{x^2}[\sqrt{g}A_2] + 2\eta\sqrt{g}C + \eta^2\partial_\eta[\sqrt{g}C] = 0, \tag{E.39}$$

which by continuity of the velocity field yields at $\eta = 0$

$$C(\xi, 0, t) = -\frac{1}{2\sqrt{g}}(\partial_{x^1}[\sqrt{g}A_1] + \partial_{x^2}[\sqrt{g}A_2]) \,|_{(\xi,0,t)}, \tag{E.40}$$

or

$$\partial_\eta^2 v^3(\xi, 0, t) = -\frac{1}{\sqrt{g}}(\partial_{x^1}[\sqrt{g}\partial_\eta v^1] + \partial_{x^2}[\sqrt{g}\partial_\eta v^2]) \,|_{(\xi,0,t)} \,. \tag{E.41}$$

The normal derivatives $\partial_\eta^2 v^1(\xi, 0, t)$ and $\partial_\eta^2 v^2(\xi, 0, t)$ can be obtained by restricting the NS equations on the boundary. The Navier Stokes equation in the contravariant components takes the form

$$\rho\frac{\hat{D}v^i}{D\tau} = -g^{ik}\partial_{x^k}p + \frac{1}{\sqrt{g}}\partial_{x_k}(\sqrt{g}\sigma^{ik}) + \Gamma^i_{lk}\sigma^{lk} + \rho f^i + \rho\left[\partial_\tau w^i + 2v^j w^i_{,j} - w^j w^i_{,j}\right], \tag{E.42}$$

where

$$\frac{\hat{D}}{D\tau} = \partial_\tau()^i + v^j()^i_{,j}, \tag{E.43}$$

is the time derivative as seen by an observer in the moving frame, σ is the *deviotoric* part of stress tensor, p is the thermodynamic pressure and $\mathbf{f} = f^i\mathbf{a}_i$ is the resultant body force. Note that due to non-inertial nature of coordinate frame (ξ, η) there is a additional body force term on the R.H.S of equation (E.42), which can be expressed in vector notation as

$$\mathbf{F}_b = \rho\left[\partial_\tau w^i + 2v^j w^i_{,j} - w^j w^i_{,j}\right]\mathbf{a}_i = \rho\left[\partial_\tau \mathbf{w} + 2(\nabla\mathbf{w})\cdot\mathbf{v} - (\nabla\mathbf{w})\cdot\mathbf{w}\right]. \tag{E.44}$$

For Newtonian flow, σ is given by

$$\sigma = (\lambda\nabla\cdot\mathbf{u})\mathbf{I} + 2\mu\mathbf{D}, \tag{E.45}$$

where, μ and λ are the first and the second coefficients of viscosity and $\mathbf{D}$ is the *rate-of-strain* tensor

$$\mathbf{D} = \frac{1}{2}[\nabla\mathbf{u} + (\nabla\mathbf{u})^T] = D^{kn}\mathbf{a}_k\mathbf{a}_n, \qquad D^{kn} = \frac{1}{2}[u^k_{,i}g^{in} + u^n_{,m}g^{mk}]. \tag{E.46}$$

Assuming the flow to be incompressible, we see that

$$\sigma^{kn} = \mu\mathbf{D}^{kn} = \mu[v^k_{,i}g^{in} + v^n_{,m}g^{mk}] - \mu[w^k_{,i}g^{in} + w^n_{,m}g^{mk}]. \tag{E.47}$$

Due to no-slip condition and continuity, on the $\eta = 0$ boundary

$$v^k_{,1} = 0, \quad v^k_{,2} = 0 \quad v^3_{,k} = 0, \quad k = 1,2,3 \tag{E.48}$$

and so

$$\sigma^{kn} = \mu[\partial_\eta v^k g^{3n} + \partial_\eta v^n g^{3k}] - \mu[w^k_{,i}g^{in} + w^n_{,m}g^{mk}], \tag{E.49}$$

from which we get for $k, n = 1, 2$

$$\sigma^{kn} = -\mu[w^k_{,i}g^{in} + w^n_{,m}g^{mk}], \tag{E.50}$$

and for $k = 1, 2, 3$

$$\sigma^{k3} = \mu\partial_\eta v^k - \mu[w^k_{,i}g^{in} + w^n_{,m}g^{mk}]. \tag{E.51}$$

Assuming μ to be constant, for $k, m = 1, 2$, at $\eta = 0$

$$\partial_{x^m}\sigma^{km} = -\mu\partial_{x^m}[w^k_{,i}g^{im} + w^m_{,l}g^{lk}], \tag{E.52}$$

and for $k = 1, 2$

$$\partial_\eta\sigma^{k3} = \mu\partial^2_\eta v^k + \mu\partial_\eta v^1[\Gamma^k_{31} + g^{km}\Gamma^3_{m1}] + \mu\partial_\eta v^2[\Gamma^k_{32} + g^{km}\Gamma^3_{m2}] - \mu\partial_\eta[w^k_{,m}g^{m3} + w^3_{,l}g^{lk}],$$

Therefore, with no body forces present the first two components (i.e. $i = 1, 2$) of the

NS equations (E.42) on the boundary $\eta = 0$, lead to

$$\begin{aligned}
\mu\partial_\eta^2 v^i(\xi,0,t) &= \left[g^{i1}\partial_{x^1}p + g^{i2}\partial_{x^2}p - \mu\partial_\eta v^1[3\Gamma^i_{13} + g^{ij}\Gamma^i_{j1}] - \mu\partial_\eta v^2[3\Gamma^i_{23} + g^{ij}\Gamma^i_{j2}]\right]_{(\xi,0,t)} \\
&+ \left[\mu\Gamma^i_{kn}[w^k_{,l}g^{ln} + w^n_{,j}g^{jk}] + \frac{\mu}{\sqrt{g}}\partial_{x_m}(\sqrt{g}[w^i_{,l}g^{lm} + w^m_{,j}g^{ji}]) - \rho\left[\partial_\tau w^i - w^j w^i_{,j}\right]\right]_{(\xi,0,t)} \\
&- \left[\mu\partial_\eta v^i\frac{1}{\sqrt{g}}\partial_\eta(\sqrt{g})\right]_{(\xi,0,t)} \qquad \text{(E.53)}
\end{aligned}$$

This shows that $\partial_\eta^2 v^1(\xi,0,t)$ and $\partial_\eta^2 v^2(\xi,0,t)$ can be expressed in terms of wall pressure derivatives $\partial_{x^1}p(\xi,0,t)$, $\partial_{x^2}p(\xi,0,t)$ and the first normal derivatives $\partial_\eta v^1(\xi,0,t), \partial_\eta v^2(\xi,0,t)$ of the wall parallel velocity.

For the coordinate system of the form (E.20), since $\mathbf{a}_3 = \mathbf{n}(x^1,x^2,t)$ is orthogonal to $\mathbf{a}_1$ and $\mathbf{a}_2$, we get

$$g_{i3} = \delta_{i3}, \qquad g^{i3} = \delta^{i3}. \qquad \text{(E.54)}$$

In this case the covariant components $g_{ij}, i,j = 1,2$ are the coefficients of the *first fundamental form* and $g = g_{11}g_{22} - g_{12}^2$. In addition there a *second fundamental form* associated with a surface, whose coefficients $\beta_{ij}, i,j = 1,2$ are such that

$$\partial_{x^i}\mathbf{n} = -\beta_{ij}g^{jk}\mathbf{a}_k. \qquad \text{(E.55)}$$

The principal curvature of the surface κ_I and κ_{II} can be expressed in terms of first and second fundamental form as

$$\kappa_I + \kappa_{II} = \kappa_m = g^{ij}\beta_{ij}, \quad \kappa_I\kappa_{II} = \kappa_g = \frac{\det\beta_{ij}}{\det g_{ij}} = \frac{1}{g}\det\beta_{ij}. \qquad \text{(E.56)}$$

As $\Gamma^3_{31} = \Gamma^3_{31} = 0$ we immediately deduce from (E.16) that

$$\Gamma^k_{3i} = -\beta_{ij}g^{jk}, \qquad \text{(E.57)}$$

where, for $k = 1,2$ and $i = 1,2$

$$\Gamma^1_{31} = \frac{1}{2g}\left[g_{22}\partial_\eta g_{11} - g_{12}\partial_\eta g_{12}\right], \quad \Gamma^2_{31} = \frac{1}{2g}\left[-g_{12}\partial_\eta g_{11} + g_{11}\partial_\eta g_{12}\right], \qquad \text{(E.58)}$$

$$\Gamma^1_{32} = \frac{1}{2g}\left[g_{22}\partial_\eta g_{12} - g_{12}\partial_\eta g_{22}\right], \quad \Gamma^2_{32} = \frac{1}{2g}\left[-g_{12}\partial_\eta g_{12} + g_{11}\partial_\eta g_{22}\right]. \qquad \text{(E.59)}$$

In addition following Christoffel symbols

$$\Gamma^1_{11} = \frac{1}{2g}\left[g_{22}\partial_{x^1}g_{11} + g_{12}(\partial_{x^2}g_{11} - 2\partial_{x^1}g_{12})\right], \quad \Gamma^2_{22} = \frac{1}{2g}\left[g_{11}\partial_{x^2}g_{22} + g_{12}(\partial_{x^1}g_{22} - 2\partial_{x^2}g_{12})\right] \qquad \text{(E.60)}$$

$$\Gamma^1_{22} = \frac{1}{2g}\left[g_{22}(2\partial_{x^2}g_{12} - \partial_{x^1}g_{22}) - g_{12}\partial_{x^2}g_{22}\right], \quad \Gamma^1_{22} = \frac{1}{2g}\left[g_{11}(2\partial_{x^1}g_{12} - \partial_{x^2}g_1) - g_{12}\partial_{x^1}g_{11}\right], \qquad \text{(E.61)}$$

$$\Gamma^1_{12} = \Gamma^1_{21} = \frac{1}{2g}\left[g_{22}\partial_{x^2}g_{11} - g_{12}\partial_{x^1}g_{22}\right], \quad \Gamma^2_{12} = \Gamma^2_{21} = \frac{1}{2g}\left[g_{11}\partial_{x^1}g_{22} - g_{12}\partial_{x^2}g_{11}\right]. \tag{E.62}$$

also arise in the description of the surface geometry. Hence, the separation slope formula can be related to the surface geometry.

E.1.3 Transforming slope formulae

In this section we give transformation laws for slope formulae. It is straightforward to see that, the separation curve at $\mathbf{r}(\overline{\mathbf{p}}) = (F(\tilde{\mathbf{p}}, 0, t_0), G(\overline{\mathbf{p}}, 0, t_0), H(\overline{\mathbf{p}}, 0, t_0))$ can be represented locally in cartesian coordinates as

$$\mathbf{x} = \mathbf{r}(\overline{\mathbf{p}}) + \mathbf{g}_0(\overline{\mathbf{p}}, t_0)z, \tag{E.63}$$

where

$$\mathbf{g}_0(\overline{\mathbf{p}}, t_0) = \mathcal{T}(\overline{\mathbf{p}}, 0, t_0)\begin{pmatrix} \overline{\mathbf{g}}_0(\overline{\mathbf{p}}) \\ 1 \end{pmatrix}, \tag{E.64}$$

where $\mathcal{T}(\xi, \eta, t_0)$ is the Jacobian of the transformation (E.3)

$$\mathcal{T}(\xi, \eta, t_0) = \begin{pmatrix} \partial_{x^1}F & \partial_{x^2}F & \partial_\eta F \\ \partial_{x^1}G & \partial_{x^2}G & \partial_\eta G \\ \partial_{x^1}H & \partial_{x^2}H & \partial_\eta H \end{pmatrix}. \tag{E.65}$$

For the separation surface $\tilde{S}(t_0)$, the vectors

$$\tilde{\eta}_1(\xi_0) = \begin{pmatrix} \overline{\mathbf{A}}(\xi_0) \\ 0 \end{pmatrix}, \qquad \tilde{\eta}_2(\xi_0) = \begin{pmatrix} \overline{\mathbf{A}}^\perp(\xi_0) \\ |\overline{\mathbf{A}}(\xi_0)| \tan\tilde{\theta}(\xi_0, t_0) \end{pmatrix}, \tag{E.66}$$

are contained in tangent space $T_{(\xi_0,0)}\tilde{S}(t_0)$. Under the linearized map (E.65) these vectors are mapped to

$$\eta_1(\xi_0, t_0) = \mathcal{T}(\xi_0, 0, t_0)\tilde{\eta}_1(\xi_0), \qquad \eta_2(\xi_0, t_0) = \mathcal{T}(\xi_0, 0, t_0)\tilde{\eta}_2(\xi_0), \tag{E.67}$$

which lie in the tangent space $T_{\mathbf{r}(\xi_0)}\mathcal{S}(t_0)$, where $\mathbf{r}(\xi_0) = (F(\xi_0, 0, t_0), G(\xi_0, 0, t_0), H(\xi_0, 0, t_0))$ and $\mathcal{S}(t_0)$ is the separation surface in the cartesian coordinates. Then we can obtain a vector $\rho(\xi_0, t_0)$ orthogonal to η_1 and contained in the normal section at ξ_0, as

$$\rho(\xi_0, t_0) = -(\eta_1 \cdot \eta_2)\eta_1 + \eta_2. \tag{E.68}$$

Hence, the tangent of the separation angle $\theta(\mathbf{r}(\xi_0), t_0)$ enclosed by $\rho(\xi_0, t_0)$ and the local normal $\mathbf{n}(\mathbf{x}_0, t_0)$ to the boundary is given by

$$\tan\theta(\mathbf{r}(\xi_0), t_0) = \frac{\sin\theta(\xi_0, t_0)}{\cos\theta(\xi_0, t_0)} = \frac{[\mathbf{n}(\xi_0, t_0) \times \rho(\xi_0, t_0)] \cdot \eta_1(\xi_0, t_0)}{|\eta_1(\mathbf{x}_0, t_0)|[\mathbf{n}(\xi_0, t_0) \cdot \rho(\xi_0, t_0)]}. \tag{E.69}$$

E.2 Orthogonal curvilinear coordinate system

Assume that the coordinate system (E.20) is triply orthogonal so that

$$g_{ij} = h_i h_j \delta_{ij}, \qquad g^{ij} = \frac{1}{h_i h_j}\delta^{ij}, \tag{E.70}$$

where

$$h_1 = |\mathbf{a}_1|, \quad h_2 = |\mathbf{a}_2|, \quad h_3 = |\mathbf{n}| = 1, \tag{E.71}$$

are known as *scale factors.* In order to distinguish an orthogonal system from a general curvilinear system, we would refer to the orthogonal coordinates by (ξ_1, ξ_2, η) with the correspondence $x^1 = \xi_1$, $x^2 = \xi_2$ and $x^3 = \eta$.

For an orthogonal coordinate system, it is customary to work with unit base vectors $\mathbf{e}_i$, which are defined as

$$\mathbf{e}_i = \frac{\mathbf{a}_i}{h_i}. \tag{E.72}$$

The components v_i of a vector $\mathbf{v}$ w.r.t to the basis $\{\mathbf{e}_i\}$ are known as *physical components*, which are related to the contravariant components v^i by

$$v_i = h_i v^i, \tag{E.73}$$

where, no sum is implied. Due to the orthogonality, the determinant of the metric tensor g_{ij} becomes

$$g = h_1^2 h_2^2, \tag{E.74}$$

and the Christoffel symbols of second kind simplify to

$$\Gamma^1_{11} = \frac{1}{h_1}\partial_{\xi_1} h_1, \Gamma^1_{12} = \frac{1}{h_1}\partial_{\xi_2} h_1, \Gamma^1_{13} = \frac{1}{h_1}\partial_{\eta} h_1, \Gamma^1_{22} = -\frac{h_2}{h_1^2}\partial_{\xi_1} h_2, \Gamma^1_{23} = 0, \Gamma^1_{33} = 0, \tag{E.75}$$

$$\Gamma^2_{11} = -\frac{h_1}{h_2^2}\partial_{\xi_2} h_1, \Gamma^2_{12} = \frac{1}{h_2}\partial_{\xi_1} h_2, \Gamma^2_{13} = 0, \Gamma^2_{22} = \frac{1}{h_2}\partial_{\xi_2} h_2, \Gamma^2_{23} = \frac{1}{h_2}\partial_{\xi_3} h_2, \Gamma^2_{33} = 0, \tag{E.76}$$

$$\Gamma^3_{11} = -h_1\partial_\eta h_1, \Gamma^3_{12} = 0, \Gamma^3_{13} = 0, \Gamma^3_{22} = -h_2\partial_\eta h_2, \Gamma^3_{23} = 0, \Gamma^3_{33} = 0. \tag{E.77}$$

E.2.1 Separation criteria in an orthogonal curvilinear coordinate system

For now assume $\mathcal{B}$ to be fixed in $\mathcal{R}$, so that $\mathbf{w} \equiv 0$ (E.24) and $\mathbf{v} = \mathbf{w}$. Also assume that one can introduce an orthogonal curvilinear system $(\xi, \eta) = (\xi_1, \xi_2, \eta)$ (see section E.2.1 for details) of the form (E.20)

$$\mathbf{r} = F(\xi, \eta)\mathbf{i} + G(\xi, \eta)\mathbf{j} + H(\xi, \eta)\mathbf{k}, \tag{E.78}$$

so that the unit coordinate base vectors $\mathbf{e}_i$

$$\mathbf{e}_i = \frac{1}{h_i}\partial_{\xi_i}\mathbf{r}, \tag{E.79}$$

are orthogonal

$$\mathbf{e}_i \cdot \mathbf{e}_j = \delta_{ij}, \tag{E.80}$$

where, h_i are the scale factors

$$h_1 = |\partial_{\xi_1}\mathbf{r}|, \quad h_2 = |\partial_{\xi_2}\mathbf{r}|, \quad h_3 = |\partial_\eta \mathbf{r}| = |\mathbf{n}(\xi)| = 1. \tag{E.81}$$

In terms of *physical components* $u_i = u^i h_i$ (where no sum on i is implied) the velocity field $\mathbf{u}$ can be expressed as

$$\mathbf{u} = u_1\mathbf{e}_1 + u_2\mathbf{e}_2 + u_3\mathbf{e}_3, \tag{E.82}$$

and induces a time-dependent *wall-shear* field

$$\tau(\xi, t) = \partial_\eta u_1(\xi, 0, t)\mathbf{e}_1 + \partial_\eta u_2(\xi, 0, t)\mathbf{e}_2, \tag{E.83}$$

on the boundary. Two key quantities required for separation analysis are

$$\overline{\mathbf{A}}(\xi) = \lim_{T\to\infty}\frac{1}{T}\int_{t_0-T}^{t_0}\tilde{\mathbf{A}}(\xi, 0, t)dt = \lim_{T\to\infty}\frac{1}{T}\int_{t_0-T}^{t_0} e^{\int_{t_0}^{t}\partial_\eta u_3(\xi,0,\tau)d\tau}\mathbf{A}(\xi, 0, t)dt, \tag{E.84}$$

where, $\mathbf{A} = (A_1, A_2)$ is as given by (E.34) with $v^1 = u^1 = \frac{u_1}{h_1}$ and $v^1 = u^2 = \frac{u_2}{h_2}$ and

$$\overline{C}(\xi) = \lim_{T\to\infty}\frac{1}{T}\int_{t_0-T}^{t_0}\tilde{\mathbf{C}}(\xi, 0, t)dt = \frac{1}{2}\lim_{T\to\infty}\frac{1}{T}\int_{t_0-T}^{t_0} e^{\int_{t_0}^{t}\partial_\eta u_3(\xi,0,\tau)d\tau}\partial_\eta^2 u_3(\xi, 0, t)dt. \tag{E.85}$$

Observe that, the components of $\overline{\mathbf{A}}$ are the contravariant components of the time averaged wall-shear field

$$\overline{\tau}(\xi) = \lim_{T\to\infty}\frac{1}{T}\int_{t_0-T}^{t_0} e^{\int_{t_0}^{t}\partial_\eta u_3(\xi,0,\tau)d\tau}\tau(\xi, t)dt, \tag{E.86}$$

and $\overline{C}(\xi)$ measures the time averaged up-welling.

The vector field $\overline{\tau}$ (4.16) induces a steady fictitious flow on the boundary whose trajectories $\xi(s, \xi_0)$ satisfy

$$\xi_1' = \frac{1}{h_1(\xi, 0)}\tau_1(\xi, 0), \qquad \xi_2' = \frac{1}{h_2(\xi, 0)}\tau_2(\xi, 0), \tag{E.87}$$

with $\xi(0, \xi_0) = \xi_0$. The above set of ODE's can be compactly expressed as

$$\xi' = \overline{\mathbf{A}}(\xi). \tag{E.88}$$

A finite connected union of wall-shear trajectories $\xi(s, \xi_0)$ will be called *wall-shear* line and denoted by $\overline{\gamma}$. Another quantity of interest is

$$S_{\perp}(s) = \frac{\langle \overline{\omega}, \overline{J}\overline{\omega} \rangle}{|\overline{\omega}|^2} |_{\xi(s,\xi_0)}, \tag{E.89}$$

where

$$\overline{J}(\xi) = \lim_{T \to \infty} \frac{1}{T} \int_{t_0 - T}^{t_0} e^{\int_{t_0}^{t} \partial_\eta u_3(\xi,0,\tau) d\tau} J(\xi, t, t_0) d\tau,$$

$$J(\xi, t, t_0) = D_\xi \mathbf{A}(\xi, 0, t) + \mathbf{A}(\xi, 0, \tau) \otimes \int_{t_0}^{t} D_\xi \partial_\eta u_3(\xi, 0, s) ds$$

and

$$\overline{\omega}(\xi) = \overline{\mathbf{A}}^{\perp}(\ \xi), \tag{E.90}$$

with $(a, b)^{\perp} = (-b, a)$. In the above $< \cdot, \cdot >$ is the standard inner product, $\otimes$ denotes the tensor product and D_ξ is the *Jacobian.* Also note that the components of $\overline{\omega}$ are the contravariant components of the time averaged *wall-vortcity* field.

Substituting the expression (E.74) for g in (E.41), we get in terms of physical components

$$\partial_\eta^2 v_3(\xi, 0, t) = -\frac{1}{h_1 h_2} (\partial_{\xi_1}[h_2 \partial_\eta v_1] + \partial_{\xi_2}[h_1 \partial_\eta v_2]) |_{(\xi,0,t)} \ . \tag{E.91}$$

Since the body is at rest in the inertial frame of reference $\mathcal{R}$, $\mathbf{w} \equiv 0$ so that $\mathbf{v} = \mathbf{u}$ and the relation(E.91) can be expressed as

$$\partial_\eta^2 u_3(\xi, 0, t) \ = \ -\nabla_\xi \cdot \tau(\xi, t), \tag{E.92}$$

where, $\nabla_\xi \cdot$ is the on-wall divergence operator

$$\nabla_\xi \cdot \tau \equiv \frac{1}{h_1(\xi, 0) h_2(\xi, 0)} \left[\partial_{\xi_1}(h_2(\xi, 0)\tau_1) + \partial_{\xi_2}(h_1(\xi, 0)\tau_2)\right]. \tag{E.93}$$

Similar the relations E.53 simplify to

$$\partial_\eta^2 u_1(\xi, 0, t)\mathbf{e}_1 + \partial_\eta^2 u_2(\xi, 0, t)\mathbf{e}_2 \ = \ \left(\frac{1}{\mu}\nabla_\xi p - \tau\left[\frac{1}{h_1}\partial_\eta h_1 + \frac{1}{h_2}\partial_\eta h_2\right]\right)_{(\xi,0,t)} \tag{E.94}$$

where, ∇_ξ is on-wall gradient operator

$$\nabla_\xi p \equiv \frac{\mathbf{e}_1}{h_1}\partial_{\xi_1} p(\xi, 0, t) + \frac{\mathbf{e}_2}{h_2}\partial_{\xi_2} p(\xi, 0, t). \tag{E.95}$$

Since for incompressible flows

$$\partial_\eta u_3(\xi, 0, t) \equiv 0, \tag{E.96}$$

the slope formulae simplify considerably. Note that for steady flows the relations

(E.94,E.92) and (E.96) are always satisfied; even when the flow is compressible.

E.2.2 Separation on rigidly moving boundaries

Let us consider now a fluid flow $\mathbf{u}(\mathbf{r},t)$ past a curved boundary $\mathcal{B}(t)$ which is moving as a rigid body. Motion of $\mathcal{B}(t)$ can be described in terms of the velocity $\mathbf{v}_{\mathcal{B}}(t)$ of it's center of mass $\mathbf{r}_O(t)$ and the angular velocity $\mathbf{\Omega}(t)$.

Let $\hat{\mathcal{R}}$ be a frame centered at $\mathbf{r}_O$ translating and rotating with $\mathbf{B}(t)$, so that in $\hat{\mathcal{R}}$, $\mathbf{B}(t)$ is stationary for all times. In such a case, the transformation (E.20), takes a special form

$$\mathbf{r} = \mathbf{r}_O(t_0) + \int_{t_0}^{t} \mathbf{v}_{\mathcal{B}}(\tau)d\tau + \hat{\mathbf{r}}, \tag{E.97}$$

where

$$\hat{\mathbf{r}} = F(\xi,\eta)\hat{\mathbf{i}} + G(\xi,\eta)\hat{\mathbf{j}} + H(\xi,\eta)\hat{\mathbf{k}}, \tag{E.98}$$

$\hat{\mathbf{i}},\hat{\mathbf{j}},\hat{\mathbf{k}}$ are the time-dependent Cartesian unit vectors in the frame $\hat{\mathcal{R}}$ and (ξ,η) is a curvilinear coordinate system in $\hat{\mathcal{R}}$ such that $\eta = 0$ defines the boundary $\mathcal{B}(t)$ for all times. Therefore

$$\mathbf{w} = -\mathbf{v}_{\mathcal{B}}(t) - \mathbf{\Omega}(t) \times \hat{\mathbf{r}}, \tag{E.99}$$

and

$$\nabla \mathbf{w} = -\mathcal{A}_{\mathbf{\Omega}}, \tag{E.100}$$

where, $\mathcal{A}_{\mathbf{\Omega}}$ is the skew-symmetric matrix corresponding to the angular velocity vector $\mathbf{\Omega}$. Therefore

$$\nabla \mathbf{w} + \nabla \mathbf{w}^T = [w^k_{,i} g^{in} + w^n_{,m} g^{mk}]\mathbf{a}^k \mathbf{a}^n \equiv 0. \tag{E.101}$$

Using the relations (E.75,E.16,E.77) and (E.101) in the equation (E.53) for $i = 1,2$, leads to

$$\begin{aligned}
\partial^2_\eta v_1(\xi,0,t) &= \left[\frac{1}{\mu h_1}\partial_{\xi_1} p - \partial_\eta v_1 (\frac{1}{h_1}\partial_\eta h_1 + \frac{1}{h_2}\partial_\eta h_2)\right]_{(\xi,0,t)} - \rho\left[\partial_\tau w^1 - w^j w^1_{,j}\right]_{(\xi,0,t)}, \\
\partial^2_\eta v_2(\xi,0,t) &= \left[\frac{1}{\mu h_2}\partial_{\xi_2} p - \partial_\eta v_2 (\frac{1}{h_1}\partial_\eta h_1 + \frac{1}{h_2}\partial_\eta h_2)\right]_{(\xi,0,t)} \\
&- \rho\left[\partial_\tau w^2 - w^j w^2_{,j}\right]_{(\xi,0,t)}.
\end{aligned} \tag{E.102}$$

Expressing the above equations in vector notation and noticing

$$[\partial_\tau \mathbf{w} - (\nabla \mathbf{w}) \cdot \mathbf{w}]_{(\xi,0,t)} = -\left[\frac{d\mathbf{v}_{\mathcal{B}}(t)}{dt} + \frac{d\mathbf{\Omega}(t)}{dt} \times \hat{\mathbf{r}} + \mathbf{\Omega}(t) \times (\mathbf{\Omega}(t) \times \hat{\mathbf{r}})\right]_{(\xi,0,t)}, \tag{E.103}$$

yields

$$\begin{aligned}
\partial^2_\eta v_1(\xi,0,t)\mathbf{e}_1 + \partial^2_\eta v_2(\xi,0,t)\mathbf{e}_2 &= \left(\frac{1}{\mu}\nabla_\xi p - \tau\left[\frac{1}{h_1}\partial_\eta h_1 + \frac{1}{h_2}\partial_\eta h_2\right]\right)_{(\xi,0,t)} \\
&+ \mathbf{F}_c(\xi,0,t),
\end{aligned} \tag{E.104}$$

where, $\mathbf{F}_c = F_1\mathbf{e}_1 + F_2\mathbf{e}_2$ is given by

$$F_1\mathbf{e}_1+F_2\mathbf{e}_2+F_3\mathbf{e}_3 = \mathbf{F}_b(\xi,0,t) = -\rho \left[\frac{d\mathbf{v}_{\mathcal{B}}(t)}{dt} + \frac{d\boldsymbol{\Omega}(t)}{dt} \times \hat{\mathbf{r}} + \boldsymbol{\Omega}(t) \times (\boldsymbol{\Omega}(t) \times \hat{\mathbf{r}})\right]_{(\xi,0,t)} . \tag{E.105}$$

Bibliography

[1] F. Abramovich, T. C. Bailey, and T. Sapantinas. Wavelet analysis and its statistical applications. *Royal Statisical Society*, 2000.

[2] M. R. Alam, W. Liu., and G. Haller. Closed-loop separation control: An analytic approach. *Phys. Fluids*, 2006.

[3] A. Antoniadis. Wavelet in statistics: A review. *J. Ital. Statist. Soc.*, 6, 1997.

[4] B. F. Armaly, F. Durst, J. C. F. Pereira, and B. Schonung. Experimental and theoretical investigation of backward-facing step flow. *J. Fluid. Mech.*, 127:473-496, 1983.

[5] A. Azzalini, M. Farge, and K. Schneider. Nonliear wavelet thresholding : A recursive method to determine the optimal denosing threshold. *in press, Applied and Computational Harmonical Analysis*, 2004.

[6] A. Babiano, J. H. E. Cartwright, O. Prio, and A. Provenzale. Dynamics of a small neutrally bouyant sphere in a fluid and targeting in hamiltonian systems. *Phys. Rev. Letters*, 84(25):5764–5767, 2000.

[7] G. Berkooz, P. Holmes, and J. L. Lumley. The proper orthogonal decomposition in the analysis of turbulent flows. *Ann. Rev. Fluid Mech.*, 25:539–575, 1993.

[8] W. G. Bickely. *Phil. Mag.*, 25:746+, 1938.

[9] G. Biswas, M. Breuer, and F. Durst. Backward-facing step flows for various expansion ratios at low and moderate reynolds numbers. *Trans. ASME*, 126:362–374, 2004.

[10] H. Brenner. Slow viscous rotation. *J. Fluid Mech.*, 127:473–496, 1983.

[11] G. T. Chapman. Topological classification of flow separation on three-dimensional bodies. *AIAA-86-0485*, 1986.

[12] C. Chicone. *Ordinary differential equations with applications.* Springer-Verlag, 2006.

[13] H. Collins. *Mathematika*, 2:42+, 1955.

[14] S. J. Cowley, L. L. Van Dommelen, and S. T. Lam. On the lagrangian variables in descriptions of unsteady boundary layer separation. *Phil. Trans. R. Soc. Lond. A*, 333:343–378, 1990.

[15] K. C.Wang. On the dispute about open separation. *AIAA paper No.*, (83), 1983.

[16] U. Dallmann. Topological structures of three-dimensional flow separation. *DFVLR*, 1, 1983.

[17] I. Daubechies. *Ten lectures on wavelets.* Philadelphia: Society of industrial and applied mathematics, 1992.

[18] M . J. A. Davis, K. Buhler, and P. D. Weidman. On secondary flow due to the coaxial rotation of two sphere: low reynolds number theory and finite reynolds number experiment. *Q. J. Mech. Appl. Math*, 56(4):547–569, 2003.

[19] A. T. Degani, J. D. A. Walker, and F. T. Smith. Unsteady separation past moving surfaces. *J. Fluid Mech.*, 375:1–38, 1998.

[20] J. M. Délery. Robert legendre and henri werlé: Toward the elucidation of three-dimensional separation. *Ann. Rev. Fluid Mech.*, 33:129–154, 2001.

[21] S. C. R. Dennis, S. N. Singh, and D. B. Ingham. The steady flow due to a rotating sphere at low and moderate reynolds numbers. *J. Fluid Mech.*, 101:257–279, 1980.

[22] T. L. Doligalski and J. D. A. Walker. The boundary layer induced by a convected twodimensional vortex. *J. Fluid Mech.*, 139:1–28, 1984.

[23] L. L. Van Dommelen and S. J. Cowley. On the lagrangian description of unsteady boundary layer separation. part 1. general theory. *J. Fluid Mech.*, 210:593, 1990.

[24] L. L. Van Dommelen and S. F. Shen. *The genesis of separation*, pages 283–311. In Numerical and Physical Aspects of Aerodynamics Flow, Ed T. Cebici. Long Beach, California, 1982.

[25] D. Donoho and I. Johnstone. Ideal spatial adaptation via wavelet shrinkage. *Biometrika*, 81:425–455, 1994.

[26] W. E and B. Engquist. Blowup of solutions of the unsteady prandtl's equation. *Comm. Pure Appl. Math.*, 50(12):1287–1293, 1997.

[27] M. C. Ece, J. D. A. Walker, and T. L. Doligalski. The boundary layer on an impulsively started rotating and translating cylinder. *Phys. Fluids*, 27:1077–1089, 1984.

[28] J. W. Elliott, F. T. Smith, and S. J. Cowle. Breakdown of boundary layers: (i) on moving surfaces; (ii) in semi-similar unsteady flow; (iii) in fully unsteady flow. *Geophys. Astrophys. Fluid Dynamics*, 25:77–138, 1983.

[29] M. Farge. Wavelet transfrom and their application to turbulence. *Ann. Rev. of Fluid Mech.*, 24:395–457, 1992.

[30] N. Fenichel. Persistence and smoothness of invariant manifolds for the flows. *Ind. Univ. Math. J.*, 21:193–226, 1971.

[31] U. Ghis, K. N. Ghia, and C. T. Shin. High-re solutions for incompressible flow using the navier-stokes equations and a multigrid method. *J. Comp. Phys.*, 48:387–411, 1982.

[32] W. B. Glauret. The flow past a rapidly rotating circular cylinder. *Proc. R. Soc. Lond. A*, 242:108–115, 1957.

[33] P. M. Gresho, D. K. Garting, K. A. Cliffe, K. H. Winters, T. J. Garratt, A. Spence, and J. H. Goodrich. Is the steady viscous incompressible two-dimensional flow over a backward-facing step at re=800 stable? *Int. J. Num. Methods in Fluids*, 17:501–541, 1993.

[34] J. Guckenheimer and P. J. Holmes. *Nonlinear Oscillations, Dynamical Systems, and Bifurcations of Vector Fields.* Springer-Verlag, New York.

[35] Wavelet Toolbox User's Guide. http://www.mathworks.com.

[36] G. Haller. *Chaos near resonance.* Springer-Verlag, New York.

[37] G. Haller. Finding finite-time invariant manifolds in two-dimensional velocity data. *Chaos*, 10:99–108, 2000.

[38] G. Haller. Finding finite-time invariant manifolds in two-dimensional velocity fields. *Chaos*, 10:99–108, 2000.

[39] G. Haller. Exact theory of unsteady separation for two-dimensional flows. *J. Fluid Mech.*, 512:257–311, 2004.

[40] G. Haller and A. Poje. Finite-time transport in aperiodic flows. *Physica D*, 119:352–380, 1998.

[41] G. Haller and T. Sapsis. Where do inertial particles go in fluid flows. *submitted, Physica D*, 2007.

[42] T. Han and V. C. Patel. Flow separation on a spheroid at incidence. *J. Fluid Mech.*, 92:643–657, 1979.

[43] P. Hartman. *Ordinary Differential Equations.* Birkhauser, Boston.

[44] T. Hsieh and K. C. Wang. Three-dimensional separated flow structure over a cylinder with a hemispherical cap. *J. Fluid Mech.*, 324:83–108, 1996.

[45] J. C. R. Hunt, C. J. Abell, J. A. Peterka, and H. Woo. Kinematical studies of the flows around free or surface mounted obstacle; applying topology to flow visualization.

[46] G. Jacobs, D. A. Kopriva, and F. Mashayek. A conservative isothermal wall boundary condition for the compressible navier-stokes equations. . *Scientific Computing -online first*, 2005.

[47] G. Jacobs, D. A. Kopriva, and F. Mashayek. Validation study of a multidomain spectral code for simulation of turbulent flows. *AIAA Journal*, 43:1256–1264, 2005.

[48] G. Kaiser. *A friendly guide to wavelets.* Birkhauser, 1994.

[49] R. P. Kanwal. Slow steady rotation of axially symmetric bodies in a viscous fluid. *J. Fluid Mech.*, 10:17–24, 1960.

[50] J. V. Kelkar, R. A. Maehelkar, and J. Ulbrecht. A rotating sphere viscometer. *Journal of Applied Polymer Science*, 17:3069–3083, 1973.

[51] D. N. Kenwright, C. Henze, and C. Levit. Feature extraction of separation and attachment lines. *IEEE Trans. Vis. Comp. Graph.*, 5:135–144, 1999.

[52] M. S. Kilic, G. Haller, and A. Neishtadt. Unsteady fluid flow separation by the method of averaging. *Phys. Fluids*, 17(067104), 2005.

[53] M. S. Kilic, G. Jacobs, J. S. Hesthaven, and G. Haller. Reduced navier-stokes equations near a flow boundary. *Physica D*, 217:161–185, 2006.

[54] S. E. Kim, S. H. Rhee, and D. Cokljat. Application of modern turbulence models to vortical flow around a 6:1 prolate spheroid at incidence. *41st Aerospace Scinece Meeting and Exhibit, AIAA 2003-429*, 2003.

[55] C. A. Koromilas and D. P. Telionis. Unsteady laminar separation: an experimental study. *J. Fluid Mech.*, 97:347–384, 1980.

[56] H. Lamb. *Hydrodynamics.* Cambridge University Press, 1932.

[57] R. Legendre. Séparation de l'écoulement laminaire tridimensionnel. La Rech. Aéronaut., 54:3–8, 1956.

[58] F. Lekien and G. Haller. Unsteady flow separation on slip boundaries. *J. Fluid Mech. submitted*, 2006.

[59] F. Lekien, T. Insperger, G. Stepan, H. Salman, and G. Haller. Control of separation in two-dimensional flows: Stability and robustness for delayed oscillatory flows. *Automatica*, 2005.

[60] M. J. Lighthill. *Attachment and separation in three-dimensional flows.* Laminar Boundary Layer Theory, Ed. L. Rosenhead. Oxford Univ. Press, New York, 1963.

[61] C. S. Liu and Y. H. Wan. A simple exact solution of the prandtl boundary layer equations containing a point of separation. *Archive for Rational Mechanics and Analysis*, 89(2):177–15, 1985.

[62] S. G. Mallat. *A signal processing tour of wavelets.* Academic Press, San Diego.

[63] B. Mena, E. Levinson, and B. Caswell. Torque on a sphere inside a rotating cylinder. *Journal of Applied Mathematics and Physics (ZAMP)*, 23:173–181, 1972.

[64] S. Mittal and B. Kumar. Flow past a rotating cylinder. *J. Fluid Mech.*

[65] A. M. Monin, A. S. & Yaglom. *Statistical fluid mechanics: Mechanics of Turbulence.* MIT Press, Cambridge.

[66] D. W. Moore. The flow past a rapidly rotating cylinder in a uniform stream. *J. Fluid Mech.*, 2:541–550, 1957.

[67] J. H. Nie and B. F. Armaly. Reattachment of three-dimensional flow adjacent to backward-facing step. *Trans. ASME*, 125:422–428, 2003.

[68] J. H. Nie and B. F. Armaly. Reverse flow regions in three-dimensional backward-facing step flow. *Int. J. Heat Mass Transfer*, 47:4713–4720, 2004.

[69] J. C. Padrino and D. D. Joseph. Numerical study of the steady state unifrom flow past a rotating cylinder. 1994.

[70] D. J. Peake and M. Tobak. Topological structure of three-dimensional separated flows. *AIAA 81-1260*, 1981.

[71] V. J. Peridier, F. T. Smith, and J. D. A. Walker. Vortex-induced boundary-layer separation part 1. the limit re. *J. Fluid Mech.*, 232:99–131, 1991.

[72] A. E. Perry and M. S. Chong. A series expansion study of the navier-stokes equations with applications to three-dimensional separation patterns. *J. Fluid Mech.*, 173:207–223, 1986.

[73] A. E. Perry and B. D. Fairlie. Critical points in flow patterns. *Adv. Geophys. B*, 18:200–215, 1974.

[74] L. Prandtl. Über flüssigkeitsbewegung beisehr kleiner reibung. *Verh. III, Int. Math. Kongr., Heidelberg*, pages 484–491, 1904.

[75] A. Rosko. Perspectives on bluff body aerodynamics. *J. Wind Engineering and Industrial Aerodynamics*, 49:79–100, 1993.

[76] J. A. Sanders and F. Verhulst. *Averaging Methods for Nonlinear Dynamical Systems.* Springer-Verlag, New York, 1985.

[77] O. Sawatzki. Das stromungsfeld um eine rotierebnde kugel. *Acta Mech.*, 9:159–214, 1970.

[78] H. Schlichting and K. Gersten. *Boundary-Layer Theory.* Springer-Verlag, New York, 2000.

[79] W. R. Sears and D. P. Tellionis. Boundary-layer separation in unsteady flow. *SIAM J. Appl. Maths.*, 23:215–234, 1975.

[80] Wikstromm N. Sevennberg, U. Alin N., and C. Fureby. Large eddy simulation of the flow around an inclined prolate spheroid. *Journal of Turbulence*, 5(29), 2004.

[81] S. C. Shadden, F. Lekien, and J. E. Marsden. Definition and properties of lagrangian coherent structures from finite-time lyapunov exponents in two-dimensional aperiodic flows. *Physica D*, 212(34):271–304, 2005.

[82] P. N. Shankar and M. D. Deshpande. Fluid mechanics in the driven cavity flow. *Ann. Rev. Fluid Mech.*, 32:93–136, 2000.

[83] T. Shen, S. F. & Wu. Unsteady separation over maneuvering bodies. *AIAA Journal*, 28:2059–2068, 1990.

[84] R. L. Simpson. Aspects of turbulent boundary layer separation. *Prog. Aerospace Sci.*, 32:457–521, 1996.

[85] S. Stentson. Boundary lyaer separation over slender cones at angle of attack. *AIAA Journal*, 10(5):642–648, 1972.

[86] G. G. Stokes. On the theories of the internal friction of fluids in motion, and of the equilibrium and motion of elsatic solids. *Trans. Camb. Phil. Soc.*, 8:287–, 1845.

[87] Gyr A. Stüer, H. and W. Kinzelbach. Laminar separation on a forward facing step. *Eur. J. Mech. B/Fluids*, 18:675–692, 1999.

[88] A. Surana, O. Grunberg, and G. Haller. Exact theory of three-dimensional flow-separation. part 1. steady separation. *J. Fluid Mech.*, 564:57–103, 2006.

[89] A. Surana and G. Haller. Ghost manifolds in slow-fast systems, with applications to fluid flow separation. *Submitted to Physica D*, 2007.

[90] A. Surana, G. Jacobs, O. Grunberg, and G. Haller. Exact theory of three-dimensional flow-separation. part 2. fixed unsteady separation. *Preprint*, 2007.

[91] A. Surana, G. Jacobs, and G. Haller. Extraction of separation and reattachment surfaces from 3d steady shear flows. *AIAA Journal*, 45(6):1290–1302, 2007.

[92] H. Takagi. Viscous flow induced by slow rotation of a sphere. *Journal of the Physical Society of Japan*, 42(1):319–325, 1977.

[93] R. H. Thomas and K. Walters. The motion of an elastico-viscous liquid due to a sphere rotating about its diameter. *Q. J. Mech. Appl. Math*, 17:39+, 1964.

[94] M. Tobak and D. J. Peake. Topology of three-dimensional separated flows. *Ann. Rev. Fluid Mech.*, 14:61–85, 1982.

[95] B. Vidakovic. *Statistical models by wavelets.* John Wiley and Sons, 1999.

[96] R. von Sachs and J. Neumann. *Wavelet thresholding: Beyond the Gaussian I.I.D. sitaution*, pages 301–329. Wavelets and Statistics, in Springer Lecture Notes in Statistics 103, Ed. A. Antoniadis and G. Oppenheim. Springer Verlag, 1995.

[97] R. von Sachs and K. Schneider. Wavelet smoothing of evolutionary spectra by non-linear thresholding. *Appl. Computational Harmonics, Anal.*, 3:268–282, 1996.

[98] K. C. Wang. Separation patterns of boundary layer over an inclined body of revolution. *AIAA Journal*, 10:1044–1050, 1972.

[99] K. C. Wang. Boundary layer over a blunt body at high incidence with an open-type separation. *Proc. Royal. Soc. London, A.*, 340:33–55, 1974.

[100] K. C. Wang, H. C. Zhou, C. H. Hu, and S. Harrington. Three-dimensional separated flow structures over prolate spheroids. *Proc. Royal. Soc. London, A*, 421:73–90, 1990.

[101] T. G. Wetzel, R. L. Simpson, and S. J. Chesnakas. Measurement of three-dimensional cross-flow separation. *AIAA Journal*, 36:557, 1998.

[102] F. M. White. *Viscous Fluid Flow.* McGraw-Hill, New York, 1991.

[103] S. Wiggins. *Chaotic Transport in Dynamical Systems.* Springer, New York, 1993.

[104] D. Wilhelm, C. Härtel, and L. Kleiser. Computational analysis of the two-dimensional–three-dimensional transition in forward-facing step flow. *J. Fluid Mech.*, 489:1, 2003.

[105] P. T. Williams and A. J. Barker. Numerical simulations of laminar flow over a 3d backward-facing step. *Int. J. Num. Meth. in Fluids*, 24:1159–1183, 1997.

[106] J. Z. Wu, J. W. Gu, and J. M. Wu. Steady three-dimensional fluid particle separation from arbitrary smooth surface and formation of free vortex layers. *AIAA*, (87), 1987.

[107] J. Z. Wu, H. Y. Ma, and M. D. Zhou. *Vorticity and Vortex Dynamics.* Springer, New York, 2006.

[108] J. Z. Wu, R. W. Tramel, F. L. Zhu, and X. Y. Yin. A vorticity dynamics theory of three-dimensional flow separation. *Phys. Fluids. A*, 12:1932–1954, 2000.

[109] L. A. Yates and G. T. Chapman. Streamlines, vorticity lines, and vortices around three-dimensional bodies. *AIAA Journal*, 30:1819–1826, 1992.

2635 - 61